UNICAMP

UNIVERSIDADE ESTADUAL DE CAMPINAS

Instituto de Física "Gleb Wataghin"

Antonio Mauricio Soares Narciso Ferreira

Vértice de três glúons não perturbativo a partir de identidades de Slavnov-Taylor com massa dinâmica do glúon

Nonperturbative three-gluon vertex from Slavnov-Taylor identities with dynamical gluon mass

CAMPINAS, SP

2020

Antonio Mauricio Soares Narciso Ferreira

Nonperturbative three-gluon vertex from Slavnov-Taylor identities with dynamical gluon mass

Vértice de três glúons não perturbativo a partir de identidades de Slavnov-Taylor com massa dinâmica do glúon

Tese apresentada ao Instituto de Física "Gleb Wataghin" da Universidade Estadual de Campinas como parte dos requisitos exigidos para a obtenção do título de Doutor em Ciências, na área de Física.

Thesis presented to the "Gleb Wataghin" Institute of Physics of the University of Campinas in partial fulfillment of the requirements for the degree of Doctor of Sciences, in the area of Physics.

Supervisor/Orientador: Arlene Cristina Aguilar

ESTE EXEMPLAR CORRESPONDE À VERSÃO FINAL DA TESE DEFENDIDA PELO ALUNO ANTONIO MAURICIO SOARES NARCISO FERREIRA, E ORIENTADA PELA PROFA. DRA. ARLENE CRISTINA AGUILAR.

CAMPINAS, SP

2020

Ficha catalográfica
Universidade Estadual de Campinas
Biblioteca do Instituto de Física Gleb Wataghin
Lucimeire de Oliveira Silva da Rocha - CRB 8/9174

F413n

Ferreira, Antonio Mauricio Soares Narciso, 1988-
Nonperturbative three-gluon vertex from Slavnov-Taylor identities with dynamical gluon mass / Antonio Mauricio Soares Narciso Ferreira. – Campinas, SP : [s.n.], 2020.

Orientador: Arlene Cristina Aguilar.
Tese (doutorado) – Universidade Estadual de Campinas, Instituto de Física Gleb Wataghin.

1. Teoria quântica de campos. 2. QCD não perturbativa. 3. Equações de Schwinger-Dyson. 4. Técnica de gauge. 5. Massa dinâmica de glúon. I. Aguilar, Arlene Cristina, 1977-. II. Universidade Estadual de Campinas. Instituto de Física Gleb Wataghin. III. Título.

Informações para Biblioteca Digital

Título em outro idioma: Vértice de três glúons não perturbativo a partir de identidades de Slavnov-Taylor com massa dinâmica do glúon
Palavras-chave em inglês:
Quantum field theory
Non-perturbative QCD
Schwinger-Dyson equations
Gauge technique
Dynamical gluon mass
Área de concentração: Física
Titulação: Doutor em Ciências
Banca examinadora:
Arlene Cristina Aguilar [Orientador]
Donato Giorgio Torrieri
Jun Takahashi
Jan Martin Pawlowski
José Rodríguez Quintero
Data de defesa: 27-10-2020
Programa de Pós-Graduação: Física

Identificação e informações acadêmicas do(a) aluno(a)
- ORCID do autor: https://orcid.org/0000-0003-2802-5296
- Currículo Lattes do autor: http://lattes.cnpq.br/3311487873554788

MEMBROS DA COMISSÃO JULGADORA DA TESE DE DOUTORADO DE **ANTONIO MAURICIO SOARES NARCISO FERREIRA – RA 73905** APRESENTADA E APROVADA AO INSTITUTO DE FÍSICA "GLEB WATAGHIN", DA UNIVERSIDADE ESTADUAL DE CAMPINAS, EM 27 / 10 / 2020.

COMISSÃO JULGADORA:

- Profa. Dra. Arlene Cristina Aguilar – Orientadora – DRCC/IFGW/UNICAMP
- Prof. Dr. Donato Giorgio Torrieri – DRCC/IFGW/UNICAMP
- Prof. Dr. Jun Takahashi – DRCC/IFGW/UNICAMP
- Prof. Dr. Jan Martin Pawlowski – Universidade de Heidelberg
- Prof. Dr. José Rodriguez Quintero – Universidade de Huelva

OBS.: Ata da defesa com as respectivas assinaturas dos membros encontra-se no SIGA/Sistema de Fluxo de Dissertação/Tese e na Secretaria do Programa da Unidade.

CAMPINAS
2020

To Betina

Agradecimentos

Para a realização deste projeto, tive o privilégio de contar com o apoio de diversas pessoas e instituições às quais gostaria de expressar minha gratidão mais profunda.

Primeiramente, agradeço à minha orientadora, Profa. Dra. Arlene Cristina Aguilar, do Instituto de Física “Gleb Wataghin” (IFGW), Universidade Estadual de Campinas, e meu orientador durante o estágio de pesquisa na Universidade de Valência, Espanha, Prof. Dr. Joannis Papavassiliou, pela oportunidade de participar de suas pesquisas e a orientação sempre atenta e cuidadosa que me dedicaram ao longo destes anos. Seria impossível descrever no corpo desta tese tudo quanto aprendi com meus orientadores e quanto sou grato a eles.

Agradeço ainda aos meus colegas, Dr. Jeyner Castro Cardona, Dra. Clara Teixeira Figueiredo e Emanuel Veras de Souza, cuja colaboração de pesquisa rendeu tanto frutos. Durante o desenvolvimento desta pesquisa, tive o prazer ainda de contar com a participação de professores do IFGW nas comissões avaliadoras de meus seminários de qualificação, especificamente o Prof. Dr. Donato Giorgio Torrieri, Prof. Dr. David Dobrigkeit Chinellato e Profa. Dra. Carola Dobrigkeit Chinellato, e de pré-requisito, Prof. Dr. Alberto Vazquez Saa e novamente o Prof. Dr. Donato Giorgio Torrieri, contribuindo com críticas e sugestões ao meu trabalho.

Durante o doutorado contei com financiamento por uma bolsa do Conselho Nacional de Desenvolvimento Científico e Tecnológico, sob o projeto de número 142226/2016-5. O presente trabalho foi realizado com apoio da Coordenação de Aperfeiçoamento de Pessoal de Nível Superior – Brasil (CAPES) – Código de Financiamento 001, pelo projeto de número 88881.188877/2018-01 para efetuar um estágio de pesquisa na Universidade de Valência, Espanha. Agradeço ainda à Universidade Estadual de Campinas e à Universidade de Valência, e seus respectivos funcionários, pela estrutura e o suporte oferecidos. Em particular, agradeço ao Centro de Computação John David Rogers, cujo sistema de computação de alto desempenho permitiu a realização da etapa computacional desta pesquisa.

Por fim, gostaria de agradecer à minha família pelo apoio para que eu pudesse prosseguir com meus estudos e, especialmente, à minha amada Betina Grosser Martins, quem sempre esteve ao meu lado, nas melhores, assim como nas mais difíceis, etapas deste projeto.

Acknowledgments

In the development of this project, I had the privilege of counting on the support of numerous persons and institutions, to which I would like to express my deepest gratitude.

Firstly, I thank my supervisor, Dr. Arlene Cristina Aguilar, of the Gleb Wataghin Institute of Physics (IFGW), University of Campinas, and my supervisor during the Interuniversity Exchange Doctorate Stage in the University of Valencia, Spain, Dr. Joannis Papavassiliou, for the opportunity to participate in their researches and the always attentive and diligent supervision and advice they dedicated to me through the years of my doctoral studies. It would be impossible to describe in the body of this thesis all I have learned with my supervisors and how much I am grateful to them.

I thank also my colleagues, Dr. Jeyner Castro Cardona, Dr. Clara Teixeira Figueiredo and Emanuel Veras de Souza, whose research collaboration has yielded so many fruits. During this research, I had the pleasure of receiving the questions and suggestions of the professors that participated in the evaluation committees for my qualify examination, specifically Dr. Donato Giorgio Torrieri, Dr. David Dobrigkeit Chinellato and Dr. Carola Dobrigkeit Chinellato, and the thesis pre-requisite examination, Dr. Alberto Vazquez Saa and, once more, Dr. Donato Giorgio Torrieri.

During my doctoral studies I had funding from a fellowship of the Brazilian National Council for Scientific and Technological Development, under the Grant No. 142226/2016-5. This study was financed in part by the Coordenação de Aperfeiçoamento de Pessoal de Nível Superior – Brasil (CAPES) – Finance Code 001, under the Grant No. 88881.188877/2018-01, for undertaking an Interuniversity Exchange Doctorate Stage in the University of Valencia, Spain. Moreover, I thank the University of Campinas and the University of Valencia, and their respective staffs, for the resources and support offered to my project. In particular, I thank the Centro de Computação John David Rogers, whose High Performance Computing systems were essential to the computational phase of this research.

Finally, I would like to thank my family for the support they provided me with to pursue my studies and, specially, to my beloved Betina Grosser Martins, who has been by me in the best, as well as the most difficult, moments of this project.

Resumo

O vértice de três glúons não perturbativo desempenha um papel fundamental na geração dinâmica de massa efetiva para o glúon sem quebrar a simetria de gauge da QCD. Isto é conseguido através do mecanismo de Schwinger pelo qual o vértice adquire polos longitudinalmente acoplados associados a excitações de estados ligados sem massa. Neste contexto, uma aplicação ingênua da Técnica de Gauge na solução da identidade de Slavnov-Taylor do vértice de três glúons distorce o seu conteúdo de polos, levando à aparição de polos espúrios em projeções transversas deste vértice. Mostramos que uma pequena modificação da Técnica de Gauge, levando em conta a longitudinalidade de seus polos geradores de massa, restaura a estrutura analítica do vértice produzindo projeções transversas regulares e em bom acordo com simulações na rede. Nossa construção é alcançada separando a identidade de Slavnov-Taylor em duas equações análogas, uma satisfeita pela parte regular do vértice, a outra pelos seus polos longitudinais, e sua principal consequência operacional é a substituição do propagador completo do glúon pelo seu "termo cinético" nas expressões clássicas de Ball-Chiu. Começamos com uma curta revisão do aparato de Teoria de Campos de gauge não Abelianos, culminando na derivação da identidade de Slavnov-Taylor do vértice de três glúons. A seguir, discutimos brevemente o papel do vértice de três glúons na geração dinâmica de massa do glúon e como esta afeta as divergências infravermelhas das funções de Green da QCD. Contudo, enfatizamos que devido aos ghosts permanecerem sem massa não-perturbativamente, divergências infravermelhas originárias dos loops de ghosts podem persistir na teoria completa. A solução de Ball-Chiu da identidade de Slavnov-Taylor é então discutida em detalhes, destacando as modificações necessárias para preservar a longitudinalidade de seus polos geradores de massa. Ato contínuo, o kernel de espalhamento ghost-glúon é avaliado numericamente sob um truncamento em um loop vestido de sua equação de Schwinger-Dyson e o resultado é utilizado na Técnica de Gauge para determinar o vértice de três glúons não perturbativo em cinemática Euclidiana geral. As principais características do vértice de três glúons resultante são a supressão e a divergência logarítmica no infravermelho do fator de forma que acompanha sua estrutura tensorial de nível de árvore. Nossos resultados concordam no infravermelho com simulações na rede e equações de Schwinger-Dyson e recuperam o comportamento perturbativo no ultravioleta.

Abstract

The nonperturbative three-gluon vertex plays a key role in the dynamical generation of an effective gluon mass without breaking the gauge symmetry of QCD. This is achieved by the Schwinger mechanism via the formation of massless bound state excitations in the three-gluon vertex which endow it with longitudinally coupled poles. In this context, a naive application of the Gauge Technique solution to the Slavnov-Taylor identity of the three-gluon vertex distorts its pole content, leading to the appearance of spurious poles in transverse projections of this vertex. We show that a slight modification of the Gauge Technique, accounting for the longitudinality of the mass-generating poles, restores the analytic structure of the vertex, entailing transverse projections that are regular and in good agreement with lattice simulations. Our construction is accomplished by splitting the Slavnov-Taylor identity into two analogous equations, one satisfied by the regular part of the vertex, and the other by its longitudinal pole part, and its main operational outcome is the substitution of the full gluon propagator by its "kinetic term" in the classic Ball-Chiu expressions. We begin with a short review of the field-theoretic apparatus of non-Abelian gauge theories, culminating in the derivation of the three-gluon vertex Slavnov-Taylor identity. Then, we briefly discuss the role of the three-gluon vertex in the generation of dynamical gluon mass and how the later affects the infrared divergences of QCD Green's functions. It is emphasized, however, that because ghosts remain massless nonperturbatively, infrared divergences originating from ghost loops may persist in the full theory. The Ball-Chiu solution of the Slavnov-Taylor identity is then discussed in detail, highlighting the modifications needed in order to account for the longitudinality of its mass generating poles. Next, the ghost-gluon scattering kernel is computed numerically under a one-loop dressed truncation of its Schwinger-Dyson equation, and the result is fed into the Gauge Technique solution to determine the nonperturbative three-gluon vertex in general Euclidean kinematics. The main features displayed by the resulting three-gluon vertex are the infrared suppression and logarithmic divergence of the form factors that accompany its tree-level tensor structure. Our results compare well in the infrared to simulations on the lattice and Schwinger-Dyson equations and recover the perturbative behavior in the ultraviolet.

List of publications during the doctoral research

The following articles, with the candidate's name underlined, have been published during the candidate's doctoral studies as direct results of his research project:

1. Aguilar, A. C., Cardona, J. C., Ferreira, M. N. & Papavassiliou, J.
   Non-Abelian Ball-Chiu vertex for arbitrary Euclidean momenta.
   Phys. Rev. **D96,** 014029.
   arXiv: `1610.06158 [hep-ph]` (2017).

2. Aguilar, A. C., Cardona, J. C., Ferreira, M. N. & Papavassiliou, J.
   Quark gap equation with non-abelian Ball-Chiu vertex.
   Phys. Rev. **D98,** 014002.
   arXiv: `1804.04229 [hep-ph]` (2018).

3. Aguilar, A. C., Ferreira, M. N., Figueiredo, C. T. & Papavassiliou, J.
   Nonperturbative structure of the ghost-gluon kernel.
   Phys. Rev. **D99,** 034026.
   arXiv: `1811.08961 [hep-ph]` (2019).

4. Aguilar, A. C., Ferreira, M. N., Figueiredo, C. T. & Papavassiliou, J.
   Nonperturbative Ball-Chiu construction of the three-gluon vertex.
   Phys. Rev. **D99,** 094010.
   arXiv: `1903.01184 [hep-ph]` (2019).

5. Souza, E. V., Ferreira, M. N., Aguilar, A. C., Papavassiliou, J., Roberts, C. D. & Xu, S.-S.
   Pseudoscalar glueball mass: a window on three-gluon interactions.
   Eur. Phys. J. **A56,** 25.
   arXiv: `1909.05875 [nucl-th]` (2020).

6. Aguilar, A. C., Ferreira, M. N., Figueiredo, C. T. & Papavassiliou, J.
   Gluon mass scale through nonlinearities and vertex interplay.
   Phys. Rev. **D100,** 094039.
   arXiv: `1909.09826 [hep-ph]` (2019).

7. Aguilar, A. C., De Soto, F., Ferreira, M. N., Papavassiliou, J., Rodríguez-Quintero, J. & Zafeiropoulos, S.
   Gluon propagator and three-gluon vertex with dynamical quarks.
   Eur. Phys. J. **C80,** 154.
   arXiv: `1912.12086 [hep-ph]` (2020).

8. Aguilar, A. C., Ferreira, M. N. & Papavassiliou, J.
   Novel sum rules for the three-point sector of QCD.
   Eur. Phys. J. **C80,** 887.
   arXiv: `2006.04587 [hep-ph]` (2020).

Also, the following has been submitted during the period:

9. Aguilar, A. C., Ferreira, M. N. & Papavassiliou, J.
   Gluon dynamics from an ordinary differential equation.
   arXiv: `2010.12714 [hep-ph]` (Oct. 2020).

Lastly, the following proceedings article has been published during the doctoral research:

10. Aguilar, A. C. & Ferreira, M. N..
    Quark mass generation with Schwinger-Dyson equations
    in *14th International Workshop on Hadron Physics*
    (May 2018).
    arXiv: `1805.09152 [hep-ph]`.

List of Acronyms

The following table collects the various acronyms used throughout the thesis, in alphabetical order, and their meanings. The page of the first occurrence of an acronym is included in the rightmost column.

Acronym	**Meaning**	**Page**
1PI	one particle irreducible	17
BC	Ball-Chiu	19
BRST	Bechi-Rouet-Stora-Tyutin	16
BSE	Bethe-Salpeter equation	53
ETC	equal time commutation relation	26
IR	infrared	15
MOM	momentum subtraction scheme	43
PT-BFM	Pinch Technique-Background Field Method	52
QCD	Quantum Chromodynamics	15
QED	Quantum Electrodynamics	15
SDE	Schwinger-Dyson equation	17
STI	Slavnov-Taylor identity	16
UV	ultraviolet	22
WI	Ward identity	36

Contents

1

Introduction

One of the most eminent challenges of current theoretical physics is to understand the highly nontrivial features of the strong nuclear interaction through the theory of Quantum Chromodynamics (QCD) [11] and its fundamental degrees of freedom, gluons and quarks. QCD is a Non-Abelian gauge theory, based on the group $SU(3)$, with quarks being fermions carrying fractional electric charges, and gluons being the gauge bosons that mediate the strong force [11]. The Non-Abelian nature of this theory implies, among other things, that the gluon field is self interacting, which makes it far more complex than the Abelian Quantum Electrodynamics (QED). But even among the Non-Abelian interactions of the Standard Model, QCD is distinguished by the fact that its interaction is *strong*.

Indeed, while a perturbative implementation of QCD is still possible at high energies, by virtue of its asymptotic freedom [12, 13], some of the most prominent features of this theory manifest in the infrared (IR) where the interaction becomes strong and transcends a perturbative analysis. Paramount among these phenomena are the confinement [14–16] of quarks and gluons, which states that free quarks and gluons are not observed at low energies; dynamical chiral symmetry breaking [2, 10, 17–26], the mechanism by which quarks acquire effective masses that far exceed their perturbative values; dynamical gluon mass generation [6, 27–35], through which the gluon propagator becomes IR finite, without adding a mass term or Higgs field to the Lagrangian; and the formation of the rich spectrum of hadrons [11, 36, 37]. Evidently, the description of these phenomena from first principles is only possible with nonperturbative tools.

In the attempt to describe QCD nonperturbatively, many approaches aim to compute its Green's functions, *i.e.* its full propagators and vertices, which encode all the information about the theory. Indeed, while the Green's functions are not physical observables, given that they are dependent on the gauge and renormalization scheme chosen, they can be appropriately combined to compute observables, which are gauge and Renormalization Group invariant. In particular, in spite of the gauge fixing, the gauge invariance of the theory manifests itself in a series of relations among the different Green's functions called Slavnov-Taylor identities (STIs) [38, 39], which encode the Bechi-Rouet-Stora-Tyutin (BRST) [40–42] generalization of the gauge transformation for the gauge fixed Lagrangian.

In recent works, a particular Green's function, the three-gluon vertex, has been the object of intense research efforts [4, 7, 8, 43–60]. This vertex plays an essential role in the gluon mass generation mechanism [6, 32, 61–63] and is an ingredient in the analysis of several nonperturbative problems, such as the formation of gluonic bound states [5, 64–66], called glueballs [67–70], and hybrid states [71], constituted by valence gluons and quarks. Especially, it has been noted that the transversely projected nonperturbative three-gluon vertex in Landau gauge exhibits a marked suppression with respect to its perturbative version [4, 7, 43–60] and the impact of this suppression in the behavior of other Green's functions, as well as the bound state spectrum, was analyzed in numerous recent works [5, 6, 56, 57, 62, 63, 71].

In this thesis, we investigate the nonperturbative behavior of the three-gluon vertex. We will restrict ourselves to the pure Yang-Mills theory, in which all the fundamental features of the three-gluon vertex are already manifest, with quark effects furnishing subleading quantitative corrections [7, 57]. It will be shown that a sufficient condition for its characteristic suppression is the masslessness of the ghost fields [4, 52], whose introduction is necessary in fixing the gauge covariantly [72]. Specifically, the masslessness of the ghosts leads to the appearance of a logarithmic divergence [52] in the form factor of the tree-level tensor structure of the transversely projected vertex. This divergence forces the form factor to change sign for sufficiently small momenta, hence vanishing at some intermediate point and being necessarily small in the neighborhood of that zero-crossing [4, 52].

In contrast, the gluon propagator was found by the combined effort of several studies to be IR finite and nonzero at the origin [6, 7, 30–35, 73–83]. Such a behavior of the gluon field may be interpreted in terms of a *dynamically* generated effective gluon mass, as pioneered by Cornwall [27]. In this picture, the effective mass is generated without breaking the gauge symmetry of the theory, nor changing the QCD Lagrangian in any way, through the Schwinger mechanism [30–32, 34, 35, 62, 84–89]. As we will discuss, this mechanism of dynamical gluon mass generation hinges on the appearance of massless bound state excitations [27, 31, 32, 34, 35, 61, 62, 90] in the three-gluon vertex, which acquires as a result a set of poles longitudinally coupled to the external gluon momenta. These poles are responsible for the evasion of the so-called "seagull cancellation" which, in the absence of such divergences, would force the gluons to remain massless under radiative corrections [31, 32, 34, 35, 61]. Vitally, the longitudinality of these mass-generating poles guarantees their decoupling from on-shell amplitudes [32, 86, 87, 89] and must be preserved in any sound approximation scheme for the computation of the three-gluon vertex.

Among the nonperturbative methods which have become standard tools for analyzing the IR behavior of QCD, we will be particularly concerned with the results of Monte Carlo simulations on the lattice, and the Schwinger-Dyson equations (SDEs) and the Gauge Technique in the continuum, each of which has a series of strengths and limitations.

Lattice QCD capitalizes on Wilson's [14] formulation of gauge theories on a discretized lattice of Euclidean space points and is suitable for numerical simulation of field configurations [91], from which Green's functions [7, 43–46, 48, 73–76, 78, 79, 81] and bound state spectra [92, 93], among other things [94], can be calculated. The main power of lattice simulations lies in the fact that it approximates the real, continuum theory, by *in principle* controllable and systematically improvable parameters, namely the lattice spacing and volume, and the number of field configurations probed by the Monte Carlo method. In the limit of vanishing lattice spacing, infinite volume and configuration sampling, the full theory is recovered. In practice, lattice simulations are extremely computationally intensive, requiring the disputed resource of supercomputer time. Moreover, lattice simulations are intrinsically limited in what they can compute. In particular, they cannot handle Minkowski space and can only directly evaluate connected Green's functions, whereas for many purposes it is important to understand the behavior of the one particle irreducible (1PI) functions. An important example where this limitation is specially important is in the study of the gluon mass generation mechanism. Given that the mass-generating vertex poles of the Schwinger mechanism are longitudinally coupled, they do not appear directly in the lattice observables of vertex functions.

On the continuum front, the SDEs [95, 96] are the equations of motion of the complete nonperturbative Green's functions [97–100]. They constitute an infinite tower of coupled nonlinear integral equations, valid at all momentum scales, which connect Green's functions of ever increasing order. The SDEs are valid in Euclidean as well as Minkowski space [101–103], *in principle*, and can isolate 1PI functions. However, the infinite system of coupled equations cannot generally be solved exactly. It is necessary to truncate the tower of SDEs, retaining a finite, and usually small, subset of Green's functions [98–100, 104, 105]. This inevitable truncation is particularly problematic because there is no parameter that controls the size of the ensuing error, and hence no *a priori* guarantee that this error is small. Moreover, preserving the fundamental symmetries of the theory - especially the gauge symmetry - under truncation is extremely difficult [2, 15, 25, 30, 59, 104–112], in general. Lastly, while the SDEs hold *in principle* in Minkowski, or equivalently in the Euclidean space with complex momenta, most SDE studies are carried out in the Euclidean metric. This is largely because the Green's functions may contain non-analiticities [101–103, 113–117] which must be dealt with carefully in the integrals that the SDEs contain, complicating their solution. For Euclidean momenta the problem is simplified because the non-analiticities of the Green's functions that are most difficult to handle are usually avoided.

Given that we lack an *a priori* systematically improvable truncation scheme for SDEs, the success of their treatment is usually judged by the *apparent convergence* of the results obtained through ever more sophisticated truncations, and by their agreement to the outputs of other methods, such as lattice QCD. In other words, one validates the approximations employed *a posteriori*. In this context, it is important to enrich the repertoire of nonperturbative techniques we compare our results to, adding to the analysis the outcomes of Gauge Technique, discussed below, Functional Renormalization Group [58, 60], the restrictions imposed by Operator Product Expansion [118], and others.

The focal point of this thesis is the analysis of the three-gluon vertex of QCD through the Gauge Technique [119–123]. This approach consists of solving the STIs satisfied by the Green's functions of the theory to determine part of the form factors of one Green's function, usually a vertex [1, 4, 7, 124–128], in terms of the others that appear in the identity. Naturally, since the STIs are valid nonperturbatively, the Gauge Technique provides nonperturbative information on the vertex computed through it. Then, the

Gauge Technique result can be used either as a nonperturbative Ansatz for the vertices appearing in SDEs [2, 6, 10, 25, 107, 108, 119–122, 129–132], facilitating their truncation, or as a point of comparison for the vertex computed by some other means.

However, in any Gauge Technique there will be a part of the vertex under consideration that is left undetermined by the STI, which is a fundamental limitation of the method [106, 108, 131]. In this context, it is essential to preserve the analytic structure of the vertex if this undetermined part is omitted in an approximation. This a nontrivial requirement, because, as we will see in Chapter 4, a naive solution of the STI usually introduces divergences, known as "kinematic divergences" [124–126], in certain kinematic limits. This latter issue has been solved in classical works [124–126] under the assumption that the vertex is regular. However, in the presence of dynamically generated gluon mass the problem is aggravated, since in this case the vertex is actually *required* to have poles which, as mentioned, must be longitudinally coupled [27, 31, 32, 34, 35, 61, 62, 90]. As it turns out, a naive Gauge Technique construction of the three-gluon vertex gives rise to poles that survive transverse projections of the vertex and are incompatible with the required longitudinality of the vertex poles in the gluon mass generation mechanism [4]. Moreover, such transverse poles are decidedly not observed on the lattice [7, 43–49]. As such, the usual Gauge Technique must be modified in the presence of dynamical gluon mass generation, properly handling the longitudinality of the mass-generating poles.

The motivation of our study of the three-gluon vertex through the Gauge Technique is threefold:

(i) On a purely theoretical side, we wish to demonstrate that a gauge technique solution of this vertex is perfectly consistent with gluon mass generation, once proper account is taken of the requirement of longitudinally coupled vertex poles. Indeed, the classical works of Ball-Chiu (BC) and others did not include the possibility of dynamical mass generation, and a direct application of the BC solution is unsuitable in this case. The source of the difficulty in the dynamically massive case is that the longitudinal vertex poles appear also in the tensor structures of the vertex that contain the form factors that are left undetermined by the STI. As a result, if the undetermined form factors are casually omitted in an approximation, the pole structure of the vertex is distorted.

As we will show, a slight modification of the Gauge Technique construction is possible, that takes explicitly into account the longitudinality of the vertex poles. The fundamental step in this improved procedure is that the longitudinal pole structure of the vertex is separated by splitting the STI into two equations, one involving only the regular part of the vertex and one involving its pole content. The two resulting equations can then be solved separately. Surely enough, the Gauge Technique vertex thus obtained still contains undetermined parts which, however, are regular, and can be safely omitted without compromising the longitudinality of the poles of the full vertex. Importantly, in the resulting solution the full gluon propagator is substituted by its "kinetic term" only, which is defined by subtracting from the inverse propagator its dynamical mass. Evidently, this means that in order to evaluate the Gauge Technique vertex, one must have knowledge of the dynamical gluon mass, which must be computed by other means.

(*ii*) Then, we aim to connect the *qualitative* features of the nonperturbative three-gluon vertex, its suppression with respect to the perturbative behavior, and its IR divergences, to the behavior of the other Green's functions that appear in its STI. Namely, the gluon and ghost propagators and the ghost-gluon scattering kernel. In particular, we will show that the kinetic term of the gluon propagator by itself encodes most of the qualitative features of the three-gluon vertex, with the ghost sector amounting to quantitative corrections.

(*iii*) Then, for a quantitative analysis, we explicitly compute an approximation to the ingredients entering the STI of the nonperturbative three-gluon vertex, allowing us to concretely evaluate its Gauge Technique solution including ghost sector corrections, and contrast it to the results obtained for this vertex by other approaches. Specifically, we use fits to lattice data for the ghost and gluon propagators that are consistent with the gluon mass generation mechanism, whereas the ghost-gluon scattering kernel is computed through a one-loop dressed truncation of its corresponding SDE. We compare our Gauge Technique results for the three-gluon vertex to lattice [44, 45] and SDE [53, 59] outputs obtained by other researchers and find satisfactory agreement, indicating convergence of the state of the art nonperturbative results for this function.

Beside achieving the above objectives, our work furnishes results that can be used as input for other computations that require knowledge about the three-gluon vertex. Especially, recent work indicates that the nonperturbative behavior of this vertex plays an important role in the description of glueballs [5] and hybrid states [71], and is a crucial ingredient in the SDE of the gluon propagator itself, with important effects on the generation of lattice-compatible gluon mass [6, 62, 63].

The material presented in this thesis is organized as follows:

In Chapter 2 we review some fundamental field theoretic concepts, such as the field equations of motion, the definition of Green's functions as expectation values of time-ordered products of fields, the BRST symmetry of the gauge fixed Lagrangian, and present a derivation of the STIs of QCD that will be used in this work. We end that chapter with a short note on the renormalization of the Green's functions related by the three-gluon vertex STI.

The next chapter, 4, is devoted to reviewing the dynamical gluon mass generation and some properties and implications of the ensuing IR finite gluon propagator. It is briefly explained how gauge invariance enforces masslessness of the gauge fields in the absence of poles in the vertices of the theory, and how the inclusion of such poles leads to the generation of a dynamical mass. To simplify those computations whose details are not essential to this work, while still being able to illustrate the main ideas, we cast the mass generation mechanism in terms of scalar QED calculations. Still in Chapter 4, we show that the dynamical gluon mass tends to reduce the degree of IR divergence of the QCD Green's functions, but that the nonperturbative masslessness of the ghost field implies that some IR divergences survive [52], and in particular that the three-gluon vertex is expected to have IR divergent form factors [52]. These divergence will be later connected to the observed behavior of the three-gluon vertex at small momenta, including its IR suppression and zero-crossing. Subsequently, we show that the IR divergences stemming from the masslessness of the ghosts have important implications for the gluon propagator, such as the existence of a maximum for this function and the divergence of its derivative. We end by presenting an Ansatz for the gluon mass and kinetic term that capture the main features of the gluon propagator and is consistent with the most up-to-date results available for these functions.

Chapter 4 follows with a detailed discussion of the Gauge Technique solution of vertices. To fix the ideas, we present first the case of scalar QED, where we can discuss more cleanly the problem of kinematic divergences and its resolution, as well as the modifications needed to perform the Gauge Technique in the presence of dynamically generated gauge boson mass. Then, the BC solution for the three-gluon vertex and its modification in the presence of dynamical gluon mass is presented. We conclude the chapter with an explicit example of the appearance of spurious transverse poles in the vertex if the Gauge Technique solution is applied in the dynamically massive case without the due account of the special tensor structure of its pole content.

In Chapter 5 we analyze in detail the ghost-gluon scattering kernel, which is the most complicated object appearing as ingredient in the Gauge Technique solution of the three-gluon vertex. After recalling some of the fundamental properties of this scattering kernel in the Landau gauge, specially its ultraviolet (UV) finiteness [39], we compute an approximation for it, in general Euclidean kinematics, using a numerically solved truncation of the SDE that it satisfies. The properties of the resulting ghost-gluon scattering kernel are then analyzed in detail, with special attention to its IR divergences, and are compared to results obtained by other means.

With all necessary ingredients at hand, we evaluate numerically the Gauge Technique solution of the three-gluon vertex in general Euclidean kinematics in Chapter 6. We discuss in depth the nonperturbative behavior of the vertex, as found in our solution, with special attention to its IR divergences and its suppression in comparison to its perturbative behavior. Then we compare our results to those obtained from SDE [53, 59] and lattice simulations [44, 45], by other authors, and discuss their agreement.

We present our conclusions and the prospects of further applications of our results in Chapter 7.

In addition, we include five appendices. Appendix A contains the Feynman rules consistent with our conventions and notations; In Appendix B we collect one-loop calculations that are used in the main text for comparison to nonperturbative results or illustration of certain concepts; In Appendix C we give expressions for the projectors that extract the scalar form factors of the ghost-gluon scattering kernel and three-gluon vertex. In Appendix D we present our conventions for converting Minkowski space expressions to Euclidean space; Lastly, in Appendix E we collect the lengthy expressions for the one-loop dressed integrals that determine the form factors of the ghost-gluon scattering kernel in general Euclidean kinematics.

2

Slavnov-Taylor identities

In this chapter we briefly review the field theoretic foundations for the work to come, aiming at the derivation of the STIs of the three-gluon vertex. We follow closely the presentation in [133], but with adaptations in notations and conventions.

Before we start, let us set some common notations.

Throughout this work, we use the convention $g_{\mu\nu} = \mathrm{diag}(1, -1, -1, -1)$ for the metric and denote the derivative with respect to space-time coordinates by ∂_μ. When products of fields at different space-time points are differentiated, it becomes necessary to specify which coordinate the fields are being differentiated with respect to. To that end, we add the symbol of the coordinate being differentiated as an index to ∂. For example,

$$\partial^x_\mu = \frac{\partial}{\partial x^\mu}\,, \qquad \partial^\mu_x = \frac{\partial}{\partial x_\mu}\,. \tag{2.1}$$

Since we will always denote Lorentz indices by Greek letters or explicit numbers, there is no risk of confusing a spacetime coordinate with a Lorentz index. Finally, summation over repeated indices is implied, except for those indices that denote a space-time coordinate, *e.g.* in $\partial^\mu_y \partial^y_\mu$ summation over μ is implied, but not over y.

The content of this chapter is organized as follows. We review the quantization of the pure Yang-Mills QCD theory in Section 2.1, following with the definition of the Green's functions as correlation functions of fields in Section 2.2. Next, we define the ghost-gluon scattering kernel and prove its relation to the usual ghost-gluon vertex in Section 2.3. In Section 2.4 we present the BRST transformations and derive the STIs of the gluon propagator and three-gluon vertex. We close this chapter with a short discussion of the constraint imposed by the three-gluon vertex STIs on the renormalization constants of the theory.

2.1 Pure Yang-Mills QCD

The fundamental fields of the pure Yang-Mills QCD are the gluon fields, to be denoted by $A_\mu^a(x)$, which are associated with the fundamental representation of the group $SU(3)$. A Latin index of a field denotes its color degree of freedom.

Our starting point is the classical Lagrangian density for the pure Yang-Mills theory,

$$\mathcal{L}_{\mathrm{YM}}(x) := -\frac{1}{4} F_a^{\mu\nu}(x) F_{\mu\nu}^a(x)\,, \tag{2.2}$$

where $F_{\mu\nu}^a(x)$ is called the "field strength tensor". $F_{\mu\nu}^a(x)$ is defined in terms of the gluon field, $A_\mu^a(x)$, by

$$F_{\mu\nu}^a(x) = \partial_\mu A_\nu^a(x) - \partial_\nu A_\mu^a(x) + g f^{abc} A_\mu^b(x) A_\nu^c(x)\,, \tag{2.3}$$

where g is the coupling constant and f^{abc} are the structure constants of the $SU(3)$ group, which are anti-symmetric under the exchange of any two indices.

As all the theories describing the interactions of the Standard Model of particle physics, QCD is a gauge theory. Specifically, the classical Lagrangian of Eq. (2.2) is invariant under the *local* gauge transformation

$$A_\mu^a(x) \to A'^a_\mu = A_\mu^a(x) + g f^{abc} \delta\theta_b(x) A_\mu^c(x) - \delta_\mu \delta\theta_a(x)\,, \tag{2.4}$$

where $\delta\theta_a(x)$ is an infinitesimal function and the prime denotes the transformed field. The last term in Eq. (2.3), $g f^{abc} A_\mu^b(x) A_\nu^c(x)$, is of fundamental importance. It manifests the non-Abelian character of the gauge group of QCD and enriches this theory with self coupling of the gluon field.

In order to quantize the theory, we need to fix the gauge. In this work we will restrict ourselves to the linear covariant gauges, which are defined by the Lorentz condition

$$\partial^\mu A_\mu^a(x) = 0\,. \tag{2.5}$$

At the level of the Lagrangian, the gauge fixing can be achieved by the method of Lagrange multipliers, adding to Eq. (2.2) the *gauge fixing* term

$$\mathcal{L}_{\rm gf}(x) := -\frac{1}{2\,\xi}[\partial^\mu A^a_\mu(x)][\partial^\nu A^a_\nu(x)]\,. \tag{2.6}$$

The Lagrange multiplier ξ is called “gauge fixing parameter”.

However, while for QED gauge fixing as above is enough to allow a covariant quantization of the theory, in non-Abelian gauge theories the S-matrix is not unitary when Eq. (2.6) is added to the Lagrangian. To restore unitarity we have to introduce the Faddeev-Popov ghosts term [72] to the Lagrangian. Specifically,

$$\mathcal{L}_{\rm FP}(x) = -[\partial_\mu \bar{c}_a(x)][\partial^\mu c_a(x) + g f^{abc} A^b_\mu(x) c_c(x)]\,, \tag{2.7}$$

where $c_a(x)$ and $\bar{c}_a(x)$ are the ghost and anti-ghost fields. The fields $c_a(x)$ and $\bar{c}_a(x)$ must be considered self-adjoint massless scalars that do not appear in the spectrum of final states. Moreover, they violate the spin-statistics theorem, *i.e.* in spite of being scalars, they anti-commute

$$\{c_a(x), c_b(y)\} := c_a(x)c_b(y) + c_b(y)c_a(x) = 0\,, \tag{2.8}$$

and similarly $\{\bar{c}_a(x), \bar{c}_b(y)\} = 0$ and $\{c_a(x), \bar{c}_b(y)\} = 0$. Nevertheless, the $c_a(x)$ and $\bar{c}_a(x)$ fields commute with the gluons, *i.e.*

$$[c_a(x), A^b_\mu(y)] := c_a(x)A^b_\mu(y) - A^b_\mu(y)c_a(x) = 0\,, \tag{2.9}$$

as well as $[\bar{c}_a(x), A^b_\mu(y)] = 0$.

The complete Lagrangian of pure Yang-Mills QCD is then given by

$$\mathcal{L}(x) = \mathcal{L}_{\rm YM}(x) + \mathcal{L}_{\rm gf}(x) + \mathcal{L}_{\rm FP}(x)\,, \tag{2.10}$$

which is suitable for covariant quantization.

The equations of motion of the fields can then be obtained from Eq. (2.10) using the Euler-Lagrange equations,

$$\frac{\partial \mathcal{L}(x)}{\partial \phi(x)} = \partial_\mu \left(\frac{\partial \mathcal{L}(x)}{\partial[\partial_\mu \phi(x)]} \right)\,, \tag{2.11}$$

where $\phi(x)$ is to be substituted by each of the fields $A^a_\mu(x)$, $c_a(x)$ and $\bar{c}_a(x)$. For the gluon field one then obtains

$$\begin{aligned}\partial^2 A^a_\mu(x) &= \left(1-\frac{1}{\xi}\right)\partial_\mu[\partial^\nu A^a_\nu(x)] + gf^{abc}\partial^\nu[A^b_\mu(x)A^c_\nu(x)] + gf^{abc}\partial^\nu[A^b_\mu(x)]A^c_\nu(x) \\ &\quad + gf^{abc}A^b_\nu(x)\partial^\mu[A^\nu_c(x)] + g^2 f^{abe}f^{cde}A^b_\nu(x)A^\nu_d(x)A^c_\mu(x) \\ &\quad - gf^{abc}[\partial_\mu\bar{c}_b(x)]c_c(x)\,, \end{aligned} \tag{2.12}$$

where $\partial^2 := \partial^\mu\partial_\mu$.

To obtain the equations of motion for the ghost fields, we must set a consistent convention for differentiation with respect to anti-commuting variables. In this work it will be understood that a derivative with respect to an anti-commuting variable is to be taken from the left. In particular, in taking derivatives of a product of anti-commuting variables, the variable that is being differentiated must be anti-commuted to the left before differentiation. For example, if C_1 and C_2 are a pair of anti-commuting variables

$$\frac{\partial[C_1C_2]}{\partial C_1} = C_2\,, \qquad \frac{\partial[C_1C_2]}{\partial C_2} = -C_1\,. \tag{2.13}$$

With this convention, Eq. (2.11) yields for the fields $c_a(x)$ and $\bar{c}_a(x)$ the equations of motion

$$\partial^2 c_a(x) = -gf^{abc}\partial^\mu[A^b_\mu(x)c_c(x)]\,, \tag{2.14}$$

$$\partial^2 \bar{c}_a(x) = -gf^{abc}A^b_\mu(x)\partial^\mu\bar{c}_c(x)\,. \tag{2.15}$$

The quantization of the theory then proceeds by promoting the fields $A^a_\mu(x)$, $c_a(x)$ and $\bar{c}_a(x)$ to operators[1] by prescribing their equal time commutation relations (ETCs). For the gluon field the ETC reads

$$\delta(x_0-y_0)[A^a_\mu(x),\pi^b_\nu(x)] = i\delta^{ab}g_{\mu\nu}\delta^{(4)}(x-y)\,, \tag{2.16}$$

where $\pi^b_\nu(x)$ is the canonical momentum conjugate to $A^b_\nu(x)$, defined as

$$\pi^b_\nu(x) := \frac{\partial\mathcal{L}(x)}{\partial[\partial_0 A^\nu_b(x)]} = \partial_\nu A^0_b(x) - \partial^0 A^b_\nu(x) - gf^{bdc}A^0_d(x)A^c_\nu(x) - \frac{1}{\xi}g^0_\nu\partial^\rho A^b_\rho(x)\,. \tag{2.17}$$

The gluon still commutes with itself at equal times, *i.e.* $\delta(x_0-y_0)[A^a_\mu(x),A^b_\nu(y)]=0$, as

[1] More accurately, operator valued distributions [134].

well as $\delta(x_0 - y_0)[\pi_\mu^a(x), \pi_\nu^b(y)] = 0$.

One special case of the gluon field ETC that will be useful in this chapter is obtained by setting $\mu = \nu = 0$ in Eqs. (2.16) and (2.17). Specifically, since f^{bdc} is anti-symmetric, then $f^{bdc} A_d^0(x) A_\nu^c(x) = 0$, such that Eq. (2.17) reduces to

$$\pi_0^b(x) = -\frac{1}{\xi}\partial^\rho A_\rho^b(x)\,. \tag{2.18}$$

Substituting the above result into Eq. (2.16) yields then

$$\delta(x_0 - y_0)[A_0^a(x), \partial^\rho A_\rho^b(y)] = -i\xi\delta^{ab}\delta^{(4)}(x-y)\,. \tag{2.19}$$

We must also prescribe ETCs for the ghost fields. First, let us define the canonical momenta conjugate to the $c_a(x)$ and $\bar{c}_a(x)$ fields by

$$\begin{aligned}
\sigma_b(x) &:= \frac{\partial\mathcal{L}(x)}{\partial[\partial_0 c_b(x)]} = \partial^0 \bar{c}_b(x)\,,\\
\bar{\sigma}_b(x) &:= \frac{\partial\mathcal{L}(x)}{\partial[\partial_0 \bar{c}_b(x)]} = -[\partial^0 c_b(x) + g f^{bdc} A_d^0(x) c_c(x)]\,,
\end{aligned} \tag{2.20}$$

from which follows that

$$\{c_a(x), \sigma_b(y)\} = \{c_a(x), \partial^0 \bar{c}_b(y)\}\,, \qquad \{\bar{c}_a(x), \bar{\sigma}_b(y)\} = -\{\bar{c}_a(x), \partial^0 c_b(y)\}\,. \tag{2.21}$$

Now, we require that $\{c_a(x), \bar{c}_b(x)\} = 0$ holds at all times [135]. Then,

$$\partial^0\{c_a(x), \bar{c}_b(x)\} = 0\,, \tag{2.22}$$

which implies

$$\{c_b(x), \partial^0 \bar{c}_a(x)\} = -\{\bar{c}_a(x), \partial^0 c_b(x)\}\,. \tag{2.23}$$

Hence, if we prescribe the ETC for the $\bar{c}_a(x)$ field, that of the $c_b(x)$ field follows by imposing Eq. (2.23).

Then, we prescribe

$$\delta(x_0 - y_0)\{\bar{c}_a(y), \partial^0 c_b(x)\} = -\delta(x_0 - y_0)\{\partial^0 c_a(y), \bar{c}_b(x)\} = i\delta^{ab}\delta^{(4)}(x-y)\,, \tag{2.24}$$

which completes the quantization, for the purposes of this work.

2.2 Correlation functions

A quantum field theory is completely determined by the content of its Green's functions, which are given by the time-ordered correlation functions

$$\langle 0| \, \mathrm{T} \left[\phi_1(x_1)\phi_2(x_2)\ldots\phi_n(x_n) \right] |0\rangle \,, \tag{2.25}$$

where the $\phi_i(x)$ can be any of the fields of the theory, $|0\rangle$ is the ground state of the Hamiltonian and T is the time ordering operator.

The action of T on a product of fields is to rearrange them in decreasing order of the time components of their arguments, x_i, reading from left to right. For example, the time-ordered product of two fields is given by

$$\mathrm{T} \left[\phi_1(x)\phi_2(y) \right] = \theta(x_0 - y_0)\phi_1(x)\phi_2(y) \pm \theta(y_0 - x_0)\phi_2(y)\phi_1(x) \,, \tag{2.26}$$

where $\theta(x)$ is the Heaviside step function, and the relative sign between the products is positive if the fields commute and negative if they anti-commute. It is a good moment to recall that, regarding $\theta(x)$ as a distribution, its derivative is

$$\frac{d\theta(x)}{dx} = \delta(x) \,. \tag{2.27}$$

The correlation functions like Eq. (2.25) contain, however, somewhat redundant information, including disconnected Feynman diagrams [136]. They can be decomposed into the so-called connected Green's functions, which are obtained by canceling from those of Eq. (2.25) their disconnected parts [136].

In this work, we will use the notation

$$\langle \, \mathrm{T} \left[\phi_1(x_1)\phi_2(x_2)\ldots\phi_n(x_n) \right] \rangle \,, \tag{2.28}$$

to represent the connected counterpart to Eq. (2.25).

At this point, we emphasize that Lorentz invariance implies that the Green's functions can only depend on the differences of the positions x_i. More specifically,

$$\langle\, \mathrm{T}\,[\phi_1(x_1)\phi_2(x_2)\ldots\phi_n(x_n)]\,\rangle = \langle\, \mathrm{T}\,[\phi_1(x_1-z)\phi_2(x_2-z)\ldots\phi_n(x_n-z)]\,\rangle\,, \tag{2.29}$$

for any four-vector z.

Of special importance are the 2-point Green's functions, called "propagators". In the pure Yang-Mills theory there are two to consider: the gluon propagator,

$$\overline{\Delta}{}^{ab}_{\mu\nu}(x-y) := \langle\, \mathrm{T}\,[A^a_\mu(x)A^b_\nu(y)]\,\rangle\,; \tag{2.30}$$

and the ghost propagator,

$$\overline{D}{}^{ab}(x-y) := -\langle\, \mathrm{T}\,[c_a(x)\bar{c}_b(y)]\,\rangle\,. \tag{2.31}$$

In practice, it is more convenient to work with the Green's functions in momentum space. Taking the Fourier transform of Eqs. (2.30) and (2.31), we define the momentum space propagators as

$$\begin{aligned} \Delta^{ab}_{\mu\nu}(q) &= \delta^{ab}\Delta_{\mu\nu}(q) := \int d^4x\, e^{-iq\cdot x}\langle\, \mathrm{T}\,[A^a_\mu(x)A^b_\nu(0)]\,\rangle\,, && (2.32)\\ D^{ab}(q) &= \delta^{ab}D(q) := -\int d^4x\, e^{-iq\cdot x}\langle\, \mathrm{T}\,[c_a(x)\bar{c}_b(0)]\,\rangle\,, && (2.33) \end{aligned}$$

where we have used Eq. (2.29) to eliminate the integration over y. By Lorentz invariance and the commuting nature of $A^a_\mu(x)$ and $A^b_\nu(0)$, it is easy to see that Eq. (2.32) implies

$$\Delta_{\mu\nu}(q) = \Delta_{\nu\mu}(q) = \Delta_{\mu\nu}(-q)\,. \tag{2.34}$$

As for the ghost propagator, since the $c_a(x)$ and $\bar{c}_b(0)$ fields are anti-commuting and self-adjoint, Eq. (2.33) leads to

$$D^{ab}(-q) = -[D^{ab}(q)]^\dagger\,, \tag{2.35}$$

where the $\dagger$ denotes Hermitian conjugation. Eq. (2.35) allows us to define the "ghost dressing function", $F(q^2)$, which is a Lorentz scalar, by

$$D^{ab}(q) = i\delta^{ab}\frac{F(q^2)}{q^2}\,. \tag{2.36}$$

In general, the connected Green's functions contain diagrams that are "one particle reducible". These are the diagrams that can be written as a product of two Green's functions by cutting a single line. The diagrams that cannot be decomposed in this way are said to be 1PI. Clearly, the 1PI functions contain all the information about the theory, since all other Green's functions can be expressed in terms of the former.

In particular, a connected 3-point Green's function is composed of the corresponding 1PI vertex multiplied by the propagators of each external line.

The focal point of this thesis is the three-gluon vertex, $\mathbb{\Gamma}^{\alpha\mu\nu}_{abc}(q,r,p)$. It is related to the connected Green's functions with three gluon fields by

$$\mathbb{\Gamma}^{\alpha'\mu'\nu'}_{abc}(q,r,p)\Delta_{\alpha'\alpha}(q)\Delta_{\mu'\mu}(r)\Delta_{\nu'\nu}(p) := \int d^4x\, d^4y\, e^{-iq\cdot x - ir\cdot y}\langle\, \mathrm{T}\,[A^a_\alpha(x)A^b_\mu(y)A^c_\nu(0)]\,\rangle\,, \tag{2.37}$$

with momentum conservation expressed as $q+p+r=0$. It is often convenient to factor out a color structure, defining

$$gf^{abc}\,\mathbb{\Gamma}_{\alpha\mu\nu}(q,r,p) := \mathbb{\Gamma}^{abc}_{\alpha\mu\nu}(q,r,p)\,. \tag{2.38}$$

The full 1PI three-gluon vertex is represented diagrammatically[2] in panel (a) of Fig. 2.1, while the connected correlation of Eq. (2.37) is represented in panel (b) of that figure.

The reason for denoting the full three-gluon vertex by the double struck letter $\mathbb{\Gamma}$ will get clearer in the next chapter. There, and in the subsequent treatment, it will be necessary to separate the vertex into a part that contains poles and a part that is regular. Then, we will employ the usual letter Γ to denote the regular part only, whereas the double struck version will refer to the *complete* vertex, *i.e.* the sum of regular and pole parts.

Another 1PI function that will be important in this work is the ghost-gluon vertex, $\Gamma^{abc}_\mu(q,p,r)$, which is defined as

$$\Gamma^{abc}_{\mu'}(q,p,r)D(q)D(p)\Delta^{\mu'}_{\mu}(r) := -\int d^4x\, d^4y\, e^{-iq\cdot x - ip\cdot y}\langle\, \mathrm{T}\,[A^c_\mu(0)c_a(x)\bar{c}_b(y)]\,\rangle\,. \tag{2.39}$$

[2]All Feynman diagrams in this work have been drawn with *JaxoDraw 2.0* [137].

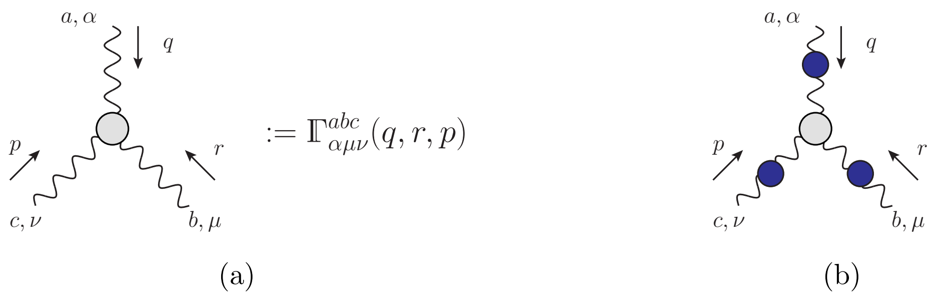

Figure 2.1: (a): Diagrammatic representation of the 1PI full three-gluon vertex. The grey circle denotes that the vertex is 1PI and dressed, whereas the wavy line represents a gluon field. The arrows denote momentum flow. (b): Diagrammatic representation of the connected correlation function of Eq. (2.37). Blue circles represent full propagators.

Again, we factor out a color structure to write

$$-\, g f^{abc} \Gamma_\mu(q, p, r) := \Gamma^{abc}_\mu(q, p, r)\,. \tag{2.40}$$

We represent diagrammatically the full 1PI ghost-gluon vertex in panel (a) of Fig. 2.2, while the connected Green's function of Eq. (2.39) is represented in panel (b) of the same figure.

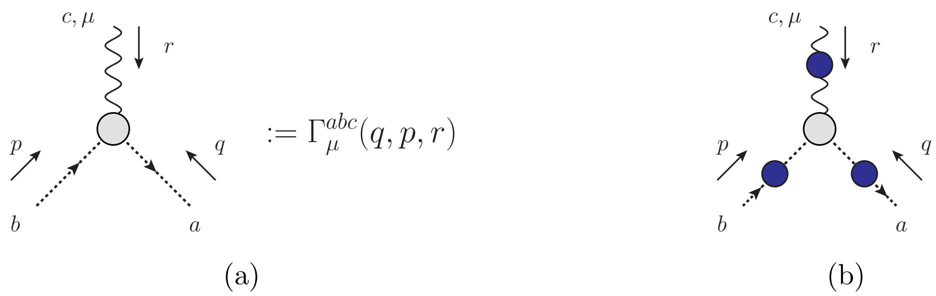

Figure 2.2: (a): Diagrammatic representation of the 1PI ghost-gluon vertex. The dashed line represents a ghost field, and the arrowhead over the line represents ghost number flow. (b): Diagrammatic representation of the connected correlation function of Eq. (2.39).

With the conventions laid down in this section, the Feynman rules for the Green's functions at lowest order in perturbation theory can be obtained. We collect them in Appendix A.

2.3 The ghost-gluon scattering kernel

The STI that will be important in this thesis relates the three-gluon vertex to the gluon and ghost propagators and a ghost-gluon interaction vertex. However, it is not the ghost-gluon vertex of Eq. (2.39) that appears in this STI, but a close relative to it called "the ghost-gluon scattering kernel", to be denoted by $H^{abc}_{\nu\mu}(q,p,r)$. In this section we present the definition of $H^{abc}_{\nu\mu}(q,p,r)$ and demonstrate its relation to the ghost-gluon vertex.

We can *define* the 1PI ghost-gluon scattering kernel as the sum of the diagrams on the right hand side of Fig. 2.3. In those diagrams, a little black cross denotes that the two fields meeting there are evaluated at the same space-time coordinate. The tree-level value of $H^{abc}_{\nu\mu}(q,p,r)$ is given by

$$H^{(0)\,abc}_{\nu\mu}(q,p,r) = -gf^{abc}g_{\nu\mu}\,. \tag{2.41}$$

It will be useful to have a more compact diagrammatic expression for $H^{abc}_{\nu\mu}(q,p,r)$. Such an expression is also shown in Fig. 2.3, but notice that the four point function denoted by a black circle there is neither 1PI nor the full connected ghost-ghost-gluon-gluon function.

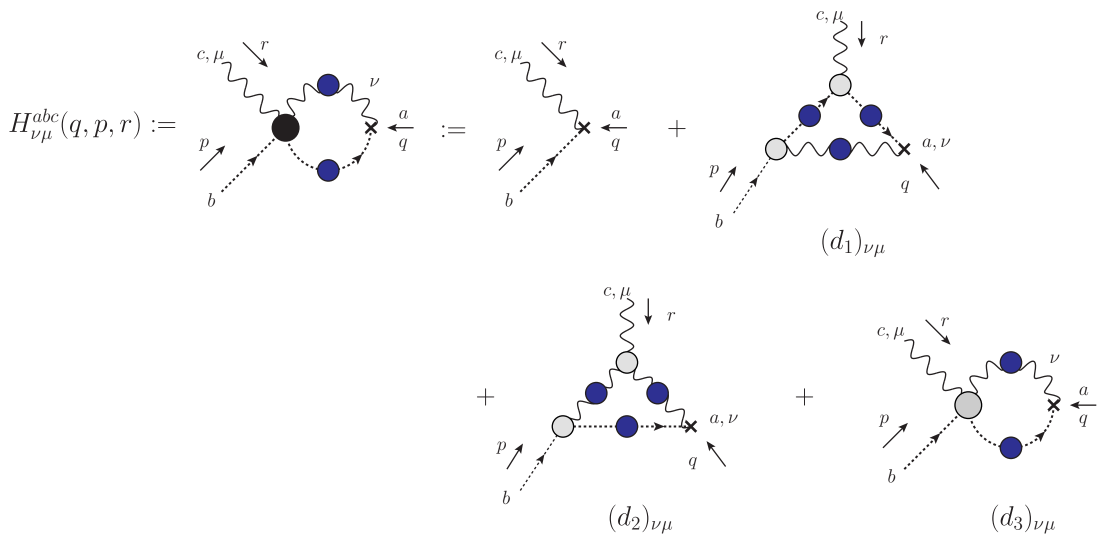

Figure 2.3: Diagrammatic definition of the ghost-gluon scattering kernel, $H^{abc}_{\nu\mu}(q,p,r)$. The first equation defines a compact diagrammatic representation in which the black circle is not 1PI. The second equation expresses $H^{abc}_{\nu\mu}(q,p,r)$ in terms of 1PI functions only. The little black cross represents two fields evaluated at the same space-time coordinate.

To relate the ghost-gluon scattering kernel to a fully connected correlation function, let us define the following Green's functions

$$\mathcal{H}^{abd}_{\nu\rho}(q,p,r) \;:=\; -gf^{amn}\int d^4x\, d^4y\, e^{-iq\cdot x - ip\cdot y}\langle\, \mathrm{T}\left[A^m_\nu(x)c_n(x)\bar{c}_b(y)A^d_\rho(0)\right]\rangle\,, \tag{2.42}$$

$$\Sigma^{ab}_\nu(q)D^{bc}(q) \;:=\; -gf^{amn}\int d^4x\, e^{-iq\cdot x}\langle\, \mathrm{T}\left[A^m_\nu(x)c_n(x)\bar{c}_c(0)\right]\rangle\,, \tag{2.43}$$

in both of which we emphasize the presence of gluon and ghost fields meeting at the same point, x. As usual, we can factor out the color structures, $\Sigma_\nu^{ab}(q) = \delta^{ab}\Sigma_\nu(q)$ and $\mathcal{H}_{\nu\mu}^{abd}(q,p,r) = -gf^{abd}\mathcal{H}_{\nu\rho}(q,p,r)$. The function $\Sigma_\nu^{ab}(q)$ and the connected correlation of Eq. (2.43) are represented diagrammatically in Fig. 2.4.

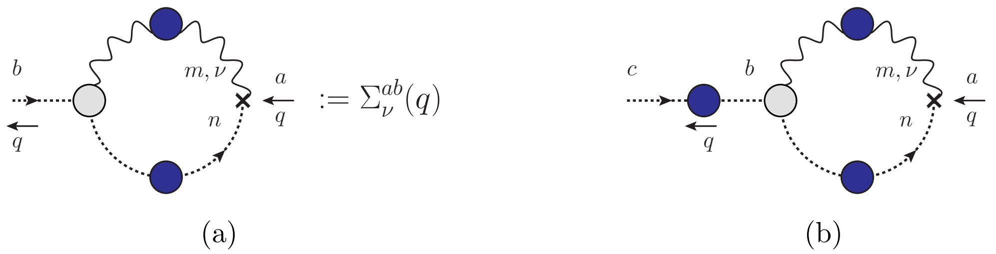

Figure 2.4: (a): Diagrammatic representation of the 1PI function $\Sigma_\nu^{ab}(q)$ appearing in the Eq. (2.43). (b): The connected correlation function of Eq. (2.43).

Decomposing Eq. (2.42) into 1PI functions, we obtain the diagrams shown in Fig. 2.5. In symbols, we write

$$\mathcal{H}_{\nu\rho}^{abd}(q,p,r) = \left[H_{\nu\mu}^{abc}(q,p,r) + \Sigma_\nu^{af}(q)D^{fe}(q)\Gamma_\mu^{ebc}(q,p,r)\right] D^{bg}(p)\Delta_{cd}^{\mu\rho}(r)\,. \tag{2.44}$$

Hence, the ghost-gluon scattering kernel is obtained from the connected $\mathcal{H}_{\nu\rho}^{abd}(q,p,r)$ of Eq. (2.42) by removing the diagram containing the $\Sigma_\nu(q)$ of Eq. (2.43) and amputating the external legs.

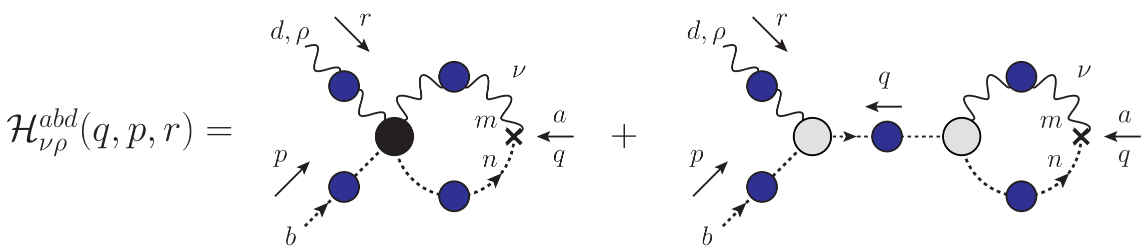

Figure 2.5: Decomposition of $\mathcal{H}_{\nu\rho}^{abd}(q,p,r)$ into 1PI functions.

Now we want to establish the relation between the ghost-gluon scattering kernel and the ghost-gluon vertex. Specifically, we will show that

$$q^\nu H_{\nu\mu}^{abc}(q,p,r) = \Gamma_\mu^{abc}(q,p,r)\,. \tag{2.45}$$

To this end, we must first demonstrate that $q^\nu \Sigma_\nu(q)$ equals the ghost "self-energy", *i.e.*

$$q^\nu \Sigma_\nu(q) = [D^{(0)}(q)]^{-1} - [D(q)]^{-1}\,, \tag{2.46}$$

where the superscript "(0)" denotes the tree-level value (see Appendix A).

To prove Eq. (2.46), we contract Eq. (2.43) with q^ν to obtain

$$q^\nu \Sigma_\nu^{ab}(q) D^{bc}(q) = igf^{amn} \int d^4x\, e^{-iq\cdot x}\, \partial_x^\nu \langle\, \mathrm{T}\, [A_\nu^m(x) c_n(x) \bar{c}_c(0)]\,\rangle\,. \tag{2.47}$$

Next, we bring the derivative inside the time ordered correlation through

$$\begin{aligned}\partial_x^\nu\, \mathrm{T}\, [A_\nu^m(x) c_n(x) \bar{c}_c(0)] &= \partial_x^\nu [\theta(x_0) A_\nu^m(x) c_n(x) \bar{c}_c(0) - \theta(-x_0) \bar{c}_c(0) A_\nu^m(x) c_n(x)] \\ &= \mathrm{T}\, \left[\partial_x^\nu \big(A_\nu^m(x) c_n(x)\big) \bar{c}_c(0)\right]\,,\end{aligned} \tag{2.48}$$

where we used Eq. (2.26) and the fact that $c_n(x)$ and $\bar{c}_c(0)$ anti-commute. Then, Eq. (2.47) reads

$$q^\nu \Sigma_\nu^{ab}(q) D^{bc}(q) = igf^{amn} \int d^4x\, e^{-iq\cdot x} \langle\, \mathrm{T}\, \left[\partial_x^\nu \big(A_\nu^m(x) c_n(x)\big) \bar{c}_c(0)\right]\,\rangle\,. \tag{2.49}$$

Now, we invoke the equation of motion of Eq. (2.15) to rewrite

$$gf^{amn}\, \mathrm{T}\, \left[\partial_x^\nu \big(A_\nu^m(x) c_n(x)\big) \bar{c}_c(0)\right] = -\mathrm{T}\, \left[\partial_x^2 c_a(x) \bar{c}_c(0)\right]\,. \tag{2.50}$$

Moving the ∂_x^2 outside the time-ordering operator using again Eq. (2.26) entails

$$\mathrm{T}\, \left[\partial_x^2 c_a(x) \bar{c}_c(0)\right] = \partial_x^2\, \mathrm{T}\, [c_a(x) \bar{c}_c(0)] - \delta(x_0) \{\bar{c}_c(0), \partial_x^0 c_a(x)\}\,. \tag{2.51}$$

The Eqs. (2.50) and (2.51), when used into Eq. (2.49), lead to

$$q^\nu \Sigma_\nu^{ab}(q) D^{bc}(q) = -i \int d^4x\, e^{-iq\cdot x} \Big(\partial_x^2 \langle\, \mathrm{T}\, [c_a(x) \bar{c}_c(0)]\,\rangle - \delta(x_0) \{\bar{c}_c(0), \partial_x^0 c_a(x)\}\Big)\,. \tag{2.52}$$

Finally, using the ETC of Eq. (2.24) into the Eq. (2.52) results in

$$q^\nu \Sigma_\nu^{ab}(q) D^{bc}(q) = -\delta^{ac} + iq^2 \int d^4x\, e^{-iq\cdot x}\, \partial_x^\nu \langle\, \mathrm{T}\, [c_a(x) \bar{c}_c(0)]\,\rangle = -\delta^{ac} - iq^2 D^{ac}(q)\,, \tag{2.53}$$

where the last equality is established by identifying the integral with that of Eq. (2.33). From Eq. (2.53) the association (2.46) follows trivially.

With Eq. (2.53) in hands, we can proceed to derive Eq. (2.45). Contracting Eq. (2.44) with q^ν and using Eq. (2.53) yields

$$\begin{aligned}\left[q^\nu H^{abc}_{\nu\mu}(q,p,r) - \Gamma^{abc}_{\mu}(q,p,r)\right] D^{bg}(p)\Delta^{\mu\rho}_{cd}(r) &= \mathcal{H}^{abd}_{\nu\rho}(q,p,r) \\ &\quad + iq^2\Gamma^{ebc}_{\mu}(q,p,r)D^{ae}(q)D^{bg}(p)\Delta^{\mu\rho}_{cd}(r)\,. \end{aligned} \tag{2.54}$$

To evaluate the right hand side of Eq. (2.54), we contract Eq. (2.42) with q^ν to find

$$\begin{aligned} q^\nu\mathcal{H}^{abd}_{\nu\rho}(q,p,r) &= igf^{amn}\int d^4x\, d^4y\, e^{-iq\cdot x - ip\cdot y}\,\partial^\nu_x\langle\, \mathrm{T}\,[A^m_\nu(x)c_n(x)\bar{c}_b(y)A^d_\rho(0)]\,\rangle \\ &= igf^{amn}\int d^4x\, d^4y\, e^{-iq\cdot x - ip\cdot y}\langle\, \mathrm{T}\,\left[\partial^\nu_x\big(A^m_\nu(x)c_n(x)\big)\bar{c}_b(y)A^d_\rho(0)\right]\,\rangle\,, \end{aligned} \tag{2.55}$$

after bringing the derivative inside the correlation appropriately. Using the equation of motion, Eq. (2.15), into Eq. (2.55) and moving the derivatives outside the correlation, leads to

$$\begin{aligned} q^\nu\mathcal{H}^{abd}_{\nu\rho}(q,p,r) &= -i\int d^4x\, d^4y\, e^{-iq\cdot x - ip\cdot y}\langle\, \mathrm{T}\,[\partial^2_x c_a(x)\bar{c}_b(y)]\,\rangle \\ &= iq^2\int d^4x\, d^4y\, e^{-iq\cdot x - ip\cdot y}\langle\, \mathrm{T}\,[c_a(x)\bar{c}_b(y)]\,\rangle \\ &= -iq^2\Gamma^{ebc}_{\mu}(q,p,r)D^{ae}(q)D^{bg}(p)\Delta^{\mu\rho}_{cd}(r)\,. \end{aligned} \tag{2.56}$$

To get the last equality in (2.56), we identify the integral appearing in this equation with that of Eq. (2.33).

Using Eq. (2.56) into Eq. (2.54) it thus follows that

$$\left[q^\nu H^{abc}_{\nu\mu}(q,p,r) - \Gamma^{abc}_{\mu}(q,p,r)\right] D^{bg}(p)\Delta^{\mu\rho}_{cd}(r) = 0\,, \tag{2.57}$$

from which Eq. (2.45) follows immediately.

2.4 BRST symmetry and the STIs

The Green's functions, unlike physical observables, are gauge dependent objects. Nevertheless, the gauge invariance of the theory is encoded into a series of relations among the different Green's functions. In Abelian theories, such as QED, these relations are the well known Ward identities (WIs), whereas in non-Abelian gauge theories the WIs are generalized to the so-called STIs.

It is important to note, though, that since we had to fix the gauge in order to appropriately quantize the theory, the full Lagrangian of Eq. (2.10) is no longer invariant under the gauge transformation of Eq. (2.4). However, it is possible to generalize Eq. (2.4) to a transformation that includes the ghost fields, as discovered by Bechi, Rouet, Stora [40, 41] and Tyutin [42], under which the Lagrangian of the quantum theory is invariant. The BRST transformation is the set of one-parameter variations

$$
\begin{aligned}
A^a_\mu(x) \quad &\rightarrow \quad {A'}^a_\mu = A^a_\mu(x) - g\omega f^{abc} c_b(x) A^c_\mu(x) + \omega\partial_\mu c_a(x)\,; && (2.58)\\
c_a(x) \quad &\rightarrow \quad {c'}_a(x) = c_a(x) - \frac{1}{2} g\omega f^{abc} c_b(x) c_c(x)\,; && (2.59)\\
\bar{c}_a(x) \quad &\rightarrow \quad {\bar{c}'}_a(x) = \bar{c}_a(x) + \frac{\omega}{\xi}\partial^\mu A^a_\mu(x)\,; && (2.60)
\end{aligned}
$$

where ω is an anti-commuting *constant*. In particular, $\omega^2 = 0$. Moreover, ω anti-commutes with ghost fields, and commutes with gluon ones, *i.e.*

$$
\begin{aligned}
[\omega, A^a_\mu(x)] =& \{\omega, c_a(x)\} = \{\omega, \bar{c}_a(x)\} = 0\,,\\
[\omega, \partial^x_\nu A^a_\mu(x)] =& \{\omega, \partial^x_\nu c_a(x)\} = \{\omega, \partial^x_\nu \bar{c}_a(x)\} = 0\,. \qquad (2.61)
\end{aligned}
$$

Using the above properties of ω it is easy to show that the transformed fields, A', c' and $\bar{c}'$, satisfy the same (anti-)commutation rules as the original ones.

Comparing the BRST transformation of the gluon field to Eq. (2.4) we notice that Eq. (2.58) is a gauge transformation with $\theta_a(x) = -\omega c_a(x)$. As such, the classical Lagrangian of Eq. (2.2) is clearly BRST invariant. Then, the variations of the gauge-fixing and the Faddeev-Popov Lagrangian terms, Eqs. (2.6) and (2.7), respectively, can be shown to cancel against each other [133] (up to a total divergence). Consequently, Eq. (2.10) is symmetric under the combined transformations of Eqs. (2.58), (2.59) and (2.60).

2.4.1 STI of the gluon propagator

By taking advantage of the BRST transformations, we are now in position to derive STIs. One of the most important and yet simplest to demonstrate is the STI satisfied by the gluon propagator, which reads

$$q^\mu q^\nu \Delta^{ab}_{\mu\nu}(q) = -i\xi\delta^{ab} \,. \tag{2.62}$$

Before proving Eq. (2.62), let us appreciate its significance. Specifically, the STI of Eq. (2.62) allows us to perform our first example of a Gauge Technique implementation, determining part of the nonperturbative propagator. We begin with the most general Lorentz structure of $\Delta^{ab}_{\mu\nu}(q)$, which is given by

$$\Delta^{ab}_{\mu\nu}(q) = -i\delta^{ab}\left[\mathrm{P}_{\mu\nu}(q)\Delta(q^2) + q_\mu q_\nu E(q^2)\right] \,, \tag{2.63}$$

where $\Delta(q^2)$ and $E(q^2)$ are scalar functions, which, by Lorentz symmetry, can only depend on q^2, and $\mathrm{P}_{\mu\nu}(q)$ is the transverse projector defined as

$$\mathrm{P}_{\mu\nu}(q) := g_{\mu\nu} - \frac{q_\mu q_\nu}{q^2} \,. \tag{2.64}$$

The STI of Eq. (2.62) is insensitive to, and hence does not determine, the function $\Delta(q^2)$, since $q^\mu \mathrm{P}_{\mu\nu}(q) = 0$. However, combining Eqs. (2.63) and (2.62) we see that $E(q^2) = \xi/q^4$. Therefore, the complete gluon propagator can be written as

$$\Delta^{ab}_{\mu\nu}(q) = -i\delta^{ab}\left[\mathrm{P}_{\mu\nu}(q)\Delta(q^2) + \xi\frac{q_\mu q_\nu}{q^4}\right] \,. \tag{2.65}$$

The physical significance of Eq. (2.65) is that the longitudinal part of the gluon propagator retains its tree-level form (see Appendix A) to all orders and even nonperturbatively. In particular, in the Landau gauge, defined by $\xi = 0$, the gluon propagator is fully transverse, *i.e.* $q^\mu \Delta^{ab}_{\mu\nu}(q) = q^\nu \Delta^{ab}_{\mu\nu}(q) = 0$.

Let us demonstrate Eq. (2.62) then. We begin by noticing that, since ghosts do not appear in the spectrum, any correlation function with an unbalanced number of ghosts and anti-ghosts vanishes. In particular,

$$\langle\, \mathrm{T}\left[\partial^\mu_x A^a_\mu(x)\bar{c}_b(y)\right] \rangle = 0 \,. \tag{2.66}$$

Since the theory is BRST invariant, Eq. (2.66) must also hold if we transform the $A^a_\mu(x)$

and $\bar{c}_b(y)$ fields in accordance with Eqs. (2.58) and (2.60). Therefore,

$$\frac{1}{\xi}\langle\, \mathrm{T}\,[\partial_x^\mu A_\mu^a(x)\partial_y^\nu A_\nu^b(y) - g f^{adc}\partial_x^\mu\big(c_d(x)A_\mu^c(x)\big)\bar{c}_b(y) + \partial_x^2 c_a(x)\bar{c}_b(y)]\,\rangle = 0\,, \tag{2.67}$$

where we used Eq. (2.66) and that $\omega^2 = 0$ to eliminate some terms.

The last two terms inside the time ordering operator in Eq. (2.67) cancel against each other on invoking the equation of motion, Eq. (2.15). Thus,

$$\langle\, \mathrm{T}\,[\partial_x^\mu A_\mu^a(x)\partial_y^\nu A_\nu^b(y)]\,\rangle = 0\,. \tag{2.68}$$

Moving the derivatives out of the time-ordered correlation then yields

$$\begin{aligned} 0 &= \partial_x^\mu\partial_y^\nu\langle\, \mathrm{T}\,[A_\mu^a(x)A_\nu^b(y)]\,\rangle + \partial_x^\mu\left(\delta(x_0-y_0)\langle\, \mathrm{T}\,[A_\mu^a(x), A_0^b(y)]\,\rangle\right) \\ &\quad -i\delta(x_0-y_0)\langle\, \mathrm{T}\,[A_0^a(x), \partial_y^\nu A_\nu^b(y)]\,\rangle \\ &= \partial_x^\mu\partial_y^\nu\langle\, \mathrm{T}\,[A_\mu^a(x)A_\nu^b(y)]\,\rangle + i\xi\delta^{ab}\delta^{(4)}(x-y)\,, \end{aligned} \tag{2.69}$$

on using the gluon ETC of Eq. (2.19). Fourier transforming Eq. (2.69) and using the Lorentz invariance of the Green's functions leads to

$$q^\mu p^\nu \int d^4x\, e^{-i(q+p)\cdot x}\int d^4y\, e^{ip\cdot(x-y)}\langle\, \mathrm{T}\,[A_\mu^a(x-y)A_\nu^b(0)]\,\rangle - i\xi\delta^{ab}\delta^{(4)}(q+p) = 0\,. \tag{2.70}$$

Now we can identify the integral in Eq. (2.70) with the definition of the momentum space gluon propagator in Eq. (2.32), to obtain

$$\left[q^\mu p^\nu \Delta_{\mu\nu}^{ab}(-p) - i\xi\delta^{ab}\right]\delta^{(4)}(q+p) = 0\,. \tag{2.71}$$

Finally, $\delta^{(4)}(q+p)$ enforces that $p=-q$ and Eq. (2.62) follows.

2.4.2 Three-gluon vertex STI

We have now reached the culminating point of this chapter, which is to derive the STI of the three-gluon vertex. We begin with the vanishing correlation

$$\langle\, \mathrm{T}\,[\bar{c}_a(x)A_\mu^b(y)A_\nu^c(z)]\,\rangle = 0\,. \tag{2.72}$$

The same result must hold if we perform a BRST transformation on the fields. Hence, using Eq. (2.72) we obtain

$$
\begin{aligned}
\frac{1}{\xi}\partial_x^\alpha\langle\, \mathrm{T}\,[A^a_\alpha(x)A^b_\mu(y)A^c_\nu(z)]\,\rangle \;=\;& -gf^{bed}\langle\, \mathrm{T}\,[A^e_\mu(y)c_d(y)\bar{c}_a(x)A^c_\nu(z)]\,\rangle \\
& -\partial^y_\mu\langle\, \mathrm{T}\,[c_b(y)\bar{c}_a(x)A^c_\nu(z)]\,\rangle \qquad (2.73)\\
& -gf^{cgf}\langle\, \mathrm{T}\,[A^g_\nu(z)c_f(z)\bar{c}_a(x)A^b_\mu(y)]\,\rangle \\
& -\partial^z_\nu\langle\, \mathrm{T}\,[c_c(z)\bar{c}_a(x)A^b_\mu(y)]\,\rangle\,, \qquad (2.74)
\end{aligned}
$$

where we have used the anti-commutation properties of the ghost fields and of ω, and moved the derivatives outside the time-ordering operation.

Next we Fourier transform the Eq. (2.74) and identify the resulting integrals with Eqs. (2.37), (2.39) and (2.42), to obtain

$$
\begin{aligned}
\frac{iq^\alpha}{\xi}\mathbb{\Gamma}^{abc}_{\alpha'\mu'\nu'}(q,r,p)\Delta^{\alpha'}_\alpha(q)\Delta^{\mu'}_\mu(r)\Delta^{\nu'}_\nu(p) \;=\;& \mathcal{H}^{bac}_{\mu\nu}(r,q,p)+\mathcal{H}^{cab}_{\nu\mu}(p,q,r)\\
&+ir_\mu\Gamma^{bac}_\rho(r,q,p)D(r)D(q)\Delta^\rho_\nu(p)\\
&+ip_\nu\Gamma^{cab}_\rho(p,q,r)D(p)D(q)\Delta^\rho_\mu(r)\,. \qquad (2.75)
\end{aligned}
$$

Now, we notice that the expression (2.65) for the full gluon propagator allows us to write into Eq. (2.75)

$$
q^\alpha\Delta^{\alpha'}_\alpha(q) = -i\xi\frac{q^{\alpha'}}{q^2}\,. \qquad (2.76)
$$

Then, we decompose $\mathcal{H}$ according to Eq. (2.44), use Eq. (2.36) and factor out the color structures, to get

$$
\begin{aligned}
q^\alpha\,\mathbb{\Gamma}_{\alpha\mu'\nu'}(q,r,p)\Delta^{\mu'}_\mu(r)\Delta^{\nu'}_\nu(p) =& iF(q^2)\Big\{\,\big[H_{\mu\rho}(r,q,p)+\big(\Sigma_\mu(r)+ir_\mu\big)D(r)\Gamma_\rho(r,q,p)\big]\,\Delta^\rho_\nu(p)\\
&-\big[H_{\nu\rho}(p,q,r)+\big(\Sigma_\nu(p)+ip_\nu\big)D(p)\Gamma_\rho(p,q,r)\big]\,\Delta^\rho_\mu(r)\Big\}\,.
\end{aligned}
\qquad (2.77)
$$

On the left hand side of Eq. (2.77) the three-gluon vertex appears contracted with gluon propagators, whereas we want an STI with $q^\alpha\Gamma_{\alpha\mu'\nu'}(q,r,p)$ in isolation. Fortunately, the gluon propagator is invertible before we settle to Landau gauge. Specifically, it is easy to verify from Eq. (2.65) that

$$
\Delta^{-1}_{\mu\rho}(q)\Delta^{\rho\nu}(q) = g^\nu_\mu\,, \qquad (2.78)
$$

with

$$\Delta^{-1}_{\mu\rho}(q) = i\left[\mathrm{P}_{\mu\rho}(q)\Delta^{-1}(q^2) + \frac{1}{\xi}q_\mu q_\rho\right]\,. \tag{2.79}$$

Then, contracting Eq. (2.77) with $\Delta_\beta^{-1\,\mu}(r)\Delta_\gamma^{-1\,\nu}(p)$ leads to

$$\begin{aligned} q^\alpha\,\mathrm{I}\Gamma_{\alpha\beta\gamma}(q,p,r) \;=\;& iF(q^2)\Big\{\left[H_{\mu\gamma}(r,q,p) + \big(\Sigma_\mu(r) + ir_\mu\big)D(r)\Gamma_\gamma(r,q,p)\right]\Delta_\beta^{-1\,\mu}(r) \\ &- \left[H_{\nu\beta}(p,q,r) + \big(\Sigma_\nu(p) + ip_\nu\big)D(p)\Gamma_\beta(p,q,r)\right]\Delta_\gamma^{-1\,\nu}(p)\Big\}\,. \end{aligned} \tag{2.80}$$

Decomposing the inverse propagators according to Eq. (2.79) then yields

$$\begin{aligned} q^\alpha\,\mathrm{I}\Gamma_{\alpha\beta\gamma}(q,p,r) \;=\;& F(q^2)\Big\{\Delta^{-1}(p^2)\mathrm{P}^\nu_\gamma(r)H_{\nu\beta}(p,q,r) - \Delta^{-1}(r^2)\mathrm{P}^\mu_\beta(r)H_{\mu\gamma}(r,q,p) \\ &-\frac{r_\beta}{\xi}\left[r^\mu H_{\mu\gamma}(r,q,p) + \big(r^\mu\Sigma_\mu(r) + ir^2\big)D(r)\Gamma_\gamma(r,q,p)\right] \\ &+\frac{p_\gamma}{\xi}\left[p^\nu H_{\nu\beta}(p,q,r) + \big(p^\nu\Sigma_\nu(p) + ip^2\big)D(p)\Gamma_\beta(p,q,r)\right]\Big\}\,, \end{aligned} \tag{2.81}$$

where we have used the fact that, by Lorentz symmetry, $\Sigma_\mu(r)$ must be of the form $\Sigma_\mu(r) = r_\mu\Sigma(r^2)$, which does not survive contraction with $\mathrm{P}^\mu_\beta(r)$.

Lastly, the terms proportional to $1/\xi$ in Eq. (2.81) vanish identically by virtue of Eqs. (2.53) and (2.45). Hence, the final form of the STI for the three-gluon vertex is given by [4, 126],

$$q^\alpha\,\mathrm{I}\Gamma_{\alpha\mu\nu}(q,r,p) = F(q^2)[\Delta^{-1}(p^2)\mathrm{P}^\alpha_\nu(p)H_{\alpha\mu}(p,q,r) - \Delta^{-1}(r^2)\mathrm{P}^\alpha_\mu(r)H_{\alpha\nu}(r,q,p)]\,, \tag{2.82}$$

after some relabeling of indices. As a check on the result, we can use the Feynman rules in Appendix A to verify that Eq. (2.82) is satisfied at tree level.

While we have derived the three-gluon vertex STI with $\mathrm{I}\Gamma_{\alpha\mu\nu}(q,r,p)$ contracted with the momentum q^α, as in Eq. (2.82), there is nothing special about this momentum. In fact, since the gluon fields commute, $\mathrm{I}\Gamma^{abc}_{\alpha\mu\nu}(q,r,p)$ is fully Bose-symmetric, *i.e.* it is invariant under the permutation of any two of its legs, for example $\mathrm{I}\Gamma^{abc}_{\alpha\mu\nu}(q,r,p) = \mathrm{I}\Gamma^{acb}_{\alpha\nu\mu}(q,p,r)$. Hence, we must obtain STIs similar to Eq. (2.82), but with $\mathrm{I}\Gamma_{\alpha\mu\nu}(q,r,p)$ contracted with either r^μ or p^ν.

Notice however, that since the structure constants f^{abc} that we have factored out are anti-symmetric, Bose symmetry of $\mathrm{I}\Gamma^{abc}_{\alpha\mu\nu}(q,r,p)$ requires that the Lorentz structure of the vertex, *i.e.* $\mathrm{I}\Gamma_{\alpha\mu\nu}(q,r,p)$, be anti-symmetric as well. Thus, the three-gluon vertex STIs with

$\Gamma_{\alpha\mu\nu}(q,r,p)$ contracted with either other momentum correspond to cyclic permutations of Eq. (2.82). Specifically,

$$r^{\mu}\,\Gamma_{\alpha\mu\nu}(q,r,p) = F(r^2)[\Delta^{-1}(q^2)\mathrm{P}^{\mu}_{\alpha}(q)H_{\mu\nu}(q,r,p) - \Delta^{-1}(p^2)\mathrm{P}^{\mu}_{\nu}(p)H_{\mu\alpha}(p,r,q)]\,, \quad (2.83)$$

$$p^{\nu}\,\Gamma_{\alpha\mu\nu}(q,r,p) = F(p^2)[\Delta^{-1}(r^2)\mathrm{P}^{\nu}_{\mu}(r)H_{\nu\alpha}(r,p,q) - \Delta^{-1}(q^2)\mathrm{P}^{\nu}_{\alpha}(q)H_{\nu\mu}(q,p,r)]\,. \quad (2.84)$$

2.4.3 The STI constraint of the ghost-sector

In addition to relating the three-gluon vertex to the gluon and ghost propagators and the ghost-gluon scattering kernel, the STIs of Eqs. (2.82), (2.83) and (2.84) also provide a constraint on the ghost sector functions by themselves. This constraint will be important later, in Chapter 4, when we decompose the $\Gamma_{\alpha\mu\nu}(q,r,p)$ and $H_{\nu\mu}(q,p,r)$ in their most general Lorentz structures and solve the STIs in favor of the three-gluon vertex. For the moment, let us just derive this additional constraint.

We begin by contracting Eq. (2.83) with p^{ν}, which yields

$$r^{\mu}p^{\nu}\,\Gamma_{\alpha\mu\nu}(q,r,p) = \; F(r^2)\Delta^{-1}(q^2)p^{\nu}\mathrm{P}^{\mu}_{\alpha}(q)H_{\mu\nu}(q,r,p)\,. \quad (2.85)$$

Similarly, contracting Eq. (2.84) with r^{μ} leads to

$$r^{\mu}p^{\nu}\,\Gamma_{\alpha\mu\nu}(q,r,p) = \; -F(p^2)\Delta^{-1}(q^2)r^{\mu}\mathrm{P}^{\nu}_{\alpha}(q)H_{\nu\mu}(q,p,r)\,. \quad (2.86)$$

The left hand sides of Eqs. (2.85) and (2.86) are the same, and hence

$$p^{\nu}\mathrm{P}^{\mu}_{\alpha}(q)F(r^2)H_{\mu\nu}(q,r,p) = -r^{\mu}\mathrm{P}^{\nu}_{\alpha}(q)F(p^2)H_{\nu\mu}(q,p,r)\,. \quad (2.87)$$

The Eq. (2.87) is an equation involving only ghost sector functions. We can bring it to a more symmetric form by contracting Eq. (2.87) with p^{α}, using momentum conservation on the right hand side, *i.e.* $p = -q - r$, and relabeling dummy indices, to obtain

$$p^{\mu}p^{\alpha}\mathrm{P}^{\nu}_{\alpha}(q)F(r^2)H_{\nu\mu}(q,r,p) = r^{\mu}r^{\alpha}\mathrm{P}^{\nu}_{\alpha}(q)F(p^2)H_{\nu\mu}(q,p,r)\,, \quad (2.88)$$

which can be readily verified at tree level using the Feynman rules of Appendix A.

In words, the Eq. (2.88) says that the combination $r^{\mu}r^{\alpha}\mathrm{P}^{\nu}_{\alpha}(q)F(p^2)H_{\nu\mu}(q,p,r)$ is symmetric under the exchange of the momenta p and r. Recalling the diagrammatic representation of $H_{\nu\mu}(q,p,r)$ in Fig. 2.3, we see that r and p correspond to the gluon and ghost momenta, respectively. Thus, Eq. (2.88) imposes a nontrivial constraint on the gluon and ghost legs of the ghost-gluon kernel. We emphasize, though, that $H_{\nu\mu}(q,p,r)$ is *not* itself symmetric under the exchange of gluon and ghost legs, even at tree level where the gluon leg has a Lorentz index, whereas the ghost leg has none. Instead, only the particular combination given in Eq. (2.88), which contains a transverse projection of $H_{\nu\mu}(q,p,r)$ combined with the ghost propagator, possesses this symmetry.

Finally, we point out that while we have derived Eq. (2.88) from the three-gluon vertex STI, it can also be obtained more directly from an STI of the ghost sector alone [127].

2.5 The STIs and renormalization

As is well known, the STIs play a key role in the renromalizability of non-Abelian gauge theories. In this work, we will not need to delve very deep into the renormalization of QCD, thanks to the special property of the ghost-gluon scattering kernel being finite in Landau gauge. Nevertheless, there is one aspect that we should discuss, which is the limited freedom in defining the finite parts of the renormalization constants of the theory.

Let us define the gluon and ghost field strength renormalization constants, Z_A and Z_c, respectively, by

$$\Delta(\mu^2) := Z_A^{-1}\Delta_{\rm U}(\mu^2)\,, \qquad F(\mu^2) := Z_c^{-1}F_{\rm U}(\mu^2)\,, \tag{2.89}$$

where the index "U" denotes an unrenormalized quantity. Then, the renormalization constants of the ghost-gluon and three-gluon vertices are defined as

$$\Gamma_\mu(q,p,r) := Z_1\,\Gamma^{\rm U}_\mu(q,p,r)\,, \qquad \mathrm{I}\Gamma_{\alpha\mu\nu}(q,r,p) := Z_3\,\mathrm{I}\Gamma^{\rm U}_{\alpha\mu\nu}(q,r,p)\,. \tag{2.90}$$

From Eq. (2.45) it is evident that $H_{\nu\mu}(q,p,r)$ must be renormalized with the same constant, Z_1, as the ghost-gluon vertex.

The STIs of the theory, in particular Eq. (2.82), are naturally satisfied by the unrenormalized functions, provided a gauge invariant regularization, such as dimensional regularization [138], is employed in their calculation. Now, we impose that the renormalized functions also satisfy the STIs. Substituting the renormalized functions as defined in Eqs. (2.89) and (2.90) into Eq. (2.82) and using the fact that the equation holds also for their unrenormalized counterparts we obtain [38, 39]

$$\frac{Z_1}{Z_3} = \frac{Z_c}{Z_A} \,. \tag{2.91}$$

In general, while the divergent parts of the renormalization constants are completely fixed by the requirement that the divergences of the Green's function be canceled, one is still left with a freedom to define their finite parts. These can be defined by imposing particular values for the Green's functions at chosen kinematic configurations and an overall scale.

For example, we will use extensively in this work the momentum subtraction schemes (MOM) [139] in which we specify that the propagators attain their tree level values at the Euclidean point $q^2 = -\mu^2$, *i.e.*

$$\Delta(-\mu^2) = -\frac{1}{\mu^2} \,, \qquad F(-\mu^2) = 1 \,. \tag{2.92}$$

However, Eq. (2.92) still does not define the finite parts of the vertex renormalization constants. At this point, we can choose either $\mathrm{I\Gamma}_{\alpha\mu\nu}(q,p,r)$ or $H_{\nu\mu}(q,p,r)$ to reduce to tree-level at some chosen kinematic configuration. Importantly, we cannot generally choose both vertices to attain tree-level values simultaneously [139], due to Eq. (2.91). Instead, once we have chosen to define either Z_1 or Z_3, the remaining renormalization constant must be *determined* by imposing Eq. (2.91) [139].

In the Section B.4 we give explicit examples of the above procedure using the one-loop results for $\mathrm{I\Gamma}_{\alpha\mu\nu}(q,p,r)$ and $H_{\nu\mu}(q,p,r)$.

3

Infrared properties of QCD with dynamical gluon mass

It is well known that adding a gluon mass term to the Lagrangian of Eq. (2.2) explicitly breaks gauge invariance. Nevertheless, Schwinger has shown [84, 85] that it is possible in gauge theories for the gauge bosons to acquire effective masses *dynamically*, without breaking gauge symmetry nor introducing a scalar Higgs field into the Lagrangian, if the interaction is sufficiently strong. Specifically, the Schwinger model [85] consists of QED in $1+1$ dimensions, which is exactly solvable, and displays a dynamically massive photon. Moreover, the fermions in the Schwinger model turn out to be confined [85], providing a tempting analogy with QCD.

Schwinger's notion of dynamically massive gauge bosons was then extended to Abelian theories in more than $1+1$ dimensions [86, 87] and non-Abelian theories followed [88–90].

In the 1980s Cornwall proposed [27] that the Schwinger mechanism is realized in QCD, *i.e.* that the gluon develops, nonperturbatively, an effective mass [27–29]. The existence of a gluon mass has several important phenomenological implications, such as the IR freezing of the running coupling [140–149], glueball masses compatible with lattice results [5, 64, 66–68], a maximum wavelength of gluons [150], and may help resolving [151] the Gribov problem [152]. For its phenomenological relevance and theoretical elegance the idea of dynamically generated gluon mass was revived in the last 15 years [6, 30–35] and gained impetus as large volume lattice simulations produced strong evidence of its reality [7, 73–77, 79–81].

In order to trigger the Schwinger mechanism in QCD it is necessary that certain vertices of the theory develop special kinds of poles [27, 90], arising from nonperturbative effects. The existence of such poles fundamentally alters the Gauge Technique construction of the three-gluon vertex, requiring us to review the mass generation mechanism before embarking on the solution of the STI of Eq. (2.82).

In this chapter, we briefly review the principles of the Schwinger mechanism, starting by recalling the recent lattice evidence of its realization in QCD, namely the observation of an IR finite gluon propagator [7, 73–81]. In Section 3.2 we present the so-called "seagull cancellation", which prevents the gauge boson propagators from acquiring masses in the perturbative setting, and proceed to explain in Section 3.3 how the presence of poles in vertices evades this cancellation. Next, in Section 3.4 we discuss how the presence of a gluon mass attenuates the IR divergences of QCD, and how some such divergences persist due to the nonperturbative masslessness of the ghosts. Then, in Section 3.5 we show that the gluon mass picture causes the gluon propagator to develop a maximum in Euclidean space, and that this feature implies positivity violation of the gluon spectral function. Finally, in Section 3.6 we present an Ansatz that captures the known properties of the Euclidean space gluon propagator and is in agreement with lattice and SDE results for this function.

3.1 Infrared finite gluon propagator

Large volume lattice QCD simulations in the Landau gauge display a clearly finite and nonzero value for the scalar function $\Delta(q^2)$ of the gluon propagator at $q^2 = 0$ [73–80]. In fact, the finiteness of $\Delta(0)$ was more recently found to persist in the presence of dynamical quarks [7, 81], for different values of the gauge fixing parameter [153, 154], ξ, as well as for nonzero temperature [155–158]. For illustration, in Fig. 3.1 we show the propagator obtained in pure Yang-Mills QCD of Refs. [73, 76] in the left panel, whereas on the right one we show the corresponding results with three dynamical quarks of Ref. [7]. In both cases the saturation of $\Delta(0)$ to a finite and nonzero value is clearly visible.

As we will show in this section, the finiteness of $\Delta(0)$ is a highly nontrivial feature of the theory, which must be realized through nonperturbative effects. Indeed, in perturbation theory $\Delta^{-1}(0) = 0$ [see the one loop propagator in Eq. (B.9)], such that $\Delta(0)$ is divergent.

The discussion of the IR finiteness of $\Delta(0)$ is better carried out by first defining the

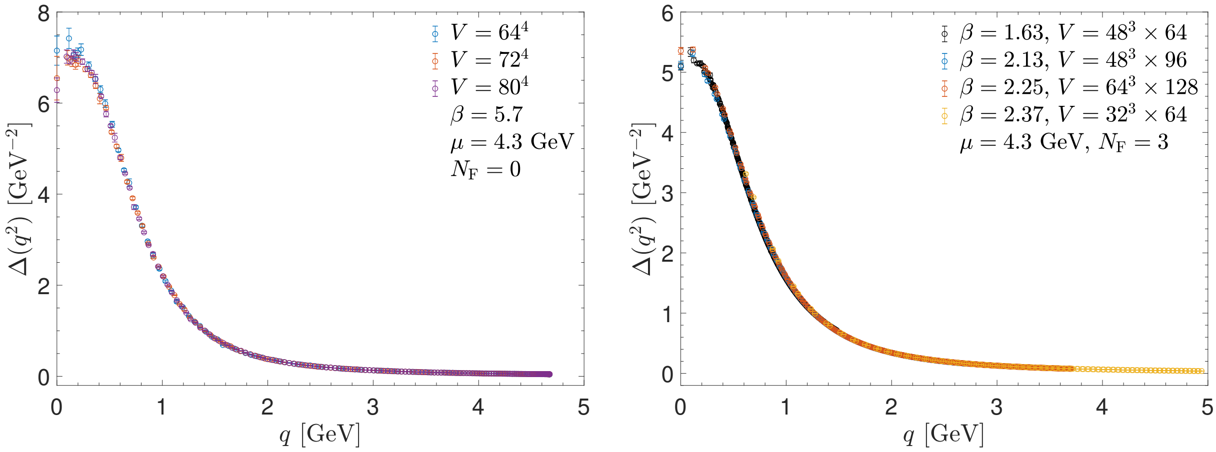

Figure 3.1: Left: Lattice results for the Landau gauge propagator of the gluon of pure Yang-Mills QCD, from Ref. [73, 76]. Right: Gluon propagator in QCD with $N_{\rm F} = 3$ quark flavors [7]. The renormalization point in both sets is $\mu = 4.3$ GeV.

gluon self-energy, $i\,\Pi^{ab}_{\mu\nu}(q)$, by

$$i\,\Pi_{\mu\nu}(q) = \Delta^{-1}_{\mu\nu}(q) - \Delta^{(0)\,-1}_{\mu\nu}(q)\,, \tag{3.1}$$

where the common color factor δ^{ab} has been extracted. It follows from the STI satisfied by $\Delta_{\mu\nu}(q)$, Eq. (2.62), that the gluon self-energy must be transverse, *i.e.* $q^\mu \Pi_{\mu\nu}(q) = 0$. Hence, we may write

$$\Pi_{\mu\nu}(q) = {\rm P}_{\mu\nu}(q)\Pi(q^2)\,, \tag{3.2}$$

where $\Pi(q^2)$ is a scalar with dimensions of mass squared. Combining Eqs. (3.1) and (3.2) with Eq. (2.79) allows us to write

$$\Delta^{-1}(q^2) = q^2 + \Pi(q^2)\,. \tag{3.3}$$

From Eq. (3.3) we see that the statement that $\Delta(0)$ is finite and nonzero amounts to saying that $\Pi(0)$ is finite and non-zero. Now, if $\Pi(q^2)$ were constant Eq. (3.3) would take the form of massive tree-level propagator, $\Delta^{(1{\rm M})}(q^2) = 1/(q^2 - m^2)$. Obviously, since QCD is asymptotically free, in the UV $\Pi(q^2)$ must recover its perturbative behavior, which is massless, from which follows that $\Pi(q^2)$ cannot be a constant. Notwithstanding that, we may still say that the gluon propagator has a *dynamical*, *i.e.* momentum dependent, mass, which falls off to zero in the UV.

In Fig. 3.2 we show the SDE for the gluon propagator in pure Yang-Mills QCD.

Evidently, the gluon self-energy is given by the sum of the diagrams (a_i), for $i = 1, \dots 5$, of that figure. Hence, IR finiteness of the gluon propagator implies that the contributions of the diagrams (a_i) must add up to a finite nonzero value as $q \to 0$.

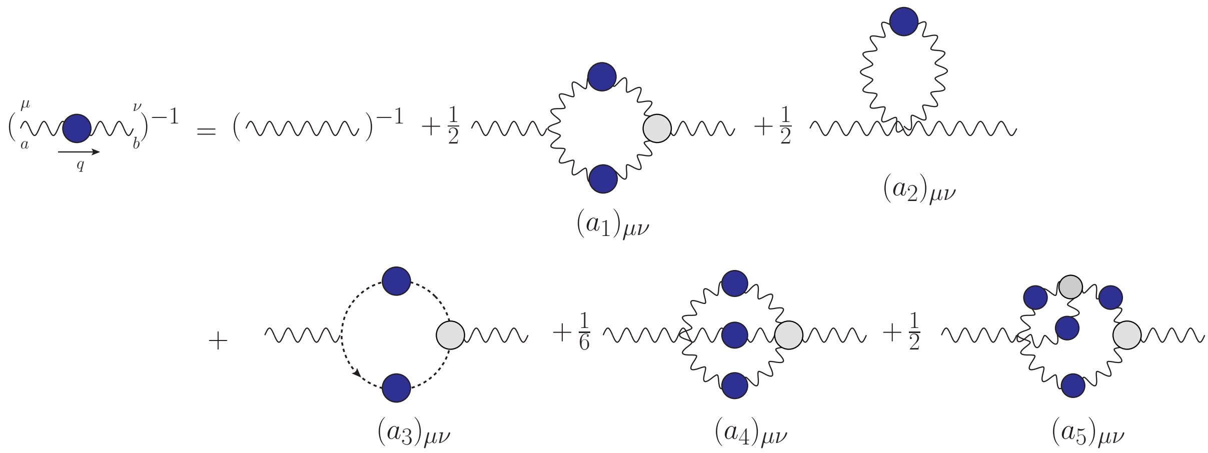

Figure 3.2: Diagrammatic representation of the gluon SDE.

This statement may seem simple at first. However, as we will discuss in the next two sections, the gauge invariance of the theory combined with an integral identity analytically continued to arbitrary dimension, known as the "seagull identity", requires that $\Pi(0) = 0$, unless some of the vertices appearing in the SDE of Fig. 3.2 possess poles at $q = 0$.

3.2 The seagull cancellation

It is not the scope of this work to treat the generation of a dynamical gluon mass in full detail, to which we refer the reader to the literature [31, 32, 34, 35], and we want to cover only the ideas that will be necessary for the Gauge Technique construction of the three-gluon vertex later. For this reason, we simplify the presentation of the Schwinger mechanism by framing it as if it were to take place in scalar QED, adapting our discussion from [34]. Naturally, it is not proposed here that the mechanism is actually realized in scalar QED, which is to be understood as a "make-believe" theory, in which the concepts and calculations we want to illustrate, but do not need in full depth, become simpler.

The SDE for the photon in scalar QED is shown in Fig. 3.3. Notice the appearance of two kinds of vertices: the 3-point vertex, $e\,\mathbb{G}_\mu(q,r,p)$, and the 4-point vertex, $e^2 G_{\mu\nu}(q,r,s,p)$, represented diagramatically in Fig. 3.4, and denoting by e the electric charge. The Feynman rules for these vertices are given by

$$\mathbb{G}^{(0)}_\mu(q,r,p) = -i(r-p)_\mu\,, \qquad G^{(0)}_{\mu\nu}(q,r,s,p) = -2ig_{\mu\nu}\,. \tag{3.4}$$

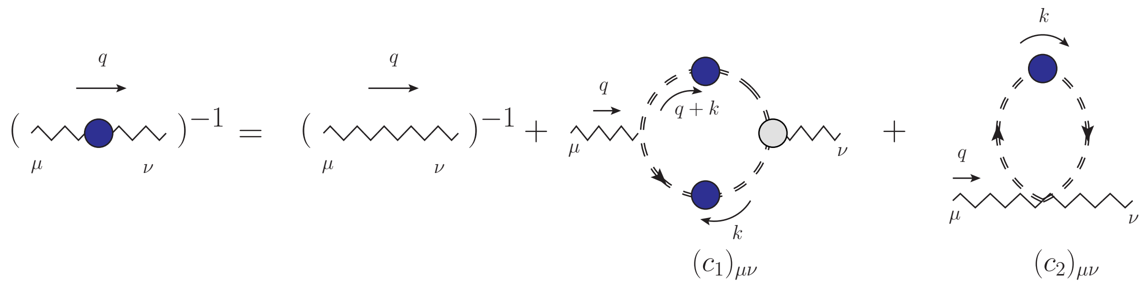

Figure 3.3: Diagrammatic representation of the photon SDE. The zig-zag lines represent photons, whereas the dashed double-lines represent scalar fields.

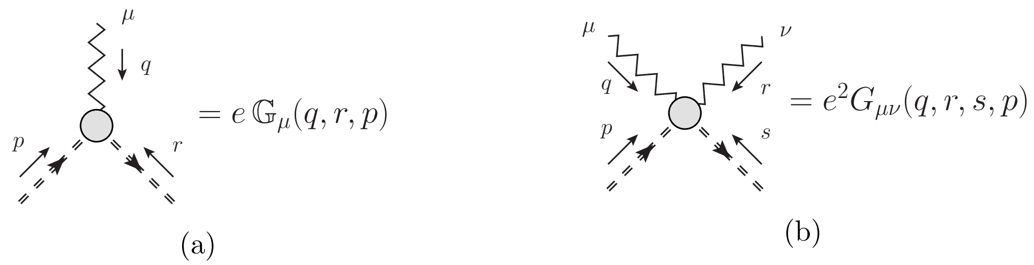

Figure 3.4: (a): Diagrammatic representation of the 1PI 3-point vertex of scalar QED. (b): Diagrammatic representation of the 1PI 4-point vertex of scalar QED.

The gauge invariance of scalar QED implies that the full photon propagator, denoted by $B_{\mu\nu}(q)$, satisfies a WI identical to Eq. (2.62), with Δs substituted for Bs. Hence,

$$B_{\mu\nu}(q) = -i\left[\mathrm{P}_{\mu\nu}(q)B(q^2) + \xi\frac{q_\mu q_\nu}{q^2}\right], \tag{3.5}$$

with $B(q^2)$ scalar. Moreover, it follows from Eq. (3.5) that the photon self-energy, $i\,C_{\mu\nu}(q)$, given by the sum of diagrams (c_1) and (c_2) in Fig. 3.3, is transverse, *i.e.*

$$C_{\mu\nu}(q) = \mathrm{P}_{\mu\nu}(q)C(q^2), \tag{3.6}$$

and

$$B^{-1}(q^2) = q^2 + C(q^2). \tag{3.7}$$

Evidently, $C(q^2)$ is the QED analog to the $\Pi(q^2)$ of Eq. (3.3).

We will then show that $C(0) = 0$, *i.e.* the photon in scalar QED remains massless in spite of radiative corrections, *unless* $\mathbb{G}_\mu(q,r,p)$ contains a special kind of pole at $q \to 0$.

Using the above notation and the Feynman rules of Eq. (3.4), the photon SDE can be written as

$$iC_{\mu\nu}(q) = e^2 \int_k \mathcal{D}(k^2)\mathcal{D}(z^2)(2k+q)_\nu \mathbb{G}_\mu(-q, q+k, -k) - 2e^2 g_{\mu\nu} \int_k \mathcal{D}(k^2)\,, \tag{3.8}$$

where $z := q+k$, $\mathcal{D}(k^2)$ denotes the propagator of the scalar field and we use the shorthand notation of Eq. (B.1) for the integral measure. At tree level

$$\mathcal{D}^{(0)}(k^2) = \frac{i}{k^2 - m_s^2}\,, \tag{3.9}$$

where m_s is the mass of the scalar.

Now, the vertex $\mathbb{G}_\mu(q, r, p)$ satisfies the WI

$$q^\mu \mathbb{G}_\mu(q, r, p) = \mathcal{D}^{-1}(p^2) - \mathcal{D}^{-1}(r^2)\,, \tag{3.10}$$

which can be checked imediately at tree level using Eqs. (3.4) and (3.9). Differentiating Eq. (3.10) with respect to q and taking the $q \to 0$ limit, we obtain the special case

$$\mathbb{G}_\mu(0, r, -r) + \lim_{q\to 0}\left[q^\rho \frac{\partial \mathbb{G}_\rho(q, r, -q-r)}{\partial q^\mu}\right] = \frac{\partial \mathcal{D}^{-1}(r^2)}{\partial r^\mu}\,, \tag{3.11}$$

where we used momentum conservation to write $p = -q-r$. At this point, if we assume $\mathbb{G}_\rho(q, r, -q-r)$ does not have poles as $q \to 0$, the term in square brackets in Eq. (3.11) vanishes in the $q = 0$ limit. In this case we obtain[1]

$$\mathbb{G}_\mu(0, r, -r) = \frac{\partial \mathcal{D}^{-1}(r^2)}{\partial r^\mu}\,. \tag{3.12}$$

In particular, it is easy to verify that the tree-level vertex of Eq. (3.4) satisfies the no-pole assumption, and that Eq. (3.12) holds at tree level.

Then, it is straightforward to show, by contracting Eq. (3.8) with q_μ, that the WI of Eq. (3.10) guarantees the transversality of $C_{\mu\nu}(q)$, *i.e.* $q^\mu C_{\mu\nu}(q) = 0$, such that Eq. (3.6) holds, as it should. Consequently, to obtain $C(q^2)$ we contract Eq. (3.8) with $\mathrm{P}^{\mu\nu}(q)$,

[1] Ward's original WI in spinor QED was actually of this form [159], and was later generalized to unequal momenta by Takahashi [160].

which leads to

$$i(d-1)C(q^2) = 2e^2 \int_k \mathcal{D}(k^2)\mathcal{D}(z^2)k_\nu \mathrm{P}^{\mu\nu}(q)\mathbb{G}_\mu(-q,q+k,-k) - 2e^2(d-1)\int_k \mathcal{D}(k^2)\,, \quad (3.13)$$

with d the space-time dimension.

Now, the $q^\mu q^\nu$ part of $\mathrm{P}^{\mu\nu}(q)$ triggers the WI of Eq. (3.10), furnishing

$$\begin{aligned} i(d-1)C(q^2) &= 2e^2 \int_k \mathcal{D}(k^2)\mathcal{D}(z^2)k^\mu \mathbb{G}_\mu(-q,q+k,-k) - \frac{2e^2 q^\rho}{q^2}\int_k k_\rho \mathcal{D}(k^2) \\ &\quad + \frac{2e^2 q^\rho}{q^2}\int_k k_\rho \mathcal{D}(z^2) - 2e^2 d \int_k \mathcal{D}(k^2)\,. \end{aligned} \quad (3.14)$$

The second term on the first line vanishes because it is odd in k. As for the first term in the second line, Lorentz symmetry allows us to shift the integration variable by $k \to k-q$, yielding

$$\int_k k_\rho \mathcal{D}(z^2) = \int_k (k-q)_\rho \mathcal{D}(k^2) = -q_\rho \int_k \mathcal{D}(k^2)\,. \quad (3.15)$$

Hence, Eq. (3.14) reads

$$i(d-1)C(q^2) = 2e^2 \int_k \mathcal{D}(k^2)\mathcal{D}(z^2)k^\mu \mathbb{G}_\mu(-q,q+k,-k) - 2e^2 d\int_k \mathcal{D}(k^2)\,. \quad (3.16)$$

Having separated $C(q^2)$ from the tensor structure of $C_{\mu\nu}(q)$, we may now set $q=0$ safely in Eq. (3.16), which in this limit reads

$$\begin{aligned} i(d-1)C(0) &= 2e^2 \int_k \mathcal{D}^2(k^2)k^\mu \mathbb{G}_\mu(0,k,-k) - 2e^2 d\int_k \mathcal{D}(k^2)\,, \\ &= 2e^2 \int_k \mathcal{D}^2(k^2)k^\mu \frac{\partial \mathcal{D}^{-1}(k^2)}{\partial k^\mu} - 2e^2 d\int_k \mathcal{D}(k^2)\,, \end{aligned} \quad (3.17)$$

where we used Eq. (3.12) to obtain the last line above.

Invoking the chain rule, the derivative term in Eq. (3.17) can be written as

$$\frac{\partial \mathcal{D}^{-1}(k^2)}{\partial k^\mu} = -\frac{2k_\mu}{\mathcal{D}^2(k^2)}\frac{\partial \mathcal{D}(k^2)}{\partial k^2}\,. \quad (3.18)$$

Inserting this result into Eq. (3.17) leads to

$$C(0) = \frac{4ie^2}{d-1}\left[\int_k k^2 \frac{\partial \mathcal{D}(k^2)}{\partial k^2} + \frac{d}{2}\int_k \mathcal{D}(k^2)\right]. \quad (3.19)$$

To evaluate the integrals in Eq. (3.19), we transform to Euclidean space, following the rules of Appendix D, and use spherical coordinates, such that

$$\int_k = \frac{i\mu^{2\epsilon}}{(2\pi)^d}\int_0^\infty \mathrm{d}|k|\,|k|^{d-1}\int d\Omega = \frac{i\mu^{2\epsilon}}{2(2\pi)^d}\int_0^\infty \mathrm{d}y\, y^{\frac{d}{2}-1}\int d\Omega\,, \tag{3.20}$$

where Ω is the solid angle, $y := k^2$ and μ is the 't Hooft mass scale, introduced to keep the coupling, e, dimensionless [161] for any d. Then, since the integrands of the two terms in Eq. (3.19) only depend on k^2, the angular integration yields the same result for both, leading to

$$\int_k k^2\frac{\partial\mathcal{D}(k^2)}{\partial k^2} + \frac{d}{2}\int_k \mathcal{D}(k^2) = \left[\int_0^\infty \mathrm{d}y\, y^{\frac{d}{2}}\frac{\partial\mathcal{D}(y)}{\partial y} + \frac{d}{2}\int_0^\infty \mathrm{d}y\, y^{\frac{d}{2}-1}\mathcal{D}(y)\right]\frac{i\mu^{2\epsilon}}{(2\pi)^d}\int d\Omega\,. \tag{3.21}$$

Now we perform an integration by parts in the first integral of Eq. (3.21), to obtain

$$\int_0^\infty \mathrm{d}y\, y^{\frac{d}{2}}\frac{\partial\mathcal{D}(y)}{\partial y} = y^{\frac{d}{2}}\mathcal{D}(y)\Big|_0^\infty - \frac{d}{2}\int_0^\infty \mathrm{d}y\, y^{\frac{d}{2}-1}\mathcal{D}(y)\,. \tag{3.22}$$

For sufficiently large space-time dimension, d, the surface term $y^{\frac{d}{2}}\mathcal{D}(y)|_0^\infty$ is undefined, but so are the integrals in Eq. (3.21). In order to make sense of Eq. (3.21) we consider d to be complex with $\mathrm{Re}(d) < d^{\max}$, where $d^{\max}$ is sufficiently small for the integrals in Eq. (3.21) to be finite and for $y^{\frac{d}{2}}\mathcal{D}(y) \to 0$ as $y \to 0$. For example, in the case of the tree-level propagator of Eq. (3.9), the integrals in Eq. (3.21) are finite and the surface term vanishes for $\mathrm{Re}(d) < 2$, *i.e.* $d^{\max} = 2$ for the tree level case.

Hence, for $\mathrm{Re}(d) < d^{\max}$, Eqs. (3.21) and (3.22) entail[2]

$$\int_k k^2\frac{\partial\mathcal{D}(k^2)}{\partial k^2} + \frac{d}{2}\int_k \mathcal{D}(k^2) = 0\,. \tag{3.23}$$

Since for $\mathrm{Re}(d) < d^{\max}$ the Eq. (3.23) defines an analytic function of d, the analytic continuation theorem guarantees that Eq. (3.23) holds for d general.

Finally, using Eq. (3.23) into Eq. (3.19) leads to the announced result,

$$C(0) = 0\,. \tag{3.24}$$

It is important to emphasize that the result $C(0) = 0$ is not realized diagram by

[2]For an alternative derivation that does no use integration by parts see [35].

diagram. Instead, the two self-energy diagrams of Fig. 3.3 cancel against each other in the $q \to 0$ limit. The diagram (c_2) of Fig. 3.3 is usually called the "seagull diagram", and is quadratically divergent, making its cancellation crucial for the renormalizability of the theory. It is for enforcing the cancellation of the seagull diagrams that Eq. (3.23) is called the seagull identity [35].

The crucial steps leading to $C(0) = 0$ are the gauge invariance of the theory, expressed by the WI of Eq. (3.10), the no-pole assumption that led to Eq. (3.12), and finally the seagull identity of Eq. (3.23).

In the case of QCD, due to its non-Abelian nature, the demonstration that the gluon is massless in perturbation theory is naturally more complicated and is better carried out by taking advantage of the synthesis of the Pinch Technique [27, 162–167] and the Background Field Method [133, 168–170], known in the literature as the Pinch Technique-Background Field Method (PT-BFM) scheme [104, 105, 110], whose Green's functions satisfy Abelian-like WIs, rather than the complicated STIs. Nevertheless, the derivations are ultimately analogous, in that the gauge symmetry of the theory triggers a set of seagull cancellations, under similar no-pole assumptions on the vertices, such that $\Pi(0) = 0$ [32, 34, 35]. Hence, to generate a mass for the gauge bosons, without introducing a mass or Higgs term in the Lagrangian, we must evade the seagull cancellation.

3.3 Evading the seagull cancellation

Consider now the possibility that $q^\rho \partial \mathbb{G}_\rho(q, r, -q-r)/\partial q^\mu$ does not vanish as $q \to 0$. To this end, let us suppose that the vertex contains a pole term,

$$\mathbb{G}_\mu(q, r, p) = G_\mu(q, r, p) + \frac{q_\mu}{q^2} U(q, r, p) \,, \tag{3.25}$$

where $G_\mu(q, r, p)$ and $U(q, r, p)$ are regular at $q \to 0$.

The onset of the pole term in Eq. (3.25) must be realized in a gauge invariant way, such that the WI of Eq. (3.10) is preserved. Setting $q = 0$ in that equation and using Eq. (3.25) leads to

$$U(0, r, -r) = 0 \,. \tag{3.26}$$

Nevertheless, the derivatives of $U(q, r, p)$ need not vanish. In fact, in the presence of the pole term in the vertex $\mathbb{G}_\mu(q,r,p)$, the Eq. (3.11) now yields

$$\lim_{q\to 0}\left[\mathbb{G}_\mu(q,r,p)-\frac{q_\mu}{q^2}U(q,r,p)\right]=G(0,r,-r)=\frac{\partial\mathcal{D}^{-1}(r^2)}{\partial r^\mu}-\left[\frac{\partial U(q,r,-q-r)}{\partial q^\mu}\right]_{q=0}, \tag{3.27}$$

instead of Eq. (3.12).

It is clear then, that if one repeats the calculations leading up to Eq. (3.24), the term of Eq. (3.27) containing the derivative of $\mathcal{D}^{-1}(k^2)$ will still trigger the seagull identity of Eq. (3.23), and cancel against the seagull diagram. However, the $\partial U/\partial q^\mu$ term survives, yielding

$$C(0)=-\frac{2ie^2}{d}\int_k \mathcal{D}^2(k^2)\left[k^\mu\frac{\partial U(-q,q+k,-k)}{\partial q^\mu}\right]_{q=0}. \tag{3.28}$$

Hence, if the full, nonperturbative, vertex $\mathbb{G}_\mu(q,r,p)$ contains a pole term as in Eq. (3.25), with nonvanishing $\partial U(q,r,-q-r)/\partial q^\mu$ at $q=0$, an effective mass is generated for the gauge boson.

An important property of the pole term in Eq. (3.25) is that it is *longitudinally coupled*, *i.e.* it does not survive a transverse projection. As a result, this pole does not appear in on-shell amplitudes, since the latter contain transversely polarized photons (see *e.g.* [86], although their discussion is for a theory with fermions).

The pole in the vertex $\mathbb{G}_\mu(q,r,p)$ can be realized if a massless bound state of scalars forms [32, 86–88, 90]. In this case, Eq. (3.25) can be represented by the two diagrams in Fig. 3.5, where the second diagram contains the massless bound state, and the first corresponds to the regular part, $G_\mu(q,r,p)$. In the massless bound state picture, the longitudinality of the pole term in Eq. (3.25) is an immediate consequence of Lorentz symmetry; the only possible Lorentz structure of the amplitude $M_\mu(q)$ of a photon to transition to a massless bound state, shown to the left of the bracket in Fig. 3.5, is $q_\mu M(q^2)$.

Evidently, the formation of such massless bound states is not captured by perturbation theory. Neither can it simply be put in by hand in the theory. Instead, like any bound state, that which generates the $q_\mu U(q,r,p)/q^2$ term in Eq. (3.25) is governed by a Bethe-Salpeter equation (BSE), represented diagrammatically in Fig. 3.6. Hence, the $\mathbb{G}_\mu(q,r,p)$ will only acquire the pole term of Eq. (3.25) if the BSE admits nontrivial solutions, which should only occur for sufficiently strong coupling.

We can thus summarize the ideas in this and the previous section as follows: if the

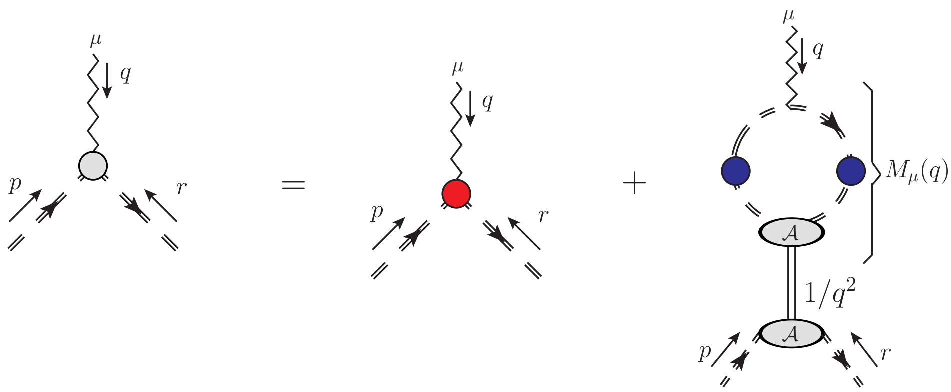

Figure 3.5: Diagrammatic representation of Eq. (3.25) with the pole part $q_\mu U(q,r,p)/q^2$ corresponding to massless bound state excitations in the photon leg. The red circle represents the regular part, $G_\mu(q,r,p)$, the continuous double line represents a bound state and $\mathcal{A}$ is the 1PI interaction vertex between the bound state and two scalar fields. The bracket defines the transition amplitude, $M_\mu(q)$, from a photon to a massless bound state.

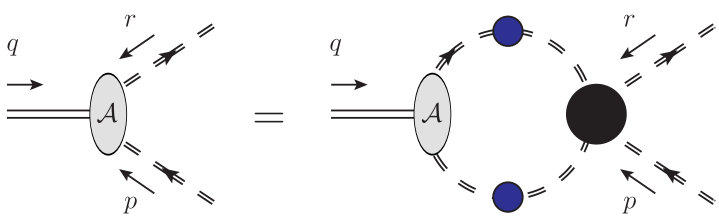

Figure 3.6: BSE governing the amplitude $\mathcal{A}$ of Fig. 3.5. The black circle represents the interaction kernel between four scalars and contains connected contributions.

interaction of the theory is sufficiently strong, massless bound states can arise in the fundamental vertices, endowing them with longitudinally coupled poles which lead to a nonzero self-energy at zero momentum, *i.e.* a mass for the gauge boson. This poles are realized without violating the WIs, and without altering the Lagrangian of the theory by introducing Higgs fields nor, gauge symmetry breaking, mass terms.

This scenario can be generalized to QCD [31, 32, 34, 35, 61]. Since QCD has a larger number of fundamental vertices, the gluon dynamical mass can have contributions from poles in the three-gluon [32], four-gluon [61] and ghost-gluon [62] vertices. Nevertheless, it is the nontrivial pole structure of the three-gluon vertex that seems to be the dominant ingredient for the Schwinger mechanism in QCD [62]. As such, we will restrict our attention to $\mathbb{\Gamma}_{\alpha\mu\nu}(q,r,p)$.

We assume that massless bound states of two gluons are formed nonperturbatively, producing poles in the three-gluon vertex [32], such that we may write

$$\mathbb{\Gamma}_{\alpha\mu\nu}(q,r,p) = \Gamma_{\alpha\mu\nu}(q,r,p) + V_{\alpha\mu\nu}(q,r,p)\,, \tag{3.29}$$

with $\Gamma_{\alpha\mu\nu}(q,r,p)$ regular and $V_{\alpha\mu\nu}(q,r,p)$ contains poles at zero momenta.

Since the pole part $V_{\alpha\mu\nu}(q,r,p)$ results from bound state excitations in each of the channels, q, r and p, as shown in Fig. 3.7, it is *necessarily* longitudinally coupled. More specifically, since the transition amplitude $I_\alpha(q)$ shown in Fig. 3.7 can only be of the form $q_\alpha I(q^2)$, the Lorentz tensor structure of $V_{\alpha\mu\nu}(q,r,p)$ must be

$$V_{\alpha\mu\nu}(q,r,p) = \left(\frac{q_\alpha}{q^2}\right) R_{\mu\nu}(q,r,p) + \left(\frac{r_\mu}{r^2}\right) S_{\alpha\nu}(q,r,p) + \left(\frac{p_\nu}{p^2}\right) T_{\alpha\mu}(q,r,p)\,, \tag{3.30}$$

for some tensor functions $R_{\mu\nu}(q,r,p)$, $S_{\mu\nu}(q,r,p)$ and $T_{\mu\nu}(q,r,p)$. As a result of Eq. (3.30), the pole term $V_{\alpha\mu\nu}(q,r,p)$ is annihilated by a totally transverse projection,

$$\mathrm{P}^{\alpha}_{\alpha'}(q)\mathrm{P}^{\mu}_{\mu'}(r)\mathrm{P}^{\nu}_{\nu'}(p)V_{\alpha\mu\nu}(q,r,p) = 0\,, \tag{3.31}$$

such that the poles in the three-gluon vertex do not appear in on-shell amplitudes [32, 89].

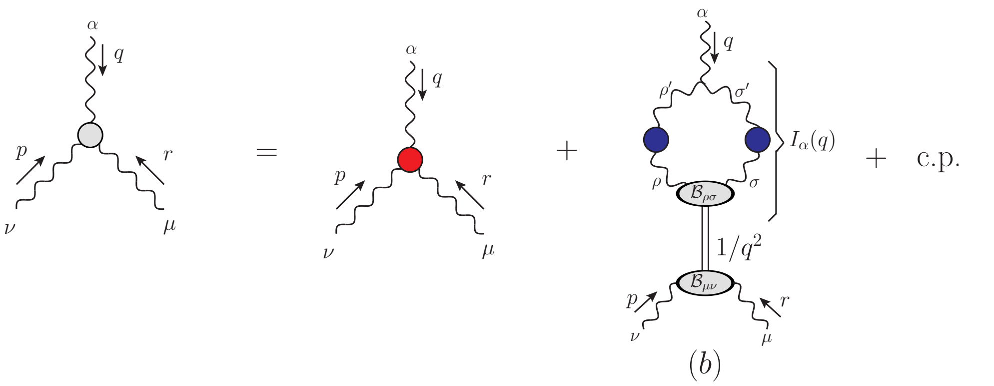

Figure 3.7: Diagrammatic representation of Eq. (3.29) with the pole part $V_{\alpha\mu\nu}$ containing massless bound state excitations in each of the channels, q, r and p. The red circle represents the regular part, $\Gamma_{\alpha\mu\nu}$. Diagram (b) represents the massless bound state excitation on the q channel, with $I_\alpha(q)$ the transition amplitude from a gluon to a massless bound state and $\mathcal{B}_{\mu\nu}$ the 1PI interaction vertex between two gluons and a massless bound state excitation. The "c.p." denotes the cyclic permutations of diagram (b).

Again, the dynamical onset of the pole part $V_{\alpha\mu\nu}$ of Eq. (3.29) is governed by a BSE [32] and the existence of nontrivial solutions for it depends on the strength of the coupling.

For illustration, in Fig. 3.8 we show the BSE satisfied by the transition amplitude $\mathcal{B}_{\mu\nu}$, defined in Fig. 3.7, assuming that only the three-gluon vertex develops massless bound state excitations. If the other fundamental vertices of the theory also contain longitudinal pole parts [61, 62], analogous to V, then Fig. 3.8 must be substituted by a system of coupled BSEs corresponding to the bound state amplitudes appearing in each of these vertices [62].

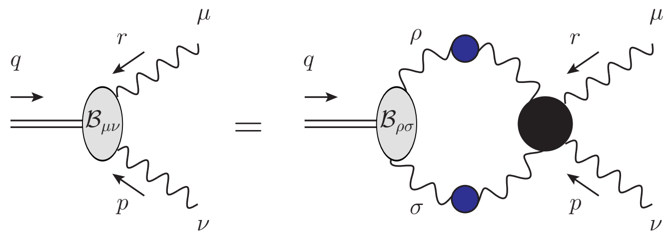

Figure 3.8: BSE governing the amplitude $\mathcal{B}_{\mu\nu}$ of Fig. 3.7. The black circle represents the interaction kernel between four gluons and contains connected contributions.

Since the pole part, $V_{\alpha\mu\nu}$, of the vertex is produced dynamically, preserving the gauge symmetry of QCD, the full vertex of Eq. (3.29) still satisfies the STI of Eq. (2.82). Then, in complete analogy to the calculations leading to Eq. (3.28), the regular part, $\Gamma_{\alpha\mu\nu}$, of the three-gluon vertex triggers a series of seagull cancellations and does not contribute to $\Pi(0)$, whereas the pole part, $V_{\alpha\mu\nu}$, evades the seagull identity, furnishing a nonzero $\Pi(0)$ [35].

Substituting Eq. (3.29) into the gluon propagator SDE of Fig. 3.2, it is natural to split the contributions to $\Delta_{\mu\nu}(q)$ coming from the regular and the pole parts of the vertices. Then, we can associate the self-energy terms containing the pole vertices to a dynamical gluon mass, $m^2(q^2)$, and determine an SDE relating it to the pole part, $V_{\alpha\mu\nu}$, of the vertex [6, 61, 171], as represented diagrammatically in Fig. 3.9. With this splitting, the gluon propagator may be written as

$$\Delta^{-1}(q^2) = q^2 J(q^2) - m^2(q^2)\,, \tag{3.32}$$

where $q^2 J(q^2)$ is called the "kinetic term" and contains all contributions from the regular vertex terms. In particular, since the perturbative vertices do not contain the mass-generating poles, $J(q^2)$ contains all the perturbative corrections to the propagator.

Combining Eqs. (3.29) and (3.32), we can split the STI of Eq. (2.82) into two equa-

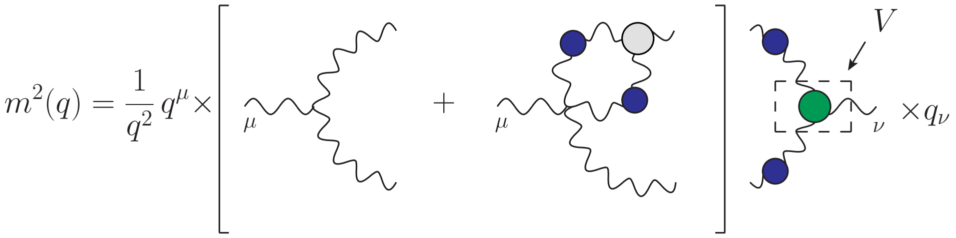

Figure 3.9: Diagrammatic representation of the dynamical gluon mass equation, derived from the gluon SDE of Fig. 3.2 by separating from it the terms which contain the pole part, $V_{\alpha\mu\nu}$, of the full three-gluon vertex of Eq. (3.29). The dashed box emphasizes the $V_{\alpha\mu\nu}$, which is represented by a green circle.

tions[3],

$$q^\alpha \Gamma_{\alpha\mu\nu}(q,r,p) = F(q^2)[p^2 J(p^2) \mathrm{P}^\alpha_\nu(p) H_{\alpha\mu}(p,q,r) - r^2 J(r^2) \mathrm{P}^\alpha_\mu(r) H_{\alpha\nu}(r,q,p)]\,, \tag{3.33}$$

and

$$q^\alpha V_{\alpha\mu\nu}(q,r,p) = F(q^2)[m^2(r^2) \mathrm{P}^\alpha_\mu(r) H_{\alpha\nu}(r,q,p) - m^2(p^2) \mathrm{P}^\alpha_\nu(p) H_{\alpha\mu}(p,q,r)]\,. \tag{3.34}$$

Evidently, the cyclically permuted versions Eqs. (3.33) and (3.34) also hold [4], following from Eqs. (2.83) and (2.84).

It remains, of course, to determine whether the QCD interaction is sufficiently strong to trigger the Schwinger mechanism, *i.e.* for the BSEs governing the massless bound state excitations, such as that of Fig. 3.8, to have nontrivial solutions. Indeed, it has been found numerically that nontrivial solutions for bound state excitation in the three-gluon vertex exist in pure Yang-Mill QCD [6, 32, 61, 62]. Moreover, the dynamical mass persists in the presence of active quarks [33] and away from Landau gauge [172], in agreement with lattice results [7, 73, 74, 76, 81, 153, 154].

Finally, the gluon mass solutions obtained numerically in Euclidean space are monotonically decreasing functions of the Euclidean momentum q^2 [6, 32, 61, 62]. Moreover, in the far UV, the leading behavior of $m^2(q^2)$ displays a power-law running [173]

$$m^2(q^2) \underset{q^2\to\infty}{\simeq} \frac{\lambda^4}{q^2}\,, \tag{3.35}$$

[3] At first it seems this splitting may not be unique. However, when supplemented with renormalization prescriptions for $\Delta(q^2)$ and the vertices, it becomes uniquely defined [9].

up to logarithmic corrections. Here, λ is a characteristic scale of the dynamical mass running. This fast fall-off of the dynamical mass in the UV is in agreement with Operator Product Expansion analysis of the gluon propagator [27, 174] and guarantees that the asymptotically free perturbative behavior of QCD is recovered for large momenta [173].

Having discussed the gluon mass generation mechanism, we now move over to explore some of the implications of the IR finiteness of the gluon propagator that will be important in this work.

3.4 Infrared divergences in nonperturbative QCD

One of the most important implications of the IR finiteness of the gluon propagator is its effect in taming numerous IR divergences in QCD. Specifically, several Green's functions that are IR divergent in perturbation theory become IR finite, or have their degree of divergence reduced, *e.g.* from pole to logarithmic, in the presence of a gluon mass.

An important example is the ghost dressing function, $F(q^2)$. Unlike the gluons, the lattice results indicate quite clearly that ghosts remain massless nonpertubatively [73, 76, 78, 81, 148, 175–177], *i.e.* the ghost propagator $D(q^2)$ diverges at $q^2 = 0$. Nevertheless, the presence of a gluon mass causes the ghost dressing function, $F(q^2)$, defined in Eq. (2.36), to saturate to a finite value at zero momentum [30, 83, 148, 177–180].

For illustration, lattice results for $F(q^2)$ are shown in Fig. 3.10, for the case of pure Yang-Mills [175] (left panel) and for $N_{\rm F} = 3$ quark flavors [148] (right panel). Indeed, quantitative analysis of these results indicate they are consistent with a finite value at the origin [30, 74, 178–180].

We can understand the saturation of $F(0)$ through a semi-perturbative calculation. We start with the SDE for the ghost propagator [180], shown diagrammatically in Fig. 3.11. If the self energy diagram in Fig. 3.11 is computed with the Feynman rules of Appendix A, one obtains the well-known result of Eq. (B.15), after renormalization, which has a logarithmic divergence of the form $\ln q^2$, as $q^2 \to 0$. Keeping the ghost propagator and the ghost-gluon vertex at tree-level, but dressing the gluon propagator with the massive model of Eq. (B.40), leads instead to

$$F^{-1}(q^2) = Z_c - g^2 C_{\rm A} \int_k \frac{[k^2 q^2 - (k\cdot q)^2]}{q^2 k^2 (k+q)^2 (k^2+m^2)}\,, \tag{3.36}$$

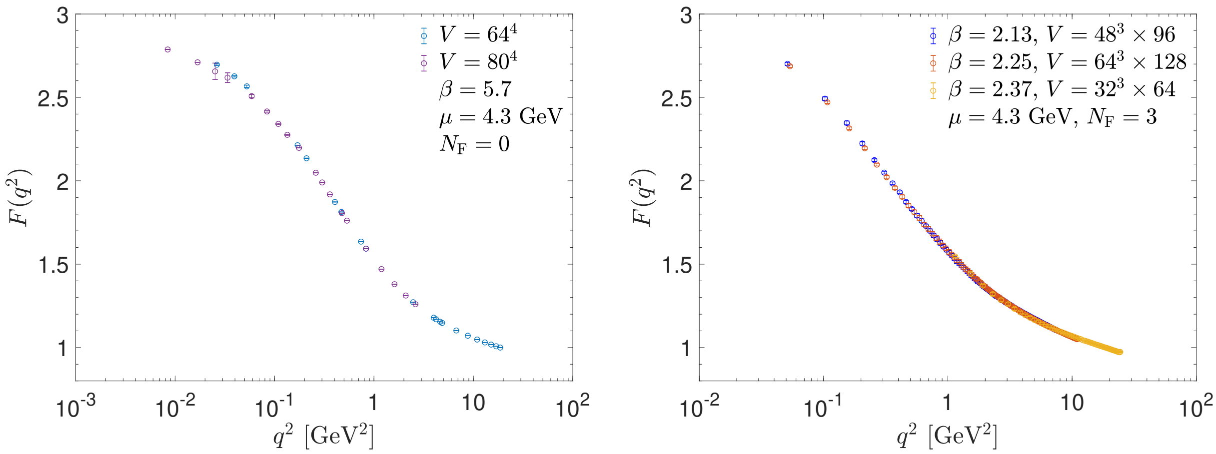

Figure 3.10: Left: Lattice results for the Landau gauge ghost dressing function, defined in Eq. (2.36), of pure Yang-Mills QCD, from Ref. [175]. Right: Ghost dressing function in QCD with 3 dynamical quarks [148]. The renormalization point in both sets is $\mu = 4.3$ GeV.

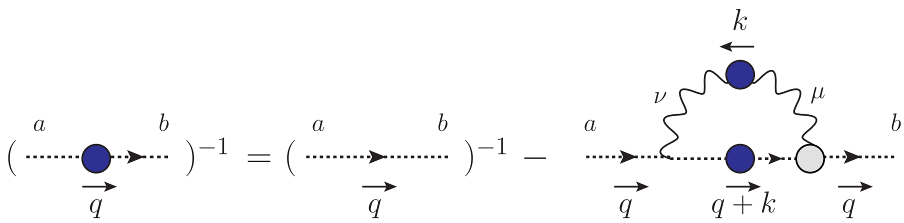

Figure 3.11: Diagrammatic representation of the ghost propagator SDE.

written here in Euclidean space, with $C_\mathrm{A} = 3$ the Casimir eigenvalue in the adjoint representation, and Z_c given by Eq. (B.13). The above integral can be computed with standard Feynman parametrization [133], yielding in Euclidean space (see Appendix D)

$$\begin{aligned} F(q^2) &= 1 + \frac{\alpha_s C_\mathrm{A}}{16\pi m^2 q^4}\left\{ 3m^2 q^4 \ln\left(\frac{\mu^2}{m^2}\right) + q^6 \ln\left(\frac{q^2}{m^2}\right) \right. \\ & \left. +(m^2+q^2)\left[m^2q^2 - (m^2+q^2)^2 \ln\left(\frac{q^2+m^2}{m^2}\right)\right]\right\}, \end{aligned} \tag{3.37}$$

where $\alpha_s := g^2/(4\pi)$.

If we expand Eq. (3.37) around $m^2 = 0$ the usual one-loop expression of Eq. (B.15) is recovered. Expanding it instead around $q^2 \to 0$, for nonzero mass, leads to

$$F(0) = 1 - \frac{3\alpha_s C_\mathrm{A}}{32\pi}\left[2\ln\left(\frac{m^2}{\mu^2}\right) + 1\right], \tag{3.38}$$

which is indeed finite.

Evidently, the above argument must be understood as a qualitative explanation, since the hard mass of Eq. (B.40) breaks gauge invariance, and we have not considered the quantitative effects of the dressings of the vertex and propagators entering the SDE of Fig. 3.11. Nevertheless, the hard mass propagator of Eq. (B.40) is a useful model for an assessment of the qualitative effect of the finiteness of $\Delta(0)$ on different Green's functions. For the case of $F(q^2)$, more sophisticated analyses including propagator and vertex dressings [3, 30, 83, 178–181] lead to the same conclusion that $F(0)$ is finite.

Similar reasoning can be applied to other diagrams containing internal gluon lines; the gluon propagators may be substituted, at a qualitative level, by Eq. (B.40), producing terms of the form $1/(k^2 + m^2)$ in the Euclidean space integrands, with k the virtual momentum. Then, the presence of a gluon mass reduces the degree of IR divergence of the diagram, in comparison to the corresponding perturbative one, which would contain terms of the form $1/k^2$ instead.

However, not all IR divergences of QCD are tamed by the advent of the dynamical gluon mass. Instead, since the ghosts remain massless, the IR divergences caused by internal ghost lines, which are of the form $1/k^2$, persist nonperturbatively [52], albeit with different coefficients, due to the various dressings of the propagators and vertices.

An important example of IR divergence that persist nonperturbatively appears in the kinetic term of the gluon propagator, $J(q^2)$, defined in Eq. (3.32). Taking a closer look at the gluon SDE of Fig. 3.2, we note that the diagram (a_3) contains only ghost lines in its loop, and explicit calculation [52] leads to a contribution of the form $q^2 \ln q^2$. The gluon propagator itself does not contain any IR divergence, since $q^2 \ln q^2 \to 0$ for $q^2 = 0$. However, factoring out the momentum q^2, as required by Eq. (3.32), leads to a logarithmically divergent $J(q^2)$.

More specifically, adding the IR finite terms coming from the diagrams that contain internal gluon lines to the IR divergence produced by diagram (a_3), implies the asymptotic behavior [52]

$$J(q^2) \underset{q^2 \to 0}{\simeq} a \ln\left(\frac{q^2}{\mu^2}\right) + b \,. \tag{3.39}$$

Moreover, the sign of the prefactor a can be determined by explicit calculation within the PT-BFM scheme and is found to be positive [52]. Hence,

$$\lim_{q^2 \to 0} J(q^2) = -\infty \,. \tag{3.40}$$

Now, in the UV the full gluon propagator must recover its perturbative behavior. Then, using the one loop result for $J(q^2)$ of Eq. (B.14), we see that

$$\lim_{q^2\to\infty} J(q^2) = \infty\,. \tag{3.41}$$

Combining the two opposite limits of Eqs. (3.40) and (3.41), it follows that $J(q^2)$ must change sign, and therefore contain a zero-crossing for some momentum $q_{_J}^2$, *i.e.* $J(q_{_J}^2) = 0$.

The logarithmic IR divergence of $J(q^2)$ has an important implication for the behavior of the three-gluon vertex. Namely, Eq. (3.33) indicates that the regular part, $\Gamma_{\alpha\mu\nu}(q,r,p)$, of the three-gluon vertex may also have logarithmic IR divergences in its form factors [52]. Indeed, although the complete SDE for the three-gluon vertex is lengthy and difficult to analyze, it is clear that it contains the two ghost triangle diagrams shown in Fig. 3.12. Then, since the ghosts remain massless nonperturbatively the two diagrams in Fig. 3.12 yield logarithmic IR divergences for $\Gamma_{\alpha\mu\nu}(q,r,p)$, just as indicated by the STI of Eq. (3.33) and the divergence of $J(q^2)$.

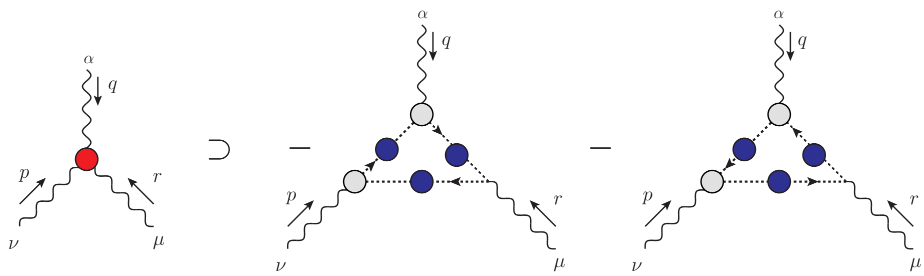

Figure 3.12: Ghost triangle diagrams contained in the full SDE of the regular part, $\Gamma_{\alpha\mu\nu}(q,r,p)$, of the three-gluon vertex. Explicit minus signs for closed ghost loops have been written to account for the Fermi statistics of the ghosts.

As a consequence of its logarithmic IR divergence, the $\Gamma_{\alpha\mu\nu}(q,p,r)$ is expected to also display a zero-crossing [52], and consequent suppression with respect to tree-level. Indeed, both features are observed on lattice simulations [7, 43–49] as well as continuum results [4, 8, 50–60]. The ensuing suppression produced by the three-gluon vertex in the integration kernels that it appears on is potentially phenomenologically relevant and has been explored in several recent works [5, 6, 56, 57, 62, 63, 71].

3.5 Maximum of the gluon propagator and positivity violation

While the full gluon propagator is finite at zero momentum, the IR divergence of $J(q^2)$ has an important implication for the qualitative behavior of $\Delta(q^2)$. Namely, $\Delta(q^2)$ has a maximum in Euclidean space [52].

Following the Wick rotation prescriptions of Appendix D, the Eq. (3.32) is transformed to

$$\Delta^{-1}(q^2) = q^2 J(q^2) + m^2(q^2)\,, \tag{3.42}$$

Differentiating Eq. (3.42) we find

$$-\frac{\Delta'(q^2)}{\Delta^2(q^2)} = J(q^2) + q^2 J'(q^2) + [m^2(q^2)]'\,, \tag{3.43}$$

where the prime denotes derivative with respect to q^2. Then we consider the q^2 limit of Eq. (3.43). Using the asymptotic behavior of $J(q^2)$ given in Eq. (3.39), we see that

$$\lim_{q^2\to 0} q^2 J'(q^2) = a\,. \tag{3.44}$$

Assuming that the derivative of $m^2(q^2)$ is finite at the origin, as found in previous numerical studies [6, 32, 63, 182], we are led to the asymptotic form for the derivative of the gluon propagator

$$\Delta'(q^2) \underset{q^2\to 0}{\simeq} -\Delta^2(0)\left[a\ln\left(\frac{q^2}{\mu^2}\right) + c\right]\,, \tag{3.45}$$

with $c := a + b + [m^2(0)]'$. Hence, the derivative of the gluon propagator diverges logarithmically at the origin.

Now, given that a and $\Delta(0)$ are positive, Eq. (3.45) gives

$$\lim_{q^2\to 0} \Delta'(q^2) = \infty\,. \tag{3.46}$$

On the other hand, for large q^2 the perturbative behavior sets in, and Eq. (B.14) leads to

$$\Delta'(q^2)\Big|_{\rm UV} < 0\,, \tag{3.47}$$

which, in combination with Eq. (3.46), implies that $\Delta'(q^2)$ changes sign. Hence, there exists some Euclidean momentum $q_{\rm M}$ such that $\Delta'(q^2_{\rm M}) = 0$, *i.e.* the gluon propagator function $\Delta(q^2)$ has an extremum. Moreover, $q_{\rm M}$ must be a maximum, given the signs of $\Delta'(q^2)$ in Eqs. (3.46) and (3.47).

The existence of a maximum of the gluon propagator has a deep theoretical implication; that the gluon propagator violates positivity of the spectral function.

To see this, consider the standard Källén-Lehmann representation [183] of the gluon propagator

$$\Delta(q^2) = \int_0^\infty \mathrm{d}t \frac{\rho(t)}{q^2 + t}\,, \tag{3.48}$$

where $\rho(t)$ is the gluon spectral function. Differentiating Eq. (3.48) with respect to q^2 leads to

$$\Delta'(q^2) = -\int_0^\infty \mathrm{d}t \frac{\rho(t)}{(q^2 + t)^2}\,, \tag{3.49}$$

and it is evident that $\Delta'(q^2)$ can only vanish if $\rho(t)$ changes sign in the interval $[0, \infty]$.

The result that $\rho(t)$ changes sign is called "positivity violation", and entails that the gluon field in Landau gauge does not satisfy the Osterwalder-Schrader axioms [184, 185], which require that $\rho(t)$ be nonnegative. The physical interpretation of positivity violation is still discussed [15, 186, 187]. Nevertheless, the IR divergence of $\Delta'(q^2)$, stated in Eq. (3.46), and the consequent maximum of the gluon propagator in Euclidean space are features that can be used to restrict the behavior of $\rho(t)$ [114], which in turn can be used to analytically continue the Euclidean space propagator to the Minkowski space.

3.6 A consistent Ansatz for $J(q^2)$ and $m^2(q^2)$

As we have seen throughout this chapter, the gluon propagator in QCD has a dynamically generated effective mass, and its kinetic term, $J(q^2)$, has an IR logarithmic divergence. To undertake the Gauge Technique determination of the three-gluon vertex, which is the main goal of this work, we will need inputs for the gluon propagator functions $J(q^2)$ and $m^2(q^2)$ that capture the aforementioned features and accurately describes the lattice data for $\Delta(q^2)$.

To begin, the existing results for the gluon dynamical mass [6, 32, 63, 182] can all be fitted accurately with the functional form [62]

$$m^2(q^2) = \frac{m_0^2}{1 + (q^2/\rho_m^2)^{1+\gamma}}\,, \tag{3.50}$$

with constants m_0, ρ_m and γ. Note that the above expression reproduces the power-law running of Eq. (3.35) for large momenta, with small logarithmic corrections embedded in γ, provided this parameter is small.

In contrast, the kinetic term $J(q^2)$ is very difficult to obtain from SDEs, given the need to truncate the complicated SDE of the gluon propagator (see Fig. 3.2), which contains various dressed vertices, in a way that preserves the transversality of the Landau gauge $\Delta_{\mu\nu}(q)$ and its multiplicative renormalizability. Nevertheless, existing results [6] can be fitted accurately with [4]

$$J(q^2) = 1 + \frac{C_{\rm A}\alpha_s}{4\pi}\left(1 + \frac{\tau_1}{q^2+\tau_2}\right)\left[2\ln\left(\frac{q^2+\rho\, m^2(q^2)}{\mu^2}\right) + \frac{1}{6}\ln\left(\frac{q^2}{\mu^2}\right)\right]\,, \tag{3.51}$$

where $m^2(q^2)$ is given in Eq. (3.50). Notice the presence of two kinds of logarithms in Eq. (3.51): an "unprotected" logarithm, $\ln(q^2/\mu^2)$, which captures the IR divergence of $J(q^2)$, stemming from the ghost loop in the gluon SDE [cf. Eq. (3.39)]; and a "protected" logarithm, $\ln[(q^2+\rho\, m^2(q))/\mu^2]$, which saturates to a finite value, $\ln(\rho\, m_0^2/\mu^2)$, at the origin and models the IR finite contributions from the gluon loops. The factors of 2 and 1/6 multiplying the protected and unprotected logarithms, respectively, can be justified by a nonperturbative toy model calculation of the gluon SDE in the PT-BFM scheme [62]. Finally, for large q^2, Eq. (3.51) recovers the one-loop behavior of $J(q^2)$, given in Minkowski space in Eq. (B.14).

Combining Eqs. (3.50) and (3.51) into Eq. (3.42) provides a model for the Euclidean gluon propagator [4] which can be fitted to the lattice data, shown in the left panel of Fig. 3.1, and captures the qualitative properties of the nonperturbative $\Delta(q^2)$ discussed in this chapter, while recovering its perturbative behavior in the UV.

Naturally, due to truncation error in the dynamical equations governing the gluon mass, different approximations [6, 32, 63, 182] lead to results for $m^2(q^2)$ with slightly different runnings. In order to accommodate the uncertainty in the gluon mass, we allow the exponent γ in Eq. (3.50) to take on values in the interval $\gamma \in [0, 0.3]$. Moreover, we fix the parameters $m_0^2 = 0.147\,\text{GeV}^2$ and $\rho_m^2 = 1.18\,\text{GeV}^2$, which are compatible with

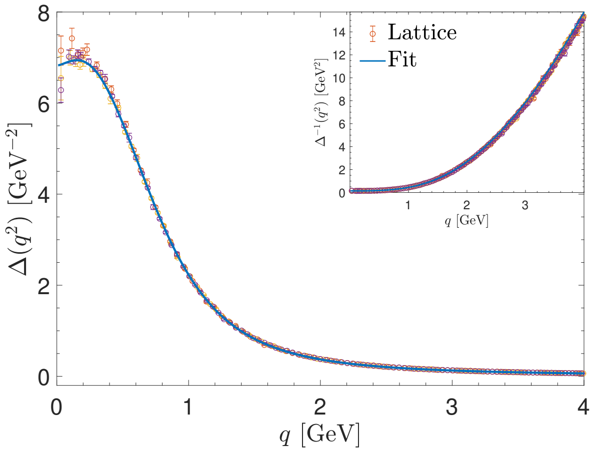

Figure 3.13: Left: Fit for the gluon propagator using Eqs. (3.42), (3.50) and (3.51) for $\gamma = 0$, compared to the lattice results of Ref. [175]. The inset shows $\Delta^{-1}(q^2)$.

the various results for $m^2(q^2)$ [6, 32, 63, 182]. Also, we fix the value of the strong coupling to $\alpha_s = 0.22$, for $\mu = 4.3$ GeV, found in previous analysis of the ghost propagator SDE [180] and which is in agreement with lattice determinations of the coupling at this renormalization point [188].

With the above restrictions, a least squares fit for the gluon propagator is obtained for each value of $\gamma = 0$, 0.1, 0.2 and 0.3 using the Eqs. (3.50) and (3.51). At the level of $\Delta(q^2)$, the different fits are visually indistinguishable and we show in Fig. 3.13 only the result with $\gamma = 0$. It can be appreciated in Fig. 3.13 that the present model for the gluon propagator has a maximum in the IR, more precisely at $q_{\rm M} = 250$ MeV. A maximum around that same region is discernible in the lattice data [73, 76], shown in the same figure, albeit with contamination of large noise in the IR.

The remaining parameters, ρ, τ_1 and τ_2, of Eq. (3.51) are found to depend smoothly on γ according to

$$\begin{aligned}
\rho(\gamma) &= 100.8 - 82.21\gamma^{1.28}\,, \\
\tau_1(\gamma) &= 9.87 - 6.96\gamma\,, \\
\tau_2(\gamma) &= 0.80 + 0.11\exp(-10\gamma)\,,
\end{aligned} \tag{3.52}$$

to very good approximation, as shown in Fig. 3.14, where the values of ρ, τ_1 and γ for $\gamma = 0$, 0.1, 0.2 and 0.3 are marked by stars, whereas the continuous curves represent Eq. (3.52).

Using the sets of parameters given in the caption of Fig. 3.14 we obtain the $J(q^2)$ and

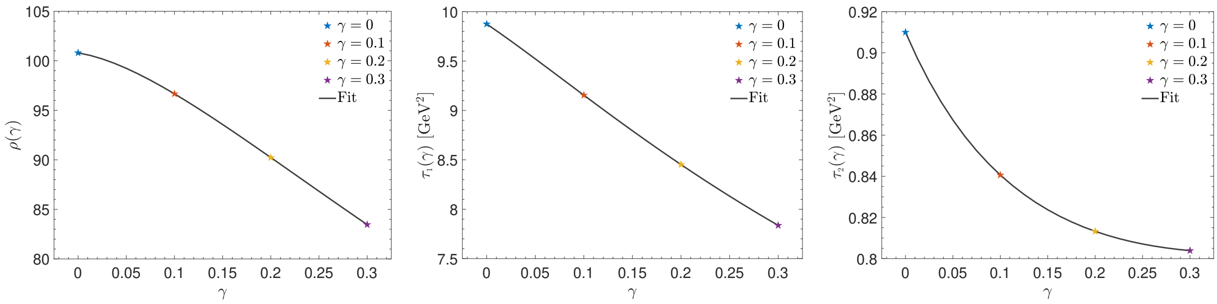

Figure 3.14: Values of ρ (left), τ_1 (center), and τ_2 (right) for Eq. (3.51) that fit the lattice data for the gluon propagator for $\gamma = 0$, 0.1, 0.2 and 0.3 are shown as stars; these values are accurately described by the functional forms given in Eq. (3.52). The values marked by stars are given by $[\gamma, \rho, \tau_1\,(\text{in GeV}^2), \tau_2\,(\text{in GeV}^2)]$: $[0, 100.8, 9.87, 0.91]$ (blue stars), $[0.1, 96.7, 9.15, 0.84]$ (red stars), $[0.2, 90.3, 8.45, 0.81]$ (yellow stars), and $[0.3, 83.5, 7.84, 0.80]$ (purple stars).

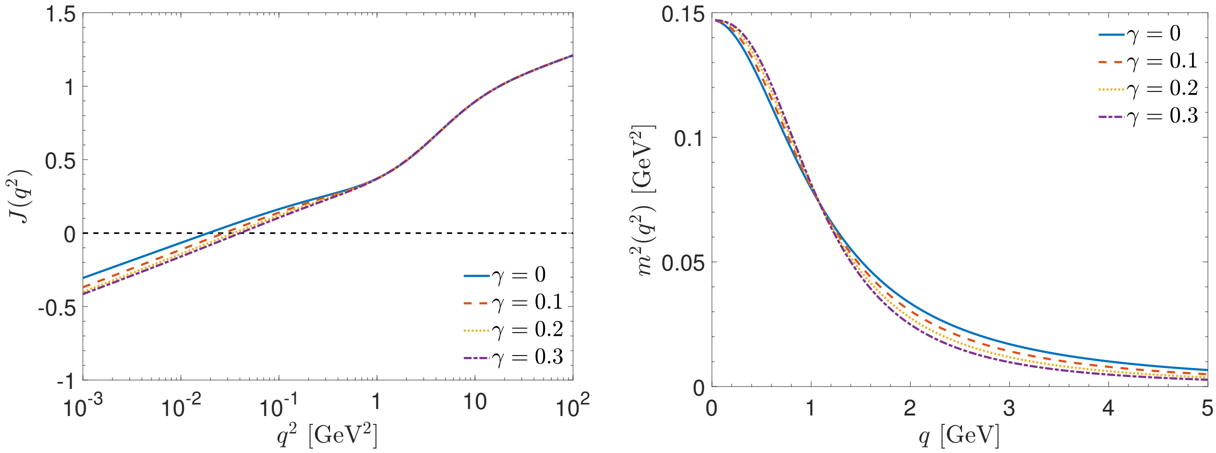

Figure 3.15: Left: kinetic term, $J(q^2)$, of the gluon propagator, defined in Eq. (3.51), for $\gamma = 0$, 0.1, 0.2 and 0.3, corresponding to the blue continuous, red dashed, yellow dotted and purple dot-dashed curves, respectively. Right: Gluon dynamical mass of Eq. (3.50), with the same color coding for different values of γ as in the left panel.

$m^2(q^2)$ shown in Fig. 3.15. The results for different values of γ are all qualitatively similar, and $J(q^2)$, in particular, shows significant quantitative variations in the IR only. In particular, the different $J(q^2)$ of Fig. 3.15 have their zero-crossings located at $q_J = 140$, 166, 187, and 202 MeV, for $\gamma = 0$, 0.1, 0.2, and 0.3, respectively.

4

The gauge technique implementation

We have already seen the simplest instance of the Gauge Technique in Subsection 2.4.1, where we determined the longitudinal part of the gluon propagator from the STI it satisfies, namely Eq. (2.62). However, it is in the study of the vertex functions that the Gauge Technique really shines [1, 4, 7, 124–128], allowing part of the vertex tensor structures to be determined from the STIs that connect them to other Green's functions.

As we will discuss in detail throughout this chapter there are, in general, tensor structures of the vertices that satisfy the STIs trivially and are left undetermined by the Gauge Technique. These are said to be the "transverse" vertex parts. Nevertheless, vertex approximations obtained through the Gauge Technique, neglecting the transverse pieces, can be used as input to truncate SDEs for other Green's functions, such as the propagators [2, 6, 25, 107, 108, 119–122, 130–132].

However, in order that the transverse pieces can be neglected safely it is fundamental that the analytic structure of the vertices under consideration be preserved, at least as far as their pole structures are considered, *i.e.* we must not introduce spurious poles in the vertices when omitting the transverse pieces. In the absence of massless bound state excitations in the vertices, a naive Gauge Technique solution may cause the vertex approximation to have spurious poles in certain kinematic configurations [108, 124, 125], known as "kinematic divergences". These divergences have to be eliminated by a careful rearrangement of the tensor bases, which we will refer to as the BC [125, 126] construction.

On the other hand, in the presence of massless bound state excitations, the vertex is allowed to have poles, but it is fundamental that they remain longitudinally coupled. In the case of the three-gluon vertex, the classical BC construction, which does not account for massless bound state excitations in the vertex, distorts the pole structure of the vertex when a massive gluon propagator is used, causing the poles to survive transverse projections if the "transverse" tensor structures are neglected. We show that a slight modification of the BC construction, which takes explicit advantage of the longitudinal nature of the massless bound state excitation poles is possible, whose main upshot is the substitution of the gluon propagator by its kinetic term only in the BC solution. This procedure leads to self-consistent vertex approximations, even if the "transverse" pieces are omitted.

We begin this chapter by reviewing in Section 4.1 the BC construction in scalar QED [125], paying special attention to the problem of kinematic divergences and their elimination. Then, in Section 4.2 we point out, still in scalar QED for illustration, how the construction should be modified in the presence of massless bound state excitations. Next, we discuss the BC construction of the regular part of the three-gluon vertex in Section 4.3 and solve for the longitudinally coupled pole terms in Section 4.4. Finally, in Section 4.5 we show, with analytic and numerical examples, that a naive application of the BC construction for the three-gluon vertex, without proper account of the longitudinality of the massless bound state poles, leads to poles that survive a transverse projection and are not compatible with lattice simulations of this vertex.

4.1 Ball-Chiu construction in scalar QED

To fix the ideas before tackling the more complex Gauge Technique solution of the three-gluon vertex, let us review the application of the method in scalar QED. We start with the case where the vertex $\mathbb{G}_\mu(q,r,p)$ has no massless poles, and follow the discussion of BC of Ref. [125] with minor adaptations. We will see the modifications needed in the presence of a longitudinally coupled pole term in the next section.

The most general Lorentz structure of the vertex $\mathbb{G}_\mu(q,r,p)$ is given by

$$\mathbb{G}_\mu(q,r,p) = p_\mu \Psi_1(q,r,p) + r_\mu \Psi_2(q,r,p)\,, \tag{4.1}$$

such that the determination of the full $\mathbb{G}_\mu(q,r,p)$ amounts to evaluating two unknown scalar functions, $\Psi_1(q,r,p)$ and $\Psi_2(q,r,p)$. Evidently, the WI of Eq. (3.10) allows us to determine one of the above form factors. Choosing to eliminate $\Psi_1(q,r,p)$, we contract

Eq. (4.1) with q^μ and use Eq. (3.10) to obtain

$$\Psi_1(q,r,p) = \frac{\mathcal{D}^{-1}(p^2) - \mathcal{D}^{-1}(r^2)}{q\cdot p} - \left(\frac{q\cdot r}{q\cdot p}\right)\Psi_2(q,r,p)\,, \tag{4.2}$$

such that Eq. (4.1) reads

$$\mathbb{G}_\mu(q,r,p) = \frac{p_\mu}{q\cdot p}[\mathcal{D}^{-1}(p^2) - \mathcal{D}^{-1}(r^2)] + \left[r_\mu - \left(\frac{q\cdot r}{q\cdot p}\right)p_\mu\right]\Psi_2(q,r,p)\,. \tag{4.3}$$

Now, it may seem that with Eq. (4.3) we are finished. However, note the presence of $q\cdot p$ denominators in Eq. (4.3). For completely general $\Psi_2(q,r,p)$, these denominators lead to kinematic divergences whenever $q\cdot p = 0$. As we will just show, these divergences are incompatible with the known $q = 0$ limit of the WI, given in Eq. (3.12). Hence Eq. (4.3) does not solve the WI completely for unconstrained $\Psi_2(q,r,p)$ and it is necessary to impose a restriction on this form factor to eliminate the divergence in $q\cdot p = 0$.

Consider the $q \to 0$ limit of Eq. (4.3). In addition, suppose we approach this limit through a trajectory (in the space of values of q) such that $q\cdot p$ is non zero except at the point $q = 0$. Then, since at $q = 0$ momentum conservation leads to $r = -p$, expanding $\mathcal{D}^{-1}(p^2)$ in a Taylor series as

$$\mathcal{D}^{-1}(p^2) = \mathcal{D}^{-1}(r^2) + 2(q\cdot r)\frac{\partial\mathcal{D}^{-1}(r^2)}{\partial r^2}\,, \tag{4.4}$$

and setting $q\cdot r = -q\cdot p$, we obtain

$$\mathbb{G}_\mu(0,r,-r) = 2r_\mu\frac{\partial\mathcal{D}^{-1}(r^2)}{\partial r^2}\,, \tag{4.5}$$

which is, correctly, equivalent to Eq. (3.12). In contrast, if we approach the $q = 0$ through a trajectory where q and p are orthogonal, *i.e.* $q\cdot p = 0$, the $q \to 0$ limit of Eq. (4.3) is undefined. This is not acceptable, since the $q = 0$ limit of the right hand side of the WI of Eq. (3.10) is path independent.

To reconcile these results, we impose on the $\Psi_2(q,r,p)$ of Eq. (4.3) the restriction

$$\lim_{q\cdot p\to 0}[(q\cdot r)\Psi_2(q,r,p)] = \lim_{q\cdot p\to 0}\left[\mathcal{D}^{-1}(p^2) - \mathcal{D}^{-1}(r^2)\right]\,, \tag{4.6}$$

which eliminates the kinematic divergence. This constraint can be implemented easily be defining a new function $\overline{\Psi}_2(q,r,p)$ by

$$\Psi_2(q,r,p) := \frac{\mathcal{D}^{-1}(p^2) - \mathcal{D}^{-1}(r^2)}{p^2 - r^2} + (q\cdot p)\overline{\Psi}_2(q,r,p)\,. \tag{4.7}$$

Indeed, by momentum conservation $p^2 - r^2 = -q\cdot(p-r)$, which implies

$$\lim_{q\cdot p\to 0}(p^2 - r^2) = q\cdot r\,, \tag{4.8}$$

such that Eq. (4.7) satisfies the constraint of Eq. (4.6) for any $\overline{\Psi}_2(q,r,p)$ that is regular at $q\cdot p\to 0$. Then, substituting Eq. (4.7) into Eq. (4.3) yields

$$\mathbb{G}_\mu(q,r,p) = (r-p)_\mu\frac{[\mathcal{D}^{-1}(p^2) - \mathcal{D}^{-1}(r^2)]}{p^2 - r^2} + [(q\cdot p)r_\mu - (q\cdot r)\,p_\mu]\overline{\Psi}_2(q,r,p)\,. \tag{4.9}$$

The solution given by Eq. (4.9) is now free of kinematic divergences; there is still the denominator $p^2 - r^2$, which vanishes when $p^2 = r^2$, but so does the numerator in this case, yielding a regular result. In particular, the $q = 0$ limit of Eq. (4.5) is now path independent, as required.

Moreover, the Eq. (4.9) is still free of kinematic divergences even if we neglect the undetermined part, *i.e.* set $\overline{\Psi}_2(q,r,p) = 0$. This latter point is key for practical applications of the Gauge Technique solution of Eq. (4.9). Given that the WI does not allow us to determine the full tensor structure of the vertex, in practice, we usually need to neglect the undetermined piece, which we can do safely, at least as far as kinematic divergences are concerned, if we use Eq. (4.9). In contrast, if the naive solution of Eq. (4.3) was used, and $\Psi_2(q,r,p)$ was set to zero, spurious kinematic divergences would have arisen.

As an overall check, we use the tree level value of the propagator, given in Eq. (3.9), and set $\overline{\Psi}_2^{(0)}(q,r,p) = 0$, to obtain indeed the tree-level form of the vertex, given by Eq. (3.4).

Finally, let us point out that if we had had the foresight of writing the most general tensor structure of $\mathbb{G}_\mu(q,r,p)$ as

$$\mathbb{G}_\mu(q,r,p) = (r-p)_\mu\overline{\Psi}_1(q,r,p) + [(q\cdot p)r_\mu - (q\cdot r)\,p_\mu]\overline{\Psi}_2(q,r,p)\,, \tag{4.10}$$

which is also perfectly general, the solution of the WI of Eq. (3.10) would have led directly to

$$\overline{\Psi}_1(q,r,p) = \frac{[\mathcal{D}^{-1}(p^2) - \mathcal{D}^{-1}(r^2)]}{p^2 - r^2}\,. \tag{4.11}$$

That is, we would have obtained Eq. (4.9) right away. Thus, we see that the appearance of kinematic divergences to eliminate depends on the tensor basis chosen to begin the Gauge Technique solution, and clever choices of bases can simplify the analysis considerably.

4.2 Ball-Chiu vertex with dynamical mass generation

Let us now reconsider the BC construction of $\mathbb{G}_\mu(q,r,p)$ in the presence of massless bound state excitations as in Eq. (3.25), which must be longitudinally coupled to the photon momentum.

Evidently, in order for the solution (4.9) for the vertex $\mathbb{G}_\mu(q,r,p)$ to have a $1/q^2$ pole as in Eq. (3.25), we must relax the condition that $\overline{\Psi}_2(q,r,p)$ is regular. Instead, we substitute in Eq. (4.9)

$$\overline{\Psi}_2(q,r,p) \to \widetilde{\Psi}_2(q,r,p) = \overline{\Psi}_2(q,r,p) + \frac{\widetilde{U}(q,r,p)}{q^2}\,, \tag{4.12}$$

with $\widetilde{U}(q,r,p)$ regular, such that we can keep using the symbol $\overline{\Psi}_2(q,r,p)$ for the regular part of this form factor.

Next, it is straightforward algebra to check the identity

$$(q\cdot p)r_\mu - (q\cdot r)\,p_\mu = \frac{1}{2}q_\mu(p^2 - r^2) - \frac{1}{2}q^2(r-p)_\mu\,. \tag{4.13}$$

Then, using Eqs. (4.12) and (4.13) into the BC solution (4.9) entails

$$\begin{aligned}\mathbb{G}_\mu(q,r,p) \;&=\; (r-p)_\mu\left\{\frac{[\mathcal{D}^{-1}(p^2) - \mathcal{D}^{-1}(r^2)]}{p^2 - r^2} - \frac{\widetilde{U}(q,r,p)}{2}\right\}\\ &\quad+[(q\cdot p)r_\mu - (q\cdot r)\,p_\mu]\overline{\Psi}_2(q,r,p) + q_\mu\frac{(p^2-r^2)\widetilde{U}(q,r,p)}{2q^2}\,.\end{aligned} \tag{4.14}$$

Comparing the above expression to Eq. (3.25), we can identify

$$\widetilde{U}(q,r,p) = \frac{2\,U(q,r,p)}{(p^2 - r^2)}\,, \tag{4.15}$$

such that Eq. (4.14) becomes

$$\begin{aligned}\mathbb{G}_\mu(q,r,p) &= (r-p)_\mu \frac{[\mathcal{D}^{-1}(p^2)-\mathcal{D}^{-1}(r^2)-U(q,r,p)]}{p^2-r^2} + [(q\cdot p)r_\mu - (q\cdot r)\,p_\mu]\overline{\Psi}_2(q,r,p) \\ &\quad + \frac{q_\mu}{q^2}U(q,r,p)\,. \end{aligned} \tag{4.16}$$

Importantly, the pole part in the last term of Eq. (4.16) is longitudinal, as it should. Moreover, it remains so even if we omit the undetermined form factor $\overline{\Psi}_2(q,r,p)$. Notice that in the present case, the longitudinality of the pole part ensued without imposing any additional restriction.

Remarkably, in Eq. (4.16) it is no longer the difference of two inverse propagators that appears in the $(r-p)_\mu$ term, as it was in Eq. (4.9), but $\mathcal{D}^{-1}(p^2)-\mathcal{D}^{-1}(r^2)-U(q,r,p)$. When we come to the case of QCD, the analog expression will have the full gluon propagator substituted by its kinetic term, of Eq. (3.32), only!

With Eq. (4.16) at hand, if the scalar propagator $\mathcal{D}(q^2)$ is known and given that $U(q,r,p)$ can be computed, in principle, from the massless bound state BSE through Figs. 3.5 and 3.6, the full vertex $\mathbb{G}_\mu(q,r,p)$ is determined, up to the "transverse" form factor, $\overline{\Psi}_2(q,r,p)$.

In the case of the three-gluon vertex of QCD the situation is considerably more complicated, for two main reasons: (*i*) the tensor structure of $\Gamma_{\alpha\mu\nu}(q,p,r)$ is much richer, which naturally makes the analysis more difficult; and (*ii*) the propagator that appears in the three-gluon vertex STI of Eq. (2.82) is that of the gluon itself. Since the gluons acquire a dynamical mass through the pole content of the vertex, the analytic structure of the three-gluon vertex STI is modified on both sides of the equation, whereas in our make-believe theory of scalar QED only the left hand side, *i.e.* $\mathbb{G}_\mu(q,r,p)$, is fundamentally changed when massless bound state excitations are added. The consequence of these additional complications, as we will see in Section 4.5, is that the longitudinality of the three-gluon vertex poles within a BC solution with dynamical gluon mass is not automatic as it was found above for scalar QED. Instead, cancellation of transverse vertex poles in the case of the three-gluon vertex restricts the pole content of its corresponding undetermined "transverse" part, analogous to $\overline{\Psi}_2(q,r,p)$.

In anticipation of the issues that will arise in the BC solution of the three-gluon vertex, we will now derive Eq. (4.16) by an alternative method, which is far more suitable for the

QCD case. The essential feature of this method is that the WI is split into two equations, one for the regular part of the vertex, and another for its pole term, $q_\mu U(q,r,p)/q^2$, taking explicit advantage of the longitudinality of the latter.

We begin by splitting the scalar propagator $\mathcal{D}^{-1}(q^2)$ as

$$\mathcal{D}^{-1}(q^2) = \mathcal{D}_{\rm R}^{-1}(q^2) + \mathcal{D}_{\rm P}^{-1}(q^2)\,, \tag{4.17}$$

with $\mathcal{D}_{\rm R}^{-1}(q^2)$ and $\mathcal{D}_{\rm P}^{-1}(q^2)$ defined by requiring that the WI of Eq. (3.10) holds for the regular and pole parts of the vertex in isolation, *i.e.*

$$\begin{aligned} q^\mu G_\mu(q,r,p) &= \mathcal{D}_{\rm R}^{-1}(p^2) - \mathcal{D}_{\rm R}^{-1}(r^2)\,, \\ U(q,r,p) &= \mathcal{D}_{\rm P}^{-1}(p^2) - \mathcal{D}_{\rm P}^{-1}(r^2)\,. \end{aligned} \tag{4.18}$$

Then, we can solve the two STIs of Eq. (4.18) separately.

In the case of scalar QED the second line of Eq. (4.18) already contains the explicit solution for $U(q,r,p)$. As for $G_\mu(q,r,p)$, the first line of Eq. (4.18) is formally identical to the original WI of the full vertex, just with the substitution of $\mathcal{D}(q^2)$ for $\mathcal{D}_{\rm R}(q^2)$. Moreover, $G_\mu(q,r,p)$ is regular, by assumption. Therefore, the BC solution of Eq. (4.9) is perfectly valid for $G_\mu(q,r,p)$ with $\mathcal{D}(q^2) \to \mathcal{D}_{\rm R}(q^2)$, *i.e.*

$$G_\mu(q,r,p) = (r-p)_\mu \frac{[\mathcal{D}_{\rm R}^{-1}(p^2) - \mathcal{D}_{\rm R}^{-1}(r^2)]}{p^2-r^2} + [(q\cdot p) r_\mu - (q\cdot r)\, p_\mu]\overline{\Psi}_2(q,r,p)\,. \tag{4.19}$$

Combining Eq. (4.19) with Eq. (3.25) then yields for the full vertex

$$\begin{aligned} \mathbb{G}_\mu(q,r,p) &= (r-p)_\mu \frac{[\mathcal{D}_{\rm R}^{-1}(p^2) - \mathcal{D}_{\rm R}^{-1}(r^2)]}{p^2-r^2} + [(q\cdot p) r_\mu - (q\cdot r)\, p_\mu]\overline{\Psi}_2(q,r,p) \\ &+ \frac{q_\mu}{q^2}[\mathcal{D}_{\rm P}^{-1}(p^2) - \mathcal{D}_{\rm P}^{-1}(r^2)]\,. \end{aligned} \tag{4.20}$$

Clearly, the pole term on the last line of Eq. (4.20) is longitudinal. Moreover, using Eqs. (4.17) and (4.18) we see that

$$\mathcal{D}_{\rm R}^{-1}(p^2) - \mathcal{D}_{\rm R}^{-1}(r^2) = \mathcal{D}^{-1}(p^2) - \mathcal{D}^{-1}(r^2) - U(q,r,p)\,, \tag{4.21}$$

which substituted in Eq. (4.20) leads *precisely* to Eq. (4.16).

At this point, it may seem odd that the pole piece is not written in the same tensor basis as the regular part. We can, of course, use again the identity (4.13) to rewrite Eq. (4.20) for the full vertex in the BC basis. Specifically

$$\mathbb{G}_\mu(q,r,p) = (r-p)_\mu \widetilde{\Psi}_1(q,r,p) + [(q\cdot p)r_\mu - (q\cdot r)\,p_\mu]\widetilde{\Psi}_2(q,r,p)\,, \tag{4.22}$$

where

$$\begin{aligned}
\widetilde{\Psi}_1(q,r,p) &= \frac{[\mathcal{D}^{-1}(p^2) - \mathcal{D}^{-1}(r^2)]}{p^2 - r^2}\,, \\
\widetilde{\Psi}_2(q,r,p) &= \overline{\Psi}_2(q,r,p) + \frac{2[\mathcal{D}_{\rm P}^{-1}(p^2) - \mathcal{D}_{\rm P}^{-1}(r^2)]}{q^2(p^2-r^2)}\,,
\end{aligned} \tag{4.23}$$

Curiously, when the full vertex is written in the BC basis the two pieces of the scalar propagator recombine in the form factor $\widetilde{\Psi}_1(q,r,p)$ into the full $\mathcal{D}^{-1}(q^2)$, using Eq. (4.17), whereas in $\widetilde{\Psi}_2(q,r,p)$ it is the $\mathcal{D}_{\rm P}^{-1}(q^2)$ that appears. Moreover, in this form the pole structure of the vertex would be missed if we were to omit $\widetilde{\Psi}_2(q,r,p)$ entirely. Instead, only $\overline{\Psi}_2(q,r,p)$ can be omitted.

A few more clarifications about the solution in Eq. (4.23) are in order.

First, in Eq. (4.23) the pole in q^2 appears in $\widetilde{\Psi}_2(q,r,p)$, which accompanies the "transverse" tensor $[(q\cdot p)r_\mu - (q\cdot r)\,p_\mu]$, *i.e.* $q^\mu[(q\cdot p)r_\mu - (q\cdot r)\,p_\mu] = 0$, in Eq. (4.22). Yet, the pole in the vertex is longitudinal. This is not a contradiction, but a semantic ambiguity. The key observation is that $[(q\cdot p)r_\mu - (q\cdot r)\,p_\mu]$ is not *strictly* transverse; it does vanish when contracted with q^μ, but contains q_μ contributions nonetheless, as Eq. (4.13) shows.

In fact, the appearance of a pole term in $\widetilde{\Psi}_2(q,r,p)$ is a crucial feature of the full vertex in the BC basis. As we will see in Section 4.4, the same situation happens in the three-gluon vertex. The important practical consequence is that only the regular part of the transverse form factors may be omitted, and it may be better, in fact, to leave the pole part in a basis that makes its longitudinality explicit.

4.3 Ball-Chiu solution for the three-gluon vertex

We consider then the gauge technique solution for the three-gluon vertex, first constructed by Kim and Baker [124], and further analyzed by BC [126]. Importantly, the original BC construction was devised without considering the possibility of massless bound state excitations in the three-gluon vertex. Hence, it must be modified to account for the pole structure of the full three-gluon vertex of QCD with dynamically generated gluon mass.

Following the second method presented in the previous section, we separate the vertex $\mathrm{I}\!\Gamma_{\alpha\mu\nu}(q,r,p)$ into its regular, $\Gamma_{\alpha\mu\nu}(q,r,p)$, and pole, $V_{\alpha\mu\nu}(q,r,p)$, parts and employ the split STIs of Eqs. (3.33) and (3.34). Since $\Gamma_{\alpha\mu\nu}(q,r,p)$ is, by assumption, regular and satisfies an STI that is formally identical to that of the full vertex, only with the substitution $\Delta^{-1}(q^2) \to q^2 J(q^2)$ [*cf.* Eqs. (3.33) and (2.82)], the BC solution can be safely applied to the regular part of the STI. As for the pole vertex, it is better to exploit the strict longitudinality of its tensor structure in the Gauge Technique solution and we postpone its treatment to the next section.

In order to solve the STI of Eq. (3.33), we decompose the tensor functions appearing in it in their most general Lorentz structures. For the ghost-gluon scattering kernel, which appears on the right hand side of that equation, the most general form is given by

$$H_{\nu\mu}(q,p,r) = g_{\mu\nu}A_1 + q_\mu q_\nu A_2 + r_\mu r_\nu A_3 + q_\mu r_\nu A_4 + r_\mu q_\nu A_5\,, \tag{4.24}$$

where the momentum dependence, $A_i \equiv A_i(q,p,r)$, has been suppressed for compactness. At tree level, only $A_1^{(0)} = 1$ is non-zero. Note that in the Eq. (3.33), $H_{\nu\mu}(q,p,r)$ appears contracted with $\mathrm{P}_\alpha^\nu(q)$. As such, only the form factors A_1, A_3 and A_4 can contribute to the STI.

As for $\Gamma_{\alpha\mu\nu}(q,r,p)$, its most general Lorentz structure has 14 independent tensors. Similarly to the case of scalar QED presented in Section 4.1, the STI of Eq. (3.33) does not allow us to determine the full vertex, but only its "non-transverse" part, *i.e.* the part that does not vanish upon contraction with the momenta q^α, r^μ and p^μ. Specifically, we can always write $\Gamma_{\alpha\mu\nu}(q,r,p)$ as

$$\Gamma^{\alpha\mu\nu}(q,r,p) = \Gamma^{\alpha\mu\nu}_{\rm STI}(q,r,p) + \Gamma^{\alpha\mu\nu}_{\rm T}(q,r,p)\,, \tag{4.25}$$

with the "transverse" part, $\Gamma^{\alpha\mu\nu}_{\rm T}(q,r,p)$, annihilated by the contractions

$$q_\alpha\Gamma^{\alpha\mu\nu}_{\rm T}(q,r,p) = r_\mu\Gamma^{\alpha\mu\nu}_{\rm T}(q,r,p) = p_\nu\Gamma^{\alpha\mu\nu}_{\rm T}(q,r,p) = 0\,. \tag{4.26}$$

Evidently, the term $\Gamma^{\alpha\mu\nu}_{\rm T}(q,r,p)$ cannot be determined through the STI.

We shall not reproduce here the lengthy algebra leading to the solution of the STI, and will go straight to the results of BC [126] instead. A detailed resolution, but in different notation, is given by Kim and Baker [124]. Nevertheless, it is instructive to count the number of independent equations that the STI constitutes, since this is what determines how many of the form factors of the vertex can be computed from the identity.

The left hand side of Eq. (3.33), namely $q^{\alpha}\Gamma_{\alpha\mu\nu}(q,r,p)$, is a function of two independent momenta (one being dependent, since $q+p+r=0$) with two free Lorentz indices. Hence, it has 5 independent tensor structures, similarly to the $H_{\nu\mu}(q,p,r)$ of Eq. (4.24), yielding thus 5 equations. Now, the cyclic permutations of Eq. (3.33) also hold, namely

$$\begin{aligned} r^{\mu}\Gamma_{\alpha\mu\nu}(q,r,p) &= F(r^2)[q^2 J(q^2)\mathrm{P}^{\mu}_{\alpha}(q)H_{\mu\nu}(q,r,p) - p^2 J(p^2)\mathrm{P}^{\mu}_{\nu}(r)H_{\mu\alpha}(p,r,q)]\,, \\ p^{\nu}\Gamma_{\alpha\mu\nu}(q,r,p) &= F(p^2)[r^2 J(r^2)\mathrm{P}^{\nu}_{\mu}(r)H_{\nu\alpha}(r,p,q) - q^2 J(q^2)\mathrm{P}^{\nu}_{\alpha}(q)H_{\nu\mu}(q,p,r)]\,, \end{aligned} \tag{4.27}$$

yielding 5 more equations each.

It may seem then that we have 15 equations for 14 tensors. However, not all of these equations are independent. Instead, as we have seen in Subsection 2.4.3, if we contract each of the STIs with one more momentum, each pair of identities leads to a cyclic permutation of the constraint of Eq. (2.88), which involves *only* the ghost sector functions, $F(q^2)$ and $H_{\nu\mu}(q,p,r)$, and does not determine form factors of the three-gluon vertex. Using the tensor decomposition of Eq. (4.24), the constraint (2.88) can be written in terms of the following ratio

$$\mathcal{R}(q^2,p^2,r^2) := \frac{F(r^2)[A_1(q,r,p) + p^2 A_3(q,r,p) + (q\cdot p)A_4(q,r,p)]}{F(p^2)[A_1(q,p,r) + r^2 A_3(q,p,r) + (q\cdot r)A_4(q,p,r)]} = 1\,. \tag{4.28}$$

Since we can make three pairs of equations by contracting the three STIs with one of the remaining momenta, there are two other constraints, namely, the Eq. (4.28) with cyclically permuted arguments. Hence, out of the 15 equations encompassed by the three-gluon vertex STI 3 are scalar constraints on the ghost sector. It is important to emphasize that the existence of *exact* solutions to the STI is conditioned to the constraints of Eq. (4.28) being satisfied.

Next, of the 12 remaining equations, there is one that appears three times, *i.e.* with two redundant repetitions. Specifically, contracting any of the three STIs of Eqs. (3.33) and (4.27) with the momenta and indices of the two remaining legs yields the exact same equation, $q^\alpha r^\mu p^\nu \Gamma_{\alpha\mu\nu}(q,r,p) = 0$. Discounting the two redundancies leaves us with 10 independent equations, plus the aforementioned 3 constraints. Therefore, 10 form factors can be determined from the STI, such that $\Gamma^{\alpha\mu\nu}_{\rm STI}(q,r,p)$ can be parametrized in terms of 10 independent tensor structures, with the remaining 4 assigned to $\Gamma^{\alpha\mu\nu}_{\rm T}(q,r,p)$.

A convenient tensor basis for the three-gluon vertex is that of BC [126]. For the 10 tensor structures of $\Gamma^{\alpha\mu\nu}_{\rm STI}(q,r,p)$, one may write

$$\Gamma^{\alpha\mu\nu}_{\rm STI}(q,r,p) = \sum_{i=1}^{10} X_i(q,r,p)\ell_i^{\alpha\mu\nu}\,, \tag{4.29}$$

where the tensors $\ell_i^{\alpha\mu\nu}$ read

$$\begin{aligned}
&\ell_1^{\alpha\mu\nu} = (q-r)^\nu g^{\alpha\mu}\,, && \ell_2^{\alpha\mu\nu} = -p^\nu g^{\alpha\mu}\,, && \ell_3^{\alpha\mu\nu} = (q-r)^\nu[q^\mu r^\alpha - (q\cdot r)g_{\alpha\mu}]\,,\\
&\ell_4^{\alpha\mu\nu} = (r-p)^\alpha g^{\mu\nu}\,, && \ell_5^{\alpha\mu\nu} = -q^\alpha g^{\mu\nu}\,, && \ell_6^{\alpha\mu\nu} = (r-p)^\alpha[r^\nu p^\mu - (r\cdot p)g^{\mu\nu}]\,,\\
&\ell_7^{\alpha\mu\nu} = (p-q)^\mu g^{\alpha\nu}\,, && \ell_8^{\alpha\mu\nu} = -r^\mu g^{\alpha\nu}\,, && \ell_9^{\alpha\mu\nu} = (p-q)^\mu[p^\alpha q^\nu - (p\cdot q)g^{\alpha\nu}]\,,\\
&\ell_{10}^{\alpha\mu\nu} = q^\nu r^\alpha p^\mu + q^\mu r^\nu p^\alpha\,.
\end{aligned} \tag{4.30}$$

As for the transverse part, the Lorentz decomposition is

$$\Gamma^{\alpha\mu\nu}_{\rm T}(q,r,p) = \sum_{j=1}^{4} Y_j(q,r,p)t_j^{\alpha\mu\nu}\,, \tag{4.31}$$

where the transverse tensors $t_j^{\alpha\mu\nu}$ read

$$\begin{aligned}
t_1^{\alpha\mu\nu} =& [(q\cdot r)g^{\alpha\mu} - q^\mu r^\alpha][(r\cdot p)q^\nu - (q\cdot p)r^\nu]\,,\\
t_2^{\alpha\mu\nu} =& [(r\cdot p)g^{\mu\nu} - r^\nu p^\mu][(p\cdot q)r^\alpha - (r\cdot q)p^\alpha]\,,\\
t_3^{\alpha\mu\nu} =& [(p\cdot q)g^{\nu\alpha} - p^\alpha q^\nu][(q\cdot r)p^\mu - (p\cdot r)q^\mu]\,,\\
t^4_{\alpha\mu\nu} =& g_{\mu\nu}[(r\cdot q)p_\alpha - (p\cdot q)r_\alpha] + g_{\nu\alpha}[(p\cdot r)q_\mu - (q\cdot r)p_\mu] + g_{\alpha\mu}[(q\cdot p)r_\nu - (r\cdot p)q_\nu]\\
&+ r_\alpha p_\mu q_\nu - p_\alpha q_\mu r_\nu\,,
\end{aligned} \tag{4.32}$$

and clearly vanish if contracted with q^α, r^μ or p^ν. Moreover, all the $t_j^{\alpha\mu\nu} \to 0$ if one of the momenta q, r or p is set to zero. Comparing the above expressions to the tree-level form of the vertex, given in the Appendix A, we see that at tree level

$$X_1^{(0)}(q,r,p) = X_4^{(0)}(q,r,p) = X_7^{(0)}(q,r,p) = 1\,, \tag{4.33}$$

with all other $X_i^{(0)} = 0$ and $Y_j^{(0)} = 0$.

A crucial property of the BC basis above is that its tensor structures have simple transformations under the Bose symmetry exchanges of momenta and corresponding indices. For example, under the simultaneous exchange $q \leftrightarrow r$ and $\alpha \leftrightarrow \mu$ the tensor $\ell_1^{\alpha\mu\nu}$ is invariant, while $\ell_4^{\alpha\mu\nu} \leftrightarrow \ell_7^{\alpha\mu\nu}$. As a result, the form factors X_i and Y_j also transform in a simple fashion. Specifically, many of the X_i and Y_j are related by cyclic permutations of the arguments, namely

$$\begin{aligned}
X_4(q,r,p) &= X_1(r,p,q)\,, & X_7(q,r,p) &= X_1(p,q,r)\,,\\
X_5(q,r,p) &= X_2(r,p,q)\,, & X_8(q,r,p) &= X_2(p,q,r)\,,\\
X_6(q,r,p) &= X_3(r,p,q)\,, & X_9(q,r,p) &= X_3(p,q,r)\,,\\
Y_2(q,r,p) &= Y_1(r,p,q)\,, & Y_3(q,r,p) &= Y_1(p,q,r)\,.
\end{aligned} \tag{4.34}$$

Moreover, the following transformations are easy to establish

$$\begin{aligned}
X_1(q,r,p) &= X_1(r,q,p)\,, & X_4(q,r,p) &= X_4(q,p,r)\,, & X_7(q,r,p) &= X_7(p,r,q)\,,\\
X_2(q,r,p) &= -X_2(r,q,p)\,, & X_5(q,r,p) &= -X_5(q,p,r)\,, & X_8(q,r,p) &= -X_8(p,r,q)\,,\\
X_3(q,r,p) &= X_3(r,q,p)\,, & X_6(q,r,p) &= X_6(q,p,r)\,, & X_9(q,r,p) &= X_9(p,r,q)\,,\\
Y_1(q,r,p) &= Y_1(r,q,p)\,, & Y_2(q,r,p) &= Y_2(q,p,r)\,, & Y_3(q,r,p) &= Y_3(p,r,q)\,,
\end{aligned} \tag{4.35}$$

whereas $X_{10}(q,r,p)$ is anti-symmetric under the exchange of any two of its arguments and $Y_4(q,r,p)$ is totally symmetric.

From Eq. (4.34), we see that only the form factors X_i for $i = 1, 2, 3, 10$ and the Y_j for $j = 1, 4$ need to be computed, the remaining ones being obtained by permuting the arguments.

Accordingly to the above observation, we only need to state the solution for the form factors X_i for $i = 1, 2, 3, 10$, with the Y_j undetermined by the STIs, and the remaining

X_i given by Eq. (4.34). Then, the BC solution may be written as [126]

$$
\begin{aligned}
X_1(q,r,p) =& \frac{1}{4}[2(a_{pqr}+a_{prq})+p^2(b_{qrp}+b_{rqp})+2(\,q\cdot p\,d_{prq}+\,r\cdot p\,d_{pqr})\\
&+(q^2-r^2)(b_{rpq}+b_{pqr}-b_{qpr}-b_{prq})]\,,\\
X_2(q,r,p) =& \frac{1}{4}[2(a_{prq}-a_{pqr})-(q^2-r^2)(b_{qrp}+b_{rqp})+2(\,q\cdot p\,d_{prq}-\,r\cdot p\,d_{pqr})\\
&+p^2(b_{prq}-b_{pqr}+b_{qpr}-b_{rpq})]\,,\\
X_3(q,r,p) =& \frac{1}{q^2-r^2}[a_{rpq}-a_{qpr}+r\cdot p\,d_{qpr}-q\cdot p\,d_{rpq}]\,,\\
X_{10}(q,r,p) =& -\frac{1}{2}[b_{qrp}+b_{rpq}+b_{pqr}-b_{qpr}-b_{rqp}-b_{prq}]\,,
\end{aligned}
\tag{4.36}
$$

where we employ the compact notation

$$
\begin{aligned}
a_{qrp} \equiv& F(r)J(p)A_1(p,r,q)\,,\\
b_{qrp} \equiv& F(r)J(p)A_3(p,r,q)\,,\\
d_{qrp} \equiv& F(r)J(p)[A_4(p,r,q)-A_3(p,r,q)]\,,
\end{aligned}
\tag{4.37}
$$

and emphasize that Eq. (4.36) solves the STIs of Eqs. (3.33) and (4.27) as long as the constraint of Eq. (4.28) and its cyclic permutations are satisfied.

At this point it is easy to check that the BC solution satisfies automatically the exchange relations of Eq. (4.35). Moreover, Eq. (4.36) is clearly free of kinematic divergences; the only non-constant denominator that appears in the solution, namely q^2-r^2, only vanishes when the numerator is also zero, yielding regular results.

Because Eq. (4.36) is Bose symmetric and free of kinematic divergences automatically, independently of the Y_i or the truncations used to evaluate $F(q^2)$ and $H_{\nu\mu}(q,p,r)$, it is rather suitable for approximations, including neglecting the Y_i, at least as far as these fundamental properties are concerned.

A particularly useful approximation consists of setting the ghost sector functions appearing in Eq. (4.36) to tree level, *i.e.* $F(q)\to 1$, $A_1\to 1$ and A_3, $A_4\to 0$. In this case, the form factors reduce to the "Abelianized" forms, denoted by $\widehat{X}_i(q,r,p)$,

$$
\begin{aligned}
\widehat{X}_1(q,r,p) &= \frac{1}{2}[J(r)+J(q)]\,, \qquad \widehat{X}_3(q,r,p) = \frac{[J(q)-J(r)]}{q^2-r^2}\,,\\
\widehat{X}_2(q,r,p) &= \frac{1}{2}[J(q)-J(r)]\,. \qquad \widehat{X}_{10}(q,r,p) = 0\,.
\end{aligned}
\tag{4.38}
$$

As it turns out, Eq. (4.38) is formally identical to performing a BC construction for an analog of the three-gluon vertex with three "background" gluons, which satisfies Abelian-like WI [127, 162, 189, 190], *i.e.* with no ghost sector functions. In fact, the only difference between Eq. (4.38) and the alluded background three-gluon vertex, is that in the later it is $J(q)[1+G(q)]^{-2}$, rather than $J(q^2)$, that appears, where $1+G(q)$ is a fundamental function of the PT-BFM formalism and has been studied extensively [30, 146, 147, 166, 170, 191].

Before long, let us point out that Eq. (4.36) holds for unrenormalized as well as renormalized ingredients, provided that a gauge invariant regularization scheme is employed. If we use for the $J(q^2)$, $F(q^2)$ and $A_i(q,r,p)$ data or expressions renormalized in some chosen scheme, the $X_i(q,r,p)$ obtained from Eq. (4.36) will be automatically consistent with that choice, *i.e.* Eq. (2.91) will be satisfied. Then, if one wants the $X_i(q,r,p)$ evaluated in a different renormalization scheme, a *finite* renormalization of the ingredients will be required. For example, if we set q, r and p in the symmetric configuration of Eq. (B.5), there is no reason to expect that the Eq. (4.36) will yield $X_1(-\mu^2)=1$ in general. If one wishes to transform to the scheme where $X_1(-\mu^2)=1$ by definition, it suffices to multiply all the X_i (and Y_j, if available) by the finite renormalization constant $z_3 = 1/X_1(-\mu^2)$ [see Section B.4 for concrete examples in perturbation theory].

4.4 The Gauge Technique solution of the pole vertex

Let us now solve the STI of Eq. (3.34) and its cyclic permutations. By virtue of the strictly longitudinal tensor structure of $V_{\alpha\mu\nu}$, given in Eq. (3.30), the Eq. (3.34) has a unique solution, which can be obtained with relatively simple algebra [182].

We begin by noticing that the longitudinality condition of Eq. (3.31) can be written as [182, 192]

$$\begin{aligned}
V_{\alpha\mu\nu}(q,r,p) &= \left[g_\alpha^\beta g_\mu^\rho g_\nu^\sigma - \mathrm{P}_\alpha^\beta(q)\mathrm{P}_\mu^\rho(r)\mathrm{P}_\nu^\sigma(p)\right] V_{\beta\rho\sigma}(q,r,p) \\
&= \left(\frac{q_\alpha q^\beta g_\mu^\rho g_\nu^\sigma}{q^2} + \frac{r_\mu r^\rho g_\alpha^\beta g_\nu^\sigma}{r^2} + \frac{p_\nu p^\sigma g_\alpha^\beta g_\mu^\rho}{p^2} - \frac{q_\alpha q^\beta r_\mu r^\rho g_\nu^\sigma}{q^2 r^2} - \frac{q_\alpha q^\beta p_\nu p^\sigma g_\mu^\rho}{q^2 p^2}\right. \\
&\quad \left. - \frac{r_\mu r^\rho p_\nu p^\sigma g_\beta^\alpha}{r^2 p^2} + \frac{q_\alpha q^\beta r_\mu r^\rho p_\nu p^\sigma}{q^2 r^2 p^2}\right) V_{\beta\rho\sigma}(q,r,p)\,,
\end{aligned} \tag{4.39}$$

by simply expanding $\mathrm{P}_\alpha^\beta(q)\mathrm{P}_\mu^\rho(r)\mathrm{P}_\nu^\sigma(p)$. Separating from Eq. (4.39) the terms that contribute to each of the tensor structures in Eq. (3.30), we see that

$$R_{\mu\nu}(q,r,p) = \left(q^\beta g^\rho_\mu g^\sigma \nu - \frac{r_\mu}{2r^2} q^\beta r^\rho g^\sigma_\nu - \frac{p_\nu}{2p^2} q^\beta p^\sigma g^\rho_\mu + \frac{r_\mu p_\nu}{3r^2p^2} q^\beta r^\rho p^\sigma \right) V_{\beta\rho\sigma}(q,r,p)\,, \quad (4.40)$$

where the factor of 1/2 in the second term appears because $q_\alpha r_\mu$ contributes to both $q_\alpha R_{\mu\nu}(q,r,p)$ and $r_\mu S_{\alpha\nu}(q,r,p)$. Similarly, it is easy to confirm the presence of the factors of 1/2 and 1/3 in the third and fourth terms, respectively.

Now, each of the contractions appearing in Eq. (4.40) can be evaluated by contracting the STI of Eq. (3.34) (or its cyclic permutations) with the appropriate momenta. In particular, the last term of that equation clearly vanishes. One thus obtains [4]

$$\begin{aligned} R_{\mu\nu}(q,r,p) = \frac{F(q^2)}{2} \{ & m^2(r^2) \mathrm{P}^\rho_\mu(r) \left[g^\sigma_\nu + \mathrm{P}^\sigma_\nu(p) \right] H_{\rho\sigma}(r,q,p) \\ & - m^2(p^2) \mathrm{P}^\rho_\nu(p) \left[g^\sigma_\mu + \mathrm{P}^\sigma_\mu(r) \right] H_{\rho\sigma}(p,q,r) \} \,. \end{aligned} \quad (4.41)$$

Naturally, repeating the same procedure for the cyclic permutations of Eq. (3.34) leads to

$$\begin{aligned} S_{\alpha\nu}(q,r,p) = \frac{F(r^2)}{2} \{ & m^2(p^2) \mathrm{P}^\rho_\nu(p) \left[g^\sigma_\alpha + \mathrm{P}^\sigma_\alpha(q) \right] H_{\rho\sigma}(p,r,q) \\ & - m^2(q^2) \mathrm{P}^\rho_\alpha(q) \left[g^\sigma_\nu + \mathrm{P}^\sigma_\nu(p) \right] H_{\rho\sigma}(q,r,p) \} \,, \\ T_{\alpha\mu}(q,r,p) = \frac{F(p^2)}{2} \{ & m^2(q^2) \mathrm{P}^\rho_\alpha(q) \left[g^\sigma_\mu + \mathrm{P}^\sigma_\mu(r) \right] H_{\rho\sigma}(q,p,r) \\ & - m^2(r^2) \mathrm{P}^\rho_\mu(r) \left[g^\sigma_\alpha + \mathrm{P}^\sigma_\alpha(q) \right] H_{\rho\sigma}(r,p,q) \} \,. \end{aligned} \quad (4.42)$$

It remains to verify that the solution in Eqs. (4.41) and (4.42) is Bose symmetric, *i.e.* that the $V_{\alpha\mu\nu}(q,r,p)$ so constructed is anti-symmetric under the simultaneous exchange of a pair of momenta and indices.

Let us consider the exchange $q,\alpha \leftrightarrow r,\mu$. It is immediate to see that $T_{\alpha\mu}(q,r,p)$ is anti-symmetric. Next, we show that the combination

$$\left(\frac{q_\alpha}{q^2} \right) R_{\mu\nu}(q,r,p) + \left(\frac{r_\mu}{r^2} \right) S_{\alpha\nu}(q,r,p)\,, \quad (4.43)$$

appearing in the full tensor structure of $V_{\alpha\mu\nu}(q,r,p)$ of Eq. (3.30), is also anti-symmetric. To this end, note that the solution in Eqs. (4.41) and (4.42) for the functions $R_{\alpha\mu\nu}(q,r,p)$

and $S_{\alpha\mu\nu}(q,r,p)$ can be rewritten, with few algebraic rearrangements, as

$$\begin{aligned}\left(\frac{q_\alpha}{q^2}\right) R_{\mu\nu}(q,r,p) &= \left(\frac{q_\alpha}{q^2}\right)\frac{F(q^2)}{2}\left\{m^2(r^2)\mathrm{P}_\mu^\rho(r)\left[g_\nu^\sigma + \mathrm{P}_\nu^\sigma(p)\right]H_{\rho\sigma}(r,q,p)\right.\\ &\left.-2m^2(p^2)\mathrm{P}_\nu^\rho(p)H_{\rho\mu}(p,q,r)\right\}\\ &+\left(\frac{q_\alpha r_\mu}{q^2r^2}\right)m^2(p^2)r^\sigma\mathrm{P}_\nu^\rho(p)H_{\rho\sigma}(p,q,r)\,, \qquad (4.44)\\ \left(\frac{r_\mu}{r^2}\right) S_{\alpha\nu}(q,r,p) &= \left(\frac{r_\mu}{r^2}\right)\frac{F(r^2)}{2}\left\{-m^2(q^2)\mathrm{P}_\alpha^\rho(q)\left[g_\nu^\sigma + \mathrm{P}_\nu^\sigma(p)\right]H_{\rho\sigma}(q,r,p)\right.\\ &\left.+2m^2(p^2)\mathrm{P}_\nu^\rho(p)H_{\rho\alpha}(p,r,q)\right\}\\ &-\left(\frac{q_\alpha r_\mu}{q^2r^2}\right)m^2(p^2)q^\sigma\mathrm{P}_\nu^\rho(p)H_{\rho\sigma}(p,r,q)\,. \qquad (4.45)\end{aligned}$$

At this point, it is clear that exchanging $q,\alpha \leftrightarrow r,\mu$ the first two lines of Eq. (4.44) transform to minus the first two lines of Eq. (4.45) and vice versa. That the third line of each of the above equations also transform into minus the other is a result of the ghost sector constraint, written in the form of Eq. (2.87). Notice that this constraint does not involve the three-gluon vertex, and hence, is not modified by splitting the STI into regular and pole parts. Thus, it follows that

$$\left(\frac{q_\alpha}{q^2}\right) R_{\mu\nu}(q,r,p) \leftrightarrow -\left(\frac{r_\mu}{r^2}\right) S_{\alpha\nu}(q,r,p)\,, \qquad (4.46)$$

under the exchange $q,\alpha \leftrightarrow r,\mu$, which guarantees that $V_{\alpha\mu\nu}(q,r,p) = -V_{\mu\alpha\nu}(r,q,p)$. Identical arguments can be used to show that $V_{\alpha\mu\nu}(q,r,p)$ is anti-symmetric under the exchange of any other pair of momenta and indices. Hence, the solution in Eqs. (4.41) and (4.42) yields a Bose symmetric $V_{\alpha\mu\nu}(q,r,p)$.

Evidently, the solution in Eqs. (4.41) and (4.42) can be written in the BC basis of Eqs. (4.29) and (4.31), if one so wishes, which can be achieved by contracting $V_{\alpha\mu\nu}(q,r,p)$ with the projectors given in Section C.2. The resulting expressions with dressed ghost sector are long and we will not use in this work. It will suffice to state the solution in the Abelianized approximation, where we set to tree level the ghost sector functions in Eqs. (4.41) and (4.42), *i.e.* $F(q^2)\to 1$ and $H_{\nu\mu}(q,p,r)\to g_{\nu\mu}$. Denoting by $\widehat{X}_i^V(q,r,p)$

and $\widehat{Y}_j^V(q,r,p)$ the Abelianized form factors of $V_{\alpha\mu\nu}(q,r,p)$ in the BC basis, we have

$$\begin{aligned}
\widehat{X}_1^V(q,r,p) &= -\frac{m^2(q^2)}{2q^2} - \frac{m^2(r^2)}{2r^2}\,, \qquad \widehat{X}_2^V(q,r,p) = \frac{1}{2}\left(\frac{m^2(r^2)}{r^2} - \frac{m^2(q^2)}{q^2}\right)\,,\\
\widehat{X}_3^V(q,r,p) &= \frac{q^2 m^2(r^2) - r^2 m^2(q^2)}{q^2 r^2\,(q^2-r^2)}\,, \quad \widehat{X}_{10}^V(q,r,p) = 0\,,\\
\widehat{Y}_1^V(q,r,p) &= \frac{q^2[-m^2(p^2)+m^2(q^2)-m^2(r^2)] + r^2[m^2(p^2)+m^2(q^2)-m^2(r^2)]}{p^2q^2r^2\,(q^2-r^2)}\,,\\
\widehat{Y}_4^V(q,r,p) &= \frac{q.r[-m^2(p^2)+m^2(q^2)+m^2(r^2)] + q^2m^2(r^2)+r^2m^2(q^2)}{p^2q^2r^2}\,,
\end{aligned} \tag{4.47}$$

with the remaining $\widehat{X}_i^V(q,r,p)$ and $\widehat{Y}_j^V(q,r,p)$ given by cyclically permuting the indices, as in Eq. (4.34).

Of fundamental importance in Eq. (4.47) is the fact that the $\widehat{Y}_j^V(q,r,p)$ do not vanish, in spite of them being associated to "transverse" tensor structures and the massless bound state poles being longitudinal. As in Section 4.2, the resolution to this apparent paradox is in the semantics of the term "transverse", as applied to the $t_j^{\alpha\mu\nu}$ tensors of Eq. (4.32). While these tensors vanish if contracted with q^α, r^μ or p^ν, they do contain contributions proportional to these momenta, and hence contribute to $V_{\alpha\mu\nu}(q,r,p)$.

In fact, it is straightforward to check that if the $\widehat{Y}_j^V(q,r,p)$ are neglected in $V_{\alpha\mu\nu}$, *i.e.* if we assume

$$V_{\alpha\mu\nu}(q,r,p) \to V^\ell_{\alpha\mu\nu}(q,r,p) := \sum_{i=1}^{10} \widehat{X}_i^V(q,r,p)\ell_i^{\alpha\mu\nu}\,, \tag{4.48}$$

and use Eq. (4.47), then the longitudinality of $V_{\alpha\mu\nu}(q,r,p)$ is lost, *i.e.*

$$\mathrm{P}^\alpha_\beta(q)\mathrm{P}^\mu_\rho(r)\mathrm{P}^\nu_\sigma(p)V^\ell_{\alpha\mu\nu}(q,r,p) \neq 0\,. \tag{4.49}$$

Hence, casually neglecting the $\widehat{Y}_j^V(q,r,p)$ causes the pole part of the vertex to develop spurious poles that are not longitudinally coupled. Instead, when the full tensor structure is preserved, including the transverse pieces, then $\mathrm{P}^\alpha_\beta(q)\mathrm{P}^\mu_\rho(r)\mathrm{P}^\nu_\sigma(p)V_{\alpha\mu\nu}(q,r,p) = 0$ as it should.

4.5 Naive BC construction and its problems

We conclude this discussion by considering what would we have obtained had we used the BC solution directly for the full vertex, in the presence of a dynamically massive gluon propagator, without care about the longitudinality of the mass-generating poles of

$V_{\alpha\mu\nu}(q,r,p)$. For simplicity, we focus on the Abelianized case, of Eq. (4.38), which already captures the properties we wish to emphasize at the moment.

It is important to keep in mind that since the pole part $V_{\alpha\mu\nu}(q,p,r)$ is longitudinally coupled, it should not appear in *fully transverse* projections of the three-gluon vertex. In particular, $V_{\alpha\mu\nu}(q,p,r)$ cannot be directly probed in lattice simulations in Landau gauge, which can only evaluate projections of the vertex that are fully transverse [7, 44–46, 48, 49], since the field theoretic quantities that the lattice evaluates are the *connected* Green's functions. Specifically, the lattice observable for the three-gluon vertex is the connected function defined in Eq. (2.37), which has the vertex contracted with three gluon propagators, which are transverse in Landau gauge. Consequently, lattice results for the three-gluon vertex should not contain poles. Yet, as we will now show, a naive application of the Gauge Technique leads to the appearance of spurious poles in the transversely projected vertex, which are eliminated on proper account of the longitudinality of $V_{\alpha\mu\nu}(q,p,r)$.

To begin, it is clear that if we apply the BC construction to the complete STI of Eq. (2.82), including pole part, we obtain results formally identical to Eq. (4.36), except that $J(q^2)$ is substituted by $\Delta^{-1}(q^2)/q^2$. Importantly, $J(q^2)$ and $\Delta^{-1}(q^2)/q^2$ have completely different behaviors near $q^2 = 0$ in the presence of a gluon mass; $J(q^2)$ is only logarithmically divergent [see Eq. (3.39)], whereas $\Delta^{-1}(q^2)/q^2 \sim -m^2(0)/q^2$, *i.e.* it behaves as a pole near $q^2 = 0$. Let us see how these different analytic behaviors manifest in a totally transverse projection of the three-gluon vertex.

Consider the totally symmetric kinematic configuration, defined in Eq. (B.5), and the most general tensor structure of the three-gluon vertex in this limit, given in Eq. (B.24). Contracting the latter equation with three transverse projectors and denoting

$$\overline{\Gamma}_{\alpha\mu\nu}(q,r,p) := \mathrm{P}_{\alpha}^{\beta}(q)\mathrm{P}_{\mu}^{\rho}(r)\mathrm{P}_{\nu}^{\sigma}(p)\Gamma_{\beta\rho\sigma}(q,r,p)\,, \tag{4.50}$$

we obtain

$$\overline{\Gamma}_{\beta\rho\sigma}(q,r,p) = L^{\rm sym}(Q^2)\overline{\Gamma}^{(0)}_{\alpha\mu\nu}(q,r,p) - T^{\rm sym}(Q^2)(r-p)_{\alpha}(p-q)_{\mu}(q-r)_{\nu}\,, \tag{4.51}$$

where $L^{\rm sym}(Q^2)$ is defined in Eq. (B.24), and

$$T^{\rm sym}(Q^2) := \frac{3}{4}X_3(Q^2) + \frac{3Q^2}{8}Y_1(Q^2) - \frac{1}{4}Y_4(Q^2)\,. \tag{4.52}$$

Let us concentrate on the form factor $L^{\rm sym}(Q^2)$, which has already been simulated on the lattice [44, 45]. Its tree level, $L^{\rm sym}(Q^2) = 1$, is obtained by setting the X_i and Y_i to their tree levels.

Now, let us denote by double struck letters, *e.g.* $\mathbb{X}_i$, the results for the form factors as obtained with the direct application of the BC construction to the full vertex, and a caret to denote the Abelianized approximation, where ghost sector functions are set to their tree level values. Substituting $J(q^2) \to \Delta^{-1}(q^2)/q^2$ into Eq. (4.38), we have

$$\widehat{\mathbb{X}}_1(Q^2) = \frac{\Delta^{-1}(Q^2)}{Q^2}\,, \qquad \widehat{\mathbb{X}}_3(Q^2) = \frac{1}{Q^2}\frac{d\Delta^{-1}(Q^2)}{dQ^2} - \frac{\Delta^{-1}(Q^2)}{Q^4}\,, \tag{4.53}$$

where we made use of the fact that the expression for $\widehat{X}_3(q,r,p)$ in Eq. (4.38) becomes a derivative in the symmetric limit, where, in particular, $q^2 = r^2$. Hence, in the Abelianized approximation

$$\widehat{\mathbb{L}}^{\rm sym}(Q^2) = \frac{1}{2}\left[\frac{\Delta^{-1}(Q^2)}{Q^2} + \frac{d\Delta^{-1}(Q^2)}{dQ^2}\right] + \frac{Q^4}{4}\widehat{\mathbb{Y}}_1(Q^2) + \frac{Q^2}{2}\widehat{\mathbb{Y}}_4(Q^2)\,. \tag{4.54}$$

Given that $\widehat{\mathbb{L}}^{\rm sym}(Q^2)$ is a transverse projection of the three-gluon vertex, it should not contain poles, since these are assumed to be longitudinally coupled. Nonetheless, the first term on the right hand side of Eq. (4.54) is a pole if the gluon propagator is massive. Hence, there must be some other pole in the remaining terms to cancel that of the first. Next, as we have seen in Section 3.5, the derivative of the gluon propagator is only logarithmically divergent, such that the pole in Eq. (4.54) cannot be canceled by $d\Delta^{-1}(Q^2)/dQ^2$. As such, the pole in $\Delta^{-1}(Q^2)/Q^2$ can only be canceled by the $\widehat{\mathbb{Y}}_i$. Specifically,

$$\lim_{Q^2\to 0}\left[\frac{\Delta^{-1}(Q^2)}{Q^2} - \frac{Q^4}{2}\widehat{\mathbb{Y}}_1(Q^2) - Q^2\widehat{\mathbb{Y}}_4(Q^2)\right] = 0\,. \tag{4.55}$$

Therefore, in order to guarantee the longitudinality of the poles of the full vertex, we must split the $\widehat{\mathbb{Y}}_j(Q^2)$ into

$$\widehat{\mathbb{Y}}_j(Q^2) = \widehat{Y}_j^P(Q^2) + \widehat{Y}_j(Q^2)\,, \tag{4.56}$$

with $\widehat{Y}_j(Q^2)$ undetermined, but regular, and the $\widehat{Y}_j^P(Q^2)$ containing poles in Q^2 satisfying

$$\lim_{Q^2\to 0}\left[\frac{\Delta^{-1}(Q^2)}{Q^2} - \frac{Q^4}{2}\widehat{Y}_1^P(Q^2) - Q^2\widehat{Y}_4^P(Q^2)\right] = 0\,. \tag{4.57}$$

At this point, we look back to the solution of the pole part of the vertex in Eq. (4.47), for comparison. Taking the symmetric limit of the $\widehat{Y}_j^V(q,r,p)$ yields

$$\widehat{Y}_1^V(Q^2) = -\frac{m^2(Q^2)}{Q^6} + \frac{2}{Q^4}\frac{dm^2(Q^2)}{dQ^2}\,, \qquad \widehat{Y}_4^V(q,r,p)\frac{3m^2(Q^2)}{2Q^4}\,, \tag{4.58}$$

such that

$$\frac{Q^4}{2}\widehat{Y}_1^V(Q^2) + Q^2\widehat{Y}_4^V(Q^2) = \frac{m^2(Q^2)}{Q^2} + \frac{dm^2(Q^2)}{dQ^2}\,. \tag{4.59}$$

It should not come as a surprise, at this stage of the discussion, that Eq. (4.59) has *exactly* the right pole structure to satisfy Eq. (4.55), since $\Delta^{-1}(0) = -m^2(0)$, and eliminate the pole in Eq. (4.54). Therefore, we can choose $\widehat{Y}_j^P(Q^2) = \widehat{Y}_j^V(Q^2)$ in Eq. (4.56). Using this splitting, Eq. (4.54) becomes

$$\widehat{\mathbb{L}}^{\rm sym}(Q^2) = \frac{1}{2}\left[\frac{\Delta^{-1}(Q^2)}{Q^2} + \frac{d\Delta^{-1}(Q^2)}{dQ^2}\right] + \frac{Q^4}{4}[\widehat{Y}_1(Q^2) + \widehat{Y}_1^V(Q^2)] + \frac{Q^2}{2}[\widehat{Y}_4(Q^2) + \widehat{Y}_4^V(Q^2)]\,, \tag{4.60}$$

with $\widehat{Y}_j(Q^2)$ undetermined. Then, using the explicit expression of Eq. (4.59), and that $\Delta^{-1}(Q^2) = Q^2 J(Q^2) - m^2(Q^2)$, we obtain the final form of $\widehat{\mathbb{L}}^{\rm sym}(Q^2)$,

$$\widehat{\mathbb{L}}^{\rm sym}(Q^2) = J(Q^2) + \frac{Q^2}{2}\frac{J(Q^2)}{dQ^2} + \frac{Q^4}{4}\widehat{Y}_1(Q^2) + \frac{Q^2}{2}\widehat{Y}_4(Q^2)\,, \tag{4.61}$$

which is manifestly free of poles, and we can drop the double striking of $\widehat{L}^{\rm sym}(Q^2)$ altogether, since Eq. (4.61) makes no explicit reference to the gluon mass.

The point we wish to emphasize, from the above discussion, is that if we had applied the BC construction directly to the full vertex, we would not have been able to neglect the undetermined "transverse" parts, $\widehat{\mathbb{Y}}_j$ in Eq. (4.54), right away. Instead, we have to first impose Eq. (4.55), in order to be consistent with the longitundinality of the massless bound state poles, and only after reaching Eq. (4.61) could the undetermined terms be omitted[1].

In contrast, if we use the modified BC construction of Sections 4.3 and 4.4, which takes advantage of the longitudinality of the pole part $V_{\alpha\mu\nu}(q,r,p)$ from the onset, the result (4.61) is obtained right away. Indeed, since $V_{\alpha\mu\nu}(q,r,p)$ is strictly longitudinal, it does not contribute to $L^{\rm sym}(Q^2)$. Then, using the solution of the regular part of the vertex,

[1]See also Section VII of [4] for a distinct, but equivalent, treatment of the cancellation of poles in $L^{\rm sym}(Q^2)$ by the pole content of the Y_i.

Eq. (4.38), into Eq. (B.24) leads directly to Eq. (4.61), without *a posteriori* rearrangements as we had to do in Eq. (4.54).

Clearly, the approach of splitting the STI into Eqs. (3.33) and (3.34), applying the usual BC construction only for the regular part and taking advantage of the explicit longitudinality of $V_{\alpha\mu\nu}(q,r,p)$, leads to the correct result more expeditiously and elegantly.

Finally, we explore the numerical impact of the proper elimination of the poles. Let us consider two approximations to $L^{\rm sym}(Q^2)$, in both of which we neglect the transverse terms Y_i. The first approximation, which we will call "naively Abelianized", consists of Eq. (4.54) with the $\widehat{\mathbb{Y}}_i$ set to zero, *i.e.*

$$L^{\rm sym}_{\rm NA}(Q^2) := \frac{z_3^{\rm NA}}{2}\left[\frac{\Delta^{-1}(Q^2)}{Q^2} + \frac{d\Delta^{-1}(Q^2)}{dQ^2}\right] , \tag{4.62}$$

with $z_3^{\rm NA}$ a *finite* renormalization constant, determined by imposing the renormalization condition

$$L^{\rm sym}_{\rm NA}(\mu^2) = 1 , \tag{4.63}$$

at a scale μ^2, usually employed on the lattice [44, 45]. The second truncation, to be referred to as "properly Abelianized", is obtained from the solution of the regular part of the split STI in the Abelianized approximation, *i.e.* Eq. (B.24) with the X_i of Eq. (4.38) and the Y_j set to zero. Specifically,

$$L^{\rm sym}_{\rm A}(Q^2) := z_3^{\rm A}\left[J(Q^2) + \frac{Q^2}{2}\frac{dJ(Q^2)}{dQ^2}\right] , \tag{4.64}$$

with $z_3^{\rm A}$ determined by the renormalization condition

$$L^{\rm sym}_{\rm A}(\mu^2) = 1 . \tag{4.65}$$

For the numerical analysis, Eqs. (4.62) and (4.64) must be understood as written in Euclidean space, and μ is chosen at 4.3 GeV. As for the ingredients $J(Q^2)$ and $\Delta(Q^2)$, we use the Ansatz of Eqs. (3.51), (3.50) and (3.42).

The results of Eqs. (4.62) and (4.64) are compared to the lattice data for $L^{\rm sym}(Q^2)$ of Ref. [44, 45] in Fig. 4.1. It is clear from that figure that the qualitative behavior of the naively Abelianized vertex is disfavored by the lattice results, which has no sign of pole divergence, whereas the properly Abelianized model of Eq. (4.64) is in qualitative agreement with the lattice. At the quantitative level, the agreement is still unsatisfactory; however, as we shall see in Chapter 6, quantitative agreement is obtained with the BC construction when the ghost sector contributions are duly taken into account. This will have to wait for the nonperturbative determination of the ghost-gluon scattering kernel, which is the subject of the next chapter.

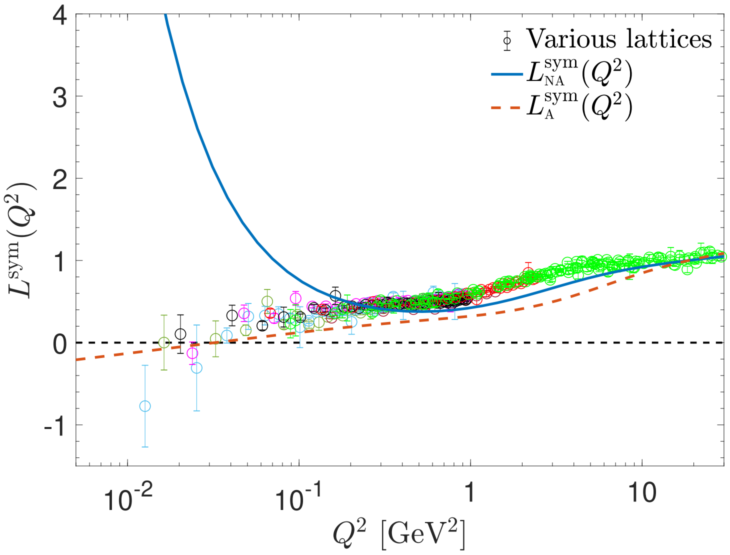

Figure 4.1: Form factor $L^{\text{sym}}(Q^2)$ of the transversely projected three-gluon vertex of Eq. (4.51). The circles represent the lattice results of [44, 45], with different colors for each lattice setup therein. The blue continuous curve represents the naive and properly Abelianized approximations of Eqs. (4.62) and (4.64), respectively.

In any case, Fig. 4.1 demonstrates quite clearly that the proper handling of the longitudinal poles is necessary in a Gauge Technique Ansatz for the three-gluon vertex in the presence of dynamical gluon mass generation through the Schwinger mechanism.

Lastly, one could posit that the IR finiteness of the gluon propagator is a result of some mechanism other than the presence of massless bound state excitations described in Chapter 3. In this case, the poles induced in the three-gluon vertex by the IR finiteness of $\Delta^{-1}(Q^2)/Q^2$ might not be longitudinal, and could have appeared in the lattice results for $L^{\text{sym}}(Q^2)$. As such, the absence of a pole behavior in the lattice data shown in Fig. 4.1 constitutes an evidence that the poles of the three-gluon vertex are indeed longitudinal, and hence, strengthen the case for the realization of the Schwinger mechanism in QCD.

5

The nonperturbative ghost-gluon scattering kernel

In order to compute the three-gluon vertex through the BC solution of the previous chapter [see Eq. (4.36)], the most complex nonpertubative ingredient is the ghost-gluon scattering kernel, $H_{\nu\mu}(q,p,r)$. Besides being an ingredient in the determination of $\Gamma_{\alpha\mu\nu}(q,r,p)$, the scattering kernel is related to the ghost-gluon vertex through Eq. (2.45), which is another fundamental vertex of QCD appearing in the SDEs of several Green's functions, including the gluon and ghost propagators [see Figs. 3.2 and 3.11]. As such, $H_{\nu\mu}(q,p,r)$ is a central object of the ghost sector of QCD.

In this chapter we focus on the nonperturbative determination of the Landau gauge ghost-gluon scattering kernel through its SDE truncated at the one-loop dressed level. We begin by reviewing some exact special properties of $H_{\nu\mu}(q,p,r)$ valid in the Landau gauge, namely, the ghost-anti-ghost symmetry, the Taylor theorem and the UV finiteness of this Green's function, in Section 5.1. Then, in Section 5.2 we discuss some general aspects of the one loop dressed truncation for the SDE governing $H_{\nu\mu}(q,p,r)$, following with a more detailed presentation of the approximations used for the inputs of that equation in Section 5.3. In Section 5.4 we present our numerical results for $H_{\nu\mu}(q,p,r)$ in general Euclidean kinematics, paying special attention to the IR divergences found for its form factors. Moreover, we show that dressing the three-gluon vertex in the calculation of $H_{\nu\mu}(q,p,r)$ tends to suppress the magnitude of its form factors. Then, in Section 5.5 we use our results to calculate also the form factors of the ghost-gluon vertex, $\Gamma_{\mu}(q,p,r)$, for which there is more extensive literature [43, 51, 55, 58, 60, 73, 118, 180, 193–197] to compare our results to. In that section, we find a general agreement between our results and those of earlier studies. Finally, in Section 5.6 we show that the STI constraint over the ghost sector, given by Eq. (4.28), is violated as a consequence of truncation. We perform a quantitative comparison of the violation of the STI constraint for two different approximations of $H_{\nu\mu}(q,p,r)$, allowing us to distinguish the truncation that minimizes this problem in the IR.

5.1 Properties of the Landau gauge $H_{\nu\mu}(q,p,r)$

In the Landau gauge, due to the transversality of the gluon propagator, the ghost-gluon scattering kernel and vertex display some additional symmetries, which we can use to guide and simplify the truncation of their SDEs. Let us take a moment to review these Landau gauge special properties.

5.1.1 Ghost-anti-ghost symmetry

The ghost-gluon vertex, $\Gamma_\mu(q,p,r)$, defined in Eq. (2.39), has for its most general Lorentz structure

$$\Gamma_\mu(q,p,r) = B_1(q,p,r)q_\mu + B_2(q,p,r)r_\mu\,. \tag{5.1}$$

Comparing Eq. (5.1) to the Feynman rule of Fig. A.2, we see that at tree level these form factors reduce to $B_1^{(0)}(q,p,r) = 1$ and $B_2^{(0)}(q,p,r) = 0$. Note also that combining Eq. (2.45) with Eqs. (4.24) and (5.1) allows us to relate the B_i to the form factors of $H_{\nu\mu}(q,p,r)$. Specifically,

$$\begin{aligned} B_1(q,p,r) &= A_1(q,p,r) + q^2 A_2(q,p,r) + (q\cdot r)A_4(q,p,r)\,; \\ B_2(q,p,r) &= (q\cdot r)A_3(q,p,r) + q^2 A_5(q,p,r)\,. \end{aligned} \tag{5.2}$$

In the Landau gauge the form factor $B_1(q,p,r)$, and only this form factor, is invariant under the exchange of the ghost and the anti-ghost momenta [15, 180], *i.e.*

$$B_1(q,p,r) = B_1(p,q,r)\,. \tag{5.3}$$

We will refer to this invariance as "ghost-anti-ghost symmetry".

We present here the proof of Eq. (5.3) given in [180]. We start with the SDE for the ghost propagator, shown in Fig. 3.11, which reads

$$D^{-1}(q) = -iq^2 - g^2 C_{\rm A} \int_k \Delta^{\mu\nu}(k) D(q+k)(q+k)_\nu \Gamma_\mu(-q, q+k, -k)\,. \tag{5.4}$$

Since in the Landau gauge $k_\mu \Delta^{\mu\nu}(k) = k_\nu \Delta^{\mu\nu}(k) = 0$, using the Lorentz decomposition (5.1) into Eq. (5.4) leads to

$$D^{-1}(q) = -iq^2 + g^2 C_{\rm A} q_\mu q_\nu \int_k \Delta^{\mu\nu}(k) D(q+k) B_1(-q, q+k, -k)\,, \tag{5.5}$$

i.e. only the form factor B_1 contributes to the ghost SDE.

As discussed in detail in [198] the SDEs for 1PI functions always have one of the external legs with a bare vertex, to avoid overcounting of diagrammatic corrections. Moreover, one can derive different SDEs for the same Green's function, with each of the external legs containing the bare vertex [198]. In the case of the ghost propagator, the SDE shown in Fig. 5.1 is also valid, and differs from that of Fig. 3.11 only by the placing of the bare vertex.

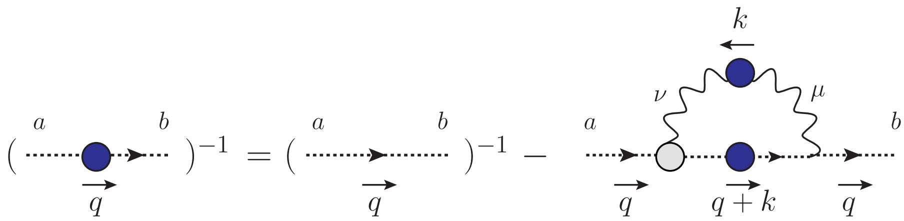

Figure 5.1: Alternative SDE for the ghost propagator, with the bare vertex on the right leg [*cf.* Fig. 3.11].

Writing down the SDE of Fig. 5.1 and using the transversality of the Landau gauge $\Delta^{\mu\nu}(k)$ furnishes

$$D^{-1}(q) = -iq^2 + g^2 C_{\rm A} q_\mu q_\nu \int_k \Delta^{\mu\nu}(k) D(q+k) B_1(-q-k, q, k)\,. \tag{5.6}$$

Then, equating (5.5) and (5.6) requires

$$B_1(-q, q+k, -k) = B_1(-q-k, q, k)\,. \tag{5.7}$$

Finally, since B_1 is a Lorentz scalar, it is unchanged if we flip the signs of all its momenta. Hence, Eq. (5.7) is equivalent to Eq. (5.3).

5.1.2 Taylor theorem

We consider now the most important property of the Landau gauge $H_{\nu\mu}(q,p,r)$, known as the Taylor theorem [39].

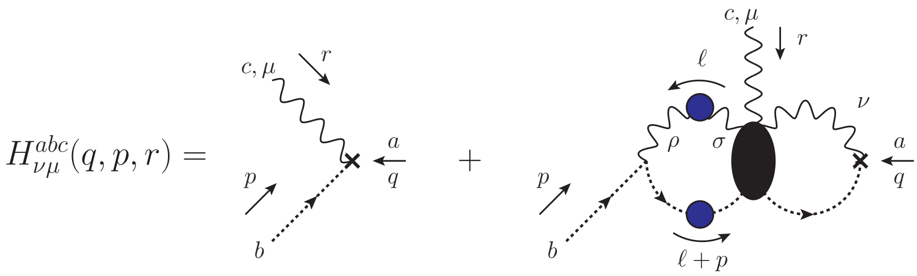

Figure 5.2: Compact representation for the SDE of the ghost-gluon scattering kernel, $H_{\nu\mu}(q,p,r)$, with the bare vertex on the ghost leg [*cf.* Fig. 2.3]. The black oval is not 1PI.

Similarly to the argument in the previous section, we can write the SDE of Fig. 2.3, for the ghost-gluon scattering kernel, with the bare vertex on the ghost leg, as shown compactly in Fig. 5.2. Then we can write

$$H_{\nu\mu}(q,p,r) = g_{\mu\nu} + \int_\ell (p+\ell)_\rho \Delta^{\rho\sigma}(\ell) D(p+\ell) \mathcal{K}_{\nu\mu\sigma}(q,r,-\ell,p+\ell)\,, \tag{5.8}$$

for some four-point kernel $\mathcal{K}_{\nu\mu\sigma}(q,r,-\ell,p+\ell)$ whose decomposition into 1PI functions is unimportant for the present discussion. Now, in the Landau gauge the transversality of the gluon propagator implies $(p+\ell)_\rho \Delta^{\rho\sigma}(\ell) = p_\rho \Delta^{\rho\sigma}(\ell)$, such that

$$H_{\nu\mu}(q,p,r) = g_{\mu\nu} + p^\rho K_{\nu\mu\rho}(q,p,r)\,, \tag{5.9}$$

with

$$K_{\nu\mu\rho}(q,p,r) := \int_\ell \Delta^\sigma_\rho(\ell) D(p+\ell) \mathcal{K}_{\nu\mu\sigma}(q,r,-\ell,p+\ell)\,. \tag{5.10}$$

Finally, setting $p = 0$ in Eq. (5.9), we obtain

$$H_{\nu\mu}(q,0,-q) = g_{\mu\nu}\,, \tag{5.11}$$

i.e. the ghost-gluon scattering kernel reduces to its tree level in the soft ghost limit ($p = 0$) in the Landau gauge. This result is what we call the Taylor theorem [39].

Now, using Eq. (2.45) to relate $H_{\nu\mu}(q,p,r)$ to the ghost-gluon vertex, we see that

$$\Gamma_\mu(q,0,-q) = q_\mu \,. \tag{5.12}$$

Comparing Eq. (5.12) to the Lorentz decomposition of Γ_μ, given by Eq. (5.1), we find that in the soft ghost configuration,

$$B_1(q,0,-1) - B_2(q,0,-q) = 1 \,. \tag{5.13}$$

It is important to emphasize that the form factors $B_1(q,p,r)$ and $B_2(q,p,r)$ do not reduce individually to their tree levels, only the combination in Eq. (5.13) does. Similarly, the $A_i(q,p,r)$ do not reduce to tree level individually in the soft ghost configuration, but satisfy

$$A_1(q,0,-q) = 1 \,; \qquad A_2(q,0,-q) + A_3(q,0,-q) - A_4(q,0,-q) - A_5(q,0,-q) = 0 \,. \tag{5.14}$$

5.1.3 Renormalization

The Taylor theorem explained in the previous subsection has a crucial consequence for the renormalization of the ghost-gluon vertex and scattering kernel. Specifically, since the UV poles of Green's functions are independent of the external momenta and Eq. (5.11) is manifestly finite, then $H_{\nu\mu}(q,p,r)$ has to be UV finite in Landau gauge [39], in all kinematic configurations. Evidently, by Eq. (2.45), the ghost-gluon vertex must be UV finite as well.

Now, Eq. (5.12) is to be understood as unrenormalized, even though its subscript "U" has been omitted for compactness. Renormalizing it according to Eq. (2.90) we obtain for the renormalized vertex

$$\Gamma_\mu(q,0,-q) = Z_1\, q_\mu \,, \tag{5.15}$$

and Z_1 must be finite, since so is $\Gamma_\mu(q,0,-q)$. In particular, if we choose as renormalization condition for the vertex that $\Gamma_\mu(q,0,-q)$ reduces to tree-level, then it follows that

$$Z_1 = 1 \,. \tag{5.16}$$

This choice of renormalization scheme is referred to as the "Taylor scheme" [4, 199, 200] throughout this work. Clearly, the renormalized $H_{\nu\mu}(q,p,r)$ also reduces to its tree level, that is $H_{\nu\mu}(q,0,-q) = g_{\mu\nu}$, in the Taylor scheme [3].

The above Eq. (5.16), sometimes called the "non-renormalization" theorem [179, 188, 199, 201], implies that the SDEs for the ghost-gluon scattering kernel and vertex can be multiplicatively renormalized in practice [3, 179, 180, 188, 198], even with truncations. In fact, the UV finiteness of the Landau gauge Γ_μ allows the ghost propagator SDE of Eq. (5.5) to also be renormalized multiplicatively in practice [179, 180, 198]. In contrast, the implementation of multiplicative renormalization in general truncated SDEs is an extremely difficult problem [106, 108, 202, 203], and usually prompts the use of additional approximations [2, 6, 25, 109, 204]. Moreover, the Taylor theorem allows the definition of an effective charge depending only on the propagators [144, 179, 188]. These simplifications regarding renormalization, enabled by the Taylor theorem, are among the many reasons why the Landau gauge is a favorite in SDE analyses. In particular, the Taylor scheme of Eq. (5.16) has been extensively employed in the SDE literature [3, 8, 179, 180, 188, 194, 198].

5.2 Truncation of the SDE for $H_{\nu\mu}(q,p,r)$

Our starting point for the nonperturbative determination of the ghost-gluon scattering kernel is its SDE of Fig. 2.3. We begin its treatment by assuming that the 1PI four-point function appearing in diagram $(d_3)_{\mu\nu}$ of Fig. 2.3 is subleading, as indicated by recent numerical studies [59, 205], and omit that diagram entirely.

Next, for the three-gluon vertex appearing in diagram $(d_1)_{\nu\mu}$ we keep only its regular part, $\Gamma_{\alpha\mu\nu}$. Because the pole part $V_{\alpha\mu\nu}$ is longitudinally coupled and the Landau gauge $\Delta^{\mu\nu}(q)$ is transverse, it is easy to see that the pole part would not contribute to the form factors A_1, A_2 and A_4. Hence, neglecting the pole part is only an additional approximation for the form factors A_3 and A_5. In any case, if the pole structure of the three-gluon vertex was kept, it would induce poles in $H_{\nu\mu}(q,p,r)$ which would also be longitudinal to the gluon momentum, and might contribute to the gluon mass. Nevertheless, there is numerical evidence that the contribution of poles in the ghost-gluon sector to the gluon mass is subleading [62].

With the above approximations, the so-called one-loop dressed truncation, the ghost-gluon scattering kernel SDE of Fig. 2.3 is substituted by Fig. 5.3. Specifically, with the

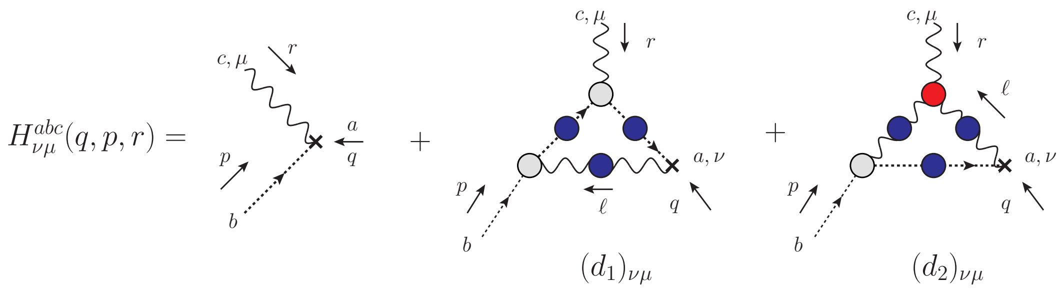

Figure 5.3: One loop dressed truncation of the ghost-gluon scattering kernel SDE. The red circle represents the regular part of the three-gluon vertex, as in Fig. 3.7.

momentum routing indicated in that figure, we have

$$H_{\nu\mu}(q,p,r) = g_{\nu\mu} + (d_1)_{\nu\mu} + (d_2)_{\nu\mu}\,, \tag{5.17}$$

with

$$\begin{aligned}(d_1)_{\nu\mu} &= \frac{1}{2}C_{\rm A}g^2\,p_\rho\int_\ell \Delta_\nu^\rho(\ell)D(\ell+p)D(\ell-q)\Gamma_\mu(q-\ell,\ell+p,r)B_1(-\ell-p,p,\ell)\,, \\ (d_2)_{\nu\mu} &= \frac{1}{2}C_{\rm A}g^2\,p_\rho\int_\ell \Delta_\nu^\beta(\ell)\Delta^{\alpha\rho}(\ell+r)D(\ell-q)\Gamma_{\mu\alpha\beta}(r,-\ell-r,\ell)B_1(q-\ell,p,\ell+r)\,.\end{aligned} \tag{5.18}$$

It is evident from Eq. (5.18) that the Taylor theorem is preserved in the one-loop dressed truncation, since both diagrams $(d_1)_{\nu\mu}$ and $(d_2)_{\nu\mu}$ are proportional to the ghost momentum, p.

Meanwhile, as a result of the truncation, the ghost-anti-ghost-symmetry of Eq. (5.3) is explicitly broken if Eq. (5.17) is used to compute the form factor B_1 through Eq. (5.2). This issue arises because the corrections to the vertex in the anti-ghost leg in the full SDE of Fig. 2.3 are allocated to the four-point function [198] present in diagram (d_3), which we omitted, ending up with corrections only to the vertex in the ghost leg. This problem can be remedied by recalling that we might have derived the SDE shown in Fig. 5.3 with the bare vertex on the ghost leg instead. Then, averaging the "ghost leg bare" and "anti-ghost leg bare" SDEs restores the ghost-anti-ghost symmetry [198]. In practice, this procedure amounts to the effective substitution in Eq. (5.18) of

$$\begin{aligned}B_1(-\ell-p,p,\ell) \to \mathcal{V}_1(\ell,q,p,r) =& \frac{1}{2}\left[B_1(-\ell-p,p,\ell)+B_1(q,\ell-q,-\ell)\right]\,, \\ B_1(q-\ell,p,\ell+r) \to \mathcal{V}_2(\ell,q,p,r) =& \frac{1}{2}\left[B_1(q-\ell,p,\ell+r)+B_1(q,\ell-q,-\ell)\right]\,.\end{aligned} \tag{5.19}$$

A similar procedure is commonly employed to restore Bose symmetry in analyses of the gluonic vertices with truncated SDEs [53, 54, 206].

Finally, Eq. (5.17) must be consistently renormalized. To this end, we first multiply that equation by Z_1 and substitute all quantities appearing in Eq. (5.18) by their renormalized counterparts using Eqs. (2.89) and (2.90) and $g = Z_1^{-1} Z_A^{1/2} Z_c\, g_{\text{U}}$. Symbolically, we find

$$\begin{aligned} H_{\nu\mu}(q,p,r) &= Z_1 \left[g_{\mu\nu} + (d_1)_{\nu\mu} + \left(\frac{Z_1 Z_A}{Z_c Z_3} \right) (d_2)_{\nu\mu} \right] , \\ &= Z_1 \left[g_{\mu\nu} + (d_1)_{\nu\mu} + (d_2)_{\nu\mu} \right] , \end{aligned} \tag{5.20}$$

where we used the STI for the renormalization constants, Eq. (2.91), to obtain the last line. At this point we may choose the renormalization prescription for the renormalized quantities. Naturally, we will take advantage of the Taylor theorem and settle for the Taylor scheme of Eq. (5.16). As for the gluon and ghost propagators that appear in Eq. (5.18), we employ the common choice of Eq. (2.92), *i.e.* the MOM scheme.

A few additional approximations will be useful for numerical purposes, which we discuss in the next section.

5.3 Inputs and further approximations

In general, the SDEs are coupled integral equations that allow, *in principle*, the determination of all the Green's functions of the theory. For example, the ghost-gluon scattering kernel SDE of Eq. (5.18), if coupled to some truncated form of the gluon and ghost SDEs of Figs. 3.2 and 3.11, respectively, and the three-gluon vertex SDE [53, 54], could be used to determine all of these functions self-consistently. In practice, technical difficulties in truncating these equations, as well as the intensive numerical effort necessary, prompts us to adopt a different strategy.

Before stating the actual inputs used, we emphasize that we have found, by experiment, that the STI constraint of Eq. (2.88) is violated in our numerical results for $H_{\nu\mu}(q,p,r)$. This violation was found, after several numerical experiments and analytic calculations, to not be a numerical issue, but an artifact of the truncation of the SDE. Moreover, the issue is aggravated for large momenta if the inputs used for the propagators and vertices contain their perturbative corrections. The reason for this behavior is that the one-loop dressed truncation contains two loop and higher corrections, but not all of them. As a result, perturbative logarithms that should be canceled if all corrections were consistently preserved end up uncanceled. These logarithms, which should be powers of $\ln(q^2/\mu^2)$, are likely negligible near the renormalization point, μ, and also probably subleading in the IR where the gluon mass becomes the dominant scale. Nevertheless, for large momenta they build up large violations of the symmetries of the theory, in particular the Eq. (2.88). A workaround, which we have validated by experiment, is to use inputs for the propagators and vertices appearing in Eq. (5.18) that tend to their tree levels in the UV. Evidently, the reason this procedure works is that it results in $H_{\nu\mu}(q,p,r)$ recovering its one-loop behavior, *by construction*, for large momenta. For definiteness, we shall denote the ingredients that are used as inputs for the SDE of $H_{\nu\mu}(q,p,r)$ by a super/subscript "in".

As was done in numerous previous works, *e.g.* Refs. [1, 2, 25, 171], we use for the gluon propagator and ghost dressing function fits to the large volume lattice results available. For the ghost dressing function, in particular, we use

$$F(q^2) \to F_{\text{in}}(q^2) = 1 + \frac{\sigma_1}{q^2 + \sigma_2}\,, \tag{5.21}$$

which fits the lattice data of [175] with the parameter values set to $\sigma_1 = 0.70$ GeV^2 and $\sigma_2 = 0.39$ GeV^2. Clearly, $\lim_{q^2\to\infty} F_{\text{in}}(q^2) = 1$, as discussed above. We compare the above fit to the lattice data of [175] in Fig. 5.4, where we see that the IR structure of $F(q^2)$ is still well captured by F_{in}.

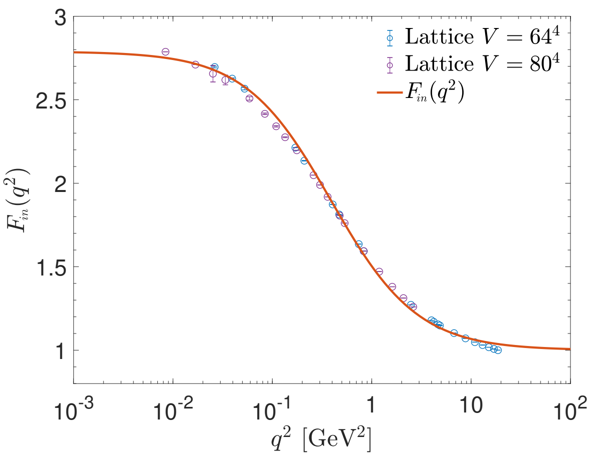

Figure 5.4: Comparison of the fit (red curve), $F_{\text{in}}(q^2)$, given by Eq. (5.21), for the ghost dressing function, $F(q^2)$, and the lattice data of Ref. [175] (circles).

As for the gluon propagator, we substitute Eq. (3.42) for

$$\Delta^{-1}(q^2) \to \Delta^{-1}_{\text{in}}(q^2) = q^2 J_{\text{in}}(q^2) + m^2(q^2)\,, \tag{5.22}$$

with $m^2(q^2)$ given by Eq. (3.50) and the input kinetic term has the parametrization

$$J_{\text{in}}(q^2) = 1 + \frac{C_{\text{A}}\alpha_s}{4\pi}\left(\frac{\tau_1}{q^2+\tau_2}\right)\left[2\ln\left(\frac{q^2+\rho\, m^2(q^2)}{\mu^2}\right) + \frac{1}{6}\ln\left(\frac{q^2}{\mu^2}\right)\right]. \tag{5.23}$$

Note that Eq. (5.23) differs from Eq. (3.51) by the substitution $\left(1+\frac{\tau_1}{q^2+\tau_2}\right) \to \left(\frac{\tau_1}{q^2+\tau_2}\right)$, which guarantees that $\lim_{q^2\to\infty} J_{\text{in}}(q^2) = 1$. The above model fits the gluon propagator data of Ref. [73, 76, 175] for $\alpha_s = 0.22$, $\tau_1 = 12.68$ GeV^2, $\tau_2 = 1.05$ GeV^2 and $\rho = 102.3$, whereas the mass parameters are unchanged, *i.e.* $m_0^2 = 0.147$ GeV^2, $\rho_m^2 = 1.18$ GeV^2 and we choose $\gamma = 0$.

On the left panel of Fig. 5.5 we compare the fit $\Delta_{\text{in}}(q^2)$ of Eq. (5.22) (blue curve) with the lattice data of [175] (circles) and the fit composed of Eqs. (3.42), (3.50) and (3.51) (red dashed line). On the right panel of that figure we compare the corresponding $J(q^2)$ and $J_{\text{in}}(q^2)$ of Eqs. (3.51) and (5.23), respectively. Notice that at the level of the gluon propagator the Δ and Δ_{in} fits are visually indistinguishable, whereas the difference between $J(q^2)$ and $J_{\text{in}}(q^2)$ increases in the UV, because for large q^2 the $J_{\text{in}}(q^2)$ sets in to tree-level while $J(q^2)$ displays the characteristic one-loop logarithm.

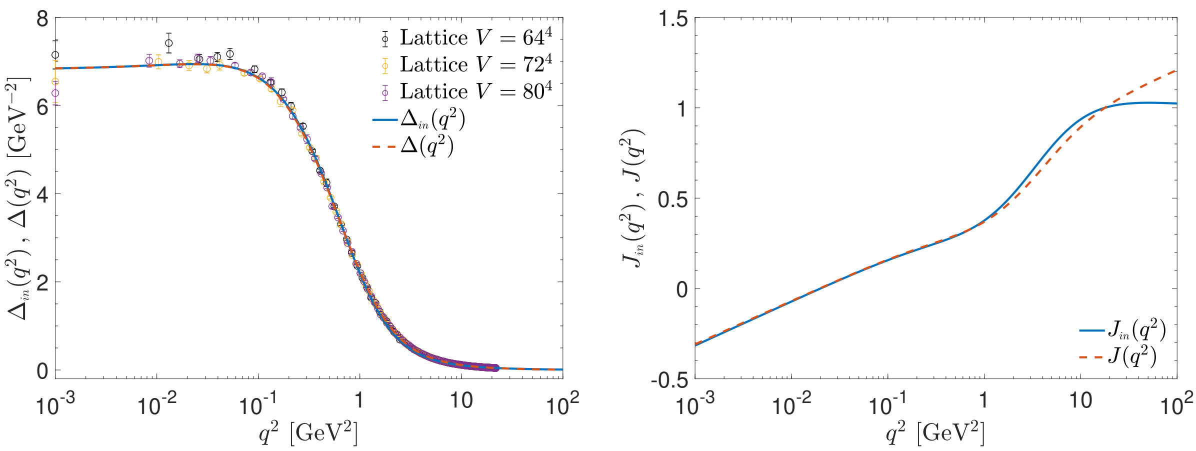

Figure 5.5: Left: comparison of fits for the gluon propagator using $\Delta_{\text{in}}(q^2)$ (blue continuous), of Eq. (5.22), and the $\Delta(q^2)$ (red dashed), given by Eqs. (3.42), (3.50) and (3.51), to the lattice data from Ref. [175]. Right: comparison of $J_{\text{in}}(q^2)$ (blue continuous) and $J(q^2)$ (red dashed), of Eqs. (3.51) and (5.23), respectively.

Moving on to the three-gluon vertex, appearing in diagram $(d_2)_{\nu\mu}$ of Fig. 5.3, we retain only the tensor structures that exist at tree level, which are expected to be dominant. Moreover, we use the Bose symmetry relation of Eq. (4.34) to write the form factors X_4 and X_7 in terms of X_1. Then, our Ansatz for the input three-gluon vertex reads

$$\begin{aligned}\Gamma_{\mu\alpha\beta}(r,v,\ell) \to \Gamma^{\text{in}}_{\mu\alpha\beta}(r,v,\ell) =& (r-v)_\beta g_{\mu\alpha} X_1^{\text{in}}(r,v,\ell) + (v-\ell)_\mu g_{\alpha\beta} X_1^{\text{in}}(v,\ell,r) \\ &+ (\ell-r)_\alpha g_{\beta\mu} X_1^{\text{in}}(\ell,r,v)\,. \end{aligned} \tag{5.24}$$

where $v = -\ell - r$. Then, for the form factor X_1^{in} we use its Abelianized approximation of Eq. (4.38), with $J(q^2)$ substituted by the $J_{\text{in}}(q^2)$ of Eq. (5.23), *i.e.*

$$X_1^{\text{in}}(r,v,\ell) = \frac{1}{2}[J_{\text{in}}(r^2) + J_{\text{in}}(v^2)]\,. \tag{5.25}$$

While certainly a simplistic approximation, the $\Gamma^{\text{in}}_{\mu\alpha\beta}(r,v,\ell)$ of Eq. (5.24) captures the logarithmic IR divergence and characteristic suppression of the three-gluon vertex that are expected on general grounds and observed in numerous previous studies, as discussed in Section 3.4 and the literature there cited. Also, $\Gamma^{\text{in}}_{\mu\alpha\beta}(r,v,\ell)$ preserves the Bose symmetry of the three-gluon vertex.

Finally, we discuss the input for the ghost-gluon vertex. First of all, similarly to what we do for the three-gluon vertex, we keep only the tree-level tensor structure of Γ_μ, such that only the form factor B_1 is taken into account. Notice that in the Landau gauge the form factor B_2 would only contribute to the A_3 and A_5 of Eq. (4.24). As such, setting $B_2 \to 0$ is valid exactly, as far as A_1, A_2 and A_4 are concerned. Then, to obtain a model for B_1, we run the SDE of Eq. (5.17) numerically with the above approximations and setting additionally the input $B_1 \to 1$, *i.e.* its tree level. Then, we project from the result the form factor B_1 in the totally symmetric configuration of Eq. (B.5) (in Euclidean space, of course) and fit the resulting data with the form

$$B_1^{\text{in}}(Q^2) = 1 + \frac{\omega_1 Q^2}{(1+\omega_2 Q^2)^{\lambda}_1}\,, \tag{5.26}$$

to force its UV tail to reduce to tree-level. The fitting parameters that result are given by $\omega_1 = 2.21$ GeV^{-2}, $\omega_2 = 2.50$ GeV^{-2} and $\lambda_1 = 1.68$. In Fig. 5.6 the $B_1^{\text{in}}(Q^2)$ of Eq. (5.26) (blue curve) is compared to the SDE result that it was fitted to (red dashed). Clearly, the fit (5.26) is accurate in the IR, while forcing the tree level to be recovered for large momenta.

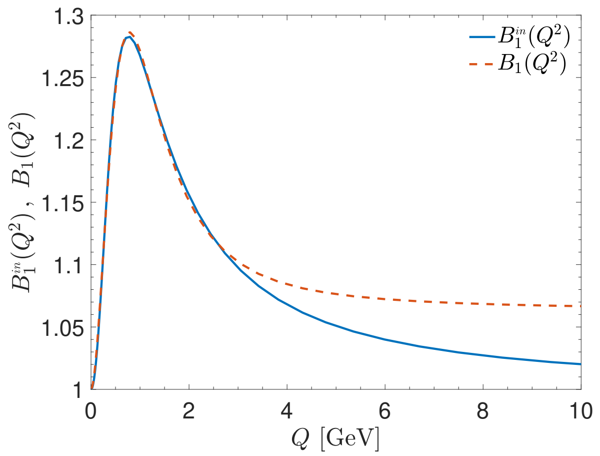

Figure 5.6: Red dashed curve: Form factor $B_1(Q^2)$ in the totally symmetric configuration of Eq. (B.5) obtained from the SDE of Eq. (5.17) with bare ghost-gluon vertex as input. Blue curve: Fit, $B_1^{\text{in}}(Q^2)$, given by Eq. (5.26), for the $B_1(Q^2)$.

Finally, the form factors B_1 that appear in the Eq. (5.18) are still functions of three momenta. To reduce the complexity of the problem, we assume that all the B_1 appearing as inputs are functions of the corresponding gluon momentum only, *i.e.* its third argument, and use Eq. (5.26). For example, $B_1(-\ell-p,p,\ell) \to B_1^{\text{in}}(\ell^2)$. In particular, with the above approximation, Eq. (5.19) reads

$$\begin{aligned}\mathcal{V}_1(\ell,q,p,r) \to \mathcal{V}_1^{\text{in}}(\ell,q,p,r) =& B_1^{\text{in}}(\ell^2)\,,\\ \mathcal{V}_2(\ell,q,p,r) \to \mathcal{V}_2^{\text{in}}(\ell,q,p,r) =& \frac{1}{2}\left[B_1^{\text{in}}(v^2)+B_1^{\text{in}}(\ell^2)\right]\,.\end{aligned} \tag{5.27}$$

Implementing all the above approximations, the diagrams $(d_1)_{\nu\mu}$ and $(d_2)_{\nu\mu}$ of the SDE for the ghost-gluon scattering kernel read

$$\begin{aligned}(d_1)_{\nu\mu} &= \frac{i}{2}C_{\text{A}}g^2\,p_\rho\int_\ell \frac{\Delta_{\text{in}}(\ell^2)F_{\text{in}}(t^2)F_{\text{in}}(s^2)}{t^2\,s^2}\text{P}^\rho_\nu(\ell)\,s_\mu\,B_1^{\text{in}}(r^2)\mathcal{V}_1^{\text{in}}(\ell,q,p,r)\,, \qquad (5.28)\\ (d_2)_{\nu\mu} &= -\frac{i}{2}C_{\text{A}}g^2\,p_\rho\int_\ell \frac{\Delta_{\text{in}}(\ell^2)\Delta_{\text{in}}(v^2)F_{\text{in}}(s^2)}{s^2}\text{P}^\beta_\nu(\ell)\text{P}^{\alpha\rho}(v)\Gamma^{\text{in}}_{\mu\alpha\beta}(r,v,\ell)\mathcal{V}_2^{\text{in}}(\ell,q,p,r)\,,\end{aligned}$$

with $s=q-\ell$, $t=-\ell-p$.

One may then project out the form factors A_i using the projectors of Eq. (C.1) and transform to Euclidean space using the rules of Appendix D. The resulting expressions for the A_i are voluminous and are collected in Appendix E.

Lastly, the renormalization scale is set by the inputs themselves, which are all renormalized at $\mu = 4.3$ GeV, since $H_{\nu\mu}$ is not further renormalized when using the Taylor scheme, as we do. For the strong charge we set $\alpha_s = 0.22$ [180, 188].

5.4 Numerical analysis

For the numerical analysis of the Eq. (5.28), it is convenient to employ spherical coordinates and regard the anti-ghost and ghost momenta, q and p, respectively, as independent. Then, using the notation of Eqs. (D.14) and (D.16), we see that the numerical evaluation of the $A_i(q^2, p^2, \theta)$, with θ the angle between q and p, consists of setting a discretized grid of values for q^2, p^2 and θ, and compute a triple integral for each triple (q^2, p^2, θ). For the squared momenta, we employed a logarithmically distributed grid of 96 values in the range $q^2,\, p^2 \in [5 \times 10^{-5}\,\text{GeV}^2, 10^4\,\text{GeV}^2]$. The extremities of this interval also set IR and UV cutoffs for numerical integration. As for the angle θ, we set a uniform grid of 19 values in the range $[0, \pi]$. Hence, since there are 5 different A_i, we have in total $96^2 \times 19 \times 5$ triple integrals to evaluate.

An efficient and accurate numerical algorithm for evaluating these integrals is the adaptative Gauss-Kronrod method of Ref. [207], employing an 11th degree polynomial rule. Still, the numerical evaluation is quite time consuming and a parallelized computation is required. We implemented the numerical program in *Fortran*, using the Message Passing Interface for parellelization and executed it in the Feynman Cluster of the John David Rogers Computation Center (CCJDR) in the Institute of Physics "Gleb Wataghin".

We present results first in general kinematics in Subsection 5.4.1, using 3D plots, and then specialize to some notable kinematic limits for a more in depth analysis in Subsection 5.4.2.

5.4.1 General kinematics

For a fixed angle θ, each $A_i(q^2, p^2, \theta)$ consists of a surface in the (q^2, p^2) space. In Figs. 5.7 and 5.8 we show all the $A_i(q^2, p^2, \theta)$ for two choices of the angle, $\theta = 0$ and π, in order that the angular dependence can be appreciated.

Let us point out the features of the general kinematics A_i that can be seen in Figs. 5.7 and 5.8: (*i*) in the IR, all the A_i display significant deviations from their corresponding tree-level values, but (*ii*) they all recover roughly their perturbative behaviors whenever one momentum is large. This restoration of perturbation theory in the UV is, of course, an automatic result of using inputs that tend to tree level for large momenta, as discussed

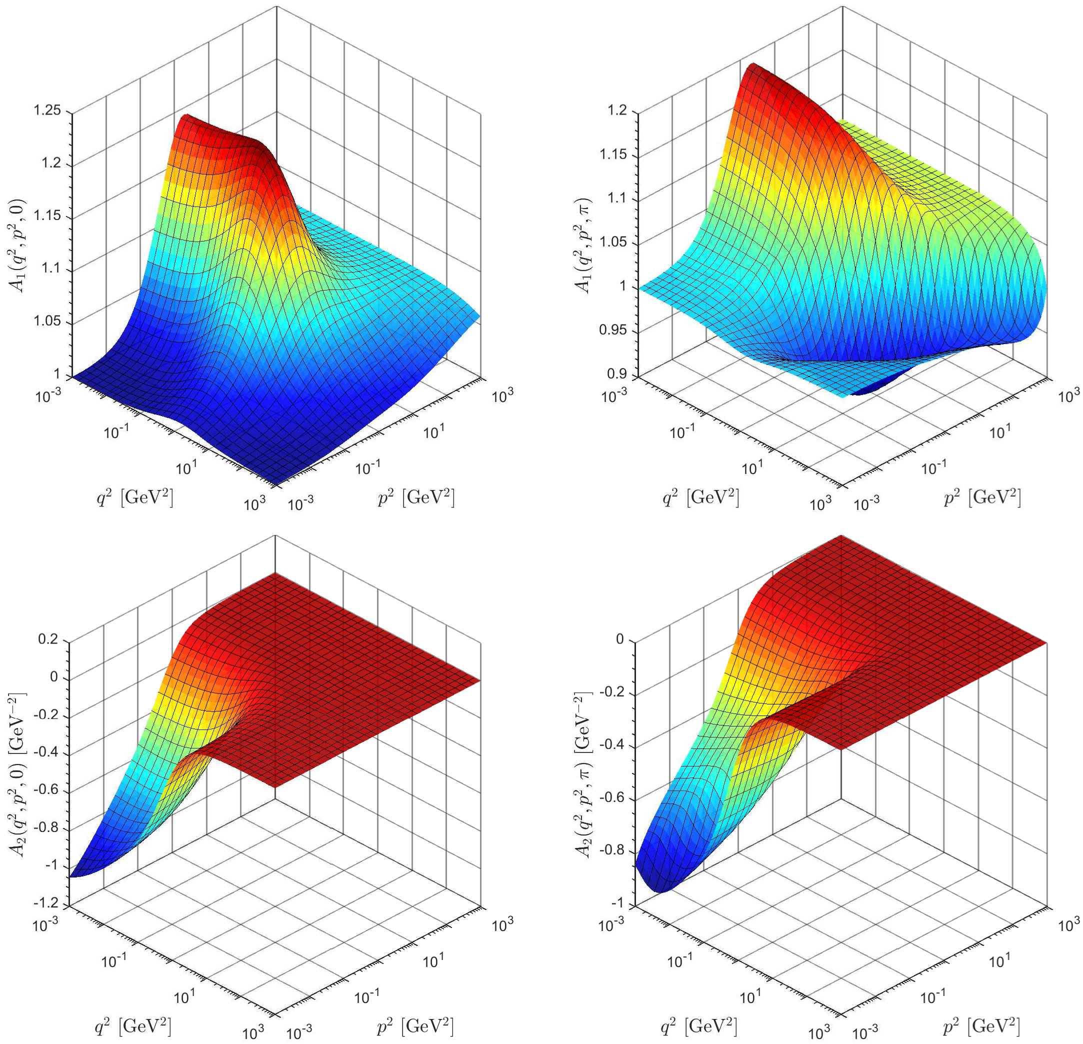

Figure 5.7: The form factors $A_1(q^2, p^2, \theta)$ (top row) and $A_2(q^2, p^2, \theta)$ (bottom row) of the ghost-gluon scattering kernel, for $\theta = 0$ (left) and $\theta = \pi$ (right).

in the previous section. Also, (*iii*) the angular dependence of the A_i is mostly mild, with the exception of A_1 which is altogether larger than 1 for small θ, but develop a "valley" for θ approaching π, with $A_1(q^2, p^2, \pi) < 1$ in the region determined approximately by the triangle $0 < p^2 < q^2$.

In what regards their deep IR behaviors, A_1 is clearly IR finite, whereas the remaining ones all display growths in magnitude consistent with logarithmic IR divergences. To interpret this behaviors, we give in Section B.5 the A_i computed at one-loop with a hard gluon mass, in the same spirit of the analyses presented in Section 3.4. In this semi-perturbative analysis, we have found that the A_1 and A_4 turn out IR finite, while A_2, A_3 and A_5 are logarithmically divergent in the deep IR, as a result of the masslessness of the ghosts. Moreover, these divergences stem from the diagram $(d_1)_{\nu\mu}$ of Fig. 5.3, which has more ghost propagators than $(d_2)_{\mu\nu}$. Comparing our numerical results to the findings

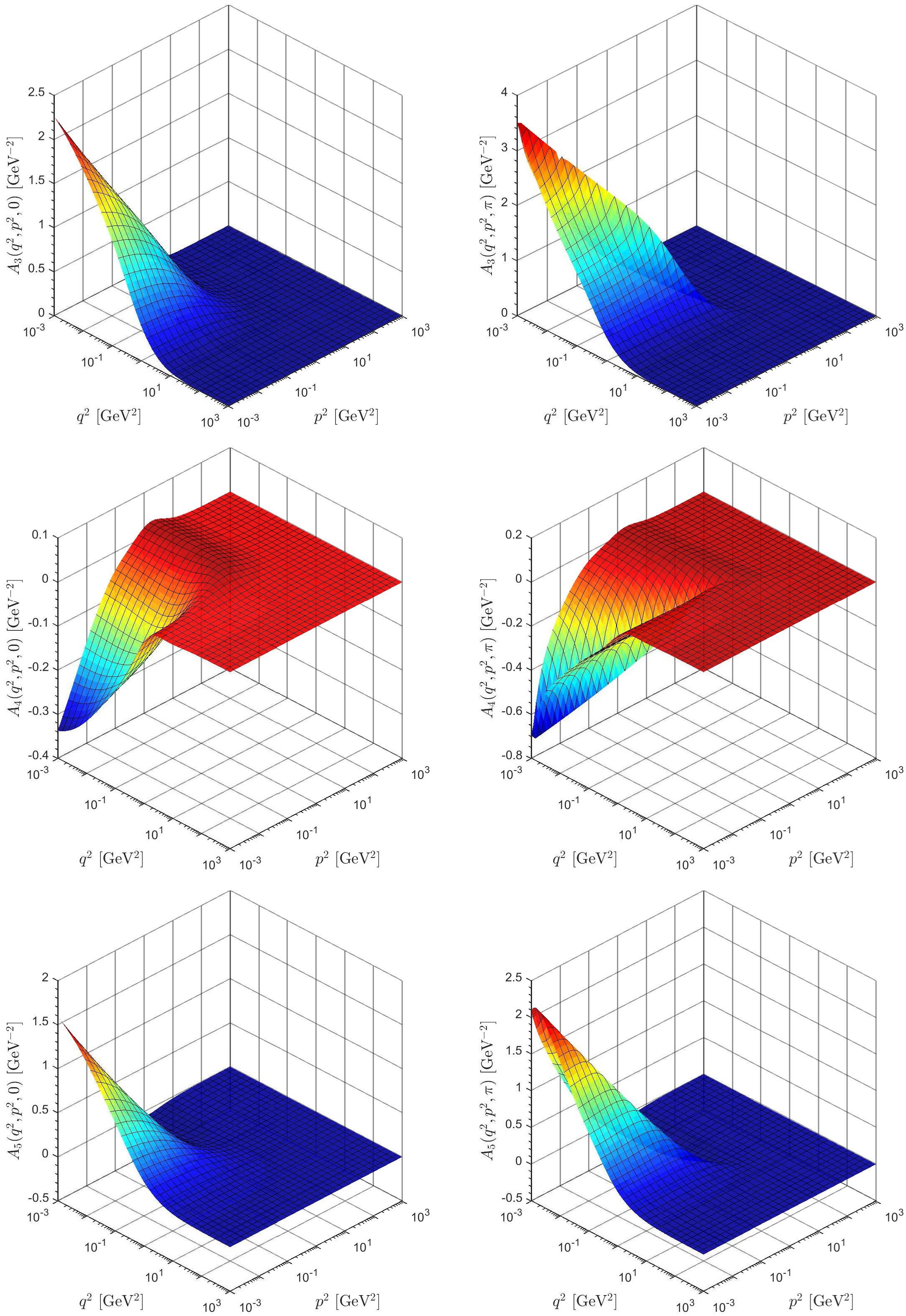

Figure 5.8: The form factors $A_3(q^2, p^2, \theta)$ (top row), $A_4(q^2, p^2, \theta)$ (middle row) and $A_5(q^2, p^2, \theta)$ (bottom row) of the ghost-gluon scattering kernel, for $\theta = 0$ (left) and $\theta = \pi$ (right).

of Section B.5 we see that almost all of the A_i behave as expected on the basis of the semi-perturbative calculations, with the surprising exception of A_4.

The unexpected divergence of A_4 was then investigated in more detail. First, by various numerical experiments we have discarded the possibility that this behavior is a numerical artifact. Then, by taking the zero momentum limit of the expression of Eq. (E.4) for the contribution of the dressed diagram $(d_2)_{\nu\mu}$ to the form factor A_4, we have found that its logarithmic divergence is induced by the three-gluon vertex. Specifically, the input three-gluon vertex of Eq. (5.24) contains logarithmic divergences in the X_1^{in}, since J_{in} has an unprotected logarithm modeling the effect of massless ghosts (see Section 3.4), and it is this divergence that contaminates A_4. To be more precise, note that the three-gluon vertex that appears in $(d_2)_{\nu\mu}$ depends on three momenta, including the integration variable, such that J_{in} appears in $(d_2)_{\nu\mu}$ with three possible arguments, r^2, ℓ^2 and $(\ell+r)^2$. Then, the logarithms of J_{in} that depend on the integration momentum are integrated an yield finite results, whereas the logarithms that depend only on the external momentum, r, are not affected by the integration and, thus, remain divergent. Symbolically, the terms of Eq. (E.4) of the generic form

$$\int_\ell J_{\text{in}}(\ell^2)f(q,p,\ell)\,, \qquad \text{and} \qquad \int_\ell J_{\text{in}}[(\ell+r)^2]f(q,p,\ell)\,, \tag{5.29}$$

furnish IR finite contributions, whereas

$$\int_\ell J(r^2)f(q,p,\ell)\,, \tag{5.30}$$

is logarithmically divergent as $r^2 \to 0$. Indeed, we have also confirmed this explanation numerically, by setting the input three-gluon vertex to its tree-level in Eq. (5.24), in which case A_4 turns out IR finite as expected.

An important conclusion to be drawn from the above analysis is that the three-gluon vertex can feed back additional IR divergences in Feynman diagrams of QCD. This observation, in turn, leads us to ask whether the IR divergences seen in A_2, A_3 and A_5 in Figs. 5.7 and 5.8 are exclusively due to the integration of massless ghost propagators, or whether they also receive contributions from the divergence of the three-gluon vertex[1]. Performing an analysis similar to the above, for the contribution in Eq. (E.4) for the remaining form factors, we have found that indeed the IR divergence of A_3 is also

[1]Of course, since the logarithmic divergence of X_1 is itself a consequence of the masslessness of the ghosts [52] (see also Section 3.4), all IR divergences considered here may be attributed to $D(q^2)$ being divergent.

contaminated by the divergence of the three-gluon vertex, while the A_1, A_2 and A_5 are not.

5.4.2 Special kinematic limits

Let us take a closer look into the nonperturbative behavior of the $H_{\nu\mu}(q,p,r)$, by selecting from the previously discussed results for the $A_i(q^2,p^2,\theta)$ some special kinematic limits. In particular, we consider: the (*i*) *soft gluon* limit, defined by vanishing gluon momentum, $r = 0$; the (*ii*) *soft anti-ghost* configuration, where $q = 0$; and the (*iii*) *totally symmetric* limit, for which all momenta have the same magnitude, Q, as given (in Minkowski space) by Eq. (B.5). For the configurations (*i*) and (*ii*), we show only the form factors whose tensor structures survive in the corresponding limit. Naturally, the vanishing of a given tensor structure does not imply that the corresponding form factor itself vanishes, but its calculation becomes more difficult and we will not pursue in the present work.

For all these limits, we show in each of Figs. 5.9, 5.10 and 5.11 four curves, turning off gradually some of our ingredients to explore their effects. Specifically: (a) the blue continuous curves represent the corresponding result of the full nonperturbative calculation of $H_{\nu\mu}(q,p,r)$, presented before as surfaces in Figs. 5.7 and 5.8; (b) the red dashed curves resulting from our truncation when, in addition, we set the three-gluon vertex to tree level, *i.e.* $X_1^{\rm in} \to 1$ in Eq. (5.24); (c) the one-loop massive results of Section B.5, which are represented by green dot-dashed curves; and, (d) the true one-loop results, *i.e.* with massless gluon propagators, of Section B.2. The comparison of cases (a) and (b) allows us to distinguish the effect on the A_i of dressing the three-gluon vertex. In combination with the set (c), we can also distinguish the IR divergence induced by the three-gluon vertex, which is not accounted for in the one-loop massive calculation. Finally, comparison to (d) allows us to see that the overall degree of IR divergence is reduced in the presence of a gluon mass and to check that our results recover their perturbative behaviors, as they should by construction with the inputs we are using.

Moreover, for the dimensionful form factors, A_i with $i = 2, \ldots, 5$, we show in the foreground of Figs. 5.9, 5.10 and 5.11 the dimensionless combinations $t^2 A_i$, with t an appropriate external momentum in the kinematic limit at hand, such that the magnitudes of the different form factors can be duly compared with each other. Simultaneously, for the dimensionful form factors we also show insets where the A_i are displayed without multiplication by an external momentum. These insets allow the IR divergences to be appreciated better; in the logarithmic scale employed, a logarithmic IR divergence manifests as an asymptotically straight line.

(*i*) *Soft gluon limit:* the configuration defined by $r = 0$ reads in our parametrization, $A_i(q, -q, 0) \equiv A_i(q^2, q^2, \pi)$. As such, it can be obtained by setting $q^2 = r^2$ and $\theta = \pi$ in $A_i(q^2, p^2, \theta)$. That is, they correspond to the "slices" defined by the intersections of the surfaces on the right columns of Figs. 5.7 and 5.8 with a vertical plane across the diagonal of each 3D "box". The tensors surviving in this limit carry the form factors $A_1(q, -q, 0)$ and $A_2(q, -q, 0)$, which are shown in Fig. 5.9.

The main feature of the nonperturbative $A_1(q, -q, 0)$ and $q^2 A_2(q, -q, 0)$ of Fig. 5.9 is the presence of a pronounced peak, centered at about 1 GeV, for both quantities. Next, we notice that the results with dressed three-gluon vertex (blue curves) are suppressed with respect to those obtained with $\Gamma^{(0)}_{\mu\alpha\beta}$. In the inset, we see clearly that the form factor A_2, whose one-loop result of Eq. (B.21) has a pole in q^2, becomes only logarithmically divergent when a gluon mass is added, and remains so in the full nonperturbative results. Finally, in the UV the one-loop behavior of Eq. (B.21) is smoothly approached.

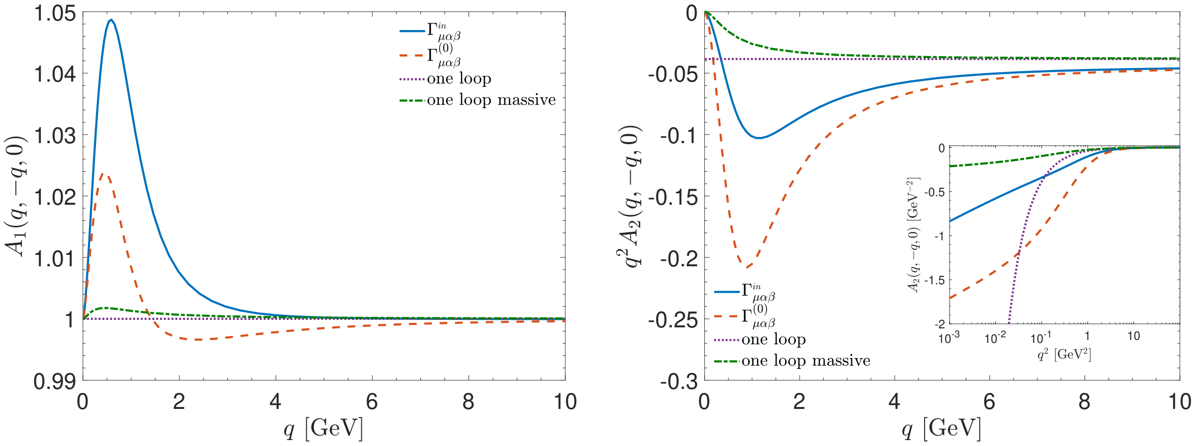

Figure 5.9: (soft gluon kinematics) Left: Comparison between the $A_1(q, -q, 0)$ computed using $\Gamma^{\rm in}_{\mu\alpha\beta}$ (blue continuous) and the one obtained when $\Gamma^{(0)}_{\mu\alpha\beta}$ is used instead (red dashed). The massless (purple dotted) and the massive (green dot-dashed) one-loop perturbative results are given by Eqs. (B.21) and (B.44), after conversion to Euclidean space, respectively. Right: Same comparison for the dimensionless combination $q^2 A_2(q, -q, 0)$. The inset shows the corresponding $A_2(q, -q, 0)$ itself, using a logarithmic scale for q^2, where the IR divergences are clearly visible. Note that the purple dotted curve shows a much steeper divergence, in fact a pole [see Eq. (B.21)].

(*ii*) *Soft anti-ghost limit:* this kinematic limit can be obtained by setting $q^2 = 0$ in our results[2] for $A_i(q^2, p^2, \theta)$. Note that this limit does not depend on θ, which, in fact, becomes undefined. In this configuration we show the form factors $A_1(0, -r, r)$ and $A_3(0, -r, r)$, whose tensor structures survive, in Fig. 5.10. This figure exhibits qualitative behavior very similar to those of Fig. 5.9, of course with A_3 in place of A_2. Dressing the three-gluon vertex furnishes an overall suppression of the result, and the gluon mass leads to a reduction of the degree of IR divergence of A_2, while the one-loop behavior of Eq. (B.19) is restored for large r^2.

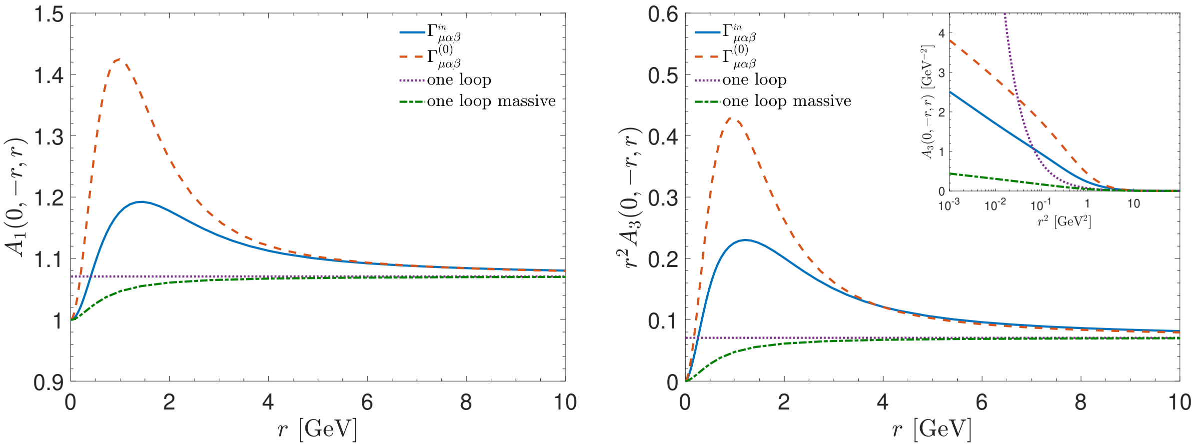

Figure 5.10: (soft gluon kinematics) Left: Comparison between the $A_1(0, -r, r)$ computed using $\Gamma^{\text{in}}_{\mu\alpha\beta}$ (blue continuous) and the one obtained when $\Gamma^{(0)}_{\mu\alpha\beta}$ is used instead (red dashed). The massless (purple dotted) and the massive (green dot-dashed) one-loop perturbative results are given by Eqs. (B.19) and (B.43), after conversion to Euclidean space, respectively. Right: Same comparison for the dimensionless combination $r^2 A_3(0, -r, r)$. The inset shows the corresponding $A_3(0, -r, r)$ itself, using a logarithmic scale for r^2, where the IR divergences are clearly visible. Again, the purple dotted curve has a clear pole divergence [see Eq. (B.19)].

(*iii*) *Totally symmetric limit:* transforming Eq. (B.5) to Euclidean space, we see that we can obtain the totally symmetric limit from our general kinematics data by setting $q^2 = p^2 = Q^2$, and $\theta = 2\pi/3$. In this kinematic limit all tensor structures of $H_{\nu\mu}(q, p, r)$ survive and the resulting form factors are shown in Fig. 5.11. In particular, we gain access to the form factors A_4 and A_5, not previously discussed in the items (*i*) and (*ii*).

For the form factors A_1, A_2 and A_3, Fig. 5.11 displays the same patterns already indicated in the previous items. Then, from the last plot, we see that A_5 is also

[2]For evident practical limitations, we actually use the lowest q^2 available, $q^2 = 5 \times 10^{-5}$ GeV^2.

logarithmically IR divergent, and is suppressed in magnitude when the three-gluon vertex is dressed. The most interesting result in this kinematics is that of A_4. We can see quite clearly in the corresponding inset, that A_4 is IR finite in the one-loop massive result of Eq. (B.46) as well as in the nonperturbative result with $\Gamma^{(0)}_{\mu\alpha\beta}$. However, when the three-gluon vertex is dressed, the IR behavior is dramatically altered; its sign in the deep IR is flipped, from positive to negative, and it becomes logarithmically divergent. Yet, as in all cases before, the degree of IR divergence of A_4 is still reduced in comparison to its one-loop result of Eq. (B.22), which is restored for large Q^2.

We summarize our observations about the presence and origin of the IR divergences of our results for the A_i in Table 5.1.

Form factors	one-loop massive		SDE with $\Gamma^{(0)}_{\mu\alpha\beta}$		SDE with $\Gamma^{\text{in}}_{\mu\alpha\beta}$		
	$(d_1)_{\nu\mu}$	$(d_2)_{\nu\mu}$	$(d_1)_{\nu\mu}$	$(d_2)_{\nu\mu}$	$(d_1)_{\nu\mu}$	$(d_2)_{\nu\mu}$	Total
A_1	F	F	F	F	F	F	F
A_2	LD	F	LD	F	LD	F	LD
A_3	LD	F	LD	F	LD	LD	LD
A_4	F	F	F	F	F	LD	LD
A_5	LD	F	LD	F	LD	F	LD

Table 5.1: Summary of the infrared limits of the individual contributions of the diagrams (d_1) and (d_2) of Fig. 5.3 to the form factors A_i of the ghost-gluon scattering kernel. The letter "F" stands for "finite", and the acronym "LD" for "logarithmically divergent". The limits are for (i) the one-loop massive results [see Eqs. (B.45), (B.43) and (B.46)]; (ii) the nonperturbative result obtained when $\Gamma^{(0)}_{\mu\alpha\beta}$ is used as input in the diagram (d_2); and (iii) the nonperturbative result obtained with $\Gamma^{\text{in}}_{\mu\alpha\beta}$.

Still regarding the IR divergences of the A_i, let us make two more remarks: (i) because the only A_i that are IR divergent are dimensionful, whereas $H_{\nu\mu}$ is dimensionless, and given that the divergences are logarithmic and only occur when all $q^2 = p^2 = r^2 = 0$, the $H_{\nu\mu}(q,p,r)$ itself is IR finite. This is enforced by the fact that the momenta appearing in the tensor structures that multiply the form factors [see Eq. (4.24)] vanish faster than the A_i diverge. In particular, the divergences observed in the A_i in the present study *do not* induce dynamical mass generation, which requires the vertices themselves, not just certain form factors, to have longitudinally coupled poles. (ii) In all cases, including A_4, the degree of IR divergence is reduced in the nonperturbative case in comparison to the true one-loop behavior (with massless gluons). Indeed only logarithmic IR divergences

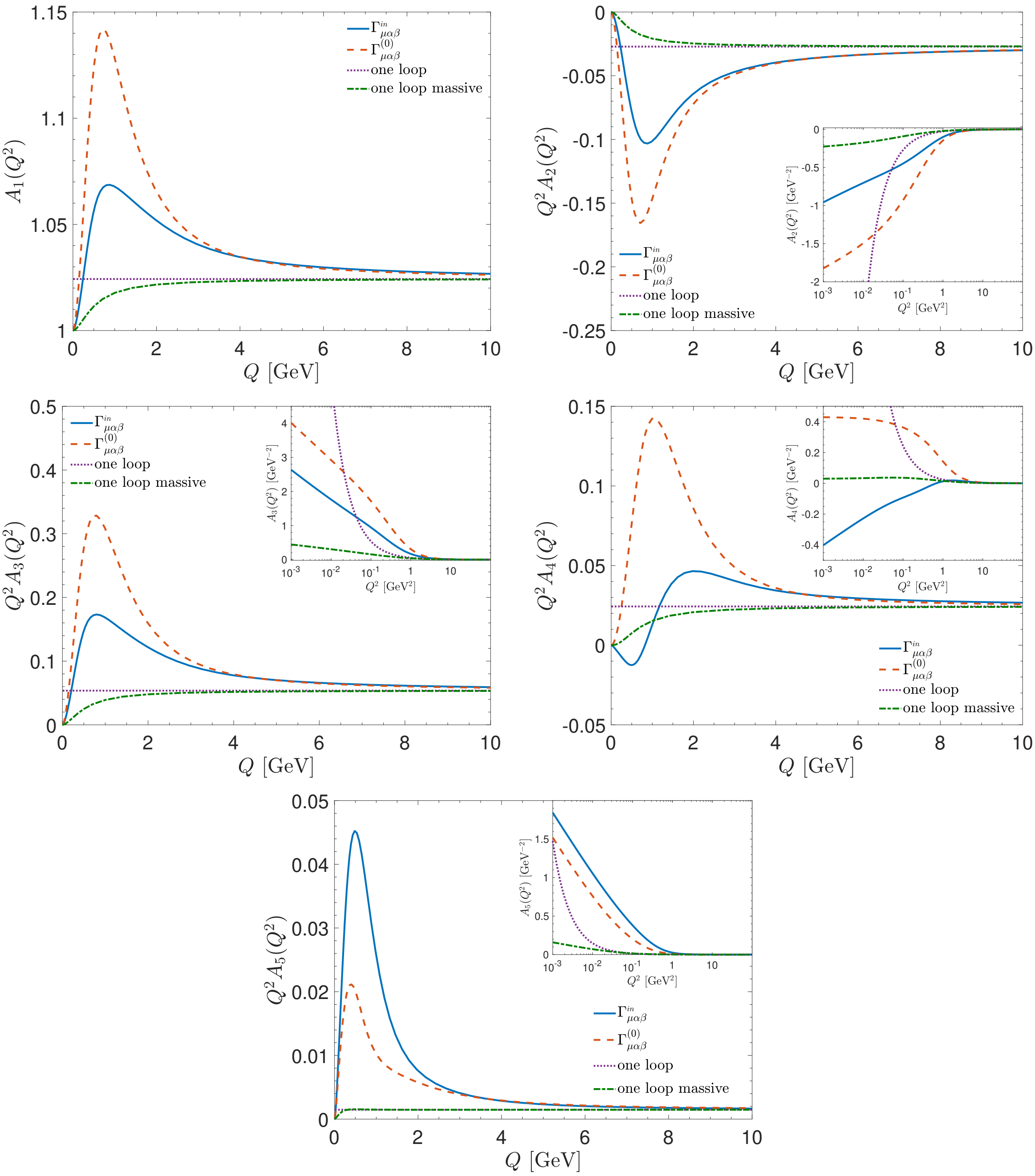

Figure 5.11: (Totally symmetric limit) $A_1(Q^2)$ and the dimensionless combinations $Q^2 A_i(Q^2)$, for $i = 2, \ldots, 5$, computed using $\Gamma^{\text{in}}_{\mu\alpha\beta}$ (blue continuous) and $\Gamma^{(0)}_{\mu\alpha\beta}$ (red dashed). The purple dotted curves correspond to the one-loop results given in Eq. (B.22), while the $Q^2 \to 0$ limits of the one-loop massive case are expressed by Eq. (B.46). The insets show the $A_i(Q^2)$ in logarithmic scale of Q^2, where we can appreciate the logarithmic divergences, when present, as well as the pole divergences of the massless one-loop result.

were found in our nonperturbative results, whereas the one-loop results of Section B.2 display poles in A_i for $i = 2, \ldots, 5$.

Before closing this section, we make one final observation, now about the IR finite form factor A_1. First, we can see from Figs. 5.9, 5.10 and 5.11, as well as from the surfaces of Fig. 5.7, that in the nonperturbative results, as well as in the one-loop massive case, $A_1(0,0,0) = 1$, *i.e.* it tends to tree-level when all momenta vanish, independently of the configuration from which the limit is approached. This observation contrasts with the one-loop behavior, whose $A_1(0,0,0)$ limit, while finite, saturates to a different value for each kinematic configuration of Figs. 5.9, 5.10 and 5.11. The result that the nonperturbative $A_1(0,0,0) = 1$ can also be understood in the general context of a reduction of the degree of IR divergence in the presence of a gluon mass. Specifically, the derivative $\partial A_1/\partial p^\rho$, is pole divergent at one-loop, and becomes either finite or logarithmically divergent with an IR finite gluon propagator [see discussion surrounding Eq. (B.47)].

5.5 Results for the ghost-gluon vertex

With the general kinematics results for the A_i at hand, it is natural to use Eq. (5.2) to compute also the form factors of the ghost-gluon vertex, B_1 and B_2. Since the focus of this thesis is on the three-gluon vertex and its determination from $H_{\nu\mu}$, we will not show here all of our results for Γ_μ, which can be found in Ref. [3]. Instead, we highlight a few findings that are relevant in the present context.

In Fig. 5.12 we show the resulting $B_1(Q^2)$ and $B_2(Q^2)$ in the totally symmetric configuration obtained from the A_i of Fig. 5.11 using Eq. (5.2). For the ghost-gluon vertex, no IR divergences were found in our nonperturbative results, and we refrain from comparing them to a one-loop massive calculation. Both form factors exhibit peaks around 1 GeV, which are suppressed in amplitude[3] by a factor of nearly 2.5 when the three-gluon vertex is dressed. In the UV they both reduce to their one-loop results, which can be computed easily from the results for $A_i^{(1)}(Q^2)$ of Eq. (B.22) using Eq. (5.2).

The main value of computing the B_i in the context of this thesis is that it allows us to compare our results to those obtained by other authors, using different methods. Indeed $H_{\nu\mu}(q,p,r)$ has not been studied much before, except in pertubation theory [126, 208], whereas the ghost-gluon vertex has. In particular, the soft gluon, $r = 0$, configuration of the form factor $B_1(q,p,r)$ has been previously studied in various approaches, including lattice simulation [73, 193], Operator Product Expansion [118], SDEs [55, 180, 194, 195], Functional Renormalization Group [58, 60] and the Refined Gribov-Zwanziger method [51,

[3]By amplitude, we mean the value of peak subtracted by the tree-level, either $B_1^{(0)} = 1$ or $B_2^{(0)} = 0$, of the corresponding form factor.

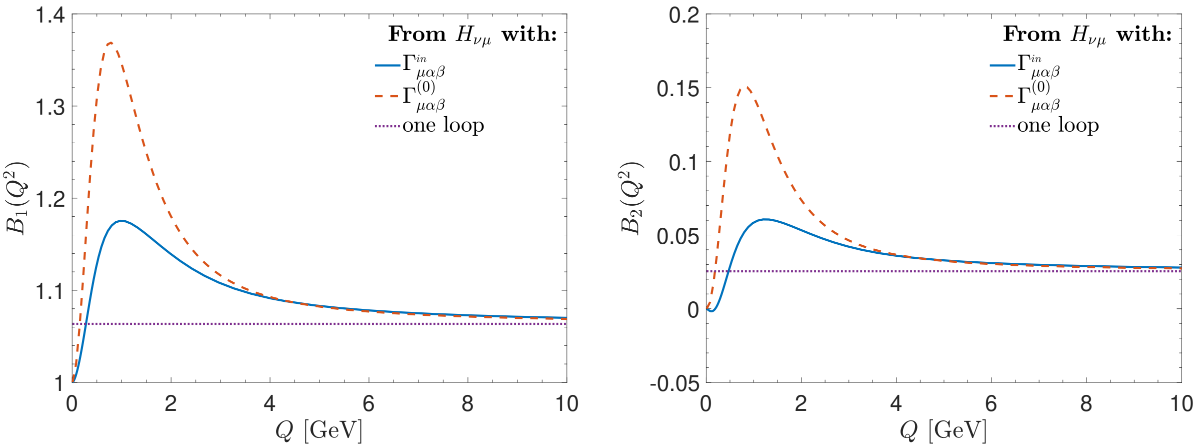

Figure 5.12: Form factors $B_1(Q^2)$ and $B_2(Q^2)$ of the ghost-gluon vertex, in the totally symmetric configuration.

196, 197].

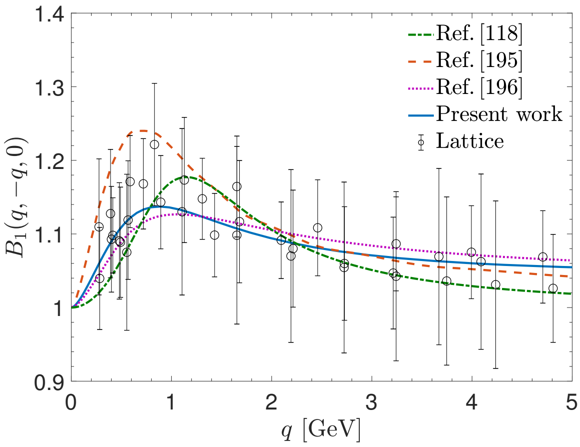

Figure 5.13: Form factor $B_1(q,-q,0)$ of the ghost-gluon vertex in the soft gluon configuration. Our results are shown in blue, whereas [118] is represented by the green dot-dashed curve, those of [195] by the red dashed, and those of [196] by the purple dotted. The lattice data is from Refs. [73, 193].

In Fig. 5.13 we compare our results for the soft gluon $B_1(q,-q,0)$ (blue continuous curve) to the lattice data of [73, 193] (circles) and continuum results of [118, 195, 196] (green dot-dashed, red dashed and purple dotted, respectively). Clearly, our results are in qualitative agreement with those of the cited literature. In particular, all studies compared display a peak for B_1 around 1 GeV, and are all within the noise of the available lattice data. In addition, all results considered are consistent with $B_1(0,0,0) = 1$.

Let us point out that we have also compared our results to those obtained on $SU(2)$ lattice simulations [43] and Functional Renormalization Group results [58], both of which contain other kinematic configurations, and found *qualitative* agreement as well. However, we do not include the results of these references in Fig. 5.13 because, for [43] a quantitative comparison between our $SU(3)$ results with $SU(2)$ lattice data is evidently inappropriate[4], whereas the results of [58] are renormalized in a very different scale and Ref. [60] considered the three-dimensional theory.

5.6 Failure of the STI constraint

It is well known that truncating SDEs often breaks the symmetries of the theory, specially when diagrams are omitted, as is the diagram $(d_3)_{\nu\mu}$ of Fig. 2.3 in our truncation (*cf.* Fig. 5.3). As such, we do expect that some symmetry has been sacrificed in our results for $H_{\nu\mu}(q,p,r)$, in spite of our efforts to retain as much as possible its fundamental properties in the truncated SDE. Indeed, we found that the constraint of Eq. (4.28) is violated, as we now discuss.

To quantify the violation of the constraint, we can use the ratio $\mathcal{R}(q^2,p^2,r^2)$ itself, defined in Eq. (4.28). If $\mathcal{R}(q^2,p^2,r^2)\neq 1$, it will manifest a breaking of the gauge symmetry, since Eq. (4.28) is a consequence of the STIs of the theory (see Subsection 2.4.3). In addition, different truncations can lead to values of $\mathcal{R}$ which differ from unity by more or less. Hence the quality of different truncations can be compared quantitatively.

For the ghost dressing function, $F(q^2)$, appearing in Eq. (4.28), we shall *not* use the $F_{\text{in}}(q^2)$ of Eq. (5.21). Since we used inputs that tend to tree level in the UV for our computation of $H_{\nu\mu}$, the latter recover its one-loop behavior for large momenta, as we have seen in Section 5.4.2. As such, it is important that the $F(q^2)$ used to evaluate $\mathcal{R}$ also contains its one-loop UV tail. For that matter, a fit for $F(q^2)$ that reduces to one-loop for large q^2 is given by [2]

$$F^{-1}(q^2) = 1 + \frac{9C_{\text{A}}\alpha_s}{48\pi}\left[1 + d\,\exp\left(-\rho_4 q^2\right)\right]\ln\left(\frac{q^2+\rho_3 M^2(q^2)}{\mu^2}\right)\,, \tag{5.31}$$

with

$$M^2(q^2) = \frac{m_1^2}{1+q^2/\rho_2^2}\,, \tag{5.32}$$

and parameters $m_1^2 = 0.16\,\text{GeV}^2$, $\rho_2^2 = 0.69\,\text{GeV}^2$, $\rho_3 = 0.89$, $\rho_4 = 0.12\,\text{GeV}^{-2}$, $d = 2.36$, and $\mu = 4.3\,\text{GeV}$. In Fig. 5.14, we compare the fit of Eq. (5.31) (black dashed) to the lattice data of [175] (circles) and the $F_{\text{in}}(q^2)$ of Eq. (5.21) (red continuous). Clearly,

[4] In [198] we have computed B_1 also for $SU(2)$, finding rough quantitative agreement. Nevertheless, there we used more rudimentary truncation and numerical methods.

both fits capture the behavior of the lattice results in the IR, but differ from each other increasingly in the UV.

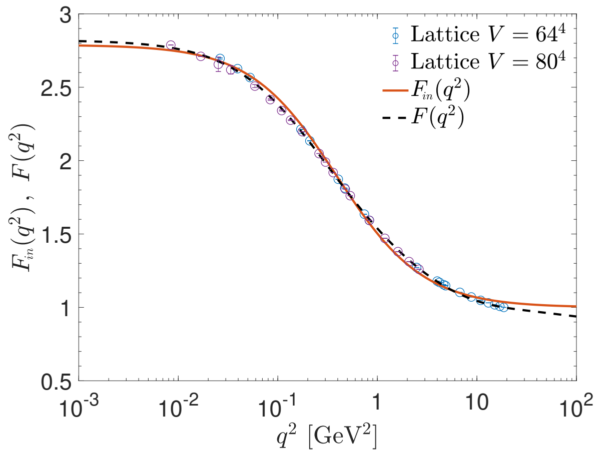

Figure 5.14: Comparison of the fit with UV logarithms given by Eq. (5.31) (black dashed) to the SDE input $F_{\rm in}(q^2)$ (red curve), of Eq. (5.21), for the ghost dressing function, $F(q^2)$. The lattice data of Ref. [175] is also shown as circles.

Now, let us emphasize that Eq. (4.28) is satisfied trivially whenever the ghost and gluon momenta have the same magnitude, *i.e.* $p^2 = r^2$. To see this, set $p^2 = r^2$ into that equation to find

$$\mathcal{R}(q^2,p^2,p^2) = \frac{A_1(q,r,p) + p^2 A_3(q,r,p) - (q^2/2)A_4(q,r,p)}{A_1(q,p,r) + p^2 A_3(q,p,r) - (q^2/2)A_4(q,p,r)}\,, \tag{5.33}$$

where we used momentum conservation to write $q\cdot r = (p^2 - q^2 - r^2)/2$ and similarly $q\cdot p = (r^2 - q^2 - p^2)/2$. Then, since the A_i are Lorentz scalars, they can only depend on the invariants q^2, p^2, and r^2, *i.e.* $A_i(q,p,r) \equiv \widetilde{A}_i(q^2,p^2,r^2)$, for some function $\widetilde{A}_i(q^2,p^2,r^2)$. Hence it follows from Eq. (5.33) that $\mathcal{R}(q^2,p^2,p^2) = 1$. In particular, the constraint is satisfied trivially in the totally symmetric ($q^2 = p^2 = r^2$) and soft anti-ghost ($q = 0$) limits. As such, we concentrate on configurations where $p^2 \neq r^2$.

We will consider two different kinematic limits of $\mathcal{R}(q^2,p^2,r^2)$. Moreover, we provide a concrete example of the usage of $\mathcal{R}$ to compare the quality of different approximations of $H_{\nu\mu}(q,p,r)$, by comparing two slightly different versions of our truncated SDE. Specifically, in Fig. 5.15 we show the ratio $\mathcal{R}$ for (i) the configuration defined by $q^2 = p^2$ and $r^2 = 3p^2$, such that we may write $\mathcal{R}(q^2,p^2,r^2) = \mathcal{R}(Q^2,Q^2,3Q^2)$, denoting the common scale by Q (left panel); and (ii) the limit $q^2 = Q^2$, $p^2 = 3Q^2$ and $r^2 = 4Q^2$ (right panel).

For both of the configurations shown in Fig. 5.15 we present the $\mathcal{R}$ corresponding to two different approximations for $H_{\nu\mu}$: (a) our full nonperturbative result (blue continuous),

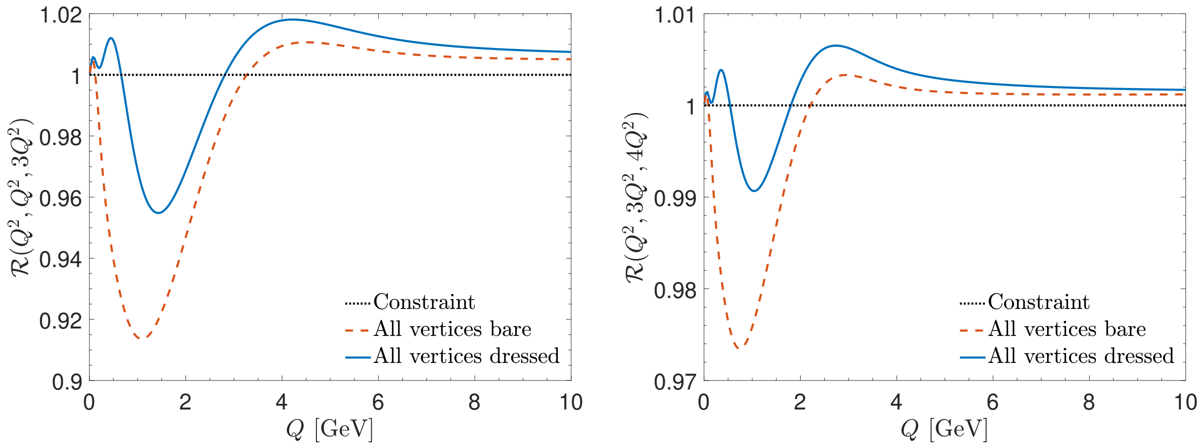

Figure 5.15: The ratio $\mathcal{R}(q^2, p^2, r^2)$ defined in Eq. (4.28), in two different kinematic configurations: $q^2 = p^2 = Q^2$ and $r^2 = 3Q^2$ (left), and $q^2 = Q^2$, $p^2 = 3Q^2$ and $r^2 = 4Q^2$ (right). The blue continuous curve corresponds to our full nonperturbative $H_{\nu\mu}(q, p, r)$ result, whereas the red dashed is obtained from our SDE truncation setting all vertices to tree-level. The black dotted line represents the STI requirement $\mathcal{R} = 1$.

using Eq. (5.28); and, (b) the result of Eq. (5.28) when in addition all the ghost-gluon and three-gluon vertices appearing in it are set to tree-level (red dashed), *i.e.* $B_1^{\text{in}} \to 1$ and $X_1^{\text{in}} \to 1$. For reference, we also show the STI requirement $\mathcal{R} = 1$ (black dotted), which would be satisfied by the ideal $H_{\nu\mu}(q, p, r)$ and $F(q^2)$.

The first observation we make from Fig. 5.15, is that for each truncation the corresponding curve on the right panel, $\mathcal{R}(Q^2, 3Q^2, 4Q^2)$, deviates less from its ideal value than the curve on the left, $\mathcal{R}(Q^2, Q^2, 3Q^2)$, *i.e.*

$$|\mathcal{R}(Q^2, 3Q^2, 4Q^2) - 1| < |\mathcal{R}(Q^2, Q^2, 3Q^2) - 1| \,. \tag{5.34}$$

This observation is in line with the discussion surrounding Eq. (5.33), according to which the constraint is satisfied trivially when $r^2/p^2 = 1$. Indeed, in the configuration shown in the right side of Fig. 5.15 we have $r^2/p^2 = 4/3$, whereas on the left $r^2/p^2 = 3$.

Next, it is clear from Fig. 5.15 that the maximum violation of the constraint, to be denoted $\delta\mathcal{R}_{\text{max}} := |\mathcal{R} - 1|$, is reduced when the vertices are dressed. Specifically, we see in the left panel of Fig. 5.15 that the maximum deviation of $\mathcal{R}(Q^2, Q^2, 3Q^2)$ occurs in the range $Q = 1$ - 1.5 GeV, and that $\delta\mathcal{R}_{\text{max}}(Q^2, Q^2, 3Q^2)$ is reduced from about 9% with tree-level vertices to less than 5% with dressed $\Gamma^{\text{in}}_{\mu\alpha\beta}$ and B_1^{in}. Then, we can appreciate that in the right panel of Fig. 5.15 the position of maximum violation of $\mathcal{R}(Q^2, 3Q^2, 4Q^2)$ from unity is shifted slightly to the IR, occurring in the range 0.8 - 1.1 GeV. Nevertheless, $\delta\mathcal{R}_{\max}(Q^2, 3Q^2, 4Q^2)$ exhibits the same overall behavior of $\delta\mathcal{R}_{\max}(Q^2, Q^2, 3Q^2)$ under dressing of the vertices appearing in the SDE. Specifically, while the truncation with dressed vertices furnishes less than 1% maximum violation in the constraint, the result with bare vertices gives almost $\delta\mathcal{R}_{\max}(Q^2, 3Q^2, 4Q^2) = 3\%$.

Also, it is seen in Fig. 5.15 that the full nonperturbative result has a larger violation than the result with bare vertices for $Q \gtrapprox 2$ GeV. Since in this thesis we are mainly interested in the IR behavior of the QCD Green's functions, this fact is not a major concern for us. In fact, for the purposes of this work, it is natural to opt for the truncation that minimizes the violation of the STI constraint in the IR. Hence, for the Gauge Technique determination of the three-gluon vertex in the following chapter, we will use the $H_{\nu\mu}(q, p, r)$ obtained with dressed vertices[5].

To wrap up this discussion, we point out that when $H_{\nu\mu}(q, p, r)$ is computed using our one loop dressed truncation, but with propagators and vertices that contain their one loop UV tails, the large momentum behavior of the $\mathcal{R}$s shown in Fig. 5.15 is substantially worsened. Instead of slowly approaching the ideal value for large Q^2 as the blue continuous and red dashed curves in Fig. 5.15 do, the results would appear to deviate increasingly from unit in the UV, at a characteristically logarithmic rate. This is the main reason we opted to use the "in" fits presented in Section 5.3.

[5]In Ref. [4] some global measures of the violation of $\mathcal{R} = 1$ were considered and also favor the result with dressed vertices.

6

The nonperturbative three-gluon vertex

We are finally in position to explore numerically the Gauge Technique construction of the three-gluon vertex, discussed in Chapter 4. As we have already covered the main theoretical concepts in previous chapters, the present one is almost entirely occupied with numerical results.

We begin in Section 6.1 with an overview of the remaining calculations needed to evaluate the regular part of the three-gluon vertex, $\Gamma_{\alpha\mu\nu}(q,r,p)$, using the BC construction, pointing out the limitations of our approach and the precautions needed in comparing our results to those obtained by other means, specially regarding the vertex renormalization. Then, we present our general Euclidean kinematics results, by means of 3D plots, and discuss the main features observed in the $X_i(q,r,p)$ form factors in Section 6.2. In Section 6.3 we select two special kinematic limits of our $X_i(q,r,p)$ and compare them to their one-loop counterparts of Section B.3, showing a general agreement in the UV regime. To study the IR behavior of our solution in more depth, we compare our results to SDE [53, 59] and lattice [44, 45] simulations in Section 6.4, where we note satisfactory agreement, thus demonstrating the adequacy of the Gauge Technique vertex when properly accounting for the longitudinality of the mass-generating poles in the BC construction, as discussed throughout Chapter 4.

6.1 General consideration

Using the BC solution of Eq. (4.36) for the STI of the regular part of the three-gluon vertex, we compute the form factors $X_i(q,r,p)$ [see Eqs. (4.29) and (4.31)] of $\Gamma_{\alpha\mu\nu}(q,r,p)$

that contribute to said STI. Evidently, the "transverse" form factors, Y_i, cannot be determined through the Gauge Technique and are not covered in this thesis, except for the perturbative results in Appendix B. Moreover, we focus our presentation on the form factors $X_i(q,r,p)$ for $i = 1$, 2, 3 and 10, since the remaining $X_i(q,r,p)$ can be calculated from the former by cyclic permutations of their arguments, as in Eq. (4.34).

To evaluate the solutions of Eq. (4.36) numerically, we use for the gluon kinetic term, $J(q^2)$, and ghost dressing function, $F(q^2)$, the fits to lattice data of Eqs. (3.51) and (5.31), respectively. As anticipated in Subsection 3.6, to model the uncertainty in the running of the dynamical gluon mass and the subsequent uncertainty in the kinetic term, we have repeated the calculation for all the $J(q^2)$ obtained by using each of the four values of the exponent $\gamma = 0$, 0.1, 0.2 and 0.3 in Eq. (3.51). We emphasize that for this calculation the fits used, Eqs. (3.51) and (5.31), are the ones that recover the corresponding one-loop behaviors of the propagators in the UV.

For the ghost-gluon scattering kernel form factors, A_i, for $i = 1$, 3 and 4, which appear in Eq. (4.36), we use the nonperturbative results of Chapter 5. More specifically, we use our most complete Ansatz, of Eq. (5.28), with dressed vertices.

Given that the validity of the BC solution of Eq. (4.36) is conditioned by the constraint (4.28), and given that our nonperturbative $H_{\nu\mu}$ violates this condition, depending on the kinematic configuration (see Section 5.6), it is important also to discuss the effect of this symmetry breaking on the X_i to be obtained. In particular, the ensuing X_i will necessarily not satisfy the STI exactly.

Notwithstanding that, we expect our results to still capture the main features of the STI part of the three-gluon vertex, since the STI will be approximately satisfied. Moreover, we recall from Section 5.6 that the violation of the constraint by our results of $H_{\nu\mu}(p_1,p_2,p_3)$ becomes smaller as the ghost and gluon momenta, p_2 and p_3, respectively, become closer in magnitude. Because the A_i appear in Eq. (4.36) in several permutations of their arguments, it is not possible to characterize the effect of the violation of Eq. (4.28) on the $X_i(q,r,p)$ in terms of two momenta only. Nevertheless, it is clear that the problem will be smaller when all three arguments of the $X_i(q,r,p)$ have similar magnitudes, in which case all the A_i that appear in Eq. (4.36) will have their respective gluon and ghost arguments close in magnitude as well. In particular, in the totally symmetric configuration, $q^2 = r^2 = p^2 = Q^2$, the A_i appearing in the calculation of the $X_i(Q^2)$ satisfy the constraint trivially. In contrast, whenever two of the momenta in $X_i(q,r,p)$ have very different magnitudes, say $q^2 \gg p^2$, one may expect the violation of the constraint by the input A_i to translate into some additional error in the three-gluon vertex results.

It is important to emphasize that, unlike the ghost-gluon scattering kernel, the three-gluon vertex in Landau gauge is an UV divergent function [133, 139, 208], which must be renormalized nontrivially in general. Since we use as input for the evaluation of the form factors X_i the ghost-gluon scattering kernel renormalized within the Taylor prescription of Eq. (5.16), our Gauge Technique three-gluon vertex results are automatically renormalized in this same scheme, as discussed in the end of Section 4.3. Evidently, in comparing our results to calculations performed in different schemes, *finite* renormalizations may be necessary, in order to have the different results in the same prescription. We will point out explicitly when this is done in this thesis.

As for the numerical methods necessary, the most difficult task was the evaluation of the A_i, already discussed in the previous chapter. Now, given the tabulated data for these form factors, the BC solution for the Eq. (4.36) at a certain triple (q,p,r) may require values of the A_i at points not existent in the table. When these points are between tabulated data we use the tensor product of B-splines method [209] for interpolation. Yet, Eq. (4.36) could require the evaluation of A_i for momenta beyond the range originally computed. To avoid this issue, we took the precaution of computing the A_i in a range much larger than that intended for the evaluation of the X_i. Specifically, as stated in Section 5.4, the A_i were computed for squared momenta in the range $[5\times 10^{-5}\,\text{GeV}^2, 10^4\,\text{GeV}^2]$, whereas we will evaluate the X_i for squared momenta between $[10^{-3}\,\text{GeV}^2, 10^3\,\text{GeV}^2]$.

6.2 General kinematics results

To present our results in general Euclidean kinematics, we will resort again to 3D plots, on the lines of those of Subsection 5.4.1, using again the spherical coordinates notation similar to Eq. (D.16), *i.e.* $X_i(q,r,p) \equiv X_i(q^2,r^2,\theta)$. Notice that θ now stands for the angle between q and r, and is not necessarily equal to the angle between q and p. The effect of varying the parameter γ in Eq. (3.51) turns out to not be appreciable in the 3D plots and we have thus chosen to present only the surfaces corresponding to $\gamma = 0$.

In the Figs. 6.1, 6.2 and 6.3, we show surfaces for the $X_i(q^2,r^2,\theta)$, for $i = 1$, 2 and 3, as functions of q^2 and r^2 and fixed θ. To cover the angular dependence, we show three

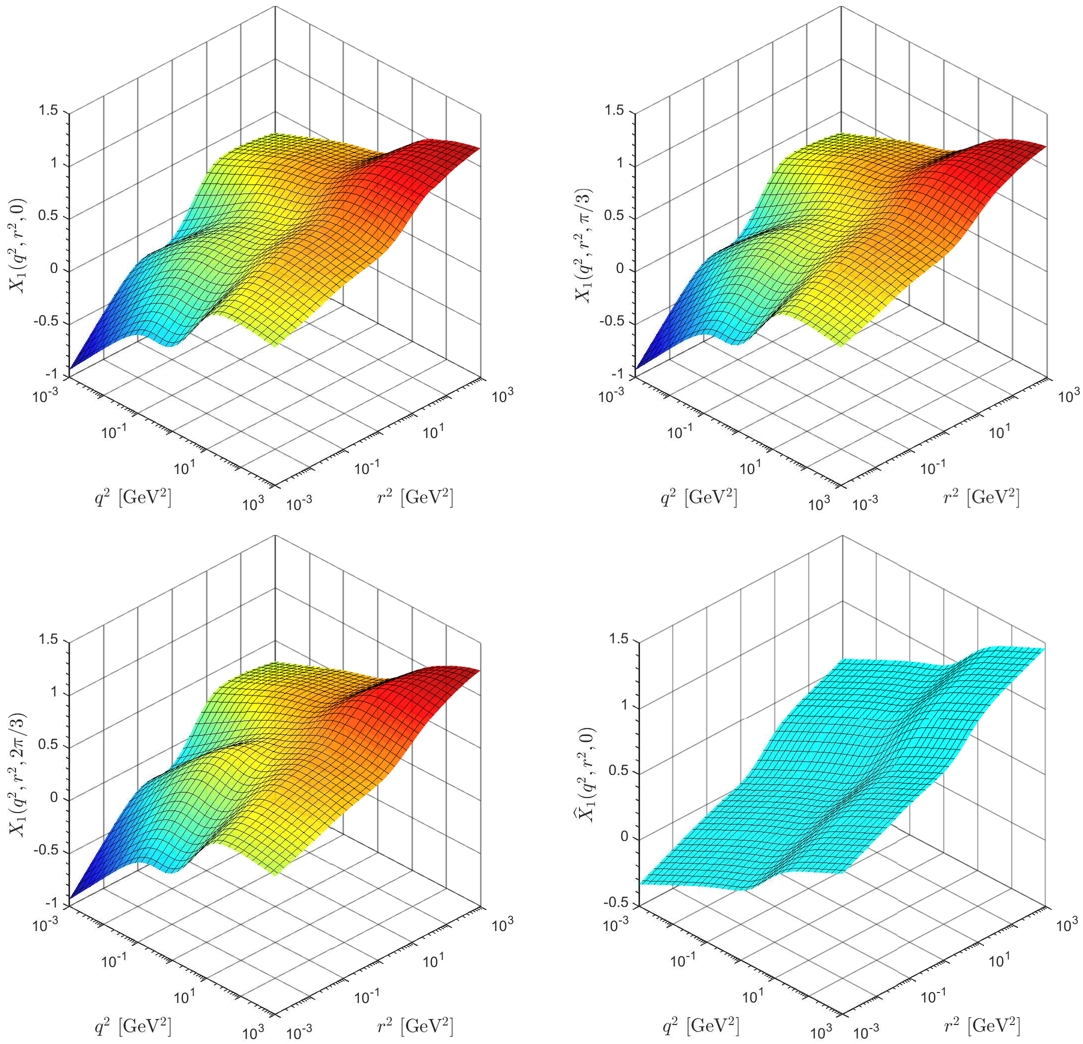

Figure 6.1: Three-gluon vertex form factor $X_1(q^2, r^2, \theta)$ for $\theta = 0$ (top left), $\pi/3$ (top right) and $2\pi/3$ (bottom left). The Abelianized $\widehat{X}_1(q^2, r^2, \theta)$ is shown on the bottom right.

plots for each X_i, with $\theta = 0$, $\pi/3$ and $2\pi/3$.

In order to assess the effect of the ghost-sector in the BC solution for each X_i, we also show in the bottom right panel of each of Figs. 6.1, 6.2 and 6.3 the corresponding Abelianized approximation, $\widehat{X}_i$, of Eq. (4.38), for which $H_{\nu\mu}$ and $F(q^2)$ are set to their tree level values. Notice that the Abelianized approximation satisfies the constraint of Eq. (4.28) trivially. In addition, the Abelianized form factors $\widehat{X}_i$ have no dependence on the angle, so we only need to show them for $\theta = 0$.

For the form factors X_i, for $i = 1$, 2 and 3, it is clear from Figs. 6.1, 6.2 and 6.3 that the angular dependence is mild and their (anti-)symmetries with respect to the exchange $q^2 \leftrightarrow r^2$, expressed by Eq. (4.35), are preserved. Moreover, we see that the Abelianized approximations, $\widehat{X}_i$, already capture the main *qualitative* features of the results, albeit quantitatively different. In particular, we see that $X_1(q^2, r^2, \theta)$ and $X_2(q^2, r^2, \theta)$ diverge

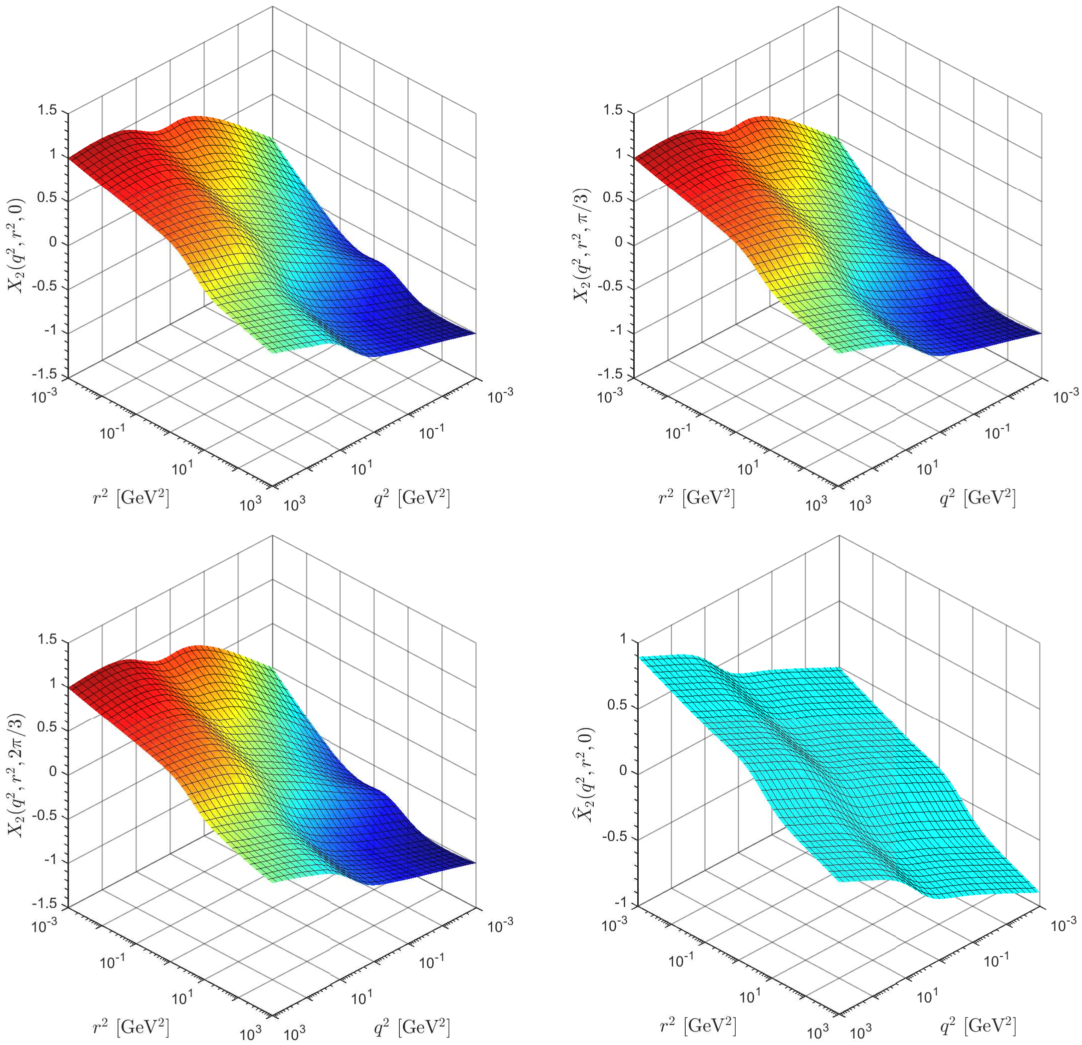

Figure 6.2: Three-gluon vertex form factor $X_2(q^2, r^2, \theta)$ for $\theta = 0$ (top left), $\pi/3$ (top right) and $2\pi/3$ (bottom left). The Abelianized $\widehat{X}_2(q^2, r^2, \theta)$ is shown on the bottom right. For better visibility, the q^2 and r^2 axes in this figure are rotated by $\pi/2$ with respect to the other $3D$ figures.

logarithmically as either q^2 or r^2 tends to zero. This behavior is solely determined by the logarithmic IR divergence of $J(q^2)$, which in turn is a consequence of the masslessness of the ghosts (see Section 3.4), and for this reason is present already in the Abelianized versions, $\widehat{X}_1(q^2, r^2, \theta)$ and $\widehat{X}_2(q^2, r^2, \theta)$.

In contrast, the form factor X_3 exhibits a much steeper divergence in comparison with $X_1(q^2, r^2, \theta)$ and $X_2(q^2, r^2, \theta)$. In fact, the divergence of X_3 is a simple pole when all momenta vanish, and for this reason, we chose to render Fig. 6.3 with logarithmic scale in the vertical axis as well.

It is seen clearly in Fig. 6.3 that the steeper divergence of $X_3(0, 0, 0)$ is present already at the Abelianized level, *i.e.* $\widehat{X}_3(0, 0, 0)$ is also a pole. Consequently, this behavior cannot

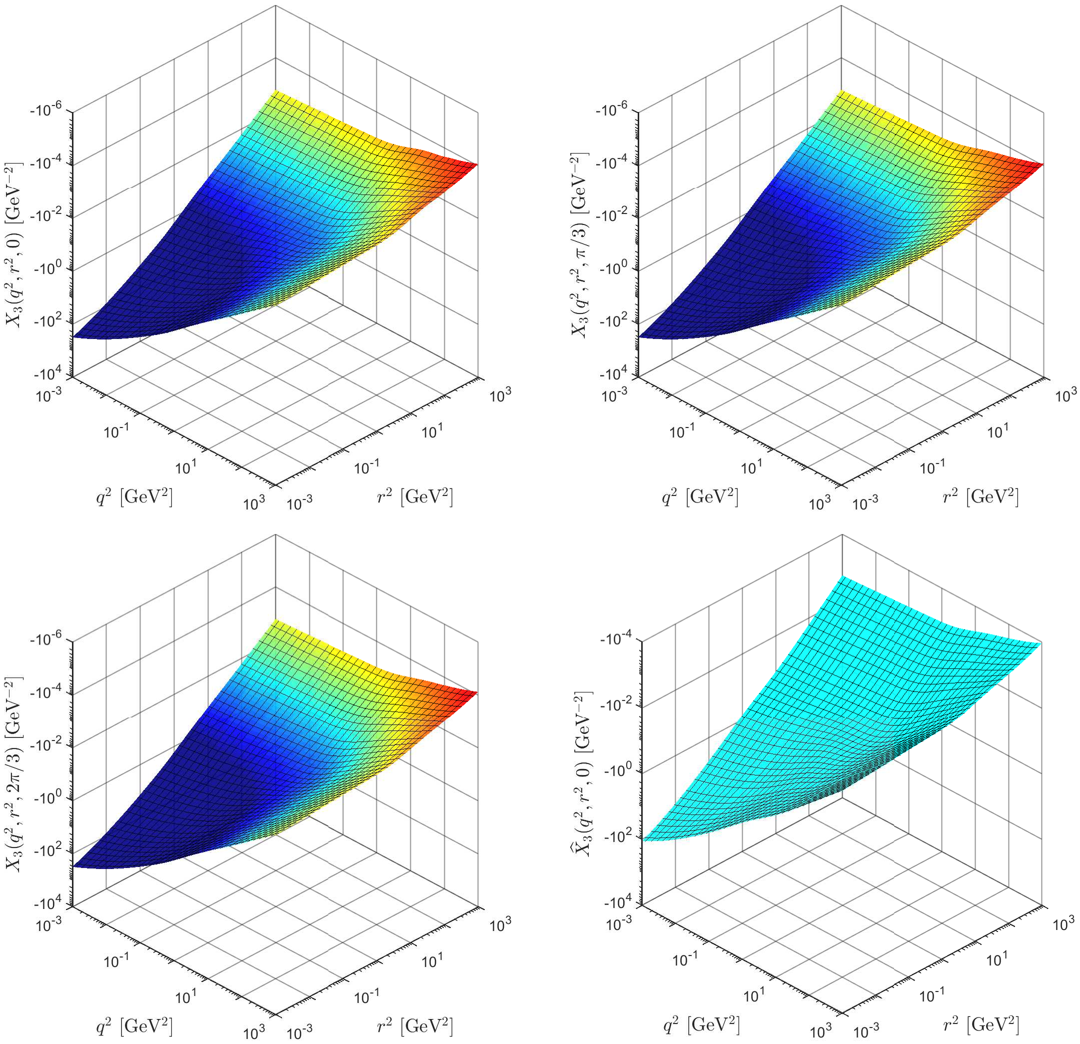

Figure 6.3: Three-gluon vertex form factor $X_3(q^2, r^2, \theta)$ for $\theta = 0$ (top left), $\pi/3$ (top right) and $2\pi/3$ (bottom left). The Abelianized $\widehat{X}_3(q^2, r^2, \theta)$ is shown on the bottom right.

be caused by the ghost sector dressings, $F(q^2)$ and A_i, and we can analyze it in the simpler Abelianized approximation.

To study the $\widehat{X}_3(0,0,0)$ behavior we start by setting $q^2 = r^2$ in Eq. (4.38), that is, we approach the all momenta vanishing limit along the diagonal of the blue surface in the bottom right panel of Fig. 6.3. Evidently, due to the $q^2 - r^2$ denominator, the expression for $\widehat{X}_3(q^2, r^2, p^2)$ in Eq. (4.38) for $q^2 = r^2$ becomes a derivative, which in Euclidean space reads

$$\widehat{X}_3\big(q^2, q^2, 2q^2(1+\cos\theta)\big) = -\frac{dJ(q^2)}{dq^2}\,, \tag{6.1}$$

where we used momentum conservation to write $p^2 = 2q^2(1+\cos\theta)$. Then, it is obvious that since $J(q^2)$ is logarithmically IR divergent, *i.e.* contains an "unprotected" $\ln(q^2/\mu^2)$, the $\widehat{X}_3\big(q^2, q^2, 2q^2(1+\cos\theta)\big)$ of Eq. (6.1) contains a simple pole, of the form $1/q^2$. Hence, the pole divergence observed in Fig. 6.3 for X_3 when all momenta vanish is a consequence of the logarithmic IR divergence of the $J(q^2)$, which in turn is the result of the masslessness of the ghosts (see Section 3.4). In particular, for the fit (3.51), the Eq. (6.1) reads

$$\widehat{X}_3(q^2, q^2, 2q^2(1+\cos\theta)) = -\frac{C_{\rm A}\alpha_s}{24\pi}\left[\frac{1}{q^2}\left(1+\frac{\tau_1}{q^2+\tau_2}\right) - \frac{\tau_1}{(q^2+\tau_2)^2}\ln\left(\frac{q^2}{\mu^2}\right)\right] + \cdots\,, \tag{6.2}$$

where the ellipses denote IR finite terms. Note that Eq. (6.2) contains in addition a logarithmic divergence, which is however, subleading.

Given the importance of pole divergences in vertices in this work, it is necessary to clarify the implications of the divergence of X_3 and distinguish it from the mass-generating poles discussed in Chapter 3 (see also [4]).

Firstly, the pole divergence of $X_3(0,0,0)$ does not produce a pole in the three-gluon vertex itself. In particular, it does not in any way contradict our assertion that we are determining the *regular* part, $\Gamma_{\alpha\mu\nu}(q,p,r)$, of the vertex. Indeed, a pole in a given form factor does *not necessarily* imply a pole in the vertex itself, since the form factors come accompanied by tensor structures that, in general, contain momenta. The X_3, in particular, appears in the BC basis of Eq. (4.29) multiplied by the tensor $\ell^3_{\alpha\mu\nu}$ of Eq. (4.30), which contains three momenta. Given that the pole divergence of X_3 happens when all momenta vanish, the tensor $\ell^3_{\alpha\mu\nu}$ goes to zero faster than enough to cancel the $1/q^2$ divergence of the form factor.

Consequently, since $\Gamma_{\alpha\mu\nu}(q,p,r)$ remains regular, the simple pole in X_3 is not the kind of divergence that triggers the gluon mass generation mechanism, explained in Chapter 3, which requires the *vertex itself* to contain (longitudinal) poles. Finally, the divergence in X_3 does not in any way appear as a pole in the transversely projected vertex discussed in Section 4.5. Indeed, since the derivative of $J(Q^2)$ appears multiplied by Q^2 in Eq. (4.61), its contribution to $L^{\rm sym}(Q^2)$ is IR finite.

Another important point we would like to discuss is the IR suppression of the three-gluon vertex with respect to its tree level, which has been the subject of much recent interest [4, 7, 8, 43–60] for its phenomenological and theoretical implications [5, 6, 56, 57, 62, 63, 71]. It is clear from Fig. 6.3 that the form factor X_1, which accompanies the tree-level tensor structure of the vertex, is suppressed with respect to its tree-level value, $X_1^{(0)} = 1$, over a large region in the IR before its logarithmic divergence flips its sign.

Additionally, we notice that the Abelianized approximation, $\widehat{X}_1$ is even *more* suppressed in the same region than the full result X_i. From this comparison we can conclude that the IR suppression of the three-gluon vertex, at the level of the Gauge Technique solution, is dominated by the corresponding suppression of the kinetic term of the gluon propagator, $J(q^2)$.

Now, it may be argued that the one-loop result already displays IR suppression with respect to tree level, since it is also logarihtmically divergent, as is clear from the expression in Eq. (B.3). Nevertheless, we find that the nonperturbative X_1 is much more suppressed than the one-loop result. For a concrete demonstration of this assertion, we computed the one-loop version of $X_1(q^2, r^2, \theta)$ for general q^2 and r^2, where we chose $\theta = \pi/2$, such that $q \cdot r = 0$, to simplify the calculation a little. The result is given (in Minkowski space) in Eq. (B.29); note that the one-loop expression must be renormalized in the Taylor scheme by using Eq. (B.34), to compare to our nonperturbative X_1. Then, in Fig. 6.4 we contrast our Gauge Technique X_1 (heat-mapped surface) to the one-loop result of Eq. (B.29) (cyan transparent surface). The comparison of the two surfaces shows clearly that the suppression of the nonperturbative X_1 is much stronger than that of its one-loop counterpart.

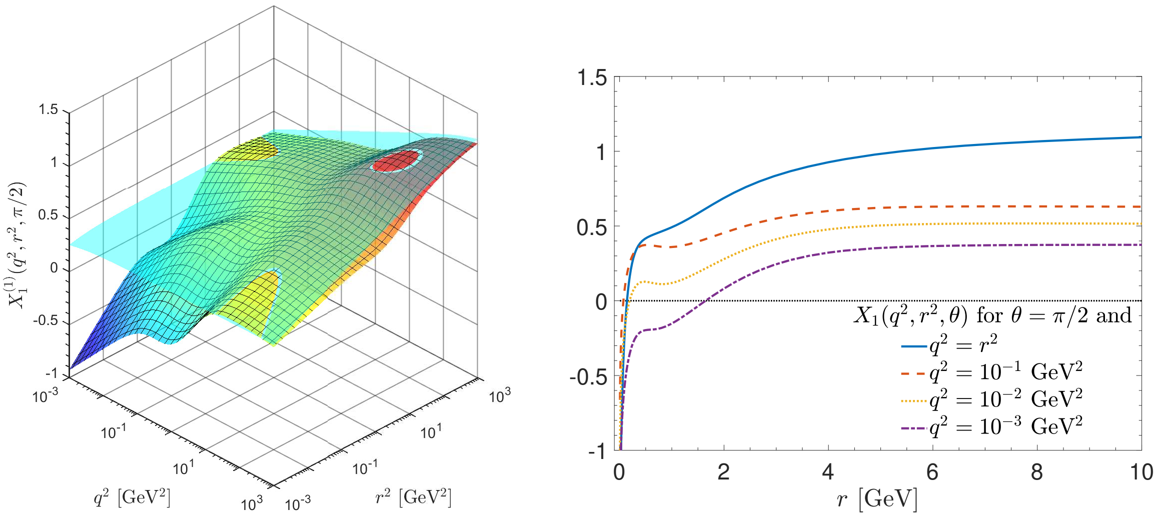

Figure 6.4: Left: Comparison of the nonperturbative (heat-mapped surface) $X_1(q^2, r^2, \theta)$, for $\theta = \pi/2$, to its one-loop counterpart (cyan surface) of Eq. (B.29). Right: Special kinematic cases of the nonperturbative $X_1(q^2, r^2, \pi/2)$. The blue continuous curve corresponds to the diagonal $q^2 = r^2$. The red dashed, yellow dotted and purple dot-dashed are obtained by fixing q^2 and varying r^2.

It is also interesting to notice that $X_1(q^2, r^2, \theta)$ is largest along the diagonal $q^2 = r^2$, decreasing as we keep one momentum fixed and vary the other. On the right panel of

Fig. 6.4 we illustrate this behavior by comparing slices of the surface on the left, and it is seen more clearly that $q^2 = r^2$ yields the highest curve.

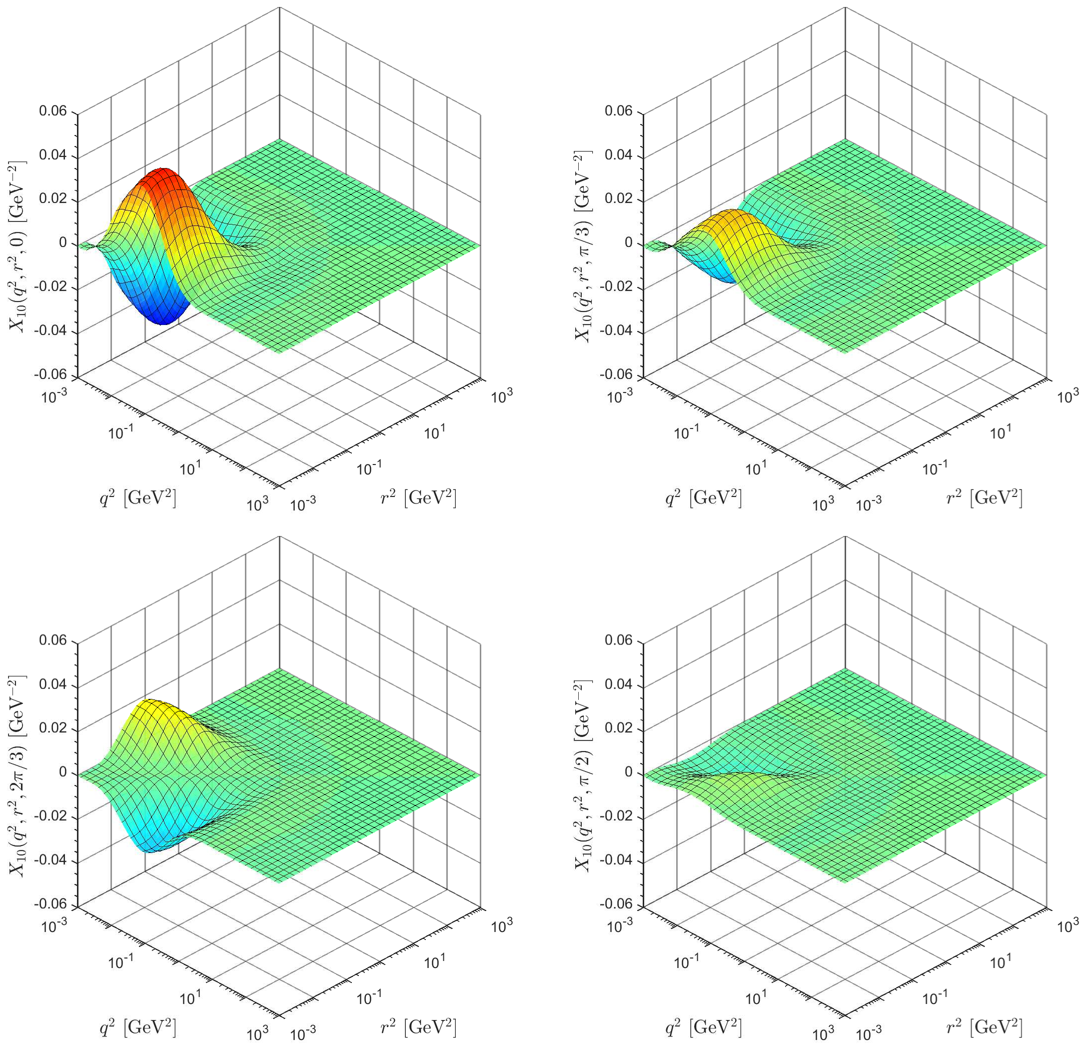

Figure 6.5: Three-gluon vertex form factor $X_{10}(q^2, r^2, \theta)$ for $\theta = 0$ (top left), $\pi/3$ (top right), $2\pi/3$ (bottom left) and $\pi/2$ (bottom right).

Finally, in Fig. 6.5 we show the form factor $X_{10}(q^2, r^2, \theta)$. Since for this function the corresponding Abelianized approximation of Eq. (4.38) vanishes identically, we fill in the bottom right panel of Fig. 6.5 with an additional angle, $\theta = \pi/2$. Interestingly, this form factor was found by Davydychev, Osland and Tarasov[1], to vanish identically at one loop [208]. In our nonperturbative results, X_{10} does *not* vanish identically; but is extremely suppressed in comparison to the other X_i. Moreover, our X_{10} shows no sign of IR divergence, in spite of the logarithmic divergences of the ingredients appearing in Eq. (4.36), namely A_3 (see Table 5.1) and $J(q^2)$, which indicates a strong cancellation of the inputs in the BC solution.

[1] Also by BC [126], in the Feynman gauge, $\xi = 1$.

6.3 Special kinematic configurations

We consider now two special kinematic limits for which we may perform additional comparisons to the one-loop behavior of $\Gamma_{\alpha\mu\nu}(q,r,p)$. Given the focus of this section on the behavior of the nonperturbative X_i for large momenta, we will restrict ourselves to the $\gamma = 0$ results, since the different values of γ furnish nearly identical UV tails for the $J(q^2)$ (see Fig. 3.15) and hence the Gauge Technique three-gluon vertex.

The first configuration we consider is the *totally symmetric* limit defined in Minkowski space in Eq. (B.5). Specifically, the totally symmetric configuration is obtained by extracting the $q^2 = r^2$ diagonals from the $\theta = 2\pi/3$ surfaces of Figs. 6.1, 6.2, 6.3 and 6.5. Evidently, by Bose symmetry, the form factors $X_2(Q^2)$ and $X_{10}(Q^2)$ vanish identically in this kinematic limit, such that we focus on $X_1(Q^2)$ and $X_3(Q^2)$.

In Fig. 6.6, the nonvanishing $X_i(Q^2)$ are represented by blue continuous curves and are compared to their one-loop values of Eq. (B.25), after conversion to Euclidean space and renormalization in the Taylor scheme using Eq. (B.34), represented by red dashed lines. In this figure we can see again and in more detail some of the features of X_1 and X_3 already discussed in the previous sections; especially, (a) the logarithmic and pole IR divergences of X_1 and X_3, respectively, and (b) the stronger suppression of the nonperturbative X_1 than exhibited by its one-loop counterpart, with respect to the tree-level value $X_1^{(0)} = 1$.

Next, we notice that while in the IR both the nonperturbative X_1 and X_3 deviate substantially from their corresponding one-loop results, they approach their perturbative behaviors for large Q^2.

Still in Fig. 6.6 we show a physically motivated fit for the nonperturbative $X_1(Q^2)$ (purple dotted line) given by,

$$
\begin{aligned}
X_1(Q^2) = & 1 + \frac{C_{\rm A}\alpha_s}{96\pi}\left[1 + \frac{\kappa_1}{1+(Q^2/\kappa_2)}\right]\left\{33\ln\left[\frac{Q^2+\rho_\ell\, m^2(Q^2)}{\mu^2}\right] + \ln\left(\frac{Q^2}{\mu^2}\right)\right\} \\
& + \frac{C_{\rm A}\alpha_s}{16\pi}(1-\mathcal{I}) \,,
\end{aligned}
\tag{6.3}
$$

with $m^2(Q^2)$ given by Eq. (3.50) with $\gamma = 0$, the constant $\mathcal{I}$ is defined in Eq. (B.7) and the fitting parameters are $\kappa_1 = 135.3$, $\kappa_2 = 0.086$ GeV^2, and $\rho_\ell = 140.4$. The above fit was designed to reproduce the one-loop behavior of $X_1(Q^2)$ for large Q^2.

The second kinematic configuration we consider is the *asymmetric limit*, defined by

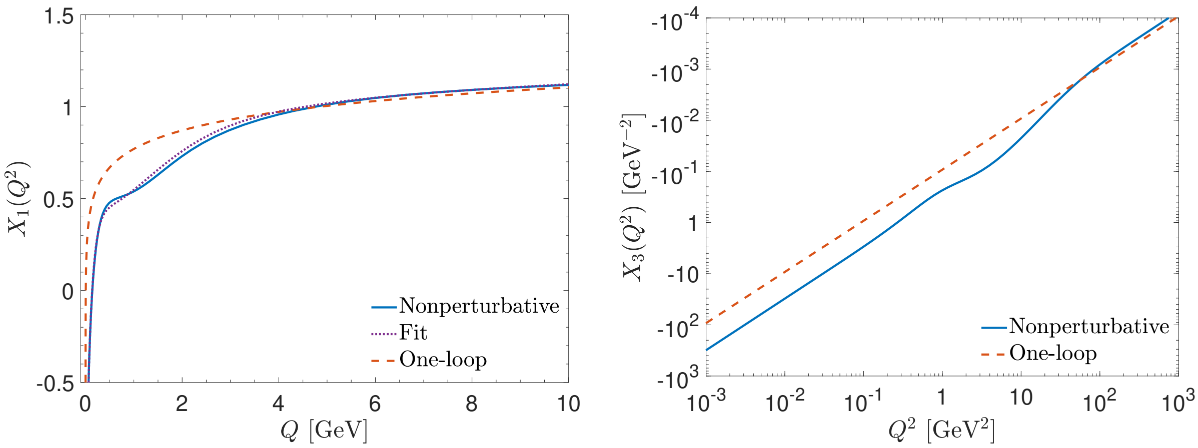

Figure 6.6: Left: Nonperturbative form factor $X_1(Q^2)$ in the totally symmetric configuration (blue continuous) compared to its one-loop counterpart of Eq. (B.25) (red dashed). Also shown is the fit of Eq. (6.3) (purple dotted) for the nonperturbative result. Right: Same comparison but for the $X_3(Q^2)$. For this form factor we have not constructed a fit.

setting the momentum $p = 0$. Note that in our spherical coordinates notation this limit corresponds to $r^2 = q^2$ with the angle $\theta = \pi$. Hence we may write equivalently $X_i(q, -q, 0)$ or $X_i(q^2, q^2, \pi)$. In this kinematic configuration, only the form factors $X_1(q^2, q^2, \pi)$ and $X_3(q^2, q^2, \pi)$ are nonvanishing and the corresponding one-loop results are given by Eq. (B.28), after duly renormalizing with Eq. (B.34) and converting to Euclidean space.

The Gauge Technique and one-loop $X_i(q^2, q^2, \pi)$ are represented in Fig. 6.7, by blue continuous and red dashed curves, respectively. Clearly, the asymmetric X_1 and X_3 exhibit the same overall features of the symmetric case of Fig. 6.6. The only additional comment we should make is that in the asymmetric limit the nonperturbative X_i seem to not recover exactly the UV tails of their one-loop results, but run parallel to them, with small offsets at large momenta.

This small discrepancy is likely due to the fact that the input A_i violate the STI constraint of Eq. (4.28) in this kinematics. Indeed, since $p = 0$, the asymmetric limit corresponds to the most extreme instance of unequal scales for the arguments of the $X_i(q, r, p)$. As we have discussed in Section 6.1, this is precisely the situation where the violation of the constraint is expected to manifest in our computation of the X_i. In contradistinction, the symmetric limit of Fig. 6.6 has the constraint of Eq. (4.28) satisfied trivially for all the A_i appearing in the BC solution. Anyhow, the nonperturbative and one-loop $X_i(q^2, q^2, \pi)$ still agree satisfactorily for most purposes.

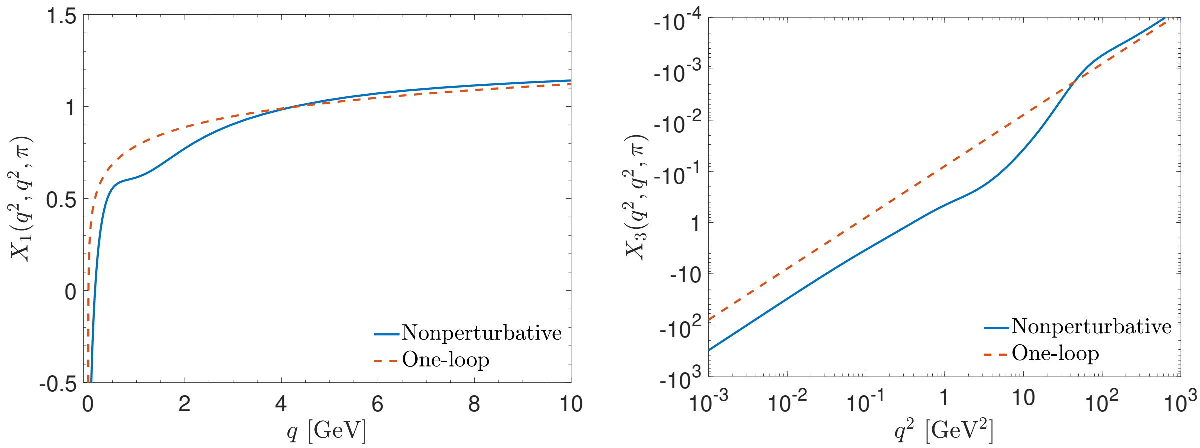

Figure 6.7: Left: Nonperturbative form factor $X_1(q^2, q^2, \pi)$ in the asymmetric configuration (blue continuous) compared to its one-loop counterpart of Eq. (B.28) (red dashed). Right: Same comparison but for the $X_3(q^2, q^2, \pi)$.

6.4 Comparison to other nonperturbative results

While the results of the previous section establishes that the nonperturbative BC construction of $\Gamma_{\alpha\mu\nu}$ adequately reproduces the perturbative regime for large momenta, it is instructive to compare our results to those obtained by different nonperturbative methods that probe the IR. In this section, we compare our three-gluon vertex results to SDE solutions [53, 59] and lattice simulations [44, 45].

Because different authors have used various tensor bases, and correspondingly different definitions of form factors, a direct comparison of their results to our X_i is not generally possible. Nevertheless, certain transverse projections of the three-gluon vertex, which can be written as linear combinations of the X_i and, in general, also the Y_i, have been studied previously. Since in the Gauge Technique the "transverse" form factors, Y_i, are undetermined, in the projections appearing below that involve these quantities we have no option at this point but to resort to the additional approximation $Y_i = 0$. Evidently, this constitutes an additional source of error, whose impact on the results cannot be fully addressed at the moment.

The transverse projections we shall consider can all be written in the general form

$$L(q,r,p) = \frac{W^{\alpha\mu\nu}(q,r,p)\overline{\Gamma}_{\alpha\mu\nu}(q,r,p)}{W^{\alpha\mu\nu}(q,r,p)W_{\alpha\mu\nu}(q,r,p)}\,, \tag{6.4}$$

for some $W^{\alpha\mu\nu}(q,r,p)$ which depends on the particular choice or needs of the different authors. In Eq. (6.4), we use again an overline to denote contraction with three transverse projectors, *i.e.*

$$\overline{\mathbb{\Gamma}}_{\alpha\mu\nu}(q,r,p) := \mathrm{P}_{\alpha}^{\beta}(q)\mathrm{P}_{\mu}^{\rho}(r)\mathrm{P}_{\nu}^{\sigma}(p)\mathbb{\Gamma}_{\beta\rho\sigma}(q,r,p)\,. \tag{6.5}$$

Moreover, we recall that the double struck $\mathbb{\Gamma}_{\alpha\mu\nu}$ represents the full vertex, including pole part. However, since the pole term $V_{\alpha\mu\nu}(q,p,r)$ in Eq. (3.29) is strictly longitudinal [Eq. (3.31)], it decouples from the transversely projected vertex, such that the Eq. (6.4) may as well be cast as

$$L(q,r,p) = \frac{W^{\alpha\mu\nu}(q,r,p)\overline{\Gamma}_{\alpha\mu\nu}(q,r,p)}{W^{\alpha\mu\nu}(q,r,p)W_{\alpha\mu\nu}(q,r,p)}\,. \tag{6.6}$$

Importantly, since the pole part $V_{\alpha\mu\nu}(q,p,r)$ does not appear in projections of the form of Eq. (6.6), calculations of the vertex that restrict themselves to such transverse projection cannot *directly* access the pole structure of the vertex.

6.4.1 Comparison to SDE results

In Refs. [53, 59] the three-gluon vertex SDE was solved numerically under certain approximations. More specifically, the authors considered the transverse projection of Eq. (6.6) with

$$W_{\alpha\mu\nu}(q,r,p) \to W^{\text{SDE}}_{\alpha\mu\nu}(q,r,p) := \overline{\Gamma}^{(0)}_{\alpha\mu\nu}(q,r,p)\,. \tag{6.7}$$

We denote this particular definition of $L(q,r,p)$ by $L^{\text{SDE}}(q,r,p)$.

Substituting the BC basis expression for $\Gamma_{\alpha\mu\nu}(q,p,r)$ given by Eqs. (4.31), (4.29) and (4.25) into Eq. (6.6) and using the above definition of $W^{\text{SDE}}_{\alpha\mu\nu}(q,r,p)$, the $L^{\text{SDE}}(q,r,p)$ can be expressed in terms of the form factors $X_i(q,r,p)$ and $Y_i(q,r,p)$. The resulting expressions are rather lengthy in general kinematics, but simplify considerably for certain limits which we consider next.

(*i*) *Totally symmetric configuration:* In the totally symmetric limit defined by Eq. (B.5), the $L^{\text{SDE}}(q,r,p)$ reads (in Euclidean space)

$$L^{\text{SDE}}(Q^2) = X_1(Q^2) - \frac{10}{11}Q^2X_3(Q^2) + \frac{5}{11}Q^4Y_1(Q^2) - \frac{4}{11}Q^2Y_4(Q^2)\,. \tag{6.8}$$

As we will have to omit the undetermined $Y_i(Q^2)$ from Eq. (6.8) in our comparison, let us at least note that at one-loop, Eq. (B.25) yields

$$\frac{5}{11}Q^4Y_1^{(1)}(Q^2) - \frac{4}{11}Q^2Y_4^{(1)}(Q^2) = 0.039\,. \tag{6.9}$$

using $\alpha_s = 0.22$ as in the rest of this work. The smallness of the one-loop value of the $Y_i(Q^2)$ terms *suggests* that their omission from Eq. (6.8) should be forgivable at a first approximation.

(*ii*) *Orthogonal symmetric configuration:* Setting the momenta q and r to be orthogonal, $\theta = \pi/2$, with equal magnitudes, $q^2 = r^2$, one obtains

$$\begin{aligned} L^{\text{SDE}}(r^2, r^2, \pi/2) =& \frac{1}{7}[X_1(r^2, r^2, \pi/2) + 6X_1(2r^2, r^2, 3\pi/4) - r^2X_3(r^2, r^2, \pi/2) \\ & - 8r^2X_3(2r^2, r^2, 3\pi/4) + r^4Y_1(r^2, r^2, \pi/2) + 4r^4Y_1(2r^2, r^2, 3\pi/4) \\ & - 3r^2Y_4(r^2, r^2, \pi/2)]\,. \end{aligned} \tag{6.10}$$

Note that in this configuration $p^2 = 2r^2$.

(*iii*) *Asymmetric limit:* In the $p = 0$ limit, equivalently $q^2 = r^2$ with $\theta = \pi$, $L^{\text{SDE}}(q, r, p)$ attains its simplest form, namely

$$L^{\text{SDE}}(q^2) = X_1(q^2, q^2, \pi) - q^2X_3(q^2, q^2, \pi)\,. \tag{6.11}$$

In Ref. [53, 59] this configuration is referred to as "orthogonal soft" and defined by letting $q = 0$ with $\theta = \pi/2$. However, by virtue of the Bose symmetry of the three-gluon vertex, $L^{\text{SDE}}(q, r, p)$ reduces to an expression exactly equivalent [4] to Eq. (6.11) whichever momentum q, r or p is set to zero, with only the substitution of q^2 by r^2 or p^2.

A remarkable property of the asymmetric configuration is that it does not involve "transverse" form factors, Y_i, which is due to the fact that the transverse tensors $t^j_{\alpha\mu\nu}$ of Eq. (4.32) all vanish if any one of q, r or p is set to zero.

Naturally, to compare our results, which are given in the Taylor renormalization scheme, to the SDE solution of Ref. [53, 59], the two sets of data must be renormalized in the same scheme. To ensure that this is the case, we rescale all sets of results

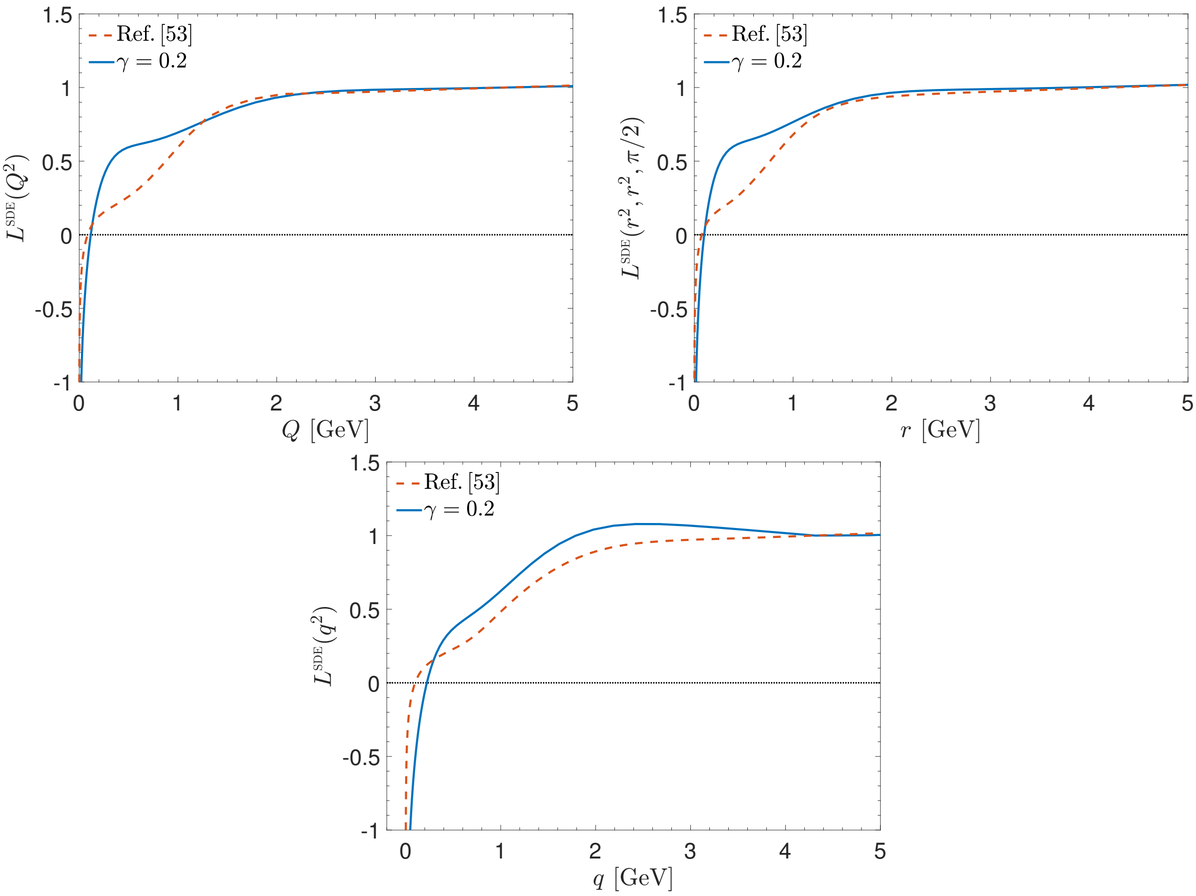

Figure 6.8: Comparison of the results for L^{SDE} using our Gauge Technique three-gluon vertex (blue continuous) to the SDE results of Refs. [53, 59] (red dashed). The kinematic configurations shown are: (i) the totally symmetric (top left), Eq. (6.8), the (ii) orthogonal symmetric (top right), Eq. (6.10), and the (iii) asymmetric (bottom), Eq. (6.11).

such that $L^{\text{SDE}}(q, r, p)$ reduces to tree-level at a point $Q^2 = \mu^2$ in the totally symmetric configuration. That is, we compute our version of $L^{\text{SDE}}(q, r, p)$ and rescale it, $L^{\text{SDE}}(q, r, p) \to z_3^{\text{SDE}} L^{\text{SDE}}(q, r, p)$, by the finite z_3^{SDE} such that

$$L^{\text{SDE}}(\mu^2) = 1\,. \tag{6.12}$$

The exact same procedure is then applied for the SDE data set. As such, both sets agree exactly at the point $L^{\text{SDE}}(\mu^2)$, and can be compared fairly.

The comparison of our results to the SDE solution of Ref. [53, 59] is shown in Fig. 6.8, represented by blue continuous and red dashed curves, respectively. For this analysis, we chose to present our results in the case $\gamma = 0.2$, although other values of γ lead to similar curves. It is clear from this figure that the Gauge Technique and SDE solutions have similar shapes, but differ significantly in the region of momenta about 0.1 - 1 GeV. In the asymmetric case the range over which the results differ is even longer and extends to the UV. Nevertheless, it is remarkable that the positions of the zero-crossings of the Gauge Technique and SDE results almost coincide.

6.4.2 Comparison to lattice simulations

Lastly, we compare our Gauge Technique results to the lattice simulations of [44, 45]. In Refs. [44, 45] two kinematic configurations were considered, which give rise to two different projections of the form (6.6).

The first configuration is again the totally symmetric limit of Eq. (B.5). However, the projection considered on the lattice simulation is different from that treated in the SDE analysis of [53, 59], furnishing a linear combination of $X_i(Q^2)$ and $Y_i(Q^2)$ different from Eq. (6.8). Specifically, the projection performed on the lattice is given by substituting [44, 45]

$$W_{\alpha\mu\nu}(q,r,p) \to W^{\rm sym}_{\alpha\mu\nu}(q,r,p) = \overline{\Gamma}^{(0)}_{\alpha\mu\nu}(q,r,p) + \frac{1}{2r^2}(r-p)_\alpha(p-q)_\mu(q-r)_\nu \,, \tag{6.13}$$

into Eq. (6.6).

In this case, the appropriate combination of BC basis form factors reads

$$L^{\rm sym}(Q^2) = X_1(Q^2) - \frac{Q^2}{2}X_3(Q^2) + \frac{Q^4}{4}Y_1(Q^2) - \frac{Q^2}{2}Y_4(Q^2) \,, \tag{6.14}$$

which is the Euclidean space version of Eq. (B.24). Once again, we will have to omit the "transverse" form factors $Y_i(Q^2)$. We nonetheless mention that at one-loop the results in Eq. (B.25) yield, for $\alpha_s = 0.22$, the small constant value

$$\frac{Q^4}{4}Y_1^{(1)}(Q^2) - \frac{Q^2}{2}Y_4^{(1)}(Q^2) = 0.08 \,. \tag{6.15}$$

The second kinematic limit considered on the lattice is the asymmetric limit, $p = 0$, with the projection [44, 45]

$$W_{\alpha\mu\nu}(q,r,p) \to W^{\rm asym}_{\alpha\mu\nu}(q,r,p) = 2q_\nu {\rm P}_{\alpha\mu}(q) \,. \tag{6.16}$$

With the above substitution into Eq. (6.6) one finds in the asymmetric limit

$$L^{\text{asym}}(q^2) = X_1(q^2, q^2, \pi) - q^2 X_3(q^2, q^2, \pi)\,. \tag{6.17}$$

Notice that the lattice projection $L^{\text{asym}}(q^2)$ leads to the exact same combination of X_i as the $L^{\text{SDE}}(q^2)$ of Eq. (6.11).

The lattice data of [44, 45] is renormalized in two different schemes for each of the above configurations. Specifically, the symmetric configuration data is renormalized such that $L^{\text{sym}}(\mu^2) = 1$, whereas the asymmetric data is renormalized with $L^{\text{asym}}(\mu^2) = 1$, where $\mu = 4.3$ GeV. In order to compare our Gauge Technique results fairly to the lattice, we rescale our expressions for $L^{\text{sym}}(Q^2)$ and $L^{\text{asym}}(q^2)$ by

$$L^{\text{sym}}(Q^2) \to z_3^{\text{sym}} L^{\text{sym}}(Q^2)\,, \qquad L^{\text{asym}}(q^2) \to z_3^{\text{asym}} L^{\text{asym}}(q^2)\,, \tag{6.18}$$

with the finite renormalization constants defined by the prescriptions

$$L^{\text{sym}}(\mu^2) = 1\,; \qquad L^{\text{asym}}(\mu^2) = 1\,. \tag{6.19}$$

Note that the constants z_3^{sym} and z_3^{asym} have different numerical values, namely $z_3^{\text{sym}} = 0.95$ and $z_3^{\text{asym}} = 0.93$. Nevertheless, they both differ only slightly from unit, as is expected for MOM schemes in general [139].

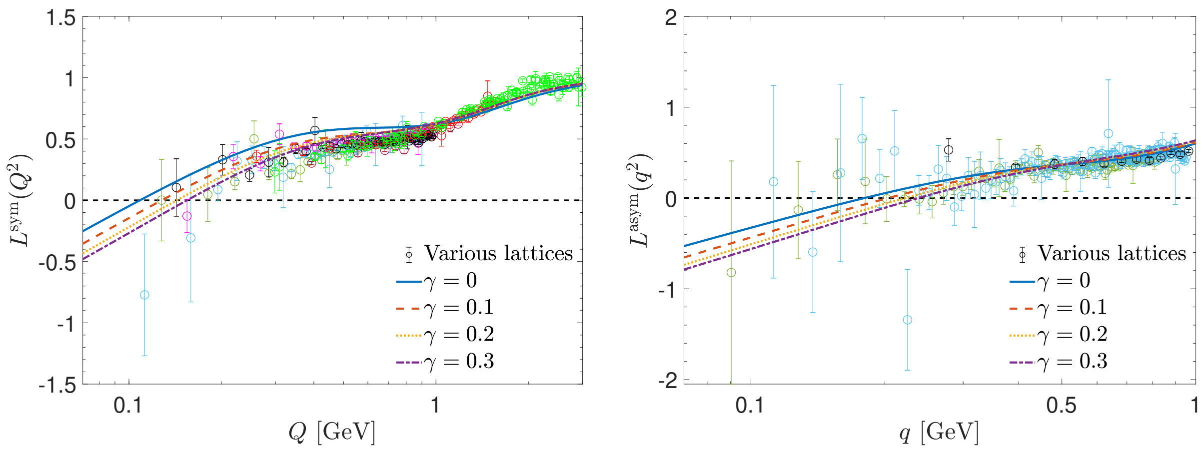

Figure 6.9: Comparison of our Gauge Technique results for $L^{\text{sym}}(Q^2)$ (left) given by Eq. (6.14), with $Y_i(Q^2) \to 0$, and for $L^{\text{asym}}(q^2)$ (right) of Eq. (6.17) to the corresponding lattice data of Refs. [44, 45] (circles). The blue continuous, red dashed, yellow dotted and purple dot-dashed curves correspond to $\gamma = 0$, 0.1, 0.2 and 0.3, respectively, in Eq. (3.51).

The comparison of our results to those of the lattice, from [44, 45], is shown in Fig. 6.9.

We focus on the IR behavior and show our results for each value of $\gamma = 0$, 0.1, 0.2 and 0.3 by blue continuous, red dashed, yellow dotted and purple dot-dashed curves, respectively.

It is clear from Fig. 6.9 that our Gauge Technique results capture the qualitative behavior of the $L^{\rm sym}(Q^2)$ and $L^{\rm asym}(q^2)$ rather well and even agree satisfactorily at a quantitative level. In particular, both lattice and Gauge Technique results exhibit distinguishably a zero-crossing for each of the kinematic limits considered, $L^{\rm sym}(Q^2)$ and $L^{\rm asym}(q^2)$. Naturally, the presence of the zero-crossing is accompanied by an overall suppression of $L^{\rm sym}(Q^2)$ and $L^{\rm asym}(q^2)$ in the IR, with respect to their tree-level values [$L^{(0)} = 1$, for both projections], and is consistent with the prediction in Section 3.4 based on the nonperturbative masslessness of the ghosts [52].

The agreement between our Gauge Technique and the lattice results in Fig. 6.9 is to be contrasted with the clear incompatibility of the *Naive* Gauge Technique construction with the lattice data, as had been shown in Fig. 4.1. When the longitudinality of the massless excitations of the three-gluon vertex, responsible for generating the dynamical gluon mass, is properly taken into account in the Gauge Technique construction, as done in this thesis, not only is the spurious pole seen in Fig. 4.1 eliminated entirely, but, with proper ghost sector corrections, even quantitative agreement is obtained in Fig. 6.9. Surely enough, the agreement seen in Fig. 6.9 is the most important result in this work.

Let us make a few more observations regarding our results:

(*i*) The main manifestation of the uncertainty in the running of the gluon mass, modeled in our analysis by varying the exponent γ in Eqs. (3.50) and (3.51), is in the position of the zero-crossings of $L^{\rm sym}(Q^2)$ and $L^{\rm asym}(q^2)$. Specifically, the positions of the zero-crossings, for both $L^{\rm sym}(Q^2)$ and $L^{\rm asym}(q^2)$, moves towards larger momenta as the mass runs faster, *i.e.* for larger values of γ. Comparing to Fig. 3.15, we see that this positive correlation between γ and the position of the zero-crossing is already present in the input $J(q^2)$.

(*ii*) Since the L projections of Eqs. (6.14) and (6.17) involve different combinations of X_1 and X_3, and each of these involves various combinations of A_i and $F(q^2)$, in addition to $J(q^2)$ in the BC solution of Eq. (4.36), there is no reason to expect the crossings of $L^{\rm sym}(Q^2)$ and $L^{\rm asym}(q^2)$ to coincide with that of the kinetic term. In Table 6.1, we give exact values for the positions of the zero-crossings of $J(q^2)$, $L^{\rm sym}(Q^2)$ and $L^{\rm asym}(q^2)$ obtained in our calculations. Indeed, from this table we

γ	q_J [in MeV]	Q_L^{sym} [in MeV]	q_L^{asym} [in MeV]
0	140	109	180
0.1	166	128	204
0.2	187	143	221
0.3	202	155	237

Table 6.1: Comparison of the zero-crossing positions q_J, Q_L^{sym} and q_L^{asym}, of the input $J(q^2)$, the $L^{\text{sym}}(Q^2)$, and the $L^{\text{asym}}(q^2)$, respectively, for each value of γ.

see that the zero-crossings of these three functions are different, even for fixed γ. Specifically, the crossing of $L^{\text{sym}}(Q^2)$ is shifted by about 20% towards the IR with respect to that of $J(q^2)$, whereas the crossing of $L^{\text{asym}}(q^2)$ is shifted about 20% to the UV.

(*iii*) We also point out that the Gauge Technique and lattice results for $L^{\text{sym}}(Q^2)$, seen in Fig. 6.9, agree acceptably in spite of the fact that we have omitted the "transverse" form factors, $Y_i(Q^2)$, in Eq. (6.14). This observation provides *a posteriori* evidence that the transverse form factors are subleading in the IR.

7

Discussion and Conclusions

We performed a detailed analysis of the implementation of the Gauge Technique for the three-gluon vertex in the presence of dynamical gluon mass generation. We have demonstrated that a proper Gauge Technique construction, in this context, requires additional care to retain the longitudinality of the massless bound state vertex poles associated with gluon mass generation in the Schwinger mechanism. Since the presence of longitudinally coupled vertex poles was not entertained in the classical works [124, 126], a naive application of the BC solution with massive gluon propagators distorts the pole content of the vertex, causing the poles to spuriously survive transverse projections [4]. Nevertheless, we demonstrated that a proper account of the longitudinal nature of the vertex poles in the BC construction cures this issue entirely, furnishing results for the transversely projected three-gluon vertex that are free of poles, as they should.

The crucial step of the Gauge Technique with dynamically massive gluons is to split the original STI into two analogous equations, one governing the regular part of the vertex, and the other relating its pole content to the gluon dynamical mass [4]. The net effect of this construction is that in the BC solution for the regular part of the vertex the full gluon propagator should be substituted by its kinetic term only [4].

Beyond establishing the theoretical viability of the Gauge Technique construction in the presence of dynamical gluon mass, we have concretely evaluated the three-gluon vertex with modern nonperturbative ingredients for the ghost propagator, gluon kinetic term and ghost-gluon scattering kernel [3]. We observed satisfactory agreement, both qualitative and quantitative, to SDE [53, 59] and lattice [44, 45] results in the IR, while the perturbative behavior of the vertex is recovered for large momenta. In this respect, it is interesting to note that the effect of the ghost sector functions appearing in the Gauge

Technique solution for the three-gluon vertex amounts to quantitative corrections only, albeit relevant ones. Indeed, the Abelianized approximation of the vertex, where only the kinetic term of the gluon propagator is retained in the calculation, already captures the main features of the more complete result, although we emphasize that quantitative agreement requires the ghost sector to be taken into account [4].

Of particular importance for future works is the observed IR suppression of the three-gluon vertex with respect to its tree level [4, 7, 43–60]. We have demonstrated that the suppression of the nonperturbative vertex is much stronger than that of its one-loop counterpart. Moreover, we have shown that in the Gauge Technique this suppression is dominantly due to the kinetic term of the gluon propagator, which is itself suppressed in comparison to its respective tree level value.

Within this thesis, we have explored the effect of the three-gluon vertex suppression on the nonperturbative ghost-gluon scattering kernel. As shown in detail in Chapter 5, dressing the three-gluon vertex that appears in the SDE governing $H_{\nu\mu}$ tends to reduce the magnitude of the form factors of the ghost-gluon scattering kernel and vertex. Nevertheless, in our truncation of the $H_{\nu\mu}$ SDE we have modeled the three-gluon vertex dressing by retaining only its tree-level tensor structures and approximated the corresponding form factors by their Abelianized forms. Importantly, while it is natural to expect that the dominant effect of the three-gluon vertex is encoded into its tree-level tensor structures, the form factors that vanish at tree-level are found to be non-zero nonperturbatively. As such, considering only the tree-level tensor structure of the three-gluon vertex could overestimate the overall suppression, which may be partially compensated by the remaining form factors. Therefore, it would be instructive to explore the impact of the full tensor structure of the three-gluon vertex in the ghost-gluon interaction, which we would like to do in the near future.

Similarly, other studies [5, 6, 56, 57, 62, 63, 71] have investigated the impact of the three-gluon vertex suppression on various quantities of theoretical and phenomenological interest, such as gluon mass generation and gluonic bound states spectra, mostly also resorting to very simplified models of the three-gluon vertex. Given the importance of this effect in the recent literature, it would be interesting to reassess the implications of the three-gluon vertex suppression with more complete models. In this regard, our Gauge Technique results could provide useful input.

Another aspect to which we have devoted special attention is the survival of *some* IR divergences in QCD in spite of the IR finiteness of the gluon propagator. Specifically, the nonperturbative masslessness of the ghost field is known to imply [52] that loop integrals containing ghost propagators *can* be IR divergent. We have shown that some form factors of the ghost-gluon scattering kernel and of the three-gluon vertex exhibit IR divergences of precisely this origin. Moreover, we have distinguished these set of divergences from the mass-generating vertex poles, emphasizing that the divergence of some form factors of a given vertex does not necessarily imply the divergence of the vertex as whole. In particular, the $H_{\nu\mu}$ and the regular part of the three-gluon vertex, $\Gamma_{\alpha\mu\nu}$, are IR finite, in spite of containing IR divergent form factors, due to the momenta in their tensor structures vanishing in the limits where their form factors diverge.

As a consequence of the IR divergence of its form factors, the transversely projected three-gluon vertex displays a characteristic zero-crossing in the deep IR, which is shared by the kinetic term of the gluon propagator. The latter fact has important implications for the gluon propagator, namely, the divergence of its derivative at the origin, and the existence of a maximum in Euclidean space, with ensuing positivity violation [7, 52], as discussed in Section 3.5. Combined, these two properties can help reconstruct the gluon propagator in the complex plane [114].

Given that the gluon kinetic term encodes such critical information about the behavior of the gluon propagator, it is clearly deserving of more extensive studies. Yet, its SDE is extremely difficult to truncate and renormalize consistently, while lattice simulations can only access the full propagator, with no direct handle over its kinetic and dynamical mass components.

A rather enticing implication of this work is that our Gauge Technique construction may as well be "inverted"; instead of using the propagator functions to compute the three-gluon vertex, we could use the lattice results for the latter to determine the so-far elusive gluon kinetic term. Indeed, we have been exploring this possibility, with a groundwork study published [8] and a more extensive analysis recently submitted [9].

Now, our analysis has evidently been carried out under approximations and simplifications, whose impact should be addressed by further work.

To begin with, this study was carried out in the more strict context of pure Yang-Mills QCD, for simplicity, but dynamical quarks should eventually be included in the analysis in order to accurately describe the physical world. In this context, it is important to stress that although in this thesis we have derived the three-gluon vertex STI from the pure Yang-Mills Lagrangian, that relation remains formally identical in the presence of dynamical quarks [38, 39, 124, 126, 133]. As such, our analysis could be carried out without major modification in the "unquenched" context, *i.e.* with quarks. To that end, it would suffice to use as ingredients the correspondingly unquenched functions $J(q^2)$, $F(q^2)$ and $H_{\nu\mu}(q,p,r)$. The latter two are expected to be only mildly affected by unquenching effects [81], since ghosts do not couple directly to quarks. Consequently, we expect that the leading unquenching effect on the Gauge Technique three-gluon vertex should be encoded in the kinetic term of the gluon propagator, which is sensitive to the quark content of the calculation [33, 210]. In fact, in a recent study we have performed such a partial unquenching of the Gauge Technique three-gluon vertex, including quark effects on $J(q^2)$ only, and found satisfactory agreement to unquenched lattice results [7].

Another limitation of our approach lies in the fact that the $H_{\nu\mu}$ we have used as input for the Gauge Technique construction violates the STI constraint of Eq. (4.28), as a result of the truncation of its SDE [3], which implies that our numerical results for the three-gluon vertex only approximately satisfy the STI. It is important to emphasize, however, that the breaking of symmetry associated with the violation of Eq. (4.28) is not related to the presence of a gluon mass, but to the practical need to truncate the SDE. Indeed, similar violation of the STI constraint would be obtained in a massless solution of the SDE, under similar truncation, and, in fact, even in a perturbative calculation beyond one loop if the diagrammatic corrections associated with $(d_3)_{\nu\mu}$ were omitted, as we had to do in the present treatment. As such, we expect that this issue does not compromise the main conclusion of this work that the Gauge Technique vertex is consistent with dynamically generated gluon mass.

Yet, it would be interesting to develop a truncation of the SDE of $H_{\nu\mu}$ that satisfies Eq. (4.28). Such a truncation would require a more sophisticated Ansatz for the vertices that appear as inputs in the full SDE of Fig. 2.3. In particular, it would be necessary to account for the ghost-ghost-gluon-gluon vertex appearing in diagram $(d_3)_{\nu\mu}$ of that equation. Granted that the overall quantitative impact of this four-point function should be small [59, 205], its inclusion in some form is needed to preserve gauge symmetry. Perhaps, a Gauge Technique construction for that four-point function would be possible, on the lines of Ref. [211].

The most fundamental drawback of the Gauge Technique framework is that it leaves the transverse form factors undetermined. For the purpose of this work, whose main objective was to establish the adequacy of a Gauge Technique construction of the three-gluon vertex in the presence of dynamical gluon mass, this issue is a minor concern. Indeed, the uncertainty on the Y_i form factors only affects our analysis inasmuch as we need to compute certain linear combinations of X_i and Y_i to compare to the results obtained by different authors, using other tensor bases, and the lattice data, which is necessarily transversely projected in Landau gauge. In fact, if we could compare our results for the X_i *directly* to data obtained by other methods for these form factors, the indetermination of the Y_i in our analysis would not be a concern at all.

However, in application of our results to the evaluation of other quantities that depend on the three-gluon vertex, *e.g.* Green's functions obtained by SDEs and bound state problems treated by BSEs, the omission of the transverse form factors, Y_i, could be more problematic. Case in point, it is well known from QED studies [106, 108, 111] that the omission of the transverse part of the photon-fermion vertex in the fermion SDE frustrates the cancellation of certain divergences, fundamentally distorting the UV behavior of the resulting fermion propagator and compromising its multiplicative renormalizability [2, 25, 106, 108, 109, 111]. It is only natural to suspect that similar problems *could* arise in SDE treatments of functions involving the three-gluon vertex, such as the dynamical gluon mass equation [6, 212], if only the Gauge Technique vertex is used.

Hence, it is imperative that the transverse part of the vertex be studied in more depth, which can only be accomplished by using other techniques, such as SDEs [50, 53, 54, 59]. Indeed, we have an ongoing investigation on the subject whose results we hope to make public soon.

A

Feynman rules

In this appendix we collect the Feynman rules of pure Yang-Mills QCD, consistent with the conventions adopted throughout this thesis.

The tree-level gluon and ghost propagators are given in Table A.1. The Feynman rules for the vertices are given in Table A.2.

In addition to the expressions in Figs. A.1 and A.2 one must also account for: (*i*) a minus sign for closed ghost loops, due to their Fermi statistics [133, 213]; and (*ii*) the appropriate symmetry factors of diagrams that are unchanged by permuting internal lines [213].

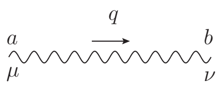	$\Delta^{(0)\,ab}_{\mu\nu}(q) = -i\delta^{ab}\left[\mathrm{P}_{\mu\nu}(q)\Delta^{(0)}(q^2) + \xi\frac{q_\mu q_\nu}{q^2}\right]$	$\Delta^{(0)}(q^2) = \frac{1}{q^2}$
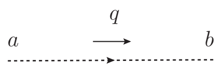	$D^{(0)}_{ab}(q) = i\delta_{ab}\frac{F^{(0)}(q^2)}{q^2}$	$F^{(0)}(q^2) = 1$

Figure A.1: Feynman rules for the tree-level gluon and ghost propagators.

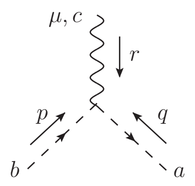	$-gf^{abc}\Gamma^{(0)}_{\mu}(q,p,r)$	$\Gamma^{(0)}_{\mu}(q,p,r) = q_{\mu}$
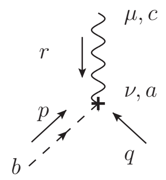	$-gf^{abc}H^{(0)}_{\nu\mu}(q,p,r)$	$H^{(0)}_{\nu\mu}(q,p,r) = g_{\nu\mu}$
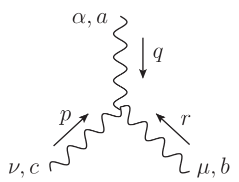	$gf^{abc}\Gamma^{(0)}_{\alpha\mu\nu}(q,r,p)$	$\Gamma^{(0)}_{\alpha\mu\nu}(q,r,p) = g_{\alpha\mu}(q-r)_{\nu} + g_{\mu\nu}(r-p)_{\alpha} + g_{\nu\alpha}(p-q)_{\mu}$
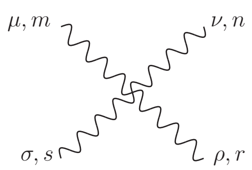	$\Gamma^{(0)\,mnrs}_{\mu\nu\rho\sigma}(q,r,p,t)$	$\Gamma^{(0)\,mnrs}_{\mu\nu\rho\sigma} = -ig^2[f^{mse}f^{ern}\,(g_{\mu\rho}g_{\nu\sigma} - g_{\mu\nu}g_{\rho\sigma}) + f^{mne}f^{esr}\,(g_{\mu\sigma}g_{\nu\rho} - g_{\mu\rho}g_{\nu\sigma}) + f^{mre}f^{esn}\,(g_{\mu\sigma}g_{\nu\rho} - g_{\mu\nu}g_{\rho\sigma})]$

Figure A.2: Feynman rules for the ghost-gluon, three-gluon and four-gluon vertices, as well as for the ghost-gluon scattering kernel at tree-level; we choose the convention in which all momenta are entering in the vertices. Note that at tree-level the four gluon vertex is momentum independent.

B

Some perturbative results

We collect here the one-loop results used throughout the text for the ghost-gluon scattering kernel and the three-gluon vertex. The calculations presented in this appendix were performed with the aid of *Package X* [214, 215].

All calculations have been carried out in Landau gauge, $\xi = 0$, using the Feynman rules of Appendix A. We employ dimensional regularization [161, 216] with $d = 4 - 2\epsilon$, and use the shorthand notation for the integral measure

$$\int_\ell := \frac{\mu^{2\epsilon}}{(2\pi)^d} \int \mathrm{d}^d \ell \,, \tag{B.1}$$

where μ is the 't Hooft mass, introduced in order to keep the coupling constant, g, dimensionless [161] for any d.

With the above conventions, the UV divergences that appear at one-loop are all proportional to

$$\frac{1}{\tilde{\epsilon}} := \frac{1}{\epsilon} - \gamma_{\mathrm{E}} + \ln(4\pi) \,, \tag{B.2}$$

where $\gamma_{\mathrm{E}} \approx 0.57722$ is the Euler-Mascheroni constant.

An integral that is ubiquitous in the one loop calculation of 3-point functions is

$$\varphi(q,p,r) := \frac{-i(4\pi)^{d/2}}{\eta} \int_\ell \frac{1}{(q+\ell)^2(p-\ell)^2\ell^2} \,, \tag{B.3}$$

where,

$$\eta := \frac{\Gamma^2(1-\epsilon)\Gamma(1+\epsilon)}{\Gamma(1-2\epsilon)} \,, \tag{B.4}$$

and $\Gamma(z)$ is the Euler function. The triangle integral of Eq. (B.3) is finite in four dimensions and attains a particularly simple closed form in the totally symmetric configuration, defined in Minkowski space by

$$\begin{aligned} q^2 &= p^2 = r^2 = Q^2 \,, \\ q \cdot p &= q \cdot r = p \cdot r = -\frac{Q^2}{2} \,. \end{aligned} \tag{B.5}$$

Specifically,

$$\lim_{q^2=p^2=r^2=Q^2} \varphi(q,p,r) := \varphi(Q^2) = \frac{\mathcal{I}}{Q^2} \,, \tag{B.6}$$

where

$$\mathcal{I} := \frac{1}{3}\left[\psi_1\left(\frac{1}{3}\right) - \psi_1\left(\frac{2}{3}\right)\right] \approx 2.34391 \,, \tag{B.7}$$

and $\psi_1(z)$ is the trigamma function, defined as

$$\psi_1(z) := \frac{d^2}{dz^2} \ln[\Gamma(z)] \,. \tag{B.8}$$

Notice that in Eq. (B.6) we simplify the functional dependence of scalar functions of three momenta to the single scale, Q, when we specialize to the symmetric configuration.

Finally, the results in this appendix are given in Minkowski metric. They can be transformed to Euclidean space using the rules of Appendix D.

The material in this Appendix is organized as follows. In Section B.1 we recall the one loop results for the ghost and gluon propagators. In Sections B.2 and B.3 we give one loop results for the ghost-gluon scattering kernel and the three-gluon vertex, respectively. In Section B.4 we discuss the renormalization of $H_{\nu\mu}(q,p,r)$ and $\Gamma_{\alpha\mu\nu}(q,r,p)$ consistent with the STI of Eq. (2.91). Lastly, in Section B.5 we extend the one loop calculation of $H_{\nu\mu}(q,p,r)$ to include a hard gluon mass as a regulator to study the IR divergences of its form factors.

B.1 Propagators

At one loop, the gluon propagator is given by the well-known form [133]

$$\Delta^{(1)\,ab}_{\mathrm{U}\;\mu\nu}(q) = -i\delta^{ab}\,\mathrm{P}_{\mu\nu}(q)\frac{1}{q^2 J^{(1)}_{\mathrm{U}}(q^2)} \,, \tag{B.9}$$

where we defined

$$\Delta^{(1)}_{\mathrm{U}}(q^2) = \frac{1}{q^2 J^{(1)}_{\mathrm{U}}(q^2)} \,, \tag{B.10}$$

and the unrenormalized $J_{\mathrm{U}}^{(1)}(q^2)$ is given by

$$J_{\mathrm{U}}^{(1)}(q^2) = 1 - \frac{\alpha_s C_{\mathrm{A}}}{144\pi} \left\{ 78 \left[\frac{1}{\tilde{\epsilon}} - \ln\left(-\frac{q^2}{\mu^2} \right) \right] + 97 \right\} , \tag{B.11}$$

with $C_{\mathrm{A}} = 3$ the Casimir eigenvalue in the adjoint representation. As for the ghost dressing function, we have [133]

$$F_{\mathrm{U}}^{(1)}(q^2) = 1 + \frac{\alpha_s C_{\mathrm{A}}}{16\pi} \left\{ 3 \left[\frac{1}{\tilde{\epsilon}} - \ln\left(-\frac{q^2}{\mu^2} \right) \right] + 4 \right\} . \tag{B.12}$$

Renormalizing Eqs. (B.9) and (B.12) in the MOM scheme of Eq. (2.92), the renormalization constants defined in Eq. (2.89), are found to be

$$\begin{aligned} Z_A &= 1 + \frac{\alpha_s C_{\mathrm{A}}}{144\pi} \left(\frac{78}{\tilde{\epsilon}} + 97 \right) , \\ Z_c &= 1 + \frac{\alpha_s C_{\mathrm{A}}}{16\pi} \left(\frac{3}{\tilde{\epsilon}} + 4 \right) . \end{aligned} \tag{B.13}$$

Hence, the renormalized $J^{(1)}(q^2)$ and $F^{(1)}(q^2)$ reduce to

$$J^{(1)}(q^2) = 1 + \frac{13\alpha_s C_{\mathrm{A}}}{24\pi} \ln\left(-\frac{q^2}{\mu^2} \right) , \tag{B.14}$$

$$F^{(1)}(q^2) = 1 - \frac{3\alpha_s C_{\mathrm{A}}}{16\pi} \ln\left(-\frac{q^2}{\mu^2} \right) . \tag{B.15}$$

B.2 Ghost-gluon scattering kernel

The Feynman diagrams for the ghost-gluon scattering kernel are shown in Fig. B.1, where it is understood that the color factor $-gf^{abc}$ is extracted.

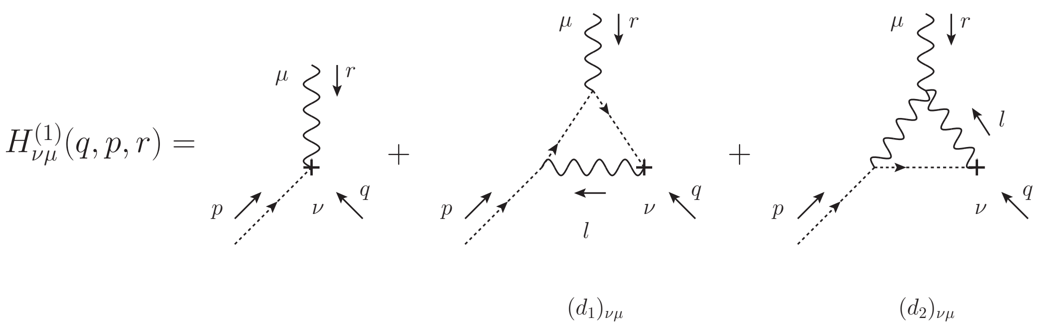

Figure B.1: Feynman diagrams for the ghost-gluon scattering kernel at one loop.

The results for the ghost-gluon scattering kernel are all found to be UV finite, in agreement with the Taylor theorem [39] (see Section 5.1.2). To avoid too much repetition, we show here the results renormalized up to a choice of the finite part of the renormalization constant (see Sections 2.5 and B.4 for more details on this freedom). Evidently, at order g^2 the multiplication of the renormalization constant Z_1 with the unrenormalized $H_{\nu\mu}(q,p,r)$ only yields contributions to the part that was nonzero at tree level. As such, we write Z_1 multiplying only the tree level term.

Below, we present results for four kinematics configurations, recalling that the most general Lorentz structure of $H_{\nu\mu}(q,p,r)$ is given in Eq. (4.24).

1. *Soft ghost limit:* This kinematic configuration is defined by setting the momentum of the ghost to $p=0$, which implies, by momentum conservation, $r=-q$. The tensorial decomposition of $H_{\nu\mu}(q,p,r)$ of Eq. (4.24) in this case collapses to

$$H^{(1)}_{\nu\mu}(q,0,-q) = A^{(1)}_1\, g_{\mu\nu} + [A^{(1)}_2 + A^{(1)}_3 - A^{(1)}_4 - A^{(1)}_5]\, q_\mu q_\nu \,, \tag{B.16}$$

   where we omitted the functional dependence of the form factors on the remaining momentum to make Eq. (B.16) compact.

   In this kinematic limit, due to the Taylor theorem (see Section 5.1.2) the unrenormalized ghost-gluon scattering kernel reduces to tree level. Then, the form factors are necessarily given by [*cf.* Eq. (5.14)]

$$\begin{aligned} &A^{(1)}_1(q,0,-q) = Z_1\,; \\ &A^{(1)}_2(q,0,-q) + A^{(1)}_3(q,0,-q) - A^{(1)}_4(q,0,-q) - A^{(1)}_5(q,0,-q) = 0\,; \end{aligned} \tag{B.17}$$

   with Z_1 finite in Landau gauge and defined in Eq. (2.90).

2. *Soft anti-ghost limit:* This limit is defined by letting the anti-ghost momentum vanish, *i.e.* $q=0$. In this case, the tensorial structure of $H^{(1)}_{\nu\mu}(q,p,r)$ becomes

$$H^{(1)}_{\nu\mu}(0,-r,r) = A^{(1)}_1(0,-r,r)\, g_{\mu\nu} + A^{(1)}_3(0,-r,r)\, r_\mu r_\nu \,, \tag{B.18}$$

   with the two surviving form factors given by

$$A^{(1)}_1(0,-r,r) = Z_1 + \frac{11\alpha_s C_{\rm A}}{32\pi}\,; \qquad A^{(1)}_3(0,-r,r) = -\frac{11\alpha_s C_{\rm A}}{32\pi r^2}\,. \tag{B.19}$$

3. *Soft gluon limit:* This kinematic configuration is defined by $r = 0$, *i.e.* vanishing gluon momentum. In this limit the tensorial structure of $H_{\nu\mu}(q,p,r)$ reduces to

$$H^{(1)}_{\nu\mu}(q,-q,0) = A^{(1)}_1(q,-q,0)g_{\mu\nu} + A^{(1)}_2(q,-q,0)q_\mu q_\nu\,, \tag{B.20}$$

and the form factors attain the forms

$$A^{(1)}_1(q,-q,0) = Z_1\,; \qquad A^{(1)}_2(q,-q,0) = \frac{3\alpha_s C_\mathrm{A}}{16\pi q^2}\,. \tag{B.21}$$

Curiously, the result for $A^{(1)}_1(q,-q,0)$ in Eq. (B.21) differs from its tree-level value, $A^{(0)}_1(q,-q,0) = 1$, only by the finite renormalization. Thus, its urenormalized value, $A^{(1)}_{1\,\mathrm{U}}(q,-q,0) = 1$, is just its tree level value. We emphasize that this result is *not* an example of the Taylor theorem, which applies to the *soft ghost*, *i.e.* $p = 0$, configuration, and holds to all orders (see Section 5.1.2). Instead, the fact that the one-loop *soft gluon* result is $A^{(1)}_{1\,\mathrm{U}}(q,-q,0) = 1$ may be a casual coincidence. At this level, the contributions of diagrams $(d_1)_{\nu\mu}$ and $(d_2)_{\nu\mu}$ of Fig. B.1 to the form factor A_1 happen to cancel in the soft gluon configuration. This cancellation seems to occur only because the gluon propagator scalar function, $\Delta(q^2)$, and the ghost propagator, $D(q)$, differ only by a $-i$ at tree level, *i.e.* $\Delta^{(0)}(q^2) = -iD^{(0)}(q)$, and would be easily spoiled by further dressing the vertices or the propagators.

4. *Symmetric configuration:* In the totally symmetric configuration, defined in the Eq. (B.5), all tensor structures of the ghost-gluon scattering kernel survive, and the form factors A_i are given by

$$\begin{aligned}
A^{(1)}_1(Q^2) =& Z_1 + \frac{\alpha_s C_\mathrm{A}}{96\pi}\left(9+\mathcal{I}\right)\,, & A^{(1)}_2(Q^2) &= \frac{\alpha_s C_\mathrm{A}}{48\pi Q^2}\left(4+\mathcal{I}\right)\,,\\
A^{(1)}_3(Q^2) =& -\frac{\alpha_s C_\mathrm{A}}{96\pi Q^2}\left(4+9\,\mathcal{I}\right)\,, & A^{(1)}_4(Q^2) &= -\frac{\alpha_s C_\mathrm{A}}{48\pi Q^2}\left(1+2\,\mathcal{I}\right)\,,\\
A^{(1)}_5(Q^2) =& \frac{\alpha_s C_\mathrm{A}}{48\pi Q^2}\left(2-\mathcal{I}\right)\,,
\end{aligned} \tag{B.22}$$

with $\mathcal{I}$ the constant defined in Eq. (B.7).

B.3 Three-gluon vertex

For the three-gluon vertex at one loop the Feynman diagrams are given in Fig. B.2. Notice that diagrams $(e_2)_{\alpha\mu\nu}$ and $(e_3)_{\alpha\mu\nu}$ contain closed loops of ghosts, which lead to a minus sign from the Fermi statistics of these fields. Moreover, the swordfish diagrams, $(e_4)_{\alpha\mu\nu}$, $(e_5)_{\alpha\mu\nu}$ and $(e_6)_{\alpha\mu\nu}$, have a symmetry factor of 1/2, since, for each of these, the two internal lines can be exchanged without changing the content of the diagram.

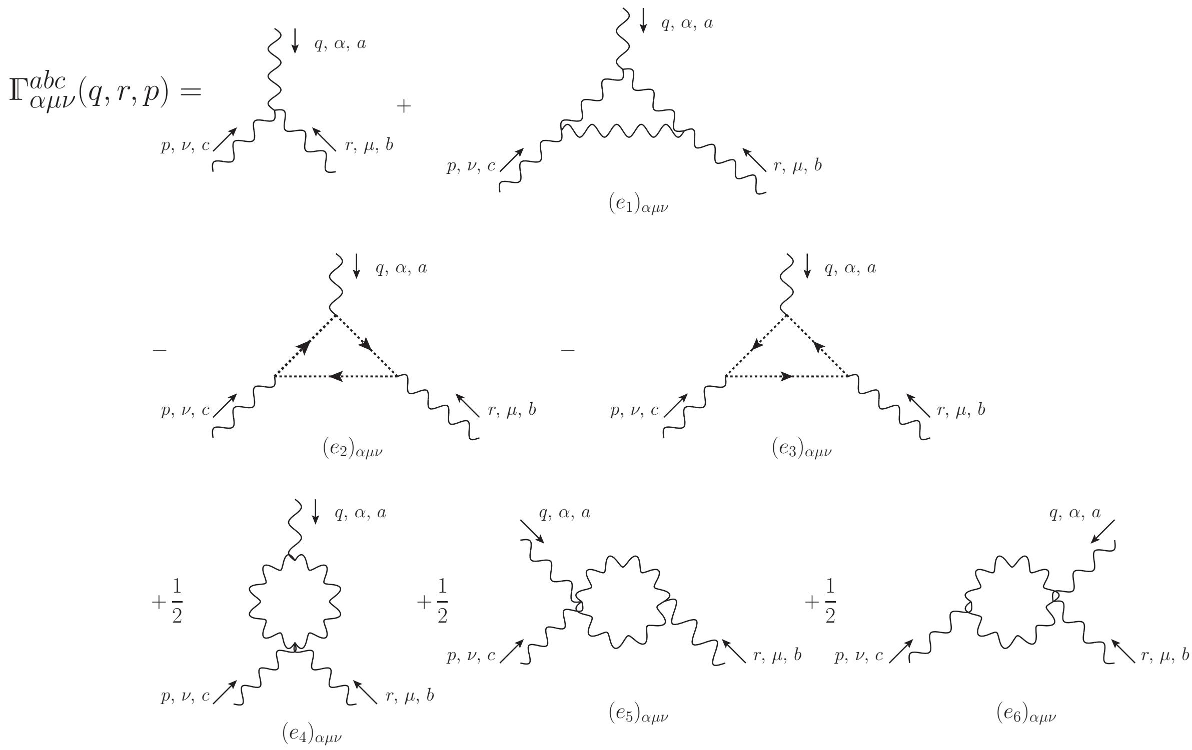

Figure B.2: Feynman diagrams for the three-gluon vertex at one loop.

In each of the kinematic configurations that we considered, the tensor structure of the three-gluon vertex collapses to only a few independent tensors, instead of the 14 of Eqs. (4.30) and (4.32). Consequently, some form factors appear in linear combinations, making it impossible to determine the individual X_i and Y_j from the final, collapsed, expressions. Instead, to compute the individual form factors, they must first be separated from the general kinematics result, and the desired kinematic limit be taken only as the last step of the calculation. This procedure is facilitated by using the projectors of Section C.2.

Unlike the ghost-gluon scattering kernel, $\Gamma_{\alpha\mu\nu}(q,p,r)$ is found to be UV divergent in Landau gauge. Importantly, in our one loop calculations we only find such divergences in the form factors that are non-zero at tree-level, namely X_1, X_4 and X_7 [see Eq. (4.33)]. This had to be the case, since the other form factors cannot pick-up a renormalization at order g^2. Thus the finiteness of the non-tree-level form factors constitutes a sanity check on our results.

We consider four kinematic limits and, again, we give the results renormalized, up to a choice of the finite part of the renormalization constant.

1. *Symmetric configuration:* In the kinematic limit of Eq. (B.5) the tensor structure of the three-gluon vertex collapses to [139, 208]

$$\begin{aligned}\Gamma_{\alpha\mu\nu}(q,r,p) &= L^{\text{sym}}(Q^2)\Gamma^{(0)}_{\alpha\mu\nu}(q,r,p) \\ &- \left[X_3(Q^2) + \frac{Q^2}{2}Y_1(Q^2)\right](r-p)_\alpha(p-q)_\mu(q-r)_\nu \\ &+ \left[X_3(Q^2) + \frac{Q^2}{2}Y_1(Q^2) + Y_4(Q^2)\right](q_\nu r_\alpha p_\mu - q_\mu r_\nu p_\alpha)\,.\end{aligned} \tag{B.23}$$

with

$$L^{\text{sym}}(Q^2) = X_1(Q^2) + \frac{Q^2}{2}X_3(Q^2) + \frac{Q^4}{4}Y_4(Q^2) + \frac{Q^2}{2}Y_4(Q^2)\,. \tag{B.24}$$

Then, the one loop results for the form factors are

$$\begin{aligned}X_1^{(1)}(Q^2) &= Z_3^{\text{fin}} + \frac{\alpha_s C_{\text{A}}}{144\pi}\left[51\ln\left(-\frac{Q^2}{\mu^2}\right) - 52 - 9\mathcal{I}\right], \quad & X_2^{(1)}(Q^2) &= 0\,, \\ X_3^{(1)}(Q^2) &= \frac{\alpha_s C_{\text{A}}}{48\pi Q^2}(38 - 7\mathcal{I})\,, & X_{10}^{(1)}(Q^2) &= 0\,, \\ Y_1^{(1)}(Q^2) &= -\frac{\alpha_s C_{\text{A}}}{432\pi Q^4}(587 - 193\mathcal{I})\,, & Y_4^{(1)}(Q^2) &= \frac{\alpha_s C_{\text{A}}}{864\pi Q^2}(365 + 179\mathcal{I})\,,\end{aligned} \tag{B.25}$$

with $\mathcal{I}$ defined in Eq. (B.7) and Z_3^{fin} the finite part of the three-gluon vertex renormalization constant, Z_3, defined by

$$Z_3^{\text{fin}} := Z_3 - \frac{17\alpha_s C_{\text{A}}}{48\pi\,\widetilde{\epsilon}}\,. \tag{B.26}$$

The remaining form factors are all obtained from the above by Bose symmetry using Eq. (4.34).

Notice that the vanishing of the form factors X_2 and X_{10} in the symmetric configuration is required by them being anti-symmetric under the exchange of $q \leftrightarrow r$ [see Eq. (4.35)].

2. *Asymmetric configuration:* The asymmetric configuration is defined by setting one of the gluon momenta to zero, specifically we choose $p = 0$. By Bose symmetry, similar results, with permuted arguments, would be obtained if we chose a different leg to carry zero momentum. The tensor structure of the three-gluon vertex in this kinematics reduces to [208]

$$\begin{aligned}\Gamma_{\alpha\mu\nu}(q,-q,0) &= 2g_{\alpha\mu}q_\nu[X_1(q,-q,0)+q^2X_3(q,-q,0)] - 2q_\alpha q_\mu q_\nu X_3(q,-q,0)\\ &\quad -(q_\alpha g_{\mu\nu}+q_\mu g_{\alpha\nu})[X_1(0,q,-q)-X_2(0,q,-q)]\,. \end{aligned} \tag{B.27}$$

Then, at one-loop the surviving form factors read

$$\begin{aligned} X_1^{(1)}(q,-q,0) &= Z_3^{\text{fin}} + \frac{\alpha_s C_{\text{A}}}{144\pi}\left[51\ln\left(-\frac{q^2}{\mu^2}\right)-61\right],\\ X_3^{(1)}(q,-q,0) &= \frac{37\alpha_s C_{\text{A}}}{96\pi q^2},\\ X_1^{(1)}(0,q,-q) - X_2^{(1)}(0,q,-q) &= X_1^{(1)}(q,-q,0)\,. \end{aligned} \tag{B.28}$$

Individually, the terms $X_1^{(1)}(0,q,-q)$ and $X_2^{(1)}(0,q,-q)$ both have a ln(0) IR divergence in this kinematics. Nevertheless, their difference is finite.

3. *General orthogonal configuration:* In this configuration, the momenta q and r have independent magnitudes, q^2 and r^2, but are set to be orthogonal, *i.e.* $q \cdot r = 0$. Consequently, by momentum conservation $p^2 = q^2 + r^2$. For this kinematic limit we have computed only the form factor X_1, which is given by

$$\begin{aligned} X_1(q^2,r^2,\pi/2) =& Z_3^{\text{fin}} + \frac{\alpha_s C_{\text{A}}}{2304\pi q^2 r^2}\Bigg\{6\left(9q^4+128q^2r^2+3r^4\right)\ln\left(-\frac{q^2}{\mu^2}\right)\\ &+6\left(3q^4+128q^2r^2+9r^4\right)\ln\left(-\frac{r^2}{\mu^2}\right) - 72\left(q^4+10q^2r^2+r^4\right)\ln\left(\frac{-q^2-r^2}{\mu^2}\right)\\ &-9i\frac{(q^2+r^2)}{\sqrt{q^2r^2}}\left(q^2-r^2\right)^2\left[\text{Li}_2\left(-z\right)-\text{Li}_2\left(z\right)+\text{Li}_2\left(z^{-1}\right)-\text{Li}_2\left(-z^{-1}\right)\right]\\ &-4(9q^4+172q^2r^2+9r^4)\Bigg\}, \end{aligned} \tag{B.29}$$

with $z = \left(\sqrt{-q^2} - i\sqrt{-r^2}\right) / \left(\sqrt{-q^2} + i\sqrt{-r^2}\right)$, and

$$\mathrm{Li}_2(z) = -\int_0^z \frac{\ln(1-t)}{t} dt\,, \tag{B.30}$$

the dilogarithm (or Spence function). Notice that the above expression is symmetric under the exchange $q^2 \leftrightarrow r^2$, as it should be from Bose-symmetry [see Eq. (4.35)].

4. *Orthogonal symmetric configuration:*

   In the special case of Eq. (B.29) with $q^2 = r^2$, we obtain

$$X_1(q^2, q^2, \pi/2) = Z_3^{\mathrm{fin}} + \frac{\alpha_s C_{\mathrm{A}}}{288\pi}\left[102\ln\left(-\frac{q^2}{\mu^2}\right) - 108\ln(2) - 95\right]. \tag{B.31}$$

Combining the above results with those of Sections B.1 and B.2, we can then check that the BC solution of Eq. (4.36) for the STI is satisfied in the special case of the X_1 form factor in the symmetric configuration, as long as the renormalization constants Z_1 and Z_3 satisfy Eq. (2.91). Specifically, in this limit Eq. (4.36) reduces to

$$X_1(Q^2) = F(Q^2)J(Q^2)\left[A_1(Q^2) + Q^2 A_3(Q^2) - \frac{Q^2}{2}A_4(Q^2)\right], \tag{B.32}$$

which can be promptly verified to order α_s from our results. More extensive checks of the STI, which confirm the correctness of our results, have been carried out, but are not detailed here.

Finally, we compared our results to those of Refs. [139, 208] and found them to agree after taking into account the differences in conventions.

B.4 Consistent renormalization schemes

As discussed in Section 2.5, we have the freedom to choose the finite part of one more renormalization constant, *i.e.* either Z_1 or Z_3^{fin}, but not both, since Eq. (2.91) must be satisfied. We now discuss a few possible choices of renormalization schemes and their consistency with Eq. (2.91).

Given that the ghost-gluon scattering kernel is UV finite in Landau gauge, we may simply choose to set $Z_1 = 1$. This choice amounts to the so-called Taylor scheme (see Section 5.1.3), and in this case the form factor $A_1(q,p,r)$ reduces to tree level to all orders in the soft ghost kinematics, $p = 0$. With this choice, we impose that Eq. (2.91) is satisfied to determine Z_3, using Eq. (B.13). Thus, we obtain

$$Z_3 = 1 + \frac{\alpha_s C_{\rm A}}{144\pi}\left(\frac{51}{\widetilde{\epsilon}} + 61\right) \,, \tag{B.33}$$

such that Eq. (B.26) yields

$$Z_3^{\rm fin} = 1 + \frac{61\alpha_s C_{\rm A}}{144\pi} \,. \tag{B.34}$$

Alternatively, one may choose to define $Z_3^{\rm fin}$ by requiring that the form factor $X_1(q, r, p)$ reduces to its tree level, $X_1^{(0)}(q, r, p) = 1$, at some desired kinematic limit. For example, we can choose the totally symmetric configuration $X_1^{(1)}(Q^2)$ of Eq. (B.25) to reduce to tree level at the Euclidean momentum $Q^2 = -\mu^2$. We will call this choice the X_1-*symmetric scheme* and denote the corresponding renormalization constants by a caret. In this case,

$$\hat{Z}_3^{\rm fin} = 1 + \frac{\alpha_s C_{\rm A}}{144\pi}\left(52 + 9\,\mathcal{I}\right) \,, \tag{B.35}$$

such that

$$\hat{Z}_3 = 1 + \frac{\alpha_s C_{\rm A}}{144\pi}\left(\frac{51}{\widetilde{\epsilon}} + 52 + 9\,\mathcal{I}\right) \,. \tag{B.36}$$

Then, using Eq. (2.91) one finds

$$\hat{Z}_1 = 1 + \frac{\alpha_s C_{\rm A}}{16\pi}\left(\mathcal{I} - 1\right) \,, \tag{B.37}$$

which is different from the Taylor scheme value of $Z_1 = 1$.

The fact that the Eq. (2.91) leads to $\hat{Z}_1 \neq Z_1$ shows that we could not have chosen them independently, as explained in Section 2.5. Let us consider one more case.

One might as well have chosen to define the value of Z_1 by requiring that the ghost-gluon scattering kernel form factor A_1 in the totally symmetric configuration, $A_1(Q^2)$, of Eq. (B.22), reduces to tree level at the Euclidean point $Q^2 = -\mu^2$, *i.e.* $A_1(-\mu^2) = 1$. Let us call this choice the A_1-*symmetric scheme* and use a tilde to denote its corresponding renormalization constants. In this case one obtains

$$\widetilde{Z}_1 = 1 - \frac{\alpha_s C_{\rm A}}{96\pi}\left(9 + \mathcal{I}\right) \,, \tag{B.38}$$

Table B.1: Comparison of numerical values of the form factors of $H_{\nu\mu}$ and $\Gamma_{\alpha\mu\nu}$ that exist at tree level, in different renormalization schemes, namely: (*i*) The Taylor scheme, where A_1 is set to tree level in the soft ghost kinematics; (*ii*) The A_1-symmetric scheme; and (*iii*) the X_1-symmetric scheme. We used $\alpha_s = 0.22$ for this example.

Scheme	$A_1(\mu, 0, -\mu)$	$A_1(\mu^2)$	$X_1(\mu^2)$
Taylor	1	1.025	0.982
A_1-Symmetric	0.975	1	0.958
X_1-Symmetric	1.018	1.042	1

Using Eqs. (B.38) and (B.13) into Eq. (2.91) yields

$$\widetilde{Z}_3 = 1 + \frac{\alpha_s C_{\rm A}}{288\pi}\left(\frac{102}{\widetilde{\epsilon}} + 95 - 3\,\mathcal{I}\right)\,, \qquad \widetilde{Z}_3^{\rm fin} = 1 + \frac{\alpha_s C_{\rm A}}{288\pi}\left(95 - 3\,\mathcal{I}\right)\,. \tag{B.39}$$

Clearly, $\widetilde{Z}_1$ is different from both, Z_1 and $\hat{Z}_1$.

Finally, the different choices of renormalization scheme discussed in this section lead to slightly different numerical values for those form factors of $H_{\nu\mu}(q,p,r)$ and $\Gamma_{\alpha\mu\nu}(q,r,p)$ that exist at tree level. We illustrate this effect in Table B.1, where it is shown the value of the form factors $A_1(q,p,r)$ and $X_1(q,r,p)$ in different configurations, as computed in each of the renormalization schemes above. Evidently, the numerical value of these form factors in different renormalization schemes depends on the value α_s. For constructing Table B.1 we used the value $\alpha_s = 0.22$, which is used throughout the main text. Notice then, from Table B.1, that the different choices of renormalization scheme lead to variations of a few percent in the numerical values of the form factors.

B.5 One loop massive results

Although a hard mass term in the Lagrangian breaks the gauge symmetry of the theory, we can often gain a better understanding of the *qualitative* behavior of the Green's functions of QCD from one loop calculations with a massive gluon propagator. For the special case of the ghost-gluon scattering kernel, we can see from the results of Section B.2 that the form factors A_i, for $i = 2, \ldots, 5$, all diverge as poles in the limit when all momenta tend to zero. In the presence of an IR finite gluon propagator, it is expected that these divergences would be attenuated, or even eliminated.

We now study the IR divergences of the A_i in the presence of an IR finite gluon propagator. To this end, we repeat the calculations of Section B.2 using the hard mass gluon propagator, which, in Landau gauge reads

$$\Delta^{(1\mathrm{M})}_{\mu\nu}(q) = -i\,\mathrm{P}_{\mu\nu}(q)\Delta^{(1\mathrm{M})}(q^2)\,, \tag{B.40}$$

with

$$\Delta^{(1\mathrm{M})}(q^2) = \frac{1}{q^2-m^2}\,, \tag{B.41}$$

The soft ghost configuration still retains the values in Eq. (B.17). We consider then the other configurations presented in Section B.2.

1. *Soft anti-ghost limit:* In the $q=0$ kinematics, we obtain

$$\begin{aligned}
A_1^{(1\mathrm{M})}(0,-r,r) =& Z_1 - \frac{C_\mathrm{A}\alpha_s}{192\pi m^6 r^4}\Bigg\{ -2m^8r^2 - 23m^6r^4 \\
&- r^6\left(2m^4+6m^2r^2+r^4\right)\ln\left(-\frac{r^2}{m^2}\right) \\
&+ (r^8+6m^2r^6-40m^4r^4)\sqrt{r^4-4m^2r^2}\,\ln\left[\frac{\left(\sqrt{r^4-4m^2r^2}+r^2\right)}{2m^2}+1\right] \\
&+ 2\left(m^2-r^2\right)^2\left(m^6+13m^4r^2-7m^2r^4-r^6\right)\ln\left(\frac{m^2}{m^2-r^2}\right)\Bigg\}\,, \\
A_3^{(1\mathrm{M})}(0,-r,r) =& \frac{C_\mathrm{A}\alpha_s}{192\pi m^6 r^6}\Bigg\{ -20m^6r^4 - 6m^4r^6 - r^6\left(8m^4+r^4\right)\ln\left(-\frac{r^2}{m^2}\right) \\
&+ (r^8+6m^2r^6-40m^4r^4)\sqrt{r^4-4m^2r^2}\,\ln\left[\frac{\left(\sqrt{r^4-4m^2r^2}-r^2\right)}{2m^2}+1\right] \\
&- 8m^8r^2 + 2\left(m^2-r^2\right)^2\left(4m^6+16m^4r^2-4m^2r^4-r^6\right)\ln\left(\frac{m^2}{m^2-r^2}\right)\Bigg\}\,.
\end{aligned} \tag{B.42}$$

Taking the $m\to 0$ limit of the above expressions we recover the one-loop result of Eq. (B.19). On the other hand, in the limit $r^2\to 0$, Eq. (B.42) leads to

$$\begin{aligned}
\lim_{r^2\to 0} A_1^{(1\mathrm{M})}(0,-r,r) =& Z_1\,, \\
\lim_{r^2\to 0} A_3^{(1\mathrm{M})}(0,-r,r) =& -\frac{C_\mathrm{A}\alpha_s}{288\pi m^2}\left[12\ln\left(-\frac{r^2}{m^2}\right)-31\right]\,.
\end{aligned} \tag{B.43}$$

Then, in the presence of a massive gluon propagator, $A_1^{(1\mathrm{M})}$ is infrared finite, whereas $A_3^{(1\mathrm{M})}$ has a logarithmic IR divergence.

2. *Soft gluon limit:* In the $r = 0$ limit, the one loop massive result is

$$\begin{aligned}A_1^{(1M)}(q,-q,0) =& Z_1 - \frac{\alpha_s C_A}{192\pi m^4 q^4}\left[(10m^8 - 8m^6q^2)\ln\left(\frac{m^2}{m^2-q^2}\right) - 10m^6q^2 + \right.\\ & \left. 3m^4q^4 - 2m^2q^6 - (4m^2q^6 + 2q^8)\ln\left(-\frac{q^2}{m^2-q^2}\right)\right],\\ A_2^{(1M)}(q,-q,0) =& \frac{\alpha_s C_A}{96\pi m^4 q^6}\left[-20m^6q^2 + 15m^4q^4 + q^6\left(4q^2+m^2\right)\ln\left(-\frac{q^2}{m^2}\right)\right.\\ & \left. + \left(20m^8 - 25m^6q^2 + m^2q^6 + 4q^8\right)\ln\left(\frac{m^2}{m^2-q^2}\right) - 4m^2q^6\right].\end{aligned} \tag{B.44}$$

In the $m \to 0$ limit of Eq. (B.44), one recovers the one-loop results of Eq. (B.21). On the other hand, in the limit $q^2 \to 0$, Eq. (B.44) yields

$$\begin{aligned}\lim_{q^2\to 0} A_1^{(1M)}(q,-q,0) =& Z_1\,,\\ \lim_{q^2\to 0} A_2^{(1M)}(q,-q,0) =& \frac{\alpha_s C_A}{576\pi m^2}\left[6\ln\left(-\frac{q^2}{m^2}\right) - 59\right].\end{aligned} \tag{B.45}$$

Therefore, in the presence of a massive gluon propagator, $A_2^{(1M)}$ has a logarithmic IR divergence.

3. *Symmetric configuration:* In the symmetric limit of Eq. (B.5) the expressions for the form factors for general Q^2 and m^2 are rather long and we choose to not report them here. Instead, we give the $Q^2 \to 0$ limit only,

$$\begin{aligned}\lim_{Q^2\to 0} A_1^{(1M)}(Q^2) =& Z_1\,,\\ \lim_{Q^2\to 0} A_2^{(1M)}(Q^2) =& \frac{C_A\alpha_s}{576\pi m^2}\left[6\ln\left(-\frac{Q^2}{m^2}\right) - 65\right],\\ \lim_{Q^2\to 0} A_3^{(1M)}(Q^2) =& -\frac{C_A\alpha_s}{144\pi m^2}\left[6\ln\left(-\frac{Q^2}{m^2}\right) - 23 + 3\mathcal{I}\right],\\ \lim_{Q^2\to 0} A_4^{(1M)}(Q^2) =& \frac{C_A\alpha_s}{48\pi m^2}\,,\\ \lim_{Q^2\to 0} A_5^{(1M)}(Q^2) =& -\frac{C_A\alpha_s}{192\pi m^2}\left[6\ln\left(-\frac{Q^2}{m^2}\right) - 1 + 4\mathcal{I}\right].\end{aligned} \tag{B.46}$$

The above results for $A_1^{(1M)}$ and $A_4^{(1M)}$ are IR finite, whereas the $A_2^{(1M)}$, $A_3^{(1M)}$ and $A_5^{(1M)}$ are logarithmically divergent.

Comparing the above one loop massive results with the expressions of Section B.2, obtained with massless gluons, we conclude that the introduction of a gluon mass reduces the degree of IR divergence of the form factors A_i, for $i = 2, 3$ and 5, from poles to logarithms, while A_4 becomes altogether finite in the massive one loop result, and A_1 is IR finite in both cases.

Furthermore, we have verified that all the IR divergences found in the one loop massive $H^{(1\mathrm{M})}_{\nu\mu}(q,p,r)$ originate from the diagram $(d_1)_{\nu\mu}$ of Fig. B.1, *i.e.* the triangle with two internal ghost lines. Indeed, the diagram $(d_2)_{\nu\mu}$ turns out IR finite contributions to all five A_i in the presence of a gluon mass. On the other hand, $(d_1)_{\nu\mu}$ contains only one internal massive propagator. Consequently, although the degree of IR divergence of $(d_1)_{\nu\mu}$ is reduced from pole to logarithmic, with respect to the result with massless gluons, some divergences persist due to the masslessness of the ghosts. Our finds are in perfect agreement with the discussion in Section 3.4.

Another qualitative feature we would like to emphasize is that in the massive gluon results the form factor A_1 reduces to tree level (up to the finite renormalization) when all momenta are set to zero, as can be seen from Eqs. (B.43), (B.45) and (B.46). In contrast, with a massless gluon propagator, the value of $A_1(0,0,0)$ depends on the configuration from which the limit is approached [cf. Eqs. (B.17), (B.19), (B.21) and (B.22)]. This behavior can be understood from the factorization of the ghost momentum demonstrated in Section 5.1.2, which leads to the Taylor theorem. This factorization implies

$$A_1(q,p,r) = Z_1 + p^\rho\,\mathfrak{I}_\rho(q,p,r)\,, \tag{B.47}$$

where $\mathfrak{I}_\rho(q,p,r)$ is some loop integral. For a massless gluon, $\mathfrak{I}_\rho(q,p,r)$ happens to develop a pole in $1/p$, when all momenta tend to zero, and Eq. (B.47) yields a finite, but path dependent value. On the other hand, in the presence of a gluon mass, $\mathfrak{I}_\rho(q,p,r)$ diverges only logarithmically as all momenta tend to zero, such that $p^\rho\,\mathfrak{I}_\rho(q,p,r) \to 0$ as $p \to 0$, independently of the path. Alternatively, it is clear from Eq. (B.47), that if $\mathfrak{I}_\rho(q,p,r)$ has a pole in $1/p$ when all momenta vanish, then the derivative of A_1 with respect to p is divergent. On the other hand, in the presence of a gluon mass this derivative becomes IR finite.

Lastly, we point out that the soft gluon kinematics $A_1^{(1\mathrm{M})}(q,-q,0)$ no longer reduces to tree level in the presence of a gluon mass [cf. Eqs. (B.44) and (B.21)], except at $q = 0$, as the cancellation between $(d_1)_{\nu\mu}$ and $(d_2)_{\nu\mu}$, discussed below Eq. (B.21) is spoiled. In contrast, the Taylor theorem still holds in the massive case, since it is a consequence of the Landau gauge gluon transversality alone (see Section 5.1.2), not depending on a cancellation between the diagrams contributing to $H_{\nu\mu}$.

C

Projectors

For some calculations it is convenient to have explicit algebraic projectors that extract the form factors of vertex functions. In this appendix we present the projectors that isolate the form factors of the ghost-gluon scattering kernel and the three-gluon vertex from the general tensorial structures of $H_{\nu\mu}(q,p,r)$ and $\Gamma_{\alpha\mu\nu}(q,r,p)$, respectively.

We express the equations in this appendix in Minkowski space.

C.1 Ghost-gluon scattering kernel form factors

The form factors A_i, for $i = 1, \ldots, 5$, of the ghost-gluon scattering kernel may be extracted from the general Lorentz decomposition of $H_{\nu\mu}(q,p,r)$ given in Eq. (4.24) through the projections [3]

$$A_i(q,p,r) = \frac{\mathcal{T}_i^{\mu\nu}(q,r)H_{\nu\mu}(q,p,r)}{2h^2(q,r)}\,, \tag{C.1}$$

where

$$\begin{aligned}
\mathcal{T}_1^{\mu\nu}(q,r) =& h(q,r)\left[h(q,r)g^{\mu\nu} + h^{\mu\nu}(q,r)\right]\,,\\
\mathcal{T}_2^{\mu\nu}(q,r) =& -h(q,r)r^2 g^{\mu\nu} - 2h(q,r)r^\mu r^\nu - 3r^2 h^{\mu\nu}(q,r)\,,\\
\mathcal{T}_3^{\mu\nu}(q,r) =& \mathcal{T}_2^{\mu\nu}(r,q)\,,\\
\mathcal{T}_4^{\mu\nu}(q,r) =& h(q,r)(r\cdot q)g^{\mu\nu} + 2h(q,r)q^\mu r^\nu + 3(r\cdot q)h^{\mu\nu}(q,r)\,,\\
\mathcal{T}_5^{\mu\nu}(q,r) =& \mathcal{T}_4^{\mu\nu}(r,q)\,,
\end{aligned} \tag{C.2}$$

and

$$h(q,r) = q^2r^2 - (q\cdot r)^2\,, \quad h^{\mu\nu}(q,r) = (q\cdot r)\left[q^\mu r^\nu + q^\nu r^\mu\right] - r^2 q^\mu q^\nu - q^2 r^\mu r^\nu\,. \tag{C.3}$$

Notice that the $h(q,r)$ and $h^{\mu\nu}(q,r)$ of Eq. (C.3) are symmetric under the exchange of $q \leftrightarrow r$, and that $h^{\mu\nu}(q,r)$ is symmetric under $\mu \leftrightarrow \nu$. Moreover, by momentum conservation, $q+p+r=0$, it is easy to show that

$$\begin{aligned} h(q,r) &= h(q,p) = h(p,r)\,, \\ h^{\mu\nu}(q,r) &= h^{\mu\nu}(q,p) = h^{\mu\nu}(p,r)\,. \end{aligned} \tag{C.4}$$

C.2 Three-gluon vertex form factors

The form factors $X_i(q,r,p)$ and $Y_j(q,r,p)$ of the three-gluon vertex can be obtained by projecting $\Gamma_{\alpha\mu\nu}(q,r,p)$ through

$$X_i(q,r,p) = \mathcal{X}_i^{\alpha\mu\nu}(q,r,p)\Gamma_{\alpha\mu\nu}(q,r,p)\,, \tag{C.5}$$

for $i = 1,\dots,10$, and

$$Y_j(q,r,p) = \mathcal{Y}_j^{\alpha\mu\nu}(q,r,p)\Gamma_{\alpha\mu\nu}(q,r,p)\,, \tag{C.6}$$

for $j = 1,\dots,4$.

The expressions for the $\mathcal{X}_i^{\alpha\mu\nu}(q,r,p)$, for $i = 1,2,3$ and 10, read

$$\begin{aligned} \mathcal{X}_1^{\alpha\mu\nu}(q,r,p) =& \frac{1}{8h^2(q,r)}\bigg\{(q\cdot r)^3\left(2q^\alpha g^{\mu\nu} - 2r^\mu g^{\alpha\nu}\right) - 3r^4 q^\alpha\left(q^\nu r^\mu + q^\mu r^\nu\right) \\ &+ (q\cdot r)^2\big[q^2 r^\nu g^{\alpha\mu} - q^2 r^\mu g^{\alpha\nu} + q^\nu\left(\left(q^2 - r^2\right)g^{\alpha\mu} + 2r^\alpha r^\mu\right) \\ &+ q^\alpha\left(-6q^\nu r^\mu + q^\mu\left(4q^\nu - 2r^\nu\right) + q^2 g^{\mu\nu} + 6r^\mu r^\nu + r^2 g^{\mu\nu}\right) - 4r^\alpha r^\mu r^\nu \\ &- r^2 r^\nu g^{\alpha\mu} - r^2 r^\mu g^{\alpha\nu}\big] + q\cdot r\big[r^2\big(3q^\mu r^\alpha\left(q^\nu + r^\nu\right) + r^\mu\left(3q^\nu r^\alpha + 2q^2 g^{\alpha\nu}\right) \\ &+ q^\alpha\left(-6q^\nu r^\mu + q^\mu\left(6q^\nu - 3r^\nu\right) - 2q^2 g^{\mu\nu} + 6r^\mu r^\nu\right)\big) \\ &- 3q^2\left(r^\mu\left(2q^\alpha\left(q^\nu - r^\nu\right) - r^\alpha\left(q^\nu - 2r^\nu\right)\right) + q^\mu\left(q^\nu r^\alpha + r^\nu\left(q^\alpha + r^\alpha\right)\right)\right)\big] \\ &+ q^4\big[q^\nu\left(3r^\alpha r^\mu - r^2 g^{\alpha\mu}\right) + q^\alpha\left(3r^\mu r^\nu - r^2 g^{\mu\nu}\right) + r^2\left(r^\mu g^{\alpha\nu} - r^\nu g^{\alpha\mu}\right)\big] \\ &+ q^2 r^2\big[q^\nu\left(r^\alpha r^\mu + r^2 g^{\alpha\mu}\right) - q^\alpha\left(3q^\nu r^\mu + q^\mu\left(r^\nu - 2q^\nu\right) - 3r^\mu r^\nu + r^2 g^{\mu\nu}\right) \\ &- 2r^\alpha r^\mu r^\nu + r^2 r^\nu g^{\alpha\mu} + r^2 r^\mu g^{\alpha\nu}\big]\bigg\}\,, \end{aligned} \tag{C.7}$$

$$
\begin{aligned}
\mathcal{X}_2^{\alpha\mu\nu}(q,r,p) =& \frac{1}{8h^2(q,r)}\Big\{ -2(q\cdot r)^3\left(q^\nu + r^\nu\right)g^{\alpha\mu} - 3r^4 q^\alpha\left(q^\nu r^\mu + q^\mu r^\nu\right)\\
& -(q\cdot r)^2\big[4q^\nu r^\alpha r^\mu - 6q^\mu r^\alpha\left(q^\nu + r^\nu\right) + r^2 q^\nu g^{\alpha\mu} - q^2 r^\mu g^{\alpha\nu} + q^2 r^\nu g^{\alpha\mu}\\
& + q^\alpha\left(-6q^\nu r^\mu + 4q^\mu\left(q^\nu + r^\nu\right) + q^2 g^{\mu\nu} - 6r^\mu r^\nu - r^2 g^{\mu\nu}\right)\\
& + q^2 q^\nu g^{\alpha\mu} + 4r^\alpha r^\mu r^\nu + r^2 r^\mu g^{\alpha\nu} + r^2 r^\nu g^{\alpha\mu}\big]\\
& + q\cdot r\big[3q^2\left(q^\mu\left(q^\nu r^\alpha + r^\nu\left(q^\alpha + r^\alpha\right)\right) + r^\mu\left(2q^\alpha q^\nu - r^\alpha\left(3q^\nu + 2r^\nu\right)\right)\right)\\
& + r^2\big(3q^\nu r^\alpha r^\mu + 3q^\mu r^\alpha\left(q^\nu + r^\nu\right) + q^\alpha\left(6r^\mu r^\nu - 3q^\mu\left(2q^\nu + 3r^\nu\right)\right)\\
& + 2q^2 r^\nu g^{\alpha\mu} + 2q^2 q^\nu g^{\alpha\mu}\big)\big] + q^2 r^2\big[q^\nu\left(r^\alpha r^\mu + r^2 g^{\alpha\mu}\right) + q^\alpha\big(3q^\nu r^\mu\\
& + q^\mu\left(r^\nu - 2q^\nu\right) + 3r^\mu r^\nu - r^2 g^{\mu\nu}\big) - 2r^\alpha r^\mu r^\nu + r^2 r^\nu g^{\alpha\mu} + r^2 r^\mu g^{\alpha\nu}\big]\\
& + q^4\big[q^\nu\left(r^2 g^{\alpha\mu} - 3r^\alpha r^\mu\right) + q^\alpha\left(r^2 g^{\mu\nu} - 3r^\mu r^\nu\right) + r^2\left(r^\nu g^{\alpha\mu} - r^\mu g^{\alpha\nu}\right)\big]\Big\}\,,\\
\mathcal{X}_3^{\alpha\mu\nu}(q,r,p) =& -\frac{\left(q^\nu + r^\nu\right)}{2\left(q^2 - r^2\right)h^2(q,r)}\Big\{3r^4 q^\alpha q^\mu + q^4\left(3r^\alpha r^\mu - r^2 g^{\alpha\mu}\right) + (q\cdot r)^2\\
& \times\big[-4q^\mu r^\alpha + 2q^\alpha\left(q^\mu - 2r^\mu\right) + q^2 g^{\alpha\mu} + 2r^\alpha r^\mu + r^2 g^{\alpha\mu}\big] + q\cdot r\\
& \times\big[r^2\left(-3q^\mu r^\alpha + q^\alpha\left(6q^\mu - 3r^\mu\right) - 2q^2 g^{\alpha\mu}\right) - 3q^2\left(q^\mu r^\alpha + r^\mu\left(q^\alpha - 2r^\alpha\right)\right)\big]\\
& + q^2 r^2\big[-2q^\mu r^\alpha + q^\alpha\left(q^\mu - 2r^\mu\right) + r^\alpha r^\mu - r^2 g^{\alpha\mu}\big] + 2(q\cdot r)^3 g^{\alpha\mu}\Big\}\,,\\
\mathcal{X}_{10}^{\alpha\mu\nu}(q,r,p) =& \frac{1}{4h^2(q,r)}\Big\{3q\cdot r\big[q^\mu\left(q^\nu r^\alpha + r^\nu\left(r^\alpha - q^\alpha\right)\right) - q^\nu r^\alpha r^\mu\big]\\
& + (q\cdot r)^2\big[-q^\nu g^{\alpha\mu} + q^\alpha g^{\mu\nu} - r^\nu g^{\alpha\mu} + r^\mu g^{\alpha\nu}\big] + 3q^2 r^\mu\left(q^\alpha r^\nu - q^\nu r^\alpha\right)\\
& + r^2\big[q^2\left(q^\nu g^{\alpha\mu} + r^\nu g^{\alpha\mu} - r^\mu g^{\alpha\nu}\right) + q^\alpha\left(3q^\nu r^\mu - 3q^\mu r^\nu - q^2 g^{\mu\nu}\right)\big]\Big\}\,, \qquad \text{(C.8)}
\end{aligned}
$$

where $h(q,r)$ is defined in Eq. (C.3).

The remaining $\mathcal{X}_i$ are given by cyclically permuting the arguments and Lorentz indices, simultaneously, of Eqs. (C.7) and (C.8) [see Eq. (4.34)]. Specifically,

$$
\begin{aligned}
\mathcal{X}_4^{\alpha\mu\nu}(q,r,p) &= \mathcal{X}_1^{\mu\nu\alpha}(r,p,q)\,, & \mathcal{X}_7^{\alpha\mu\nu}(q,r,p) &= \mathcal{X}_1^{\nu\alpha\mu}(p,q,r)\,,\\
\mathcal{X}_5^{\alpha\mu\nu}(q,r,p) &= \mathcal{X}_2^{\mu\nu\alpha}(r,p,q)\,, & \mathcal{X}_8^{\alpha\mu\nu}(q,r,p) &= \mathcal{X}_2^{\nu\alpha\mu}(p,q,r)\,,\\
\mathcal{X}_6^{\alpha\mu\nu}(q,r,p) &= \mathcal{X}_3^{\mu\nu\alpha}(r,p,q)\,, & \mathcal{X}_9^{\alpha\mu\nu}(q,r,p) &= \mathcal{X}_3^{\nu\alpha\mu}(p,q,r)\,. \qquad \text{(C.9)}
\end{aligned}
$$

The form factors $\mathcal{Y}_j$, for $j = 1$ and 4, are then given by

$$
\begin{aligned}
\mathcal{Y}_1^{\alpha\mu\nu}(q,r,p) =& \frac{1}{2\left(q^2-r^2\right)h^3(q,r)}\Big\{ -2\left(q^\nu+r^\nu\right)g^{\alpha\mu}(q\cdot r)^4+(q\cdot r)^3\big[-2q^\nu r^\alpha r^\mu \\
& -2r^\alpha r^\nu r^\mu+q^2 g^{\alpha\nu}r^\mu-r^2 g^{\alpha\nu}r^\mu-q^2q^\nu g^{\alpha\mu}+r^2q^\nu g^{\alpha\mu}+q^2r^\nu g^{\alpha\mu}-r^2r^\nu g^{\alpha\mu} \\
& +q^\mu\left(4q^\nu r^\alpha+4r^\nu r^\alpha+\left(r^2-q^2\right)g^{\alpha\nu}\right)+q^2r^\alpha g^{\mu\nu}-r^2r^\alpha g^{\mu\nu} \\
& +q^\alpha\left(4q^\nu r^\mu+4r^\nu r^\mu-2q^\mu\left(q^\nu+r^\nu\right)-q^2g^{\mu\nu}+r^2g^{\mu\nu}\right)\big] \\
& +(q\cdot r)^2\big[\left(q^\nu g^{\alpha\mu}+q^\mu g^{\alpha\nu}+q^\alpha g^{\mu\nu}\right)r^4-\big(-4q^\nu r^\alpha r^\mu+q^2g^{\alpha\nu}r^\mu-3q^2q^\nu g^{\alpha\mu} \\
& -3q^2r^\nu g^{\alpha\mu}+q^\mu\left(2q^\nu r^\alpha-4r^\nu r^\alpha+q^2g^{\alpha\nu}\right)+q^2r^\alpha g^{\mu\nu} \\
& +q^\alpha\left(2q^\nu r^\mu-4r^\nu r^\mu+4q^\mu\left(q^\nu+2r^\nu\right)+q^2g^{\mu\nu}\right)\big)r^2+q^2\big(-8q^\nu r^\alpha r^\mu \\
& +2q^\alpha\left(2q^\nu-r^\nu\right)r^\mu-4r^\alpha r^\nu r^\mu+q^2g^{\alpha\nu}r^\mu+q^\mu\left(4q^\nu r^\alpha+2\left(2q^\alpha-r^\alpha\right)r^\nu\right) \\
& +q^2r^\nu g^{\alpha\mu}+q^2r^\alpha g^{\mu\nu}\big)\big]+q\cdot r\big[-q^4\big(5q^\alpha r^\mu r^\nu-5r^\alpha r^\mu r^\nu+r^2g^{\alpha\mu}r^\nu \\
& +q^\nu\left(5r^\alpha r^\mu-r^2g^{\alpha\mu}\right)+r^2r^\mu g^{\alpha\nu}+q^\mu\left(5r^\alpha r^\nu-r^2g^{\alpha\nu}\right)-r^2q^\alpha g^{\mu\nu} \\
& +r^2r^\alpha g^{\mu\nu}\big)+q^2r^2\big(7q^\nu r^\alpha r^\mu-3r^\alpha r^\nu r^\mu+r^2g^{\alpha\nu}r^\mu-r^2q^\nu g^{\alpha\mu}+r^2r^\nu g^{\alpha\mu} \\
& +q^\mu\left(q^\nu r^\alpha+r^\nu r^\alpha-r^2g^{\alpha\nu}\right)+r^2r^\alpha g^{\mu\nu}+q^\alpha(q^\nu r^\mu+r^\nu r^\mu+q^\mu\left(7r^\nu-3q^\nu\right) \\
& -r^2g^{\mu\nu})\big)+5r^4\left(q^\alpha\left(q^\mu\left(q^\nu-r^\nu\right)-q^\nu r^\mu\right)-q^\mu q^\nu r^\alpha\right)\big]+5r^6q^\alpha q^\mu q^\nu \\
& +q^6\left(r^\alpha\left(5r^\mu r^\nu-r^2g^{\mu\nu}\right)-r^2\left(r^\nu g^{\alpha\mu}+r^\mu g^{\alpha\nu}\right)\right)+q^4r^2\big[3q^\nu r^\alpha r^\mu-r^\alpha r^\nu r^\mu \\
& +r^2g^{\alpha\nu}r^\mu-r^2q^\nu g^{\alpha\mu}-r^2r^\nu g^{\alpha\mu}+q^\mu\left(q^\nu r^\alpha-3r^\nu r^\alpha+q^\alpha r^\nu+r^2g^{\alpha\nu}\right) \\
& +r^2r^\alpha g^{\mu\nu}+q^\alpha\left(q^\nu r^\mu-3r^\nu r^\mu+r^2g^{\mu\nu}\right)\big]-q^2r^4\big[q^\mu\left(3q^\nu r^\alpha-r^\nu r^\alpha+r^2g^{\alpha\nu}\right) \\
& +q^\nu\left(r^2g^{\alpha\mu}-r^\alpha r^\mu\right)+q^\alpha\left(3(q^\nu r^\mu-q^\mu r^\nu)-r^\nu r^\mu+q^\mu q^\nu+r^2g^{\mu\nu}\right)\big]\Big\}, \\
\mathcal{Y}_4^{\alpha\mu\nu}(q,r,p) =& -\frac{1}{4h^3(q,r)}\Big\{(q\cdot r)^4\big[q^\nu g^{\alpha\mu}+2q^\mu g^{\alpha\nu}+q^\alpha g^{\mu\nu}-r^\nu g^{\alpha\mu}-r^\mu g^{\alpha\nu}-2r^\alpha g^{\mu\nu}\big] \\
& +(q\cdot r)^3\big[5q^\nu r^\alpha r^\mu+2r^2q^\nu g^{\alpha\mu}+q^\mu\left(-5q^\nu r^\alpha-5q^\alpha r^\nu+5r^\alpha r^\nu+2r^2g^{\alpha\nu}\right) \\
& +q^\alpha\left(-2q^\nu r^\mu+2r^\mu r^\nu+2r^2g^{\mu\nu}\right)-2q^2r^\mu g^{\alpha\nu}-2q^2r^\nu g^{\alpha\mu}-2q^2r^\alpha g^{\mu\nu}\big] \\
& +(q\cdot r)^2\big[q^2\left(7q^\nu r^\alpha r^\mu+r^\nu\left(10q^\mu r^\alpha+r^\mu\left(7q^\alpha-8r^\alpha\right)\right)\right) \\
& +r^2\left(q^\alpha\left(q^\mu\left(8q^\nu-7r^\nu\right)-7q^\nu r^\mu\right)+2q^2r^\alpha g^{\mu\nu}-2q^\mu\left(5q^\nu r^\alpha+q^2g^{\alpha\nu}\right)\right)\big] \\
& +q\cdot r\big[-10q^4r^\alpha r^\mu r^\nu-2r^4\left(q^2\left(q^\nu g^{\alpha\mu}+q^\mu g^{\alpha\nu}\right)+q^\alpha\left(q^2g^{\mu\nu}-5q^\mu q^\nu\right)\right) \\
& +q^2r^2\big(5q^\nu r^\alpha r^\mu+8q^\alpha r^\mu\left(r^\nu-q^\nu\right)-5q^\mu\left(q^\nu r^\alpha+r^\nu\left(q^\alpha-r^\alpha\right)\right)+2q^2r^\mu g^{\alpha\nu} \\
& +2q^2r^\nu g^{\alpha\mu}+2q^2r^\alpha g^{\mu\nu}\big)\big]+q^2r^2\big[q^2r^\mu\left(3q^\nu r^\alpha+r^\nu\left(3q^\alpha-2r^\alpha\right)\right)+r^2 \\
& \times\left(q^2\left(r^\nu g^{\alpha\mu}+r^\mu g^{\alpha\nu}-q^\nu g^{\alpha\mu}\right)-q^\alpha\left(3(q^\nu r^\mu+q^\mu r^\nu)-2q^\mu q^\nu+q^2g^{\mu\nu}\right)\right)\big]\Big\}.
\end{aligned}
\tag{C.10}
$$

Finally, the remaining $\mathcal{Y}_i$ are given by cyclically permuting the arguments and Lorentz indices, simultaneously, of Eqs. (C.10) [see Eq. (4.34)]. Namely,

$$\mathcal{Y}_2^{\alpha\mu\nu}(q,r,p) = \mathcal{Y}_1^{\mu\nu\alpha}(r,p,q)\,, \qquad \mathcal{Y}_3^{\alpha\mu\nu}(q,r,p) = \mathcal{Y}_1^{\nu\alpha\mu}(p,q,r)\,. \tag{C.11}$$

D

Euclidean space

In order to transform expressions given in Minkowski metric to Euclidean space, the time component of any four vector, $q = (q_0, q_1, q_2, q_3)$, becomes imaginary, *i.e.*

$$q \to (iq_0^{\rm E}, q_1^{\rm E}, q_2^{\rm E}, q_3^{\rm E})\,, \tag{D.1}$$

where the $q_i^{\rm E}$ are real and a sub/superscript "E" denotes the Euclidean version of a quantity. Simultaneously, the metric is transformed to $g_{\mu\nu} \to \delta_{\mu\nu}$. Consequently, $q_{\rm E}^2 = -q^2$. Additionally, the integral measure of Eq. (B.1) becomes

$$\int_k \to i \int_{k_{\rm E}}\,. \tag{D.2}$$

For most of the scalar functions used in this work, we *define* their Euclidean versions by just substituting the momenta in their arguments by i times their Euclidean versions, *e.g.*

$$F_{\rm E}(q_{\rm E}^2) := F\big((iq_{\rm E})^2\big) = F(-q_{\rm E}^2) = F(q^2)\,. \tag{D.3}$$

Then, the form factors A_j, for $j = 1, \ldots, 5$, of the ghost-gluon scattering kernel are written as

$$A_j^{\rm E}(q_{\rm E}, p_{\rm E}, r_{\rm E}) := A_j(iq_{\rm E}, ip_{\rm E}, ir_{\rm E})\,, \tag{D.4}$$

and similar definitions are used for the scalar form factors of other vertex functions.

An exception to the above rule is the gluon propagator scalar function $\Delta(q^2)$. It is convenient to define its Euclidean space version with an extra sign,

$$\Delta_{\rm E}(q_{\rm E}^2) := -\Delta\big((iq_{\rm E})^2\big) = -\Delta(q^2)\,, \tag{D.5}$$

such that it is positive for $q_{\mathrm{E}}^2 > 0$, *e.g.* $\Delta_{\mathrm{E}}^{(0)}(q_{\mathrm{E}}^2) = 1/q_{\mathrm{E}}^2$.

D.1 Spherical coordinates

To evaluate loop integrals numerically, it is convenient to parametrize the momenta in spherical coordinates. Moreover, in practice we set the space time dimension to $d = 4$. In this case the internal momentum, k_{E}, is expressed as

$$k_{\mathrm{E}} = |k_{\mathrm{E}}|(\cos\varphi_1,\, \sin\varphi_1\cos\varphi_2,\, \sin\varphi_1\sin\varphi_2\cos\varphi_3,\, \sin\varphi_1\sin\varphi_2\sin\varphi_3)\,, \tag{D.6}$$

where $|k_{\mathrm{E}}| := \sqrt{k_{\mathrm{E}}^2}$ is the Euclidean modulus of k_{E}. Then, the integral measure of Eq. (D.2) reads explicitly

$$\int_{k_{\mathrm{E}}} = \frac{1}{(2\pi)^4}\int_0^\infty \mathrm{d}|k_{\mathrm{E}}|\,|k_{\mathrm{E}}|^3 \int_0^\pi \mathrm{d}\varphi_1 \sin^2\varphi_1 \int_0^\pi \mathrm{d}\varphi_2 \sin\varphi_2 \int_0^{2\pi} \mathrm{d}\varphi_3\,. \tag{D.7}$$

Consider next a scalar integral of the form

$$\int_{k_{\mathrm{E}}} f(q_{\mathrm{E}}, k_{\mathrm{E}})\,, \tag{D.8}$$

for some scalar function $f(q_{\mathrm{E}}, k_{\mathrm{E}})$ of an external momentum q_{E} and the loop momentum k_{E}. Without loss of generality, we can do the integral in the rest frame of q_{E}, *i.e.*

$$q_{\mathrm{E}} = |q_{\mathrm{E}}|(1,0,0,0)\,. \tag{D.9}$$

Since $f(q_{\mathrm{E}}, k_{\mathrm{E}})$ is scalar, it can only depend on q_{E}^2, k_{E}^2 and $q_{\mathrm{E}}\cdot k_{\mathrm{E}} = |q_{\mathrm{E}}||k_{\mathrm{E}}|\cos\varphi_1$. Hence, the integrals over φ_2 and φ_3 can be performed analytically, yielding

$$\int_{k_{\mathrm{E}}} f(q_{\mathrm{E}}, k_{\mathrm{E}}) = \frac{2}{(2\pi)^3}\int_0^\infty \mathrm{d}|k_{\mathrm{E}}|\,|k_{\mathrm{E}}|^3 \int_0^\pi \mathrm{d}\varphi_1 \sin^2\varphi_1 f(q_{\mathrm{E}}, k_{\mathrm{E}})\,. \tag{D.10}$$

In the evaluation of 3-point functions it is necessary to deal with scalar integrals depending on two external momenta, say q_{E} and p_{E}, such as

$$\int_{k_{\mathrm{E}}} g(q_{\mathrm{E}}, p_{\mathrm{E}}, k_{\mathrm{E}})\,. \tag{D.11}$$

To compute these, we may still use the parametrization of Eq. (D.9) for q_{E}. As for p_{E}, we may choose without loss of generality

$$p_{\mathrm{E}} = |p_{\mathrm{E}}|(\cos\theta, \sin\theta, 0, 0)\,, \tag{D.12}$$

where θ is the angle between q_{E} and p_{E}, and is then limited to the interval $[0, \pi]$. Then, a scalar function $g(q_{\mathrm{E}}, p_{\mathrm{E}}, k_{\mathrm{E}})$ can depend on q_{E}^2, p_{E}^2, k_{E}^2, as well as on the inner products

$$\begin{aligned}
q_{\mathrm{E}} \cdot p_{\mathrm{E}} &= |q_{\mathrm{E}}|\,|p_{\mathrm{E}}| \cos\theta\,, \\
q_{\mathrm{E}} \cdot k_{\mathrm{E}} &= |q_{\mathrm{E}}|\,|k_{\mathrm{E}}| \cos\varphi_1\,, \\
p_{\mathrm{E}} \cdot k_{\mathrm{E}} &= |p_{\mathrm{E}}|\,|k_{\mathrm{E}}|(\cos\theta\cos\varphi_1 + \sin\theta\sin\varphi_1\cos\varphi_2)\,.
\end{aligned} \tag{D.13}$$

Hence, in Eq. (D.11) we can generally only perform analytically the integration over φ_3, yielding

$$\int_{k_{\mathrm{E}}} g(q_{\mathrm{E}}, p_{\mathrm{E}}, k_{\mathrm{E}}) = \frac{1}{(2\pi)^3} \int_0^\infty \mathrm{d}|k_{\mathrm{E}}|\,|k_{\mathrm{E}}|^3 \int_0^\pi \mathrm{d}\varphi_1 \sin^2\varphi_1 \int_0^\pi \mathrm{d}\varphi_2 \sin^2\varphi_2\, g(q_{\mathrm{E}}, p_{\mathrm{E}}, k_{\mathrm{E}})\,. \tag{D.14}$$

In all above integrals, it may be convenient to perform the change of variables $y := k_{\mathrm{E}}^2$, such that

$$\int_0^\infty \mathrm{d}|k_{\mathrm{E}}|\,|k_{\mathrm{E}}|^3 = \frac{1}{2}\int_0^\infty \mathrm{d}y\, y\,. \tag{D.15}$$

Let us also take the chance to define a notation that will be employed in the presentation of numerical results in general kinematics. For any scalar form factor that depends on three-external momenta, *e.g.* $A_j^{\mathrm{E}}(q_{\mathrm{E}}, p_{\mathrm{E}}, r_{\mathrm{E}})$, momentum conservation, $q_{\mathrm{E}} + p_{\mathrm{E}} + r_{\mathrm{E}} = 0$, implies that only two of the momenta are independent, say q_{E} and p_{E}. Then, using the parametrization of Eqs. (D.9) and (D.12), we can always express the functional dependence of A_j^{E} on the momenta in terms of their squares, q_{E}^2 and p_{E}^2, and the angle between them, $\theta = \arccos[(q_{\mathrm{E}} \cdot p_{\mathrm{E}})/(|q_{\mathrm{E}}|\,|p_{\mathrm{E}}|)]$. Therefore, we can express the A_j^{E} as

$$A_j^{\mathrm{E}}(q_{\mathrm{E}}, p_{\mathrm{E}}, r_{\mathrm{E}}) \equiv A_j^{\mathrm{E}}(q_{\mathrm{E}}^2, p_{\mathrm{E}}^2, \theta)\,. \tag{D.16}$$

We will use the two notations in Eq. (D.16) interchangeably in the main text.

Finally, the subscripts "E" will be omitted outside the present appendix, for compactness. It will be clear, either by context, or by explicit assertion, when expressions are written in Euclidean space.

E

Expressions for the Euclidean space A_i

In this appendix we present the expressions obtained for the form factors A_i of the ghost-gluon scattering kernel by projecting Eq. (5.17) with the projectors of Eq. (C.1). We use the approximations discussed in Section 5.3 and transform to Euclidean space using the rules of Appendix D. The lengthy Lorentz algebra was done using *Package X* [214, 215].

We will express the A_i as the sum of their tree-level values and the contributions from each of the diagrams $(d_1)_{\nu\mu}$ and $(d_2)_{\nu\mu}$, which will be specified by a superscript, *i.e.* $A_i = A_i^{(0)} + A_i^{(d_1)} + A_i^{(d_2)}$.

To make the expressions somewhat more compact we introduce the auxiliary variables $s = q - \ell\,,\ t = -\ell - p\,,\ u = -p - q\,,$ and $v = -\ell + p + q$, with the notation $a_1 = \ell \cdot p\,,$ $a_2 = \ell \cdot q\,,\ a_3 = p \cdot q\,,$ for the inner products, and define

$$
\begin{aligned}
&T_1 := h_{pq} + 3(p^2 + a_3)^2\,, && T_2 := h_{pq} + 3(q^2 + a_3)^2\,,\\
&T_3 := -p^2q^2 + p^4 - 2a_3(q^2 + a_3)\,, && T_4 := -p^2q^2 + q^4 - 2a_3(p^2 + a_3)\,,\\
&T_5 := p^2a_2^2 + q^2a_1^2 - 2a_1a_2a_3\,. &&
\end{aligned}
\tag{E.1}
$$

Also, the arguments of the various functions appearing in the expressions are denoted as a super/subscript, *e.g.* $f(x, y, z) = f_{xyz}$ and $f(x, y, z) = f^{xyz}$.

Lastly, all the propagator and vertex form factors are understood to mean their "input" approximations, namely $\Delta_{\text{in}}(q)$, $X_1^{\text{in}}(r, t, \ell)$, $F_{\text{in}}(q)$, and $B_1^{\text{in}}(Q)$, presented in Section 5.3.

Then, the contributions from diagram $(d_1)_{\nu\mu}$ to each form factor read

$$
\begin{aligned}
A_1^{(d_1)} &= \frac{ig^2 C_A}{4}\int_\ell \mathcal{K}^{(d_1)}\left\{\frac{a_1\left[h_{pq}\,\ell^2 - T_5\right]}{h_{pq}\,\ell^2}\right\}\,,\\
A_2^{(d_1)} &= -\frac{ig^2 C_A}{4}\int_\ell \frac{\mathcal{K}^{(d_1)}}{h_{pq}^2\,\ell^2}\Big\{h_{pq}\ell^2\Big[a_1\left(4a_3+p^2+3q^2\right) - 2a_2\left(a_3+p^2\right)+2h_{pq}\Big]\\
&\quad - a_1\Big[a_2^2 h_{pq} - 2a_2\left(p^2\left(3a_1a_3+2a_1q^2+h_{pq}\right)+a_3\left(4a_1a_3+3a_1q^2+h_{pq}\right)\right)\\
&\quad + a_1\left(q^2\left(6a_1a_3+a_1p^2+3a_1q^2+2h_{pq}\right)+2a_3(a_1a_3+h_{pq})\right)+3a_2^2\left(a_3+p^2\right)^2\Big]\Big\}\,,\\
A_3^{(d_1)} &= \frac{i\,g^2 C_A}{4}\int_\ell \frac{\mathcal{K}^{(d_1)}}{h_{pq}^2\,\ell^2}\left\{3a_1^3q^4 + a_1q^2\left[a_2\left(a_2p^2-6a_1a_3\right)-3h_{pq}\ell^2\right]\right.\\
&\quad \left.+2a_2a_3\left(a_1a_2a_3+h_{pq}\ell^2\right)\right\}\,,\\
A_4^{(d_1)} &= -\frac{i\,g^2 C_A}{4}\int_\ell \frac{\mathcal{K}^{(d_1)}}{h_{pq}^2\,\ell^2}\left\{h_{pq}\ell^2\left[3a_1\left(a_3+q^2\right)-2a_2\left(a_3+p^2\right)+2h_{pq}\right]\right.\\
&\quad + a_1\left[-a_1q^2\left(3a_1a_3+3a_1q^2-6a_2a_3+2h_{pq}\right)+2a_2a_3(2a_1a_3-a_2a_3+h_{pq})\right.\\
&\quad \left.\left.-a_2p^2\left(q^2(a_2-2a_1)+3a_2a_3\right)\right]\right\}\,,\\
A_5^{(d_1)} &= \frac{i\,g^2 C_A}{4}\int_\ell \frac{\mathcal{K}^{(d_1)}}{h_{pq}^2\,\ell^2}\Big\{a_1\Big[a_2(a_2-2a_1)\left(3a_3^2+h_{pq}\right)+3a_1q^2\left(a_1a_3+a_1q^2-2a_2a_3\right)\\
&\quad + 3a_2^2a_3p^2\Big] - h_{pq}\ell^2\left[a_3(a_1-2a_2)+3a_1q^2\right]\Big\}\,,
\end{aligned}
\tag{E.2}
$$

where

$$
\mathcal{K}^{(d_1)} := \frac{\Delta\left(\ell^2\right)F\left(t^2\right)F\left(s^2\right)B_1(s,-t,u)\mathcal{V}_1(\ell,q,p,r)}{s^2\,t^2}\,. \tag{E.3}
$$

The contributions of diagram $(d_2)_{\nu\mu}$ may be written as

$$
A_i^{(d_2)} = \frac{ig^2 C_A}{2}\int_\ell \frac{\mathcal{K}_{\ell uv}S_i^{\ell uv}+\mathcal{K}_{uv\ell}S_i^{uv\ell}+\mathcal{K}_{v\ell u}S_i^{v\ell u}}{h_{pq}^2\,\ell^2}\,, \tag{E.4}
$$

with

$$
\mathcal{K}_{xyz} := \frac{\Delta\left(\ell^2\right)\Delta\left(v^2\right)F\left(s^2\right)\mathcal{V}_2(\ell,q,p,r)X_1^{xyz}}{s^2\,v^2}\,. \tag{E.5}
$$

Then, the S_i are given by

$$
\begin{aligned}
S_1^{\ell uv} &= -h_{pq}\left\{a_1\left[\left(a_3+q^2\right)\left(T_5+h_{pq}\,\ell^2\right)-a_2\left(\ell^2\left(2a_3\left(a_3+p^2\right)+h_{pq}\right)+T_5\right)\right]\right.\\
&\quad \left.+a_1^2\left[a_3\,\ell^2\left(a_3+q^2\right)-T_5\right]+\left(a_3+p^2\right)\left[-a_2\,T_5+a_2\,\ell^2\left(a_2\,p^2-h_{pq}\right)+h_{pq}\,\ell^4\right]\right\}\,,\\
S_1^{uv\ell} &= -h_{pq}(a_1+a_2)\left(-a_1+a_3+p^2\right)\left[h_{pq}\,\ell^2-T_5\right]\,,
\end{aligned}
$$

$$
\begin{aligned}
S_1^{v\ell u} &= -h_{pq}\left\{T_5\left[a_1^2+a_1\left(a_2-a_3-q^2\right)+a_2\left(a_3+p^2\right)\right]+a_1h_{pq}\,\ell^4-\ell^2\left[a_1^2(h_{pq}-2a_2a_3)\right.\right.\\
&\qquad\left.\left.+a_1q^2\left(a_1^2-h_{pq}\right)+a_1h_{pq}(a_2-a_3)+a_2\,p^2(a_1a_2+h_{pq})+a_2a_3h_{pq}\right]\right\}\ , \qquad \text{(E.6)}\\
S_2^{\ell uv} &= -a_1^4\,T_2+a_1^3\left[3a_2\left(2a_3\left(a_3+p^2\right)+p^2q^2-q^4\right)+\left(a_3+q^2\right)\left(3\left(a_3+q^2\right)^2+h_{pq}\right)\right]\\
&\quad-a_1^2\Big[3a_2^2\,T_3+a_2\left(q^2\left(20a_3^2+17a_3p^2+p^4\right)+2a_3^2\left(5a_3+4p^2\right)+q^4\left(9a_3+7p^2\right)\right)\\
&\quad-\ell^2\left(3a_3\left(3q^2\left(a_3+p^2\right)+a_3p^2+q^4\right)+2h_{pq}\left(p^2+2q^2\right)\right)\Big]+\left(\ell^2-a_2\right)\left(a_3+p^2\right)\\
&\quad\times\Big[a_2^2T_1-h_{pq}\ell^2\left(2a_3+p^2+q^2\right)\Big]-a_1\Big[a_2^3\,T_1+h_{pq}\ell^2\left(a_3+q^2\right)\left(2a_3+p^2+q^2\right)\\
&\quad-a_2^2\left(p^2\left(20a_3^2+17a_3q^2+q^4\right)+2a_3^2\left(5a_3+4q^2\right)+p^4\left(9a_3+7q^2\right)\right)\\
&\quad+a_2\ell^2\left(p^2\left(15a_3^2+8a_3q^2-q^4\right)+a_3^2\left(10a_3+7q^2\right)+3p^4\left(2a_3+q^2\right)\right)\Big]\,,\\
S_2^{uv\ell} &= a_1^2\Big[3a_2^2T_3+a_2\Big(6a_3p^4+p^2\left(15a_3^2+9a_3q^2-h_{pq}\right)+h_{pq}\left(5q^2-2a_3\right)\\
&\quad-3a_3q^2\left(a_3+q^2\right)\Big)-h_{pq}\left(\ell^2\left(4a_3+p^2+3q^2\right)+2\left(a_3+q^2\right)(p+q)^2\right)\Big]\\
&\quad+a_1^3\Big[q^4\left(3a_2-3a_3+p^2\right)-2a_3\left(p^2(3a_2+a_3)+3a_3(a_2+a_3)\right)\\
&\quad-q^2\left(3p^2(a_2+a_3)+10a_3^2+p^4\right)\Big]+a_1^4T_2\\
&\quad+a_1\Big[a_2^3T_1+a_2^2\left(p^2\left(14a_3^2+5a_3q^2+4q^4\right)+2a_3^2\left(5a_3+q^2\right)-p^4\left(3a_3+5q^2\right)-3p^6\right)\\
&\quad+a_2h_{pq}\left(\ell^2\left(-2a_3+p^2-3q^2\right)+2\left(p^2-q^2\right)(p+q)^2\right)+h_{pq}\ell^2\left(a_3+p^2\right)(p+q)^2\Big]\\
&\quad+a_2\left(a_3+p^2\right)\left[(p+q)^2\left(h_{pq}\ell^2+2a_2h_{pq}-3a_2^2p^2\right)+2a_2h_{pq}\left(\ell^2-a_2\right)\right]\ ,\\
S_2^{v\ell u} &= a_1^4T_2+a_1^3\left[3a_2T_4-\left(a_3+q^2\right)\left(3\left(a_3+q^2\right)^2+h_{pq}\right)\right]+a_1^2a_2\Big[3a_2T_3\\
&\quad+2a_3^2\left(5a_3+4p^2\right)+q^4\left(9a_3+7p^2\right)\Big]+\ell^2\Big[a_1\Big(a_2h_{pq}\left(-2a_3+3p^2-5q^2\right)\\
&\quad+3h_{pq}\left(a_3+q^2\right)(p+q)^2-a_2^2T_1\Big)+a_1^2\Big(p^2\left(6a_2a_3+4a_2q^2-h_{pq}\right)\\
&\quad+q^2(6a_2a_3-5h_{pq})+2a_3(4a_2a_3-3h_{pq})\Big)-a_1^3T_2+a_2h_{pq}\left(a_3+p^2\right)\\
&\quad\times\left(4a_2-3(p+q)^2\right)\Big]+a_1a_2^2\left[a_2T_1-2a_3^2\left(5a_3+4q^2\right)-p^4\left(9a_3+7q^2\right)\right]\\
&\quad+a_1a_2\left[20a_3^2\left(a_1q^2-a_2p^2\right)+17a_3p^2q^2\left(a_1-a_2\right)+p^2q^2\left(p^2a_1-q^2a_2\right)\right]\\
&\quad+h_{pq}\ell^4\left[a_1\left(4a_3+p^2+3q^2\right)-2a_2\left(a_3+p^2\right)\right]+a_2^3T_1\left(a_3+p^2\right)\ , \qquad \text{(E.7)}
\end{aligned}
$$

$$
\begin{aligned}
S_3^{\ell uv} &= 3a_1^3q^6 - 2a_2^2a_3^2\left[a_1^2 + a_1a_2 - a_1a_3 + a_2a_3 + a_2p^2 - \ell^2\left(a_3+p^2\right)\right]\\
&- a_1q^4\left[3a_1\left(a_1^2 + a_1a_2 - a_1a_3 + 3a_2a_3\right) + \ell^2\left(-3a_1a_3 - 3a_1p^2 + h_{pq}\right) - a_2^2p^2\right]\\
&- q^2\Big[-\ell^2\Big(h_{pq}\left(a_1^2 + a_1(a_2-a_3) + a_2a_3\right) + a_2p^2\left(-6a_1a_3 + a_2a_3 + a_2p^2 + h_{pq}\right)\\
&- 6a_1a_2a_3^2\Big) + h_{pq}\ell^4\left(a_3+p^2\right) + a_2\Big(a_2p^2\left(a_1^2 + a_1a_2 - 7a_1a_3 + a_2a_3 + a_2p^2\right)\\
&+ a_1(a_3^2(9a_1 - 8a_2) - 6a_1a_3(a_1+a_2) + 3a_1h_{pq})\Big)\Big]\,,\\
S_3^{uv\ell} &= (a_1+a_2)\Big[2a_2\left(a_3^2(a_1a_3 + h_{pq}) + q^2\left(a_3(a_1(a_3 - 3a_1) + h_{pq}) + 2a_1p^2\left(a_3+q^2\right)\right)\right)\\
&- a_1q^2\left(q^2\left(a_1\left(-3a_1 + 3a_3 + p^2\right) + 2h_{pq}\right) + 2a_3(a_1a_3 + h_{pq})\right)\\
&+ a_2^2\left(\left(a_1 - p^2\right)\left(3a_3^2 + h_{pq}\right) - 3a_3^3 - 5a_3h_{pq}\right)\Big] + 2h_{pq}^2\ell^4 + \ell^2\Big[q^2\Big(a_1a_3^2(5a_1+3a_2)\\
&+ a_3h_{pq}(3a_1+a_2) + 2h_{pq}^2\Big) + 2a_3\Big(-a_2a_3^2(2a_1+a_2) + h_{pq}^2 + a_3h_{pq}(a_1+a_2)\Big)\\
&+ p^2\left(q^2\left(2a_2a_3(2a_1+a_2) + h_{pq}(a_1 - 3a_2) - a_1q^2(5a_1+3a_2)\right) - 2a_2a_3h_{pq}\right)\Big]\,,\\
S_3^{v\ell u} &= -3a_1^3q^6 + q^2\Big[a_2p^2\left(a_1^2(a_2+a_3) + a_1\left(a_2^2 - 6a_2a_3 - h_{pq}\right) + a_2^2a_3 + a_2^2p^2\right)\\
&+ a_1a_3\left(a_1^2(a_3 - 6a_2) + a_1\left(-6a_2^2 + 7a_2a_3 + h_{pq}\right) - 2a_2(4a_2a_3 + h_{pq})\right)\Big]\\
&+ a_2a_3\Big[a_3\left(a_1^2(2a_2 - a_3) + a_1\left(2a_2^2 - 3a_2a_3 - h_{pq}\right) + a_2(2a_2a_3 + h_{pq})\right)\\
&+ a_2p^2(2a_2a_3 + h_{pq})\Big] + \ell^2\Big[-a_3\left(a_1a_3(a_2(2a_2+a_3) + h_{pq}) + (2a_2a_3 + h_{pq})^2\right)\\
&+ q^2\Big(3a_1q^2\left(h_{pq} - a_1^2\right) + p^2\left(a_1(a_2(a_3 - a_2) + h_{pq}) - a_1q^2(2a_1 + 5a_2)\right.\\
&\left.+ a_2(4a_2a_3 + h_{pq})\right) + 3a_3h_{pq}(a_1 - a_2) + a_1a_3(2a_1(3a_2 + a_3) + 5a_2a_3) - h_{pq}^2\Big)\Big]\\
&+ a_1q^4\Big[-p^2(a_1 - a_2)^2 + a_1(-3a_3(a_1 - 3a_2) + 3a_1(a_1+a_2) + h_{pq})\Big]\\
&- h_{pq}\ell^4\left(-3a_1q^2 + 2a_2a_3 + h_{pq}\right)\,, \qquad \text{(E.8)}\\
S_4^{\ell uv} &= -\left[a_1^2 + a_1\left(a_2 - a_3 - q^2\right) + a_2\left(a_3 + p^2\right)\right]\Big[a_2^2\left(3a_3\left(a_3 + p^2\right) + h_{pq}\right)\\
&- 2a_1a_2\left(3a_3\left(a_3+q^2\right) + h_{pq}\right) + 3a_1^2q^2\left(a_3+q^2\right)\Big] - h_{pq}\ell^4\left(a_3+p^2\right)\left(a_3+q^2\right)\\
&- \ell^2\Big[a_1\left(a_3+q^2\right)\left(q^2\left(-3a_1a_3 - 4a_1p^2 + h_{pq}\right) + a_3(a_1a_3 + h_{pq})\right)\\
&+ a_2\Big(-p^2\left(q^2\left(-7a_1a_3 + a_1q^2 + h_{pq}\right) + a_3(h_{pq} - 4a_1a_3)\right)\\
&+ a_3\left(q^2(7a_1a_3 - h_{pq}) + a_3(5a_1a_3 - h_{pq})\right) + 2a_1p^4q^2\Big)\\
&- a_2^2\left(a_3+p^2\right)\left(3a_3\left(a_3+p^2\right) + h_{pq}\right)\Big]\,,
\end{aligned}
$$

$$\begin{aligned}
S_4^{uv\ell} &= 2h_{pq}^2\ell^4 + (a_1+a_2)\Big[a_1q^2\Big(a_3\left(3a_1^2-7a_1a_3-4h_{pq}\right)+p^2\left(-3a_1a_3+a_1q^2-2h_{pq}\right)\\
&\quad + q^2(3a_1(a_1-a_3)-2h_{pq})\Big) + a_2^2\Big(2a_1a_3^2+a_1p^2\left(3a_3+q^2\right)-h_{pq}\left(2a_3+p^2\right)\\
&\quad - 3a_3p^2\left(2a_3+p^2+q^2\right)\Big) + 2a_2\Big(a_3\left(2a_3\left(-a_1^2+2a_1a_3+h_{pq}\right)+p^2(2a_1a_3+h_{pq})\right)\\
&\quad + q^2\left(a_1\left(\left(a_3+p^2\right)^2-a_1\left(3a_3+p^2\right)\right)+a_3h_{pq}\right)+2a_1p^2q^4\Big)\Big]\\
&\quad + \ell^2\Big[q^2\left(-5a_1^2h_{pq}+3a_1a_3(a_2a_3+h_{pq})+h_{pq}(a_2a_3+2h_{pq})\right)-3a_1a_2a_3^3\\
&\quad + a_3h_{pq}\left(-3a_1^2+7a_1a_3+a_2(2a_2+3a_3)\right)-2a_2p^4\left(h_{pq}-a_1q^2\right)+4a_3h_{pq}^2\\
&\quad - p^2\Big(q^2\left(-3a_1a_2a_3+3a_1a_2q^2+a_1h_{pq}+3a_2h_{pq}\right)+a_1a_3(2a_2a_3-3h_{pq})\\
&\quad + h_{pq}(3a_2a_3-2h_{pq})\Big)\Big]\,,\\
S_4^{v\ell u} &= \left[a_1^2+a_1\left(a_2-a_3-q^2\right)+a_2\left(a_3+p^2\right)\right]\Big[3a_1^2q^2\left(a_3+q^2\right)-2a_1a_2\Big(3a_3\left(a_3+q^2\right)\\
&\quad + h_{pq}\Big)+a_2^2\left(3a_3\left(a_3+p^2\right)+h_{pq}\right)\Big]-\ell^2\Big[a_1^2\Big(q^2\left(3h_{pq}-2a_2\left(3a_3+p^2\right)\right)\\
&\quad + a_3(3h_{pq}-4a_2a_3)\Big)+a_1\Big(a_2^2\left(3a_3\left(a_3+p^2\right)+h_{pq}\right)+a_2\left(3a_3-2p^2+5q^2\right)h_{pq}\\
&\quad - 3h_{pq}\left(a_3+q^2\right)^2\Big)+3a_1^3q^2\left(a_3+q^2\right)+a_2h_{pq}\left(a_3+p^2\right)\left(3\left(a_3+q^2\right)-4a_2\right)\Big]\\
&\quad - h_{pq}\ell^4\left[2a_2\left(a_3+p^2\right)-3a_1\left(a_3+q^2\right)\right]\,, \qquad\qquad \text{(E.9)}\\
S_5^{\ell uv} &= -\left[a_1^2+a_1\left(a_2-a_3-q^2\right)+a_2\left(a_3+p^2\right)\right]\Big[-2a_1a_2\left(3a_3\left(a_3+q^2\right)+h_{pq}\right)\\
&\quad + 3a_1^2q^2\left(a_3+q^2\right)+a_2^2\left(3a_3\left(a_3+p^2\right)+h_{pq}\right)\Big]-h_{pq}\ell^4\left(a_3+p^2\right)\left(a_3+q^2\right)\\
&\quad - \ell^2\Big[a_2\Big(-p^2\left(q^2\left(-7a_1a_3+a_1q^2+h_{pq}\right)+a_3(h_{pq}-4a_1a_3)\right)+2a_1p^4q^2\\
&\quad + a_3\left(q^2(7a_1a_3-h_{pq})+a_3(5a_1a_3-h_{pq})\right)\Big)-a_2^2\left(a_3+p^2\right)\left(3a_3\left(a_3+p^2\right)+h_{pq}\right)\\
&\quad + a_1\left(a_3+q^2\right)\Big(q^2\left(-3a_1a_3-4a_1p^2+h_{pq}\right)+a_3(a_1a_3+h_{pq})\Big)\Big]\,,\\
S_5^{uv\ell} &= (a_1+a_2)\Big\{3a_1^3q^2\left(a_3+q^2\right)-a_1^2\left(2a_2+a_3+q^2\right)\left[2a_3^2+q^2\left(3a_3+p^2\right)\right]\\
&\quad + a_1\Big[a_2^2\left(3a_3\left(a_3+p^2\right)+h_{pq}\right)+2a_2\left(a_3+q^2\right)\left(3a_3\left(a_3+p^2\right)+2h_{pq}\right)\\
&\quad + \left(a_3+q^2\right)\left(-3\ell^2h_{pq}-2h_{pq}\left(a_3+q^2\right)\right)\Big]-\left(a_3+p^2\right)\Big[\ell^2\Big(a_3(2a_2a_3-h_{pq})\\
&\quad - q^2\left(2a_2p^2+h_{pq}\right)\Big)+a_2\left(2h_{pq}\left(a_2-a_3-q^2\right)+3a_2p^2\left(a_3+q^2\right)\right)\Big]\Big\}\,,
\end{aligned}$$

$$
\begin{aligned}
S_5^{v\ell u} = & -a_1^3 \left[q^2 \left(3q^2 \left(-a_2 + 2a_3 + q^2\right) + 3a_3(a_2 + a_3) + 2a_2p^2 + h_{pq}\right) + a_3(4a_2a_3 + h_{pq})\right] \\
& - a_1^2 \Big[- a_2 \left(4a_3^3 + p^2 \left(5a_3q^2 + h_{pq} + 4q^4\right) + a_3q^2 \left(14a_3 + 9q^2\right)\right) - h_{pq} \left(a_3 + q^2\right)^2 \\
& + a_2^2 \left(3a_3 \left(a_3 - p^2 + 2q^2\right) + h_{pq}\right) \Big] - \ell^2 \Big[a_3 \Big(2a_2a_3 \left(-2a_1^2 + a_1(a_2 + a_3) + 2a_2a_3\right) \\
& + a_2p^2(3a_1a_2 - a_1a_3 + 3h_{pq}) + a_3h_{pq}(a_1 + 7a_2) \Big) \\
& + a_1q^4 \left(3a_1^2 + p^2(4a_1 + 5a_2) - 3h_{pq}\right) + h_{pq}^2(p + q)^2 \\
& - q^2 \Big(p^2 \left(2a_1^2a_2 - a_1a_2 \left(a_2 + p^2\right) + 4a_1h_{pq} + a_2h_{pq}\right) + a_1a_3^2(4a_1 + 5a_2) \\
& + a_3 \left(-3a_1^3 + 6a_1^2a_2 + 2a_2p^2(a_1 + 2a_2) + 6a_1h_{pq} - 3a_2h_{pq}\right) \Big) \Big] + 3a_1^4q^2 \left(a_3 + q^2\right) \\
& - a_1a_2 \Big[a_2p^2 \left(8a_3^2 + 11a_3q^2 + q^4 + p^2q^2\right) + a_2a_3^2 \left(7a_3 + 8q^2\right) - a_2^2 \Big(3a_3 \left(a_3 + p^2\right) \\
& + h_{pq}\Big) + 2h_{pq} \left(a_3 + p^2\right) \left(a_3 + q^2\right) \Big] + h_{pq}\ell^4 \left[a_3(a_1 - 2a_2 + a_3) + q^2 \left(3a_1 - p^2\right)\right] \\
& + a_2^2 \left(a_3 + p^2\right) \left[a_2 \left(3a_3 \left(a_3 + p^2\right) + h_{pq}\right) + h_{pq} \left(a_3 + p^2\right)\right] \, . \qquad \text{(E.10)}
\end{aligned}
$$

References

1. Aguilar, A. C., Cardona, J. C., Ferreira, M. N. & Papavassiliou, J. Non-Abelian Ball-Chiu vertex for arbitrary Euclidean momenta. *Phys. Rev.* **D96,** 014029. arXiv: 1610.06158 [hep-ph] (2017).

2. Aguilar, A. C., Cardona, J. C., Ferreira, M. N. & Papavassiliou, J. Quark gap equation with non-abelian Ball-Chiu vertex. *Phys. Rev.* **D98,** 014002. arXiv: 1804.04229 [hep-ph] (2018).

3. Aguilar, A. C., Ferreira, M. N., Figueiredo, C. T. & Papavassiliou, J. Nonperturbative structure of the ghost-gluon kernel. *Phys. Rev.* **D99,** 034026. arXiv: 1811.08961 [hep-ph] (2019).

4. Aguilar, A. C., Ferreira, M. N., Figueiredo, C. T. & Papavassiliou, J. Nonperturbative Ball-Chiu construction of the three-gluon vertex. *Phys. Rev.* **D99,** 094010. arXiv: 1903.01184 [hep-ph] (2019).

5. Souza, E. V., Ferreira, M. N., Aguilar, A. C., Papavassiliou, J., Roberts, C. D. & Xu, S.-S. Pseudoscalar glueball mass: a window on three-gluon interactions. *Eur. Phys. J.* **A56,** 25. arXiv: 1909.05875 [nucl-th] (2020).

6. Aguilar, A. C., Ferreira, M. N., Figueiredo, C. T. & Papavassiliou, J. Gluon mass scale through nonlinearities and vertex interplay. *Phys. Rev.* **D100,** 094039. arXiv: 1909.09826 [hep-ph] (2019).

7. Aguilar, A. C., De Soto, F., Ferreira, M. N., Papavassiliou, J., Rodríguez-Quintero, J. & Zafeiropoulos, S. Gluon propagator and three-gluon vertex with dynamical quarks. *Eur. Phys. J.* **C80,** 154. arXiv: 1912.12086 [hep-ph] (2020).

8. Aguilar, A. C., Ferreira, M. N. & Papavassiliou, J. Novel sum rules for the three-point sector of QCD. *Eur. Phys. J.* **C80,** 887. arXiv: 2006.04587 [hep-ph] (2020).

9. Aguilar, A. C., Ferreira, M. N. & Papavassiliou, J. Gluon dynamics from an ordinary differential equation. arXiv: 2010.12714 [hep-ph] (Oct. 2020).

10. Aguilar, A. C. & Ferreira, M. N. *Quark mass generation with Schwinger-Dyson equations* in *14th International Workshop on Hadron Physics* (May 2018). arXiv: `1805.09152 [hep-ph]`.

11. Marciano, W. J. & Pagels, H. Quantum Chromodynamics: A Review. *Phys. Rept.* **36,** 137 (1978).

12. Gross, D. J. & Wilczek, F. Ultraviolet Behavior of Nonabelian Gauge Theories. *Phys. Rev. Lett.* **30,** 1343–1346 (1973).

13. Politzer, H. D. Reliable Perturbative Results for Strong Interactions? *Phys. Rev. Lett.* **30,** 1346–1349 (1973).

14. Wilson, K. G. Confinement of quarks. *Phys. Rev.* **D10,** 2445–2459 (1974).

15. Alkofer, R. & von Smekal, L. The infrared behavior of QCD Green's functions: Confinement, dynamical symmetry breaking, and hadrons as relativistic bound states. *Phys. Rept.* **353,** 281. eprint: `hep-ph/0007355` (2001).

16. Greensite, J. *An introduction to the confinement problem* (2011).

17. Nambu, Y. & Jona-Lasinio, G. Dynamical model of elementary particles based on an analogy with superconductivity. I. *Phys. Rev.* **122,** 345–358 (1961).

18. Politzer, H. D. Effective Quark Masses in the Chiral Limit. *Nucl. Phys.* **B117,** 397 (1976).

19. Miransky, V. & Fomin, P. Chiral Symmetry Breakdown and the Spectrum of Pseudoscalar Mesons in Quantum Chromodynamics. *Phys. Lett. B* **105,** 387–391 (1981).

20. Miransky, V. On Dynamical Chiral Symmetry Breaking. *Phys. Lett. B* **165,** 401–404 (1985).

21. Atkinson, D. & Johnson, P. Chiral Symmetry Breaking in QCD. 1. The Infrared Domain. *Phys. Rev. D* **37,** 2290–2295 (1988).

22. Atkinson, D. & Johnson, P. W. Chiral Symmetry Breaking in QCD. 2. Running Coupling Constant. *Phys. Rev.* **D37,** 2296–2299 (1988).

23. Atkinson, D., Johnson, P. & Stam, K. Chiral Symmetry Breaking in QCD. 3. Arbitrary Covariant Gauge. *Phys. Rev. D* **37,** 2996 (1988).

24. Krein, G., Tang, P. & Williams, A. G. Dynamical Chiral Symmetry Breaking in Quantum Chromodynamics With Confinement and Asymptotic Freedom. *Phys. Lett. B* **215,** 145–150 (1988).

25. Aguilar, A. C. & Papavassiliou, J. Chiral symmetry breaking with lattice propagators. *Phys. Rev.* **D83,** 014013. arXiv: `1010.5815 [hep-ph]` (2011).

26. Mitter, M., Pawlowski, J. M. & Strodthoff, N. Chiral symmetry breaking in continuum QCD. *Phys. Rev.* **D91,** 054035. arXiv: `1411.7978 [hep-ph]` (2015).

27. Cornwall, J. M. Dynamical Mass Generation in Continuum QCD. *Phys. Rev. D* **26,** 1453 (1982).

28. Bernard, C. W. Adjoint Wilson Lines and the Effective Gluon Mass. *Nucl. Phys. B* **219,** 341–357 (1983).

29. Donoghue, J. F. The Gluon "Mass" in the Bag Model. *Phys. Rev. D* **29,** 2559 (1984).

30. Aguilar, A. C., Binosi, D. & Papavassiliou, J. Gluon and ghost propagators in the Landau gauge: Deriving lattice results from Schwinger-Dyson equations. *Phys. Rev.* **D78,** 025010. arXiv: `0802.1870 [hep-ph]` (2008).

31. Aguilar, A. C. & Papavassiliou, J. Gluon mass generation without seagull divergences. *Phys. Rev.* **D81,** 034003. arXiv: `0910.4142 [hep-ph]` (2010).

32. Aguilar, A. C., Ibanez, D., Mathieu, V. & Papavassiliou, J. Massless bound-state excitations and the Schwinger mechanism in QCD. *Phys. Rev.* **D85,** 014018. arXiv: `1110.2633 [hep-ph]` (2012).

33. Aguilar, A. C., Binosi, D. & Papavassiliou, J. Gluon mass generation in the presence of dynamical quarks. *Phys. Rev.* **D88,** 074010. arXiv: `1304.5936 [hep-ph]` (2013).

34. Aguilar, A. C., Binosi, D. & Papavassiliou, J. The Gluon Mass Generation Mechanism: A Concise Primer. *Front. Phys.(Beijing)* **11,** 111203. arXiv: `1511.08361 [hep-ph]` (2016).

35. Aguilar, A. C., Binosi, D., Figueiredo, C. T. & Papavassiliou, J. Unified description of seagull cancellations and infrared finiteness of gluon propagators. *Phys. Rev.* **D94,** 045002. arXiv: `1604.08456 [hep-ph]` (2016).

36. Cloet, I. C. & Roberts, C. D. Explanation and Prediction of Observables using Continuum Strong QCD. *Prog. Part. Nucl. Phys.* **77,** 1–69. arXiv: `1310.2651 [nucl-th]` (2014).

37. Eichmann, G., Sanchis-Alepuz, H., Williams, R., Alkofer, R. & Fischer, C. S. Baryons as relativistic three-quark bound states. *Prog. Part. Nucl. Phys.* **91,** 1–100. arXiv: `1606.09602 [hep-ph]` (2016).

38. Slavnov, A. A. Ward Identities in Gauge Theories. *Theor. Math. Phys.* **10,** 99–107 (1972).

39. Taylor, J. C. Ward Identities and Charge Renormalization of the Yang- Mills Field. *Nucl. Phys.* **B33,** 436–444 (1971).

40. Becchi, C., Rouet, A. & Stora, R. Renormalization of the Abelian Higgs-Kibble Model. *Commun. Math. Phys.* **42,** 127–162 (1975).

41. Becchi, C., Rouet, A. & Stora, R. Renormalization of Gauge Theories. *Annals Phys.* **98,** 287–321 (1976).

42. Tyutin, I. Gauge Invariance in Field Theory and Statistical Physics in Operator Formalism. arXiv: `0812.0580 [hep-th]` (1975).

43. Cucchieri, A., Maas, A. & Mendes, T. Three-point vertices in Landau-gauge Yang-Mills theory. *Phys. Rev.* **D77,** 094510. arXiv: `0803.1798 [hep-lat]` (2008).

44. Athenodorou, A., Binosi, D., Boucaud, P., De Soto, F., Papavassiliou, J., Rodríguez-Quintero, J. & Zafeiropoulos, S. On the zero crossing of the three-gluon vertex. *Phys. Lett.* **B761,** 444–449. arXiv: `1607.01278 [hep-ph]` (2016).

45. Boucaud, P., De Soto, F., Rodríguez-Quintero, J. & Zafeiropoulos, S. Refining the detection of the zero crossing for the three-gluon vertex in symmetric and asymmetric momentum subtraction schemes. *Phys. Rev.* **D95,** 114503. arXiv: `1701.07390 [hep-lat]` (2017).

46. Duarte, A. G., Oliveira, O. & Silva, P. J. Further Evidence For Zero Crossing On The Three Gluon Vertex. *Phys. Rev.* **D94,** 074502. arXiv: `1607.03831 [hep-lat]` (2016).

47. Rodríguez-Quintero, J., Athenodorou, A., Binosi, D., Boucaud, P., de Soto, F., Papavassiliou, J. & Zafeiropoulos, S. Three-gluon Green functions: low-momentum

instanton dominance and zero-crossing. *EPJ Web Conf.* **137** (eds Foka, Y., Brambilla, N. & Kovalenko, V.) 03018 (2017).

48. Sternbeck, A., Balduf, P.-H., Kizilersu, A., Oliveira, O., Silva, P. J., Skullerud, J.-I. & Williams, A. G. Triple-gluon and quark-gluon vertex from lattice QCD in Landau gauge. *PoS* **LATTICE2016,** 349. arXiv: `1702.00612 [hep-lat]` (2017).
49. Maas, A. & Vujinović, M. More on the three-gluon vertex in SU(2) Yang-Mills theory in three and four dimensions. arXiv: `2006.08248 [hep-lat]` (June 2020).
50. Huber, M. Q., Maas, A. & von Smekal, L. Two- and three-point functions in two-dimensional Landau-gauge Yang-Mills theory: Continuum results. *JHEP* **11,** 035. arXiv: `1207.0222 [hep-th]` (2012).
51. Pelaez, M., Tissier, M. & Wschebor, N. Three-point correlation functions in Yang-Mills theory. *Phys. Rev.* **D88,** 125003. arXiv: `1310.2594 [hep-th]` (2013).
52. Aguilar, A. C., Binosi, D., Ibañez, D. & Papavassiliou, J. Effects of divergent ghost loops on the Green's functions of QCD. *Phys. Rev.* **D89,** 085008. arXiv: `1312.1212 [hep-ph]` (2014).
53. Blum, A., Huber, M. Q., Mitter, M. & von Smekal, L. Gluonic three-point correlations in pure Landau gauge QCD. *Phys. Rev.* **D89,** 061703. arXiv: `1401.0713 [hep-ph]` (2014).
54. Eichmann, G., Williams, R., Alkofer, R. & Vujinovic, M. The three-gluon vertex in Landau gauge. *Phys. Rev.* **D89,** 105014. arXiv: `1402.1365 [hep-ph]` (2014).
55. Williams, R., Fischer, C. S. & Heupel, W. Light mesons in QCD and unquenching effects from the 3PI effective action. *Phys. Rev.* **D93,** 034026. arXiv: `1512.00455 [hep-ph]` (2016).
56. Blum, A. L., Alkofer, R., Huber, M. Q. & Windisch, A. Unquenching the three-gluon vertex: A status report. *Acta Phys. Polon. Supp.* **8,** 321. arXiv: `1506.04275 [hep-ph]` (2015).
57. Blum, A. L., Alkofer, R., Huber, M. Q. & Windisch, A. Three-point vertex functions in Yang-Mills Theory and QCD in Landau gauge. *EPJ Web Conf.* **137,** 03001. arXiv: `1611.04827 [hep-ph]` (2017).
58. Cyrol, A. K., Fister, L., Mitter, M., Pawlowski, J. M. & Strodthoff, N. Landau gauge

Yang-Mills correlation functions. *Phys. Rev.* **D94,** 054005. arXiv: 1605.01856 [hep-ph] (2016).

59. Huber, M. Q. On nonperturbative Yang-Mills correlation functions. arXiv: 1808.05227 [hep-ph] (2018).

60. Corell, L., Cyrol, A. K., Mitter, M., Pawlowski, J. M. & Strodthoff, N. Correlation functions of three-dimensional Yang-Mills theory from the FRG. *SciPost Phys.* **5,** 066. arXiv: 1803.10092 [hep-ph] (2018).

61. Binosi, D., Ibañez, D. & Papavassiliou, J. The all-order equation of the effective gluon mass. *Phys. Rev.* **D86,** 085033. arXiv: 1208.1451 [hep-ph] (2012).

62. Aguilar, A. C., Binosi, D., Figueiredo, C. T. & Papavassiliou, J. Evidence of ghost suppression in gluon mass scale dynamics. *Eur. Phys. J.* **C78,** 181. arXiv: 1712.06926 [hep-ph] (2018).

63. Binosi, D. & Papavassiliou, J. Coupled dynamics in gluon mass generation and the impact of the three-gluon vertex. *Phys. Rev.* **D97,** 054029. arXiv: 1709.09964 [hep-ph] (2018).

64. Meyers, J. & Swanson, E. S. Spin Zero Glueballs in the Bethe-Salpeter Formalism. *Phys. Rev.* **D87,** 036009. arXiv: 1211.4648 [hep-ph] (2013).

65. Sanchis-Alepuz, H., Fischer, C. S., Kellermann, C. & von Smekal, L. Glueballs from the Bethe-Salpeter equation. *Phys. Rev.* **D92,** 034001. arXiv: 1503.06051 [hep-ph] (2015).

66. Huber, M. Q., Fischer, C. S. & Sanchis-Alepuz, H. Spectrum of scalar and pseudoscalar glueballs from functional methods. arXiv: 2004.00415 [hep-ph] (Apr. 2020).

67. Szczepaniak, A., Swanson, E. S., Ji, C.-R. & Cotanch, S. R. Glueball Spectroscopy in a Relativistic Many-Body Approach to Hadron Structure. *Phys. Rev. Lett.* **76,** 2011–2014. eprint: hep-ph/9511422 (1996).

68. Hou, W.-S. & Wong, G.-G. The glueball spectrum from a potential model. *Phys. Rev.* **D67,** 034003. eprint: hep-ph/0207292 (2003).

69. Mathieu, V., Kochelev, N. & Vento, V. The Physics of Glueballs. *Int. J. Mod. Phys.* **E18,** 1–49. arXiv: 0810.4453 [hep-ph] (2009).

70. Ochs, W. The Status of Glueballs. *J. Phys. G* **40,** 043001. arXiv: 1301.5183 [hep-ph] (2013).

71. Xu, S.-S., Cui, Z.-F., Chang, L., Papavassiliou, J., Roberts, C. D. & Zong, H.-S. New perspective on hybrid mesons. *Eur. Phys. J.* **A55,** 113. arXiv: 1805.06430 [nucl-th] (2019).

72. Faddeev, L. D. & Popov, V. N. Feynman diagrams for the Yang-Mills field. *Phys. Lett.* **B25,** 29–30 (1967).

73. Ilgenfritz, E.-M., Muller-Preussker, M., Sternbeck, A., Schiller, A. & Bogolubsky, I. Landau gauge gluon and ghost propagators from lattice QCD. *Braz.J. Phys.* **37,** 193–200. arXiv: hep-lat/0609043 [hep-lat] (2007).

74. Cucchieri, A. & Mendes, T. What's up with IR gluon and ghost propagators in Landau gauge? A puzzling answer from huge lattices. *PoS* **LAT2007,** 297. arXiv: 0710.0412 [hep-lat] (2007).

75. Cucchieri, A. & Mendes, T. Constraints on the IR behavior of the gluon propagator in Yang-Mills theories. *Phys. Rev. Lett.* **100,** 241601. arXiv: 0712.3517 [hep-lat] (2008).

76. Bogolubsky, I., Ilgenfritz, E., Muller-Preussker, M. & Sternbeck, A. Lattice gluodynamics computation of Landau gauge Green's functions in the deep infrared. *Phys. Lett.* **B676,** 69–73. arXiv: 0901.0736 [hep-lat] (2009).

77. Oliveira, O. & Bicudo, P. Running Gluon Mass from Landau Gauge Lattice QCD Propagator. *J. Phys. G* **G38,** 045003. arXiv: 1002.4151 [hep-lat] (2011).

78. Pawlowski, J. M., Spielmann, D. & Stamatescu, I.-O. Lattice Landau gauge with stochastic quantisation. *Nucl. Phys. B* **830,** 291–314. arXiv: 0911.4921 [hep-lat] (2010).

79. Cucchieri, A., Dudal, D., Mendes, T. & Vandersickel, N. Modeling the Gluon Propagator in Landau Gauge: Lattice Estimates of Pole Masses and Dimension-Two Condensates. *Phys. Rev.* **D85,** 094513. arXiv: 1111.2327 [hep-lat] (2012).

80. Maas, A. Some more details of minimal-Landau-gauge SU(2) Yang-Mills propagators. *Phys. Rev. D* **91,** 034502. arXiv: 1402.5050 [hep-lat] (2015).

81. Ayala, A., Bashir, A., Binosi, D., Cristoforetti, M. & Rodríguez-Quintero, J. Quark

flavour effects on gluon and ghost propagators. *Phys. Rev.* **D86,** 074512. arXiv: `1208.0795 [hep-ph]` (2012).

82. Dudal, D., Sorella, S. P., Vandersickel, N. & Verschelde, H. New features of the gluon and ghost propagator in the infrared region from the Gribov-Zwanziger approach. eprint: `arXiv:0711.4496[hep-th]` (2007).
83. Boucaud, P., Leroy, J. P., Yaouanc, A. L., Micheli, J., Pene, O. & Rodríguez-Quintero, J. The Infrared Behaviour of the Pure Yang-Mills Green Functions. *Few Body Syst.* **53,** 387–436. arXiv: `1109.1936 [hep-ph]` (2012).
84. Schwinger, J. S. Gauge Invariance and Mass. *Phys. Rev.* **125,** 397–398 (1962).
85. Schwinger, J. S. Gauge Invariance and Mass. 2. *Phys. Rev.* **128,** 2425–2429 (1962).
86. Jackiw, R. & Johnson, K. Dynamical Model of Spontaneously Broken Gauge Symmetries. *Phys. Rev.* **D8,** 2386–2398 (1973).
87. Cornwall, J. M. & Norton, R. E. Spontaneous Symmetry Breaking Without Scalar Mesons. *Phys. Rev.* **D8,** 3338–3346 (1973).
88. Poggio, E. C., Tomboulis, E. & Tye, S. .-H. H. Dynamical Symmetry Breaking in Nonabelian Field Theories. *Phys. Rev.* **D11,** 2839 (1975).
89. Smit, J. On the Possibility That Massless Yang-Mills Fields Generate Massive Vector Particles. *Phys. Rev. D* **10,** 2473 (1974).
90. Eichten, E. & Feinberg, F. Dynamical Symmetry Breaking of Nonabelian Gauge Symmetries. *Phys. Rev.* **D10,** 3254–3279 (1974).
91. Creutz, M. Monte Carlo Study of Quantized SU(2) Gauge Theory. *Phys. Rev.* **D21,** 2308–2315 (1980).
92. Morningstar, C. J. & Peardon, M. J. The Glueball spectrum from an anisotropic lattice study. *Phys. Rev.* **D60,** 034509. arXiv: `hep-lat/9901004 [hep-lat]` (1999).
93. Durr, S. *et al.* Ab-Initio Determination of Light Hadron Masses. *Science* **322,** 1224–1227. arXiv: `0906.3599 [hep-lat]` (2008).
94. Gattringer, C. & Lang, C. B. *Quantum chromodynamics on the lattice* ISBN: 978-3-642-01849-7, 978-3-642-01850-3 (Springer, Berlin, 2010).

95. Schwinger, J. S. On the Green's functions of quantized fields. 1. *Proc. Nat. Acad. Sci.* **37,** 452–455 (1951).

96. Dyson, F. J. The S matrix in quantum electrodynamics. *Phys. Rev.* **75,** 1736–1755 (1949).

97. Rivers, R. *Path integral methods in quantum field theory* ISBN: 978-0-521-36870-4, 978-1-139-24186-1 (Cambridge University Press, Oct. 1988).

98. Roberts, C. D. & Williams, A. G. Dyson-Schwinger equations and their application to hadronic physics. *Prog. Part. Nucl. Phys.* **33,** 477–575. eprint: `hep-ph/9403224` (1994).

99. Maris, P. & Roberts, C. D. Dyson-Schwinger equations: A Tool for hadron physics. *Int. J. Mod. Phys.* **E12,** 297–365. arXiv: `nucl-th/0301049 [nucl-th]` (2003).

100. Swanson, E. S. A Primer on Functional Methods and the Schwinger-Dyson Equations. *AIP Conf. Proc.* **1296** (eds Nielsen, M., Navarra, F. S. & Bracco, M. E.) 75–121. arXiv: `1008.4337 [hep-ph]` (2010).

101. Strauss, S., Fischer, C. S. & Kellermann, C. Analytic structure of the Landau gauge gluon propagator. *Phys. Rev. Lett.* **109,** 252001. arXiv: `1208.6239 [hep-ph]` (2012).

102. Strauss, S., Fischer, C. S. & Kellermann, C. Analytic structure of Landau gauge ghost and gluon propagators. *Prog. Part. Nucl. Phys.* **67** (eds Faessler, A. & Rodin, V.) 239–244 (2012).

103. Fischer, C. S. & Huber, M. Q. Landau gauge Yang-Mills propagators in the complex momentum plane. arXiv: `2007.11505 [hep-ph]` (July 2020).

104. Binosi, D. & Papavassiliou, J. Gauge-invariant truncation scheme for the Schwinger-Dyson equations of QCD. *Phys. Rev.* **D77,** 061702. arXiv: `0712.2707 [hep-ph]` (2008).

105. Binosi, D. & Papavassiliou, J. New Schwinger-Dyson equations for non-Abelian gauge theories. *JHEP* **11,** 063. arXiv: `0805.3994 [hep-ph]` (2008).

106. King, J. E. The transverse vertex and gauge technique in Quantum Electrodynamics. *Phys. Rev.* **D27,** 1821 (1983).

107. Haeri Bijan, J. The Ultraviolet Improved Gauge Technique and the Effective Quark Propagator in QCD. *Phys. Rev. D* **38,** 3799 (1988).

108. Curtis, D. C. & Pennington, M. R. Truncating the Schwinger-Dyson equations: How multiplicative renormalizability and the Ward identity restrict the three point vertex in QED. *Phys. Rev.* **D42,** 4165–4169 (1990).

109. Fischer, C. S. & Alkofer, R. Nonperturbative propagators, running coupling and dynamical quark mass of Landau gauge QCD. *Phys. Rev.* **D67,** 094020. arXiv: `hep-ph/0301094 [hep-ph]` (2003).

110. Aguilar, A. C. & Papavassiliou, J. Gluon mass generation in the PT-BFM scheme. *JHEP* **12,** 012. eprint: `hep-ph/0610040` (2006).

111. Kizilersu, A. & Pennington, M. Building the Full Fermion-Photon Vertex of QED by Imposing Multiplicative Renormalizability of the Schwinger-Dyson Equations for the Fermion and Photon Propagators. *Phys. Rev.* **D79,** 125020. arXiv: `0904.3483 [hep-th]` (2009).

112. Narciso Ferreira, A. M. S. & Aguilar, A. C. Gluon Schwinger-Dyson equation in the PT-BFM scheme. *J. Phys. Conf. Ser.* **706,** 052004 (2016).

113. Windisch, A., Huber, M. Q. & Alkofer, R. How to determine the branch points of correlation functions in Euclidean space. *Acta Phys. Polon. Supp.* **6** (eds Bicudo, P., Giacosa, F., Malek, M. & Parganlija, D.) 887–892. arXiv: `1304.3642 [hep-ph]` (2013).

114. Cyrol, A. K., Pawlowski, J. M., Rothkopf, A. & Wink, N. Reconstructing the gluon. *SciPost Phys.* **5,** 065. arXiv: `1804.00945 [hep-ph]` (2018).

115. Binosi, D. & Tripolt, R.-A. Spectral functions of confined particles. *Phys. Lett. B* **801,** 135171. arXiv: `1904.08172 [hep-ph]` (2020).

116. Frederico, T., Duarte, D. C., de Paula, W., Ydrefors, E., Jia, S. & Maris, P. Towards Minkowski space solutions of Dyson-Schwinger Equations through un-Wick rotation. arXiv: `1905.00703 [hep-ph]` (May 2019).

117. Falcão, A. F., Oliveira, O. & Silva, P. J. The analytic structure of the lattice Landau gauge gluon and ghost propagators. arXiv: `2008.02614 [hep-lat]` (Aug. 2020).

118. Boucaud, P., Dudal, D., Leroy, J., Pene, O. & Rodríguez-Quintero, J. On the

leading OPE corrections to the ghost-gluon vertex and the Taylor theorem. *JHEP* **12,** 018. arXiv: `1109.3803 [hep-ph]` (2011).

119. Salam, A. Renormalizable electrodynamics of vector mesons. *Phys. Rev.* **130,** 1287–1290 (1963).

120. Salam, A. & Delbourgo, R. Renormalizable electrodynamics of scalar and vector mesons. II. *Phys. Rev.* **135,** B1398–B1427 (1964).

121. Delbourgo, R. & West, P. C. A Gauge Covariant Approximation to Quantum Electrodynamics. *J. Phys.* **A10,** 1049 (1977).

122. Delbourgo, R. & West, P. C. Infrared Behavior of a Gauge Covariant Approximation. *Phys. Lett.* **B72,** 96 (1977).

123. Cornwall, J. M. & Hou, W.-S. Extension of the Gauge Technique to broken symmetry and finite temperature. *Phys. Rev.* **D34,** 585 (1986).

124. Kim, S. K. & Baker, M. Consequences of Gauge Invariance for the Interacting Vertices in Nonabelian Gauge Theories. *Nucl. Phys. B* **164,** 152–170 (1980).

125. Ball, J. S. & Chiu, T.-W. Analytic Properties of the Vertex Function in Gauge Theories. 1. *Phys. Rev.* **D22,** 2542 (1980).

126. Ball, J. S. & Chiu, T.-W. Analytic Properties of the Vertex Function in Gauge Theories. 2. *Phys. Rev. D* **22.** [Erratum: Phys.Rev.D 23, 3085 (1981)], 2550 (1980).

127. Binosi, D. & Papavassiliou, J. Gauge invariant Ansatz for a special three-gluon vertex. *JHEP* **03,** 121. arXiv: `1102.5662 [hep-ph]` (2011).

128. Aguilar, A. C., Binosi, D., Ibañez, D. & Papavassiliou, J. New method for determining the quark-gluon vertex. *Phys. Rev.* **D90,** 065027. arXiv: `1405.3506 [hep-ph]` (2014).

129. Ball, J. & Zachariasen, F. Infrared Properties of the Glue Propagator in Nonabelian Gauge Theories. *Nucl. Phys. B* **143,** 148–162 (1978).

130. Bar-Gadda, U. Infrared behavior of the effective coupling in quantum chromodynamics: a nonperturbative approach. *Nucl. Phys.* **B163,** 312–332 (1980).

131. Kondo, K.-I. Transverse Ward-Takahashi identity, anomaly and Schwinger-Dyson equation. *Int. J. Mod. Phys.* **A12,** 5651–5686. arXiv: `hep-th/9608100 [hep-th]`

(1997).

132. Hauck, A., Alkofer, R. & von Smekal, L. *A Solution to coupled Dyson-Schwinger equations for gluons and ghosts in Landau gauge* in *Workshop on Methods of Non-perturbative Quantum Field Theory* (Feb. 1998), 81–89. arXiv: `hep-ph/9804387`.

133. Pascual, P. & Tarrach, R. QCD: Renormalization for the practitioner. *Lect. Notes Phys.* **194,** 1–277 (1984).

134. Streater, R. & Wightman, A. *PCT, spin and statistics, and all that* ISBN: 978-0-691-07062-9 (Princeton University Press, 1989).

135. Nemeschansky, D., Preitschopf, C. & Weinstein, M. A BRST primer. *Annals Phys.* **183,** 226 (1988).

136. Schwartz, M. D. *Quantum Field Theory and the Standard Model* ISBN: 978-1-107-03473-0, 978-1-107-03473-0 (Cambridge University Press, Mar. 2014).

137. Binosi, D., Collins, J., Kaufhold, C. & Theussl, L. JaxoDraw: A Graphical user interface for drawing Feynman diagrams. Version 2.0 release notes. *Comput. Phys. Commun.* **180,** 1709–1715. arXiv: `0811.4113 [hep-ph]` (2009).

138. 't Hooft, G. & Veltman, M. Regularization and Renormalization of Gauge Fields. *Nucl. Phys. B* **44,** 189–213 (1972).

139. Celmaster, W. & Gonsalves, R. J. The Renormalization Prescription Dependence of the QCD Coupling Constant. *Phys. Rev.* **D20,** 1420 (1979).

140. Parisi, G. & Petronzio, R. On Low-Energy Tests of QCD. *Phys. Lett.* **B94,** 51 (1980).

141. Badalian, A. M. & Morgunov, V. L. Determination of alpha(s)(1-GeV) from the charmonium fine structure. *Phys. Rev.* **D60,** 116008. eprint: `hep-ph/9901430` (1999).

142. Aguilar, A., Natale, A. & Rodrigues da Silva, P. Relating a gluon mass scale to an infrared fixed point in pure gauge QCD. *Phys. Rev. Lett.* **90,** 152001. arXiv: `hep-ph/0212105` (2003).

143. Aguilar, A. C., Mihara, A. & Natale, A. A. Phenomenological tests for the freezing of the QCD running coupling constant. *Int. J. Mod. Phys.* **A19,** 249–269 (2004).

144. Aguilar, A. C., Binosi, D., Papavassiliou, J. & Rodríguez-Quintero, J. Non-perturbative comparison of QCD effective charges. *Phys. Rev.* **D80,** 085018. arXiv: `0906.2633 [hep-ph]` (2009).

145. Aguilar, A. C., Binosi, D. & Papavassiliou, J. QCD effective charges from lattice data. *JHEP* **07,** 002. arXiv: `1004.1105 [hep-ph]` (2010).

146. Binosi, D., Chang, L., Papavassiliou, J. & Roberts, C. D. Bridging a gap between continuum-QCD and ab initio predictions of hadron observables. *Phys. Lett.* **B742,** 183–188. arXiv: `1412.4782 [nucl-th]` (2015).

147. Binosi, D., Mezrag, C., Papavassiliou, J., Roberts, C. D. & Rodríguez-Quintero, J. Process-independent strong running coupling. *Phys. Rev.* **D96,** 054026. arXiv: `1612.04835 [nucl-th]` (2017).

148. Cui, Z.-F., Zhang, J.-L., Binosi, D., de Soto, F., Mezrag, C., Papavassiliou, J., Roberts, C. D., Rodríguez-Quintero, J., Segovia, J. & Zafeiropoulos, S. Effective charge from lattice QCD. arXiv: `1912.08232 [hep-ph]` (2019).

149. Roberts, C. D. Empirical Consequences of Emergent Mass. *Symmetry* **12,** 1468. arXiv: `2009.04011 [hep-ph]` (2020).

150. Brodsky, S. J. & Shrock, R. Maximum Wavelength of Confined Quarks and Gluons and Properties of Quantum Chromodynamics. *Phys. Lett.* **B666,** 95–99. arXiv: `0806.1535 [hep-th]` (2008).

151. Gao, F., Qin, S.-X., Roberts, C. D. & Rodríguez-Quintero, J. Locating the Gribov horizon. *Phys. Rev.* **D97,** 034010. arXiv: `1706.04681 [hep-ph]` (2018).

152. Gribov, V. N. Quantization of non-Abelian gauge theories. *Nucl. Phys.* **B139,** 1 (1978).

153. Cucchieri, A., Mendes, T. & Santos, E. M. Covariant gauge on the lattice: A New implementation. *Phys. Rev. Lett.* **103,** 141602. arXiv: `0907.4138 [hep-lat]` (2009).

154. Bicudo, P., Binosi, D., Cardoso, N., Oliveira, O. & Silva, P. J. Lattice gluon propagator in renormalizable ξ gauges. *Phys. Rev.* **D92,** 114514. arXiv: `1505.05897 [hep-lat]` (2015).

155. Cucchieri, A., Maas, A. & Mendes, T. Infrared properties of propagators in Landau-gauge pure Yang-Mills theory at finite temperature. *Phys. Rev. D* **75,** 076003. arXiv: `hep-lat/0702022` (2007).

156. Cucchieri, A. & Mendes, T. Electric and magnetic Landau-gauge gluon propagators in finite-temperature SU(2) gauge theory. *PoS* **FACESQCD,** 007. arXiv: `1105.0176 [hep-lat]` (2010).

157. Aouane, R., Bornyakov, V., Ilgenfritz, E., Mitrjushkin, V., Muller-Preussker, M. & Sternbeck, A. Landau gauge gluon and ghost propagators at finite temperature from quenched lattice QCD. *Phys. Rev. D* **85,** 034501. arXiv: `1108.1735 [hep-lat]` (2012).

158. Silva, P., Oliveira, O., Bicudo, P. & Cardoso, N. Gluon screening mass at finite temperature from the Landau gauge gluon propagator in lattice QCD. *Phys. Rev. D* **89,** 074503. arXiv: `1310.5629 [hep-lat]` (2014).

159. Ward, J. C. An Identity in Quantum Electrodynamics. *Phys. Rev.* **78,** 182 (1950).

160. Takahashi, Y. On the generalized Ward identity. *Nuovo Cim.* **6,** 371 (1957).

161. 't Hooft, G. Dimensional regularization and the renormalization group. *Nucl. Phys. B* **61,** 455–468 (1973).

162. Cornwall, J. M. & Papavassiliou, J. Gauge Invariant Three Gluon Vertex in QCD. *Phys. Rev. D* **40,** 3474 (1989).

163. Binosi, D. & Papavassiliou, J. The pinch technique to all orders. *Phys. Rev.* **D66,** 111901(R). eprint: `hep-ph/0208189` (2002).

164. Binosi, D. & Papavassiliou, J. Pinch technique and the Batalin-Vilkovisky formalism. *Phys. Rev.* **D66,** 025024. arXiv: `hep-ph/0204128 [hep-ph]` (2002).

165. Binosi, D. & Papavassiliou, J. Pinch technique selfenergies and vertices to all orders in perturbation theory. *J. Phys. G* **G30,** 203. arXiv: `hep-ph/0301096 [hep-ph]` (2004).

166. Binosi, D. & Papavassiliou, J. Pinch Technique: Theory and Applications. *Phys. Rept.* **479,** 1–152. arXiv: `0909.2536 [hep-ph]` (2009).

167. Cornwall, J. M., Papavassiliou, J. & Binosi, D. *The Pinch Technique and its Applications to Non-Abelian Gauge Theories* (Cambridge University Press, 2010).

168. Abbott, L. F. Introduction to the Background Field Method. *Acta Phys. Polon.* **B13,** 33 (1982).

169. Abbott, L. F. The Background Field Method Beyond One Loop. *Nucl. Phys.* **B185,** 189 (1981).

170. Grassi, P. A., Hurth, T. & Steinhauser, M. Practical algebraic renormalization. *Annals Phys.* **288,** 197–248. eprint: `hep-ph/9907426` (2001).

171. Aguilar, A. C., Binosi, D. & Papavassiliou, J. The dynamical equation of the effective gluon mass. *Phys. Rev.* **D84,** 085026. arXiv: `1107.3968 [hep-ph]` (2011).

172. Aguilar, A. C., Binosi, D. & Papavassiliou, J. Schwinger mechanism in linear covariant gauges. *Phys. Rev.* **D95,** 034017. arXiv: `1611.02096 [hep-ph]` (2017).

173. Aguilar, A. C. & Papavassiliou, J. Power-law running of the effective gluon mass. *Eur.Phys.J.* **A35,** 189–205. arXiv: `0708.4320 [hep-ph]` (2008).

174. Lavelle, M. Gauge invariant effective gluon mass from the operator product expansion. *Phys. Rev.* **D44,** 26–28 (1991).

175. Bogolubsky, I. L., Ilgenfritz, E. M., Muller-Preussker, M. & Sternbeck, A. The Landau gauge gluon and ghost propagators in 4D SU(3) gluodynamics in large lattice volumes. *PoS* **LATTICE2007,** 290. arXiv: `0710.1968 [hep-lat]` (2007).

176. Cucchieri, A. & Mendes, T. Numerical test of the Gribov-Zwanziger scenario in Landau gauge. *PoS* **QCD-TNT09,** 026. arXiv: `1001.2584 [hep-lat]` (2009).

177. Cucchieri, A. & Mendes, T. Constraints on the IR behavior of the ghost propagator in Yang-Mills theories. *Phys. Rev. D* **78,** 094503. arXiv: `0804.2371 [hep-lat]` (2008).

178. Boucaud, P., Leroy, J.-P., Yaouanc, A. L., Micheli, J., Pene, O., *et al.* IR finiteness of the ghost dressing function from numerical resolution of the ghost SD equation. *JHEP* **06,** 012. arXiv: `0801.2721 [hep-ph]` (2008).

179. Boucaud, P., Leroy, J., A., L. Y., Micheli, J., Pène, O. & Rodríguez-Quintero, J. On the IR behaviour of the Landau-gauge ghost propagator. *JHEP* **06,** 099. arXiv: `0803.2161 [hep-ph]` (2008).

180. Aguilar, A. C., Ibañez, D. & Papavassiliou, J. Ghost propagator and ghost-gluon vertex from Schwinger-Dyson equations. *Phys. Rev.* **D87,** 114020. arXiv: `1303.`

3609 [hep-ph] (2013).

181. Pennington, M. & Wilson, D. Are the Dressed Gluon and Ghost Propagators in the Landau Gauge presently determined in the confinement regime of QCD?. *Phys. Rev.* **D84,** 119901. arXiv: 1109.2117 [hep-ph] (2011).

182. Ibañez, D. & Papavassiliou, J. Gluon mass generation in the massless bound-state formalism. *Phys. Rev.* **D87,** 034008. arXiv: 1211.5314 [hep-ph] (2013).

183. Kallen, G. On the definition of the Renormalization Constants in Quantum Electrodynamics. *Helv. Phys. Acta* **25.** [,509(1952)], 417 (1952).

184. Osterwalder, K. & Schrader, R. Axioms for Euclidean Green's functions. *Commun. Math. Phys.* **31,** 83–112 (1973).

185. Osterwalder, K. & Schrader, R. Axioms for Euclidean Green's Functions. 2. *Commun. Math. Phys.* **42,** 281 (1975).

186. Cornwall, J. M. Positivity violations in QCD. *Mod. Phys. Lett.* **A28,** 1330035. arXiv: 1310.7897 [hep-ph] (2013).

187. Kondo, K.-I., Watanabe, M., Hayashi, Y., Matsudo, R. & Suda, Y. Reflection positivity and complex analysis of the Yang-Mills theory from a viewpoint of gluon confinement. *Eur. Phys. J. C* **80,** 84. arXiv: 1902.08894 [hep-th] (2020).

188. Boucaud, P., De Soto, F., Leroy, J., Le Yaouanc, A., Micheli, J., *et al.* Ghost-gluon running coupling, power corrections and the determination of Lambda(MS-bar). *Phys. Rev.* **D79,** 014508. arXiv: 0811.2059 [hep-ph] (2009).

189. Binosi, D., Ibanez, D. & Papavassiliou, J. QCD effective charge from the three-gluon vertex of the background-field method. *Phys. Rev.* **D87,** 125026. arXiv: 1304.2594 [hep-ph] (2013).

190. Binger, M. & Brodsky, S. J. The form factors of the gauge-invariant three-gluon vertex. *Phys. Rev.* **D74,** 054016. eprint: hep-ph/0602199 (2006).

191. Aguilar, A. C., Binosi, D. & Papavassiliou, J. Indirect determination of the Kugo-Ojima function from lattice data. *JHEP* **11,** 066. arXiv: 0907.0153 [hep-ph] (2009).

192. Ibanez, D. Explicit Construction of the Pole Part of the Three-Gluon Vertex. *PoS* **QCD-TNT-II** (eds Binosi, D., Aguilar, A. C., Cornwall, J. M. & Papavassiliou, J.)

025. arXiv: `1112.5081 [hep-ph]` (2011).

193. Sternbeck, A. The Infrared behavior of lattice QCD Green's functions. arXiv: `hep-lat/0609016 [hep-lat]` (2006).

194. Schleifenbaum, W., Maas, A., Wambach, J. & Alkofer, R. Infrared behaviour of the ghost-gluon vertex in Landau gauge Yang-Mills theory. *Phys. Rev. D* **72,** 014017. arXiv: `hep-ph/0411052` (2005).

195. Huber, M. Q. & von Smekal, L. On the influence of three-point functions on the propagators of Landau gauge Yang-Mills theory. *JHEP* **04,** 149. arXiv: `1211.6092 [hep-th]` (2013).

196. Mintz, B. W., Palhares, L. F., Sorella, S. P. & Pereira, A. D. Ghost-gluon vertex in the presence of the Gribov horizon. *Phys. Rev.* **D97,** 034020. arXiv: `1712.09633 [hep-th]` (2018).

197. Barrios, N., Peláez, M., Reinosa, U. & Wschebor, N. The ghost-antighost-gluon vertex from the Curci-Ferrari model: Two-loop corrections. arXiv: `2009.00875 [hep-th]` (Sept. 2020).

198. Ferreira, A. M. S. N. *Comportamento infravermelho do vértice ghost-gluon e suas implicações* Dissertação de Mestrado (Universidade Estadual de Campinas, 2016).

199. Blossier, B., Boucaud, P., De soto, F., Morenas, V., Gravina, M., Pene, O. & Rodríguez-Quintero, J. Ghost-gluon coupling, power corrections and $\Lambda_{\overline{\mathrm{MS}}}$ from twisted-mass lattice QCD at Nf=2. *Phys. Rev. D* **82,** 034510. arXiv: `1005.5290 [hep-lat]` (2010).

200. Zafeiropoulos, S., Boucaud, P., De Soto, F., Rodríguez-Quintero, J. & Segovia, J. Strong Running Coupling from the Gauge Sector of Domain Wall Lattice QCD with Physical Quark Masses. *Phys. Rev. Lett.* **122,** 162002. arXiv: `1902.08148 [hep-ph]` (2019).

201. Cucchieri, A., Mendes, T. & Mihara, A. Numerical study of the ghost-gluon vertex in Landau gauge. *JHEP* **12,** 012. eprint: `hep-lat/0408034` (2004).

202. Bloch, J. C. R. Multiplicative renormalizability of gluon and ghost propagators in QCD. *Phys. Rev.* **D64,** 116011. eprint: `hep-ph/0106031` (2001).

203. Bloch, J. C. R. Multiplicative renormalizability and quark propagator. *Phys. Rev.* **D66,** 034032. arXiv: `hep-ph/0202073 [hep-ph]` (2002).

204. Albino, L., Bashir, A., Guerrero, L. X. G., Bennich, B. E. & Rojas, E. Transverse Takahashi Identities and Their Implications for Gauge Independent Dynamical Chiral Symmetry Breaking. arXiv: `1812.02280 [nucl-th]` (2018).

205. Huber, M. Q. On non-primitively divergent vertices of Yang–Mills theory. *Eur. Phys. J.* **C77,** 733. arXiv: `1709.05848 [hep-ph]` (2017).

206. Cyrol, A. K., Huber, M. Q. & von Smekal, L. A Dyson–Schwinger study of the four-gluon vertex. *Eur. Phys. J.* **C75,** 102. arXiv: `1408.5409 [hep-ph]` (2015).

207. Berntsen, J., Espelid, T. O. & Genz, A. Algorithm 698: DCUHRE: An Adaptive Multidemensional Integration Routine for a Vector of Integrals. *ACM Trans. Math. Softw.* **17,** 452–456. ISSN: 0098-3500. `http://doi-acm-org.ez88.periodicos.capes.gov.br/10.1145/210232.210234` (Dec. 1991).

208. Davydychev, A. I., Osland, P. & Tarasov, O. Three gluon vertex in arbitrary gauge and dimension. *Phys. Rev. D* **54.** [Erratum: Phys.Rev.D 59, 109901 (1999)], 4087–4113. arXiv: `hep-ph/9605348` (1996).

209. De Boor, C. *A Practical Guide to Splines* (Springer New York, 2001).

210. Aguilar, A. C., Binosi, D. & Papavassiliou, J. Unquenching the gluon propagator with Schwinger-Dyson equations. *Phys. Rev.* **D86,** 014032. arXiv: `1204.3868 [hep-ph]` (2012).

211. Bashir, A., Concha-Sanchez, Y., Delbourgo, R. & Tejeda-Yeomans, M. On the Compton scattering vertex for massive scalar QED. *Phys. Rev. D* **80,** 045007. arXiv: `0906.4164 [hep-ph]` (2009).

212. Aguilar, A. C., Binosi, D. & Papavassiliou, J. Renormalization group analysis of the gluon mass equation. *Phys. Rev.* **D89,** 085032. arXiv: `1401.3631 [hep-ph]` (2014).

213. Peskin, M. E. & Schroeder, D. V. *An Introduction to quantum field theory* (Reading, USA: Addison-Wesley, 842 p, 1995).

214. Patel, H. H. Package-X: A Mathematica package for the analytic calculation of one-loop integrals. *Comput. Phys. Commun.* **197,** 276–290. arXiv: `1503.01469`

[hep-ph] (2015).

215. Patel, H. H. Package-X 2.0: A Mathematica package for the analytic calculation of one-loop integrals. *Comput. Phys. Commun.* **218,** 66–70. arXiv: 1612.00009 [hep-ph] (2017).

216. Ashmore, J. A Method of Gauge Invariant Regularization. *Lett. Nuovo Cim.* **4,** 289–290 (1972).